NTIA Report TR-06-437

Interference Potential of Ultrawideband Signals

Part 3: Measurement of Ultrawideband Interference to C-band Satellite Digital Television Receivers

Michael Cotton
Robert Achatz
Jeffery Wepman
Roger Dalke

report series

U.S. DEPARTMENT OF COMMERCE • National Telecommunications and Information Administration

NTIA Report TR-06-437

Interference Potential of Ultrawideband Signals

Part 3: Measurement of Ultrawideband Interference to C-Band Satellite Digital Television Receivers

Michael Cotton
Robert Achatz
Jeffery Wepman
Roger Dalke

U.S. DEPARTMENT OF COMMERCE
Carlos M. Gutierrez, Secretary

Michael D. Gallagher, Assistant Secretary
for Communications and Information

February 2006

DISCLAIMER

Certain commercial equipment, software, and materials are identified in this report to specify the technical aspects of the reported results. In no case does such identification imply recommendation or endorsement by the National Telecommunications and Information Administration, nor does it imply that the material or equipment identified is necessarily the best available for the purpose.

ACKNOWLEDGMENTS

The authors recognize John McCorkle of Freescale, Inc. for his leadership, insight, and insistence on the highest quality. We learned a great deal from working with John in all relevant technical areas. Dr. Paul Runkle of Signal Innovations provided a wealth of expertise in the field of digital signal processing. Given that signal processing was the crux of this project, Paul made significant contributions by ensuring the integrity and efficient execution of our simulations.

This investigation required the services of a number of ITS engineers with a broad range of expertise, some of whom are not included in the list of authors. The authors recognize Brent Bedford for his expertise in test and measurement equipment and techniques; Randy Hoffman, Richard Statz, and Steve Engelking for developing much of the low level software routines needed to automate the experiment via software control; Stephen Wolf for his expertise in video quality assessment; Frank Sanders for sharing knowledge learned in previous interference tests on C-band earth station receivers [9]; Andrew Rogers and Michael Mitchell for their attention to detail in hardware production and signal characterization measurements; and Dr. William Kissick for his support and leadership.

CONTENTS

Page

FIGURES

TABLES

Page

INTERFERENCE POTENTIAL OF ULTRAWIDEBAND SIGNALS

PART 3: MEASUREMENTS OF ULTRAWIDEBAND INTERFERENCE TO C-BAND SATELLITE DIGITAL TELEVISION RECEIVERS

Michael Cotton, Robert Achatz, Jeffery Wepman, and Roger Dalke*

This report provides results from tests that measured digital television (DTV) susceptibility to ultrawideband (UWB) interference. A test system was developed to inject interference with known characteristics into a victim receiver and quantitatively measure susceptibility. In this experiment, a C-band satellite DTV victim receiver was injected with Dithered-Pulse (DP), Direct-Sequence (DS), and Multi-Band OFDM (MB) UWB interference. Results showed that the UWB signals could be categorized into three signal sets of common DTV susceptibility behavior. Interestingly, the categorized signals, band-limited by the DTV receiver filter, also had common characteristics. Set 1 consists of signals whose DTV susceptibility and band-limited signal characteristics resemble Gaussian noise. Set 2 consists of signals more deleterious than Gaussian noise interference. Notably, these signals had a wide range of band-limited signal characteristics and susceptibilities. Set 3 consists of a signal that is relatively benign. Results also showed that measurable band-limited characteristics, e.g., burst duration (*BD*), burst interval (*BI*), fractional on-time (ζ_{DTV}), and peak-to-average ratio (*P/A*), of the interfering signal are useful for predicting susceptibility. Finally, it was determined that continuous and gated noise signals can be used to emulate the interference effects of DS and MB signals for the DTV victim receiver and operational scenarios tested in this study. This might not be true, however, for testing the susceptibility of other victim receivers operating in narrower bandwidths as indicated by amplitude probability distributions as a function of frequency for MB signals band-limited to relatively narrow bandwidths.

Key words: digital television; interference; satellite communications; ultrawideband

1. INTRODUCTION

In April 2002, the Federal Communications Commission (FCC) released *FCC 02-48* [1] legalizing intentional, low-power ultrawideband (UWB) emissions between 3.1 GHz and 10.6 GHz for communications devices operated indoors. UWB emissions were limited to -41 dBm average power in 1-MHz bandwidth and 0 dBm peak power in 50-MHz bandwidth, where average power is measured over a 1-millisecond integration time and peak power measurement duration is unspecified. The rules define a UWB device as one that emits signals with 10-dB bandwidth greater than 500 MHz or greater than 20% of the center frequency.

---

* The authors are with the Institute for Telecommunication Sciences, National Telecommunications and Information Administration, U.S. Department of Commerce, Boulder, Colorado 80305.

The FCC rules do not specify how the bandwidth requirement is achieved, consequently allowing industry considerable breadth in choosing a modulation. This breadth is exemplified by the development of Direct-Sequence (DS) and Multi-band Orthogonal Frequency-Division Multiplexing (MB) ultrawideband technologies. Proponents of DS and MB technologies have both sought standardization from IEEE (Institute of Electrical and Electronics Engineers) 802.15 working group 3a on high-rate (greater than 20 million bits per second) Wireless Personal Area Networks (WPAN). As the name implies, WPAN is intended for short-distance (nominally less than 10 meters) wireless networking of devices such as PCs, personal digital assistants, and mobile phones.

Both DS and MB transmitters are based on state-of-the-art integrated circuitry. DS modulation controls pulse polarity and hence supports phase shifting modulations. It achieves its ultra-wide bandwidth by transmitting sufficiently narrow pulses. An MB device simultaneously modulates 122 carriers spaced 4.125 MHz apart to achieve the ultra-wide bandwidth and frequency hops the modulated carriers between non-overlapping bands.

Since previous work performed at the Institute for Telecommunication Sciences (ITS) [2 – 5] did not specifically look at susceptibility of receivers to interference from DS or MB signals, and since there is little published information on this subject, ITS entered into a Cooperative Research and Development Agreement (CRADA) with the Freescale subsidiary of Motorola, Inc. to study how UWB interference might be predicted.

1.1. Experiment

Interference potential is a general concept where performance degradation of a victim receiver is predicted from interference signal characteristics. Interference potential is derived from numerous susceptibility tests on receivers with a variety of bandwidths and signal demodulation techniques. This 3-part report series describes one such susceptibility test on a C-band satellite DTV receiver. This victim receiver was chosen because it demodulates signals transmitted in the 3.7 to 4.2 GHz frequency range, which lies within the band allocated for UWB operation. It also uses a variety of bandwidths and signal demodulation techniques, which makes it an ideal victim receiver for the study of interference potential. Additionally, instruments capable of providing quantitative DTV signal quality data from various receiver subsystems are readily available.

Part 1 [6] of this report series describes procedures to characterize UWB signal emissions and measure DTV susceptibility. These procedures were executed on a test bed consisting of a satellite signal generator, a vector signal generator (VSG) emitting software-simulated UWB waveforms, a DTV signal monitor, and a vector signal analyzer (VSA). Specifically, the procedures describe how signal quality metrics from various receiver subsystems within the DTV signal monitor can be used to quantify susceptibility and how signal characterization metrics can be obtained from the VSA.

The complexity of the UWB signals made experimental verification difficult. Part 2 [7] of this report series describes how continuous and gated noise signals were used in their place for verification purposes. These signals eliminated the complexities of the UWB signals and provided a simple parameterized theoretical basis for understanding DTV susceptibility results. These tests verified the pre-Viterbi bit error rate (*BER*) and post-Reed-Solomon segment error rate (*SER*) DTV signal quality metrics.

Beyond verification, insight into DTV susceptibility to UWB signals was gained from the gated-noise experiment. Results clearly showed that DTV susceptibility was dependent on the interfering signal gating parameters, such as on-time (τ_{on}) and off-time (τ_{off}), and the bandwidth of the DTV receiver in addition to the more commonly used average and peak power metrics. This dependence on τ_{on} and τ_{off} motivated an investigation into the effects of band-limiting on the temporal parameters and their subsequent correlation to DTV susceptibility. These band-limited metrics include burst duration (*BD*) and burst interval (*BI*), corresponding to τ_{on} and τ_{off}, respectively.

In this report, Part 3 of the report series, the experiment is extended to actual UWB signals. The primary objective of this report is to evaluate the susceptibility of the DTV receiver to the UWB signals. The secondary objective is to determine if DTV susceptibility can be predicted from UWB signal parameters and the bandwidth of the victim receiver as well as band-limited metrics such as *BD* and *BI*. The final objective is to determine if continuous and gated Gaussian noise can be used in place of DS and MB signals, respectively, in susceptibility tests.

1.2. Organization of Report

UWB signals addressed in this report can be divided into two categories: Dithered-Pulse (DP) and DS signals that are specified with pulse parameters, i.e., pulse width (w), pulse repetition period (T_{pulse}), and fractional dither (f_D), and MB signals that are specified with gating parameters, i.e., τ_{on} and τ_{off}. Accordingly, DTV susceptibility and signal characterization results for DP and DS signals are given in Section 2, while results for MB signals are given in Section 3.

DTV susceptibility results are plotted in two different ways. First, post-Reed-Solomon *SER* and pre-Viterbi *BER* of the DTV victim receiver are plotted as a function of interference-to-noise ratio (*INR*) to demonstrate how DTV performance depends on average power of the interfering signals. Second, *INR* and *BER* at the threshold of visibility (TOV), i.e., INR_{TOV} and BER_{TOV}, are plotted as a function of the reciprocal fractional on-time ($1/\zeta$) in dB. These plots demonstrate how DTV susceptibility and forward error correction (FEC) performance depend on pulse and gating parameters of the interfering signals. Signal characterization includes temporal and amplitude analyses of measured UWB signals, which demonstrate the effects of band-limiting by the victim receiver. The temporal analyses are based on crossing statistics. Measured *BD* and *BI* of the band-limited signals are compared to w and T_{pulse} of the DP and DS signals and to τ_{on} and τ_{off} of the MB signals. Amplitude analyses are based on the amplitude probability distribution (*APD*). Measured peak-to-average ratios (*P/A*s) of the band-limited DP and DS signals are compared to *P/A* of band-limited Gaussian noise, measured *P/A*s of the band-limited MB signals are compared to *P/A*s of corresponding band-limited gated Gaussian noise signals. Also provided are spectral analyses based on the power spectral density (*PSD*).

Section 4 summarizes DTV susceptibility test results, identifies signals with common DTV susceptibility behavior, plots DTV susceptibility results as a function of band-limited metrics, i.e, BD, BI, ζ_{DTV}, and P/A, to illustrate correlations, and evaluates the significance and scope of the findings. Finally, the validity of using continuous and gated noise signals to replicate DS and MB signals in this and other susceptibility tests is discussed.

Appendices to this report contain information supporting the main body. Appendix A develops theoretical expressions for the *PSD* of the DP and DS signals. Appendix B provides measured crossing statistics of the UWB signals measured at the satellite radio frequency (RF) and band-limited to the bandwidth of the victim receiver (B_{DTV}), *APD*s of the UWB signals measured at the satellite RF in a variety of bandwidths, *APD*s of the UWB signals measured at the first intermediate frequency (IF) of the victim receiver in the presence of low-noise block downconverter (LNB) noise for interference powers corresponding to INR_{TOV}, and *APD* statistics as a function of frequency and bandwidth of the UWB signals measured at the satellite RF.

2. DP AND DS INTERFERENCE

This section provides DTV susceptibility test results and characterization measurements for DP and DS interference.

2.1. Pulse Parameters

DP and DS signals achieve their ultra-wide bandwidth by transmitting pulses of short duration. These signals are specified by pulse width (w), the nominal pulse period (T_{pulse} = 1/PRF, where PRF is the pulse repetition frequency), and fractional dither (f_D) to quantify pulse offset from T_{pulse}. Table 1 specifies parameters that define the DP signals considered in this report. Fractional on-time is approximated as $\zeta \approx w/T_{pulse}$. Figure 1 illustrates pulse parameters for DP-04.

Table 1. DP Pulse Parameters

Type	Index	w (ns)	T_{pulse} (ns)	ζ	f_D
DP	01	0.094	10,000	9.4×10^{-6}	0.5
	02		1000	9.4×10^{-5}	
	03		100	9.4×10^{-4}	
	04		10	9.4×10^{-3}	

Table 2 specifies parameters that define the DS signals considered in this report. Recall that DS devices multiply each data bit by a code word consisting of L chips. The chips have values of {-1, 0, 1} and are transmitted every $T_{chip} = 1/f_{chip}$, where f_{chip} = 1320 million chips per second. The coded data phase modulates pulses that are approximately 0.58 ns wide. Sparse codes used for DS-02, DS-03, and DS-05 are all zeros except for a single one, which results in distinct pulses every $T_{pulse} = LT_{chip}$. DS codes used for DS-04 and DS-06 have relatively few zeros, which results in tightly-packed pulses every $T_{pulse} = T_{chip}$. Figure 2 illustrates pulse parameters for DS-03 and DS-04.

Table 2. DS Pulse Parameters†

Type	Index	DS Parameters		Pulse Parameters			
		L	Code Type	w (ns)	T_{pulse} (ns)	ζ	f_D
DS	01	1	N/A	0.58	0.758	0.77	0.0
	02	3	Sparse		2.27	0.26	
	03	6	Sparse		4.55	0.13	
	04	12	DS		0.758	0.77	
	05	12	Sparse		9.09	0.064	
	06	24	DS		0.758	0.77	

---

† The specific codes are [1] for DS-01, [0 1 0] for DS-02, [0 0 1 0 0 0] for DS-03, [0 -1 -1 -1 1 1 1 -1 1 1 -1 1] for DS-04, [0 0 0 0 0 0 0 0 1 0 0 0] for DS-05, and [-1 1 -1 -1 1 -1 -1 1 -1 0 -1 0 -1 -1 1 1 1 -1 1 1 1 -1 -1 -1] for DS-06.

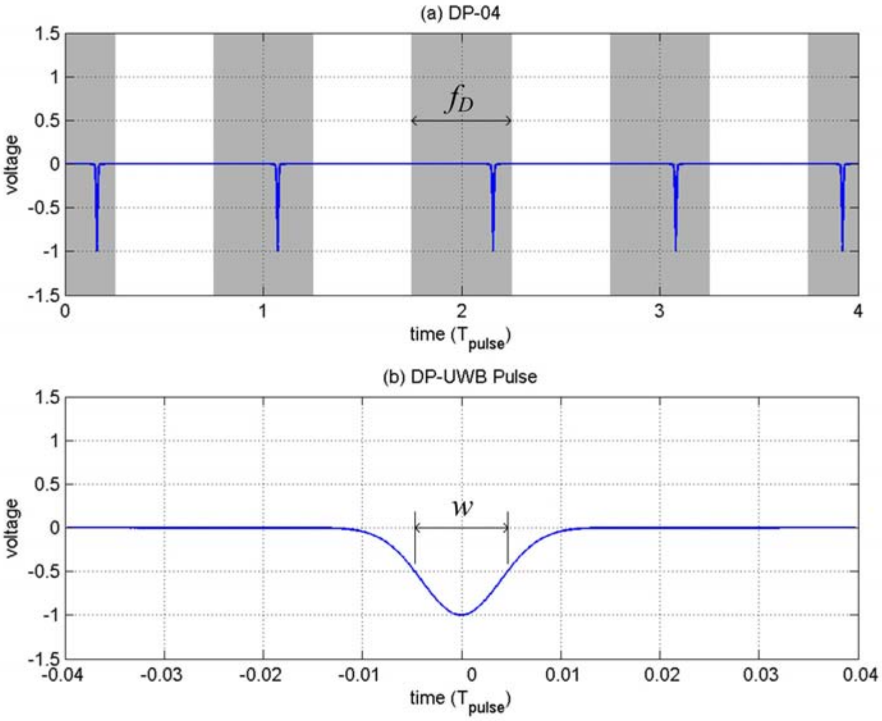

Figure 1. Simulated DP-04 (T_{pulse} = 10 ns).

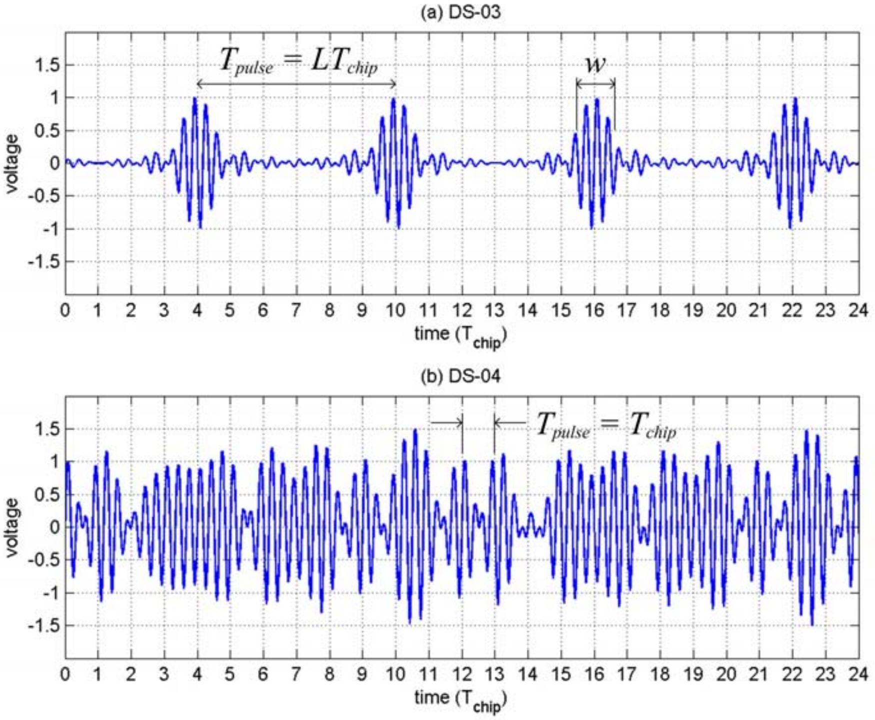

Figure 2. Simulated (a) DS-03 and (b) DS-04 transmitting random data (T_{chip} = 0.758 ns).

2.2. DTV Susceptibility to DP and DS Interference

Results of the DTV susceptibility tests for DP and DS interference are described in this section. Post-Reed-Solomon segment error rate and pre-Viterbi bit error rate are plotted versus the ratio of average interference power to average noise power. Additionally, DTV susceptibility and FEC performance metrics, i.e., INR_{TOV} and BER_{TOV}, are plotted versus $1/\zeta$ in dB. Figure 3 illustrates reference points for signal powers and DTV signal quality metrics acquired during the DTV susceptibility tests.

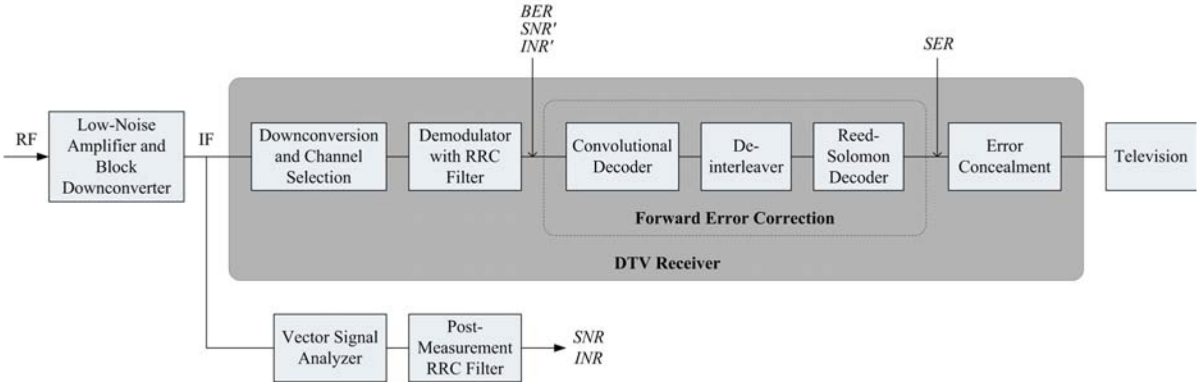

Figure 3. *SNR*, *SNR′*, *INR*, *INR′*, *BER*, and *SER* reference points.

2.2.1. DTV Signal Quality as a Function of Interference Average Power

Figures 4 – 9 provide composite plots of measured *SER* and *BER* as a function of *INR* for measured $SNR = \{9, 12, 15\}$ dB corresponding to $SNR' = \{8.2, 10.5, 12.5\}$ dB at the output of the demodulator. Each page is dedicated to a single *SNR*, each plot is dedicated to a specific signal type, and each curve represents a single T_{pulse}. Figures 4, 6, and 8 provide composite plots of *SER*, while Figures 5, 7, and 9 provide composite plots of *BER*. For each plot, Gaussian noise (GN-01) results are provided as a reference.

The following are general comments regarding the shift, separation, and slope of these *SER* and *BER* curves. Both *BER* and *SER* shifted toward greater *INR* with increasing *SNR*. This occurred because more interference was needed to degrade stronger satellite signals. The shift of DP-01 *BER* and *SER* was significantly greater than the other interference signals. *SER* due to DS signals was similar to *SER* due to GN-01. *SER* due to DP signals showed separation from GN-01 only when T_{pulse} was greater than 100 ns. Relative to Gaussian-noise degradation, the DTV receiver was more susceptible to DP-02 and less susceptible to DP-01. With the exception of DP-01 and DP-02, all DP and DS *SER* curves were steeper than corresponding *BER* curves, which indicates that *SER* was more sensitive than *BER* to changes in average interference power as expected with forward error correction. When $T_{pulse} > 100$ ns, the *SER* slope flattened with increasing T_{pulse}. In fact, the slope of DP-01 *SER* was so low that oscillations indicative of the systematic error mentioned in Appendix B of Part 2 of this report series were revealed.

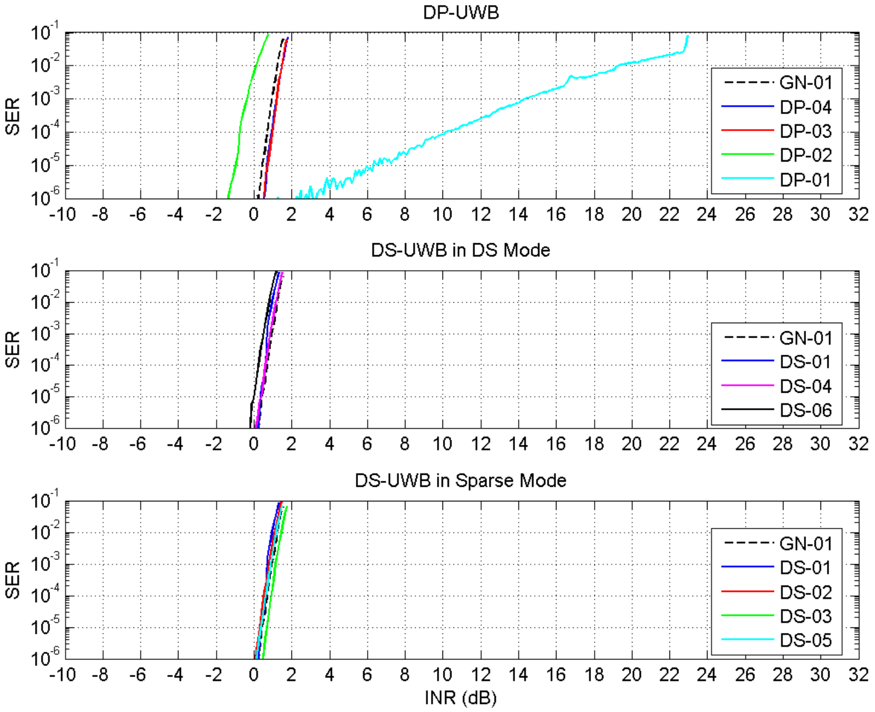

Figure 4. *SER* versus *INR* for a DTV channel operating at *SNR* = 9 dB and exposed to DP and DS interference.

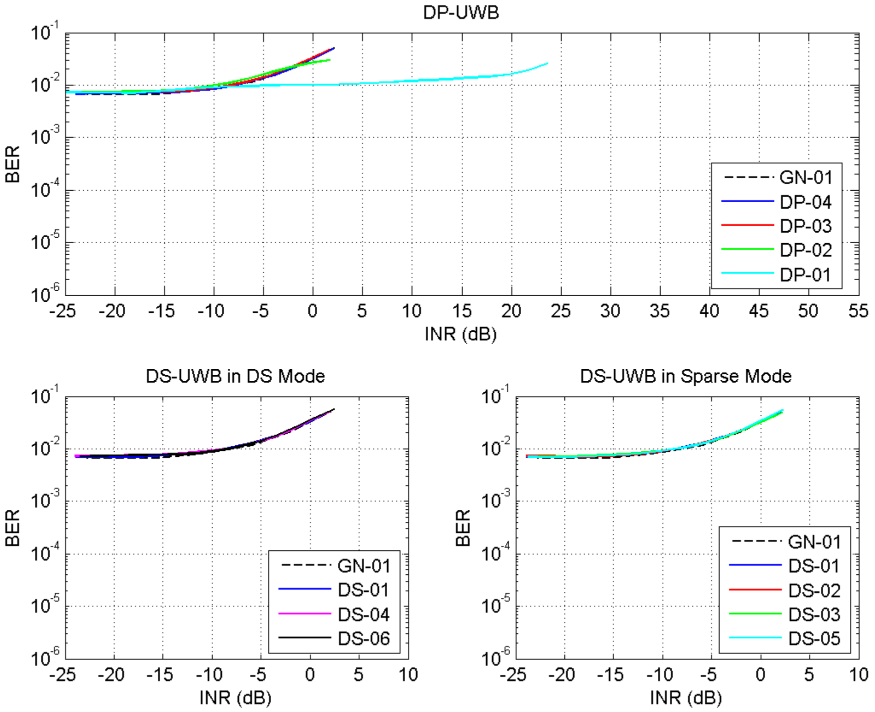

Figure 5. *BER* versus *INR* for a DTV channel operating at *SNR* = 9 dB and exposed to DP and DS interference.

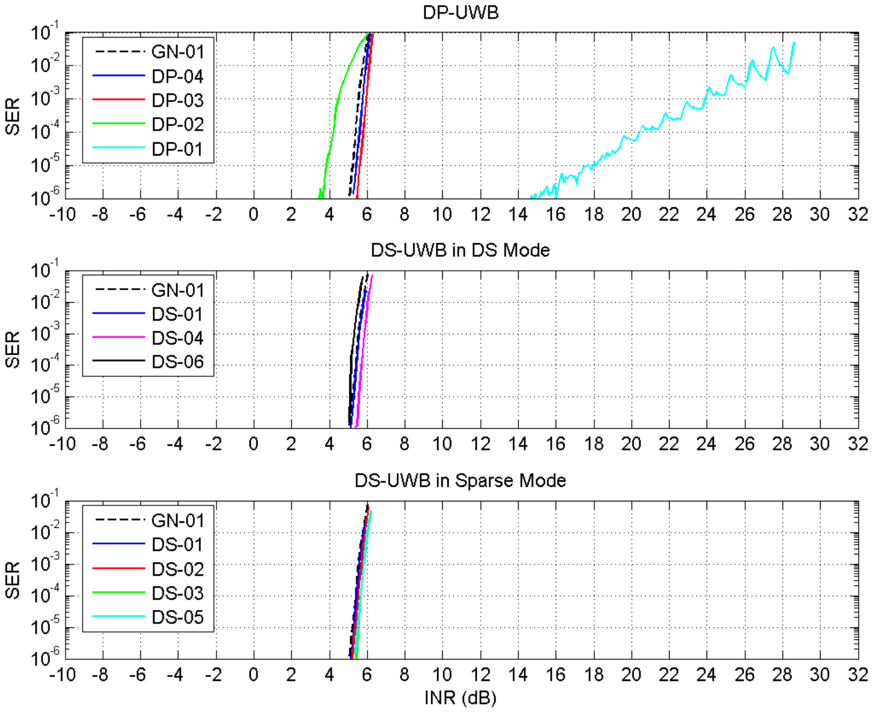

Figure 6. *SER* versus *INR* for a DTV channel operating at *SNR* = 12 dB and exposed to DP and DS interference.

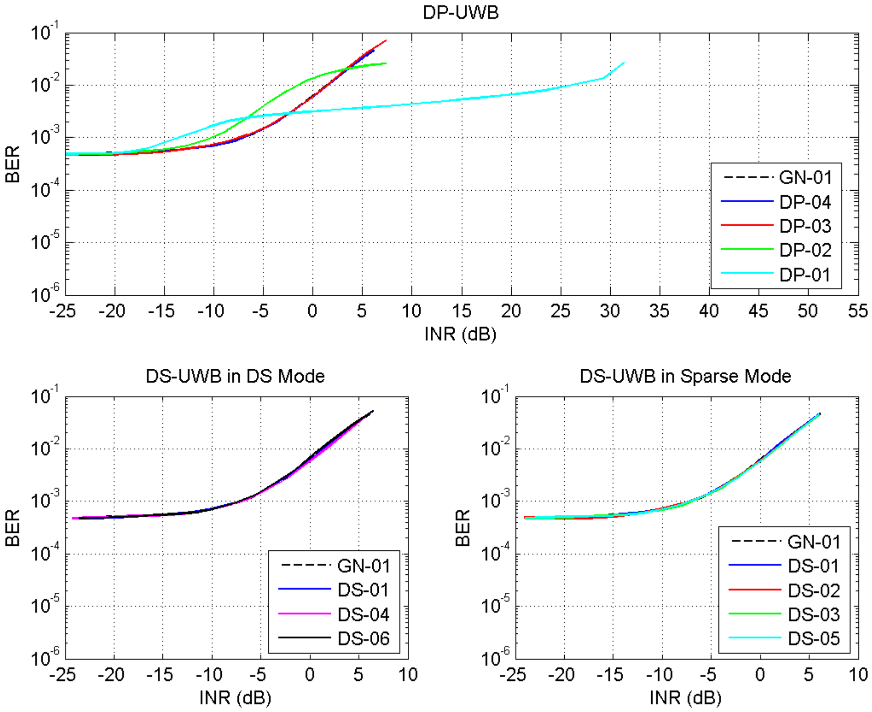

Figure 7. *BER* versus *INR* for a DTV channel operating at *SNR* = 12 dB and exposed to DP and DS interference.

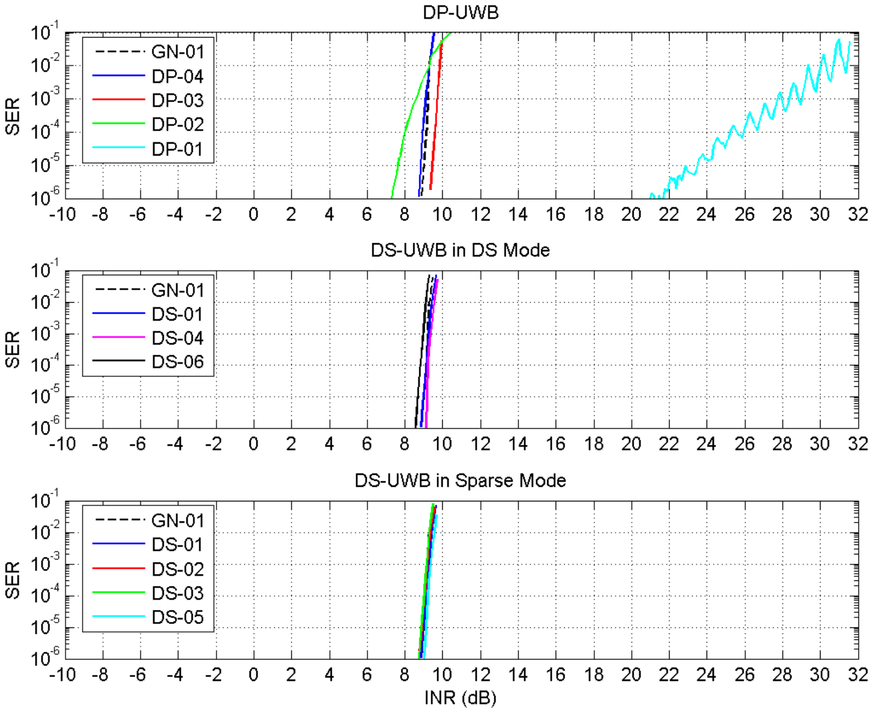

Figure 8. *SER* versus *INR* for a DTV channel operating at *SNR* = 15 dB and exposed to DP and DS interference.

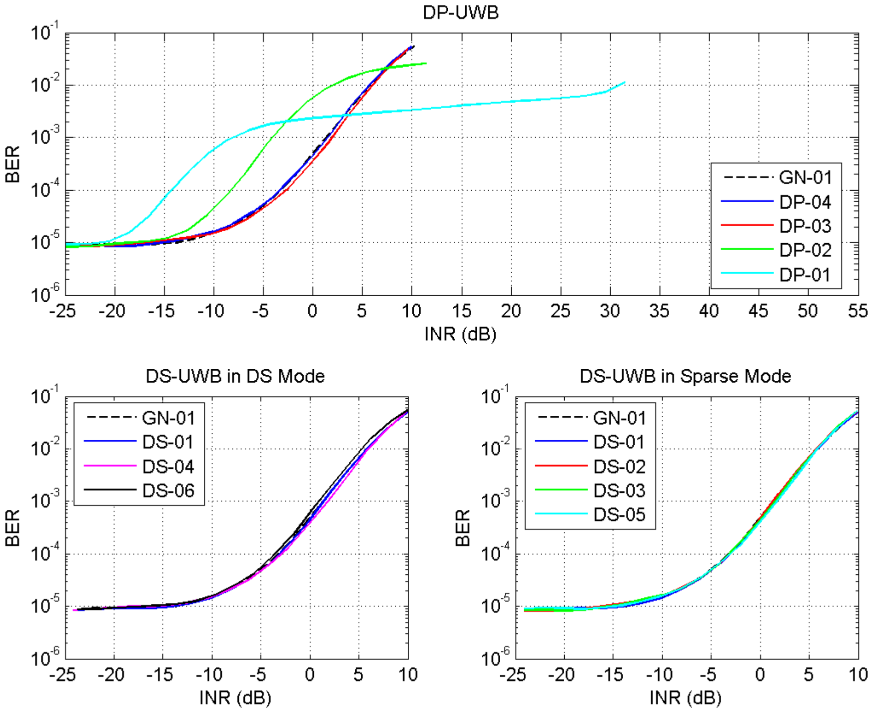

Figure 9. *BER* versus *INR* for a DTV channel operating at *SNR* = 15 dB and exposed to DP and DS interference.

2.2.2. DTV Susceptibility as a Function of Fractional On-Time

Figure 10 displays measured *SER* and *BER* curves for a DTV victim receiver operating at *SNR* = 15 dB and exposed to increasing levels of Gaussian noise interference. This figure also identifies important DTV susceptibility and FEC performance metrics. Importantly, $SER_{TOV} = 10^{-4}$ is a level identified by video quality studies [8] as the threshold of visibility (TOV) where video quality degradation is first evident.

The *INR* that corresponds to SER_{TOV}, INR_{TOV}, is our primary DTV susceptibility metric. That is, receiver susceptibility increases as INR_{TOV} decreases. The *BER* that corresponds to SER_{TOV}, BER_{TOV}, is our FEC performance metric. This metric quantifies the ability of the FEC to overcome bit errors caused by interference to achieve SER_{TOV}. In other words, larger BER_{TOV} indicates more corrected bits and better FEC performance at the threshold of visibility.

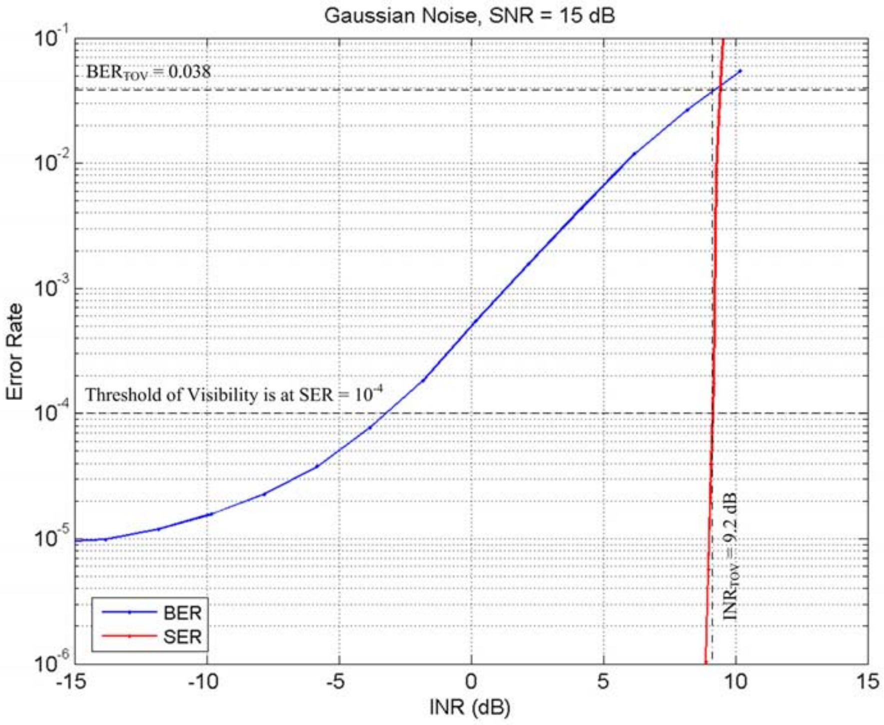

Figure 10. Illustration of threshold-of-visibility metrics.

Table 3 gives INR_{TOV} and BER_{TOV} results for DP and DS interference; GN-01 results from Part 2 of this report series are also included for comparison purposes. Differences between INR_{TOV} of DS, DP-03, DP-04, and GN-01 results were less than 0.5 dB.

Table 3. Measured DTV Susceptibility and FEC Performance for DP and DS Interference

Type	Index	$SNR \approx$ 9 dB		$SNR \approx$ 12 dB		$SNR \approx$ 15 dB	
		INR_{TOV} (dB)	BER_{TOV}	INR_{TOV} (dB)	BER_{TOV}	INR_{TOV} (dB)	BER_{TOV}
DP	01	10.2	0.012	20.4	0.007	25.2	0.006
	02	-0.7	0.025	4.2	0.021	8.0	0.022
	03	1.0	0.041	5.8	0.045	9.6	0.049
	04	0.9	0.038	5.6	0.039	9.0	0.040
DS	01	0.6	0.038	5.4	0.038	9.1	0.038
	02	0.5	0.038	5.5	0.038	9.1	0.039
	03	0.9	0.038	5.7	0.039	9.0	0.040
	04	0.6	0.039	5.7	0.041	9.2	0.042
	05	0.6	0.039	5.7	0.041	9.2	0.042
	06	0.2	0.037	5.2	0.038	8.8	0.039
GN	01	0.7	0.038	5.4	0.038	9.2	0.038

Recall from Part 2 of this report series that high DTV susceptibility, i.e., low INR_{TOV}, correlated with poor FEC performance, i.e., low BER_{TOV}. This demonstrated that DTV susceptibility was related to how effective the FEC was at overcoming bit errors caused by the interference at TOV. DP-01 demonstrates a distinct contrast with this trend, i.e., high DTV susceptibility did not correspond to poor FEC performance based on the chosen metric BER_{TOV}.

Figures 11 – 16 provide plots of INR_{TOV} and BER_{TOV} as a function of $10\log(1/\zeta)$, where DP pulse parameters $w = 0.094$ ns and $T_{pulse} = \{10^4, 10^3, 10^2, 10\}$ ns correspond to $\zeta = \{9.4\times10^{-6}, 9.4\times10^{-5}, 9.4\times10^{-4}, 9.4\times10^{-3}\}$ and $10\log(1/\zeta) = \{50, 40, 30, 20\}$ dB, and DS pulse parameters $w = 0.58$ ns and $T_{pulse} = \{0.758, 2.27, 4.55, 9.09\}$ ns correspond to $\zeta = \{0.77, 0.26, 0.13, 0.064\}$ and $10\log(1/\zeta) = \{1.6, 5.9, 8.9, 12\}$ dB. The independent variable $10\log(1/\zeta)$ was chosen because average power is proportional to ζ. Data points for DS-04 and DS-06 were excluded from the plots because they have the same ζ as DS-01. The horizontal dashed reference line in each INR_{TOV} plot corresponds to DTV susceptibility to Gaussian noise interference. Results demonstrate that DTV susceptibility can be related to particular pulse parameters. Generally speaking, DTV susceptibility to DS interference and DP interference with $10\log(1/\zeta) \leq 30$ dB was comparable to that of Gaussian noise interference. At larger $10\log(1/\zeta)$, however, the DTV receiver was relatively more susceptible to DP-02 and less susceptible to DP-01.

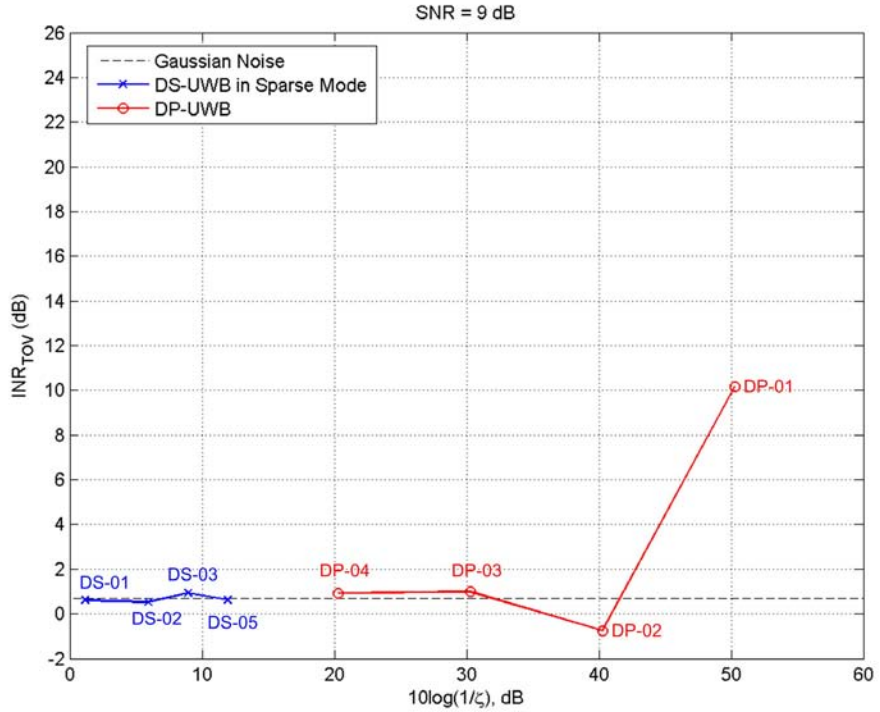

Figure 11. INR_{TOV} versus 10log(1/ζ) for a DTV channel operating at SNR = 9 dB and exposed to DP and DS interference.

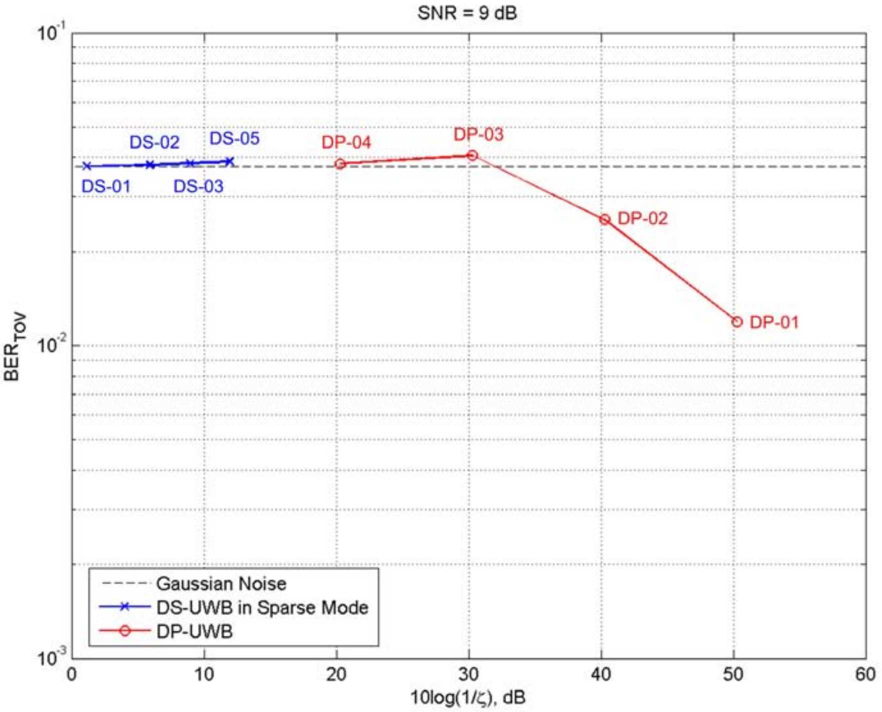

Figure 12. BER_{TOV} versus 10log(1/ζ) for a DTV channel operating at SNR = 9 dB and exposed to DP and DS interference.

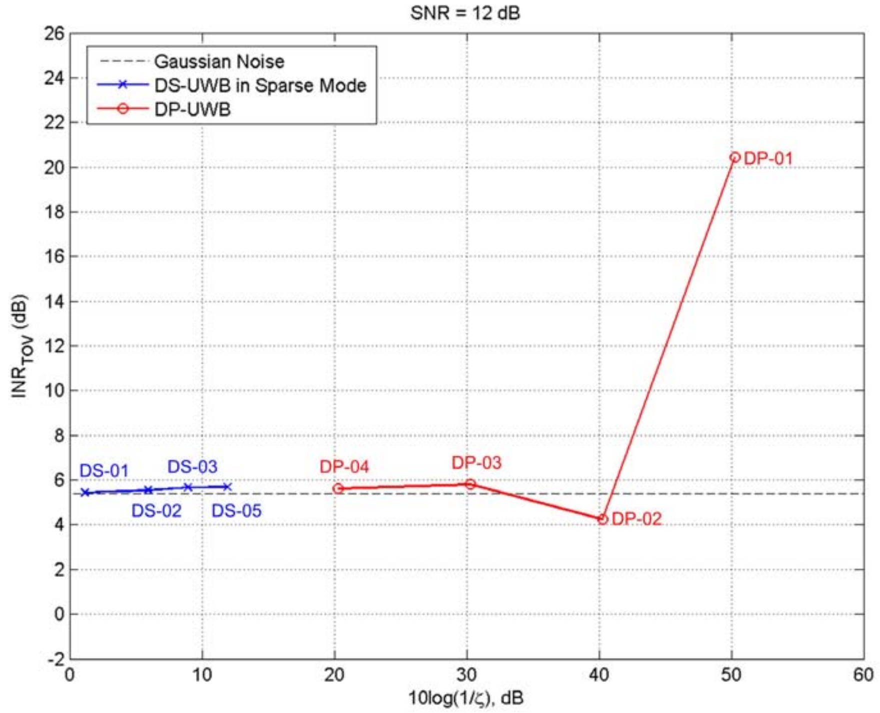

Figure 13. INR_{TOV} versus 10log(1/ζ) for a DTV channel operating at SNR = 12 dB and exposed to DP and DS interference.

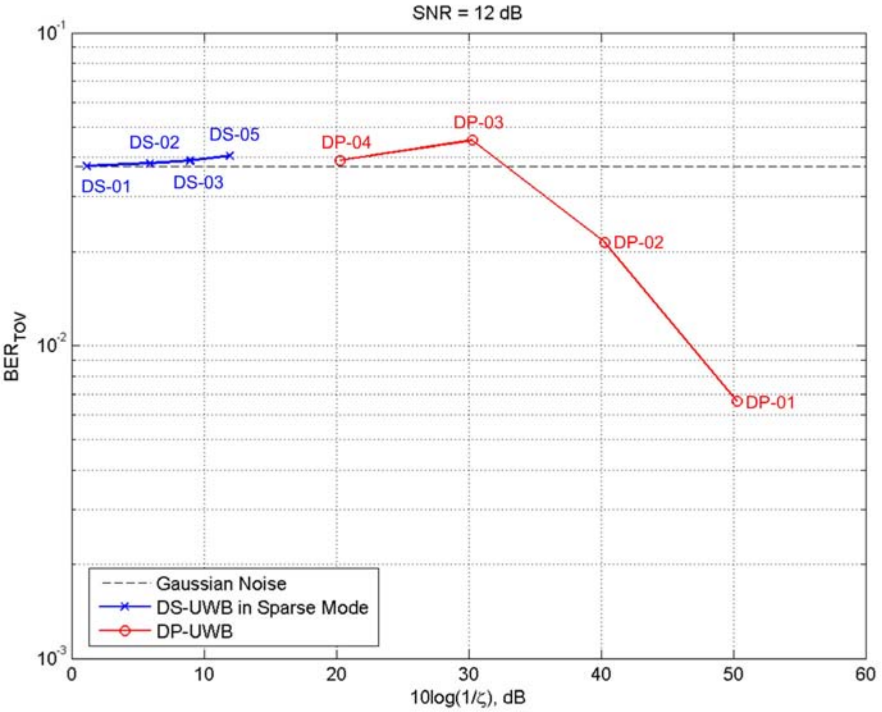

Figure 14. BER_{TOV} versus 10log(1/ζ) for a DTV channel operating at SNR = 12 dB and exposed to DP and DS interference.

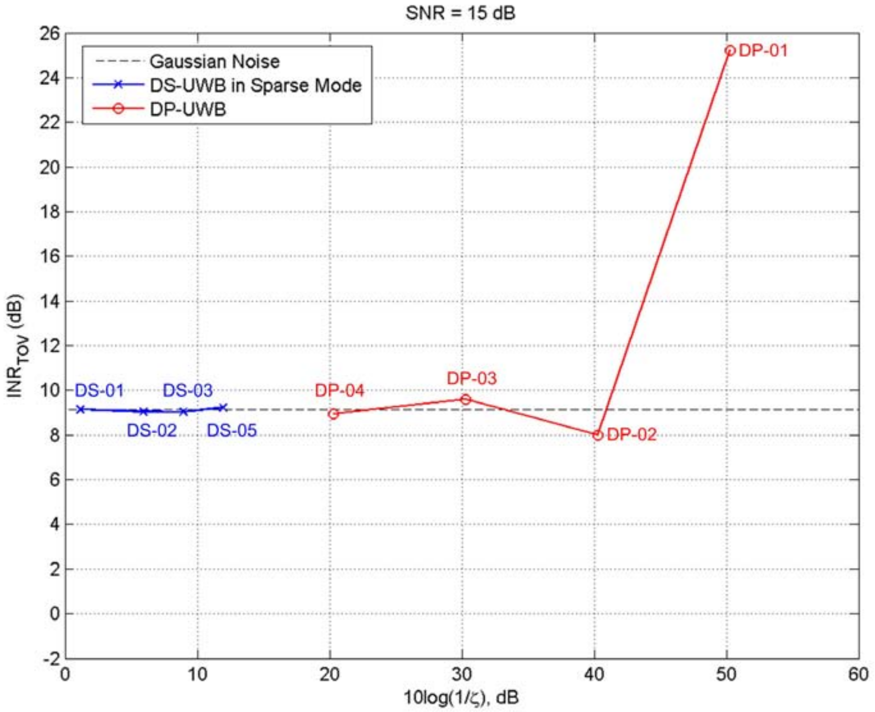

Figure 15. INR_{TOV} versus 10log(1/ζ) for a DTV channel operating at SNR = 15 dB and exposed to DP and DS interference.

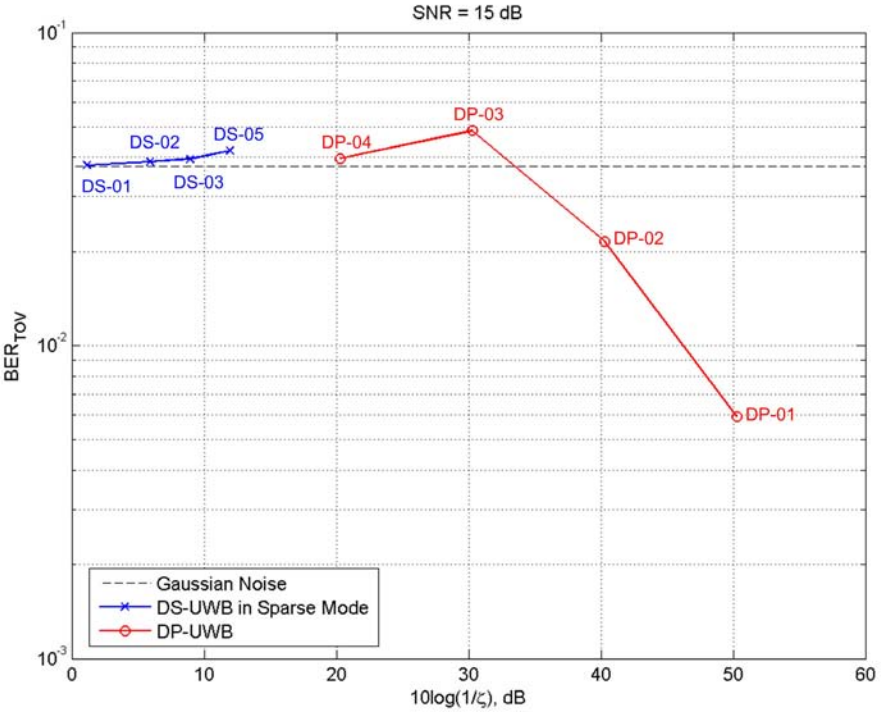

Figure 16. BER_{TOV} versus 10log(1/ζ) for a DTV channel operating at SNR = 15 dB and exposed to DP and DS interference.

2.3. Characterization of DP and DS Signals

Characterization of the DP and DS signals was accomplished via temporal, amplitude, and spectral analyses. The UWB signals were measured with the vector signal analyzer under optimal measurement conditions at the RF output of the vector signal generator. Appendix B discusses the measurement setup and provides an extensive set of results. This section provides band-limited signal characterization results for the B_{DTV} = 19.51-MHz DTV receiver root-raised-cosine (RRC) filter.

2.3.1. Temporal Analysis

Temporal characteristics of the DP and DS signals were evaluated with crossing statistics, i.e., probabilities of the time duration that commences when a signal crosses an amplitude threshold and stays either above or below that threshold. Measured cumulative distribution functions for pulse duration (*PD*) and pulse interval (*PI*) statistics are given in Section B.2. Burst duration (*BD*) and burst interval (*BI*) are defined as the 10th percentile of *PD* and *PI*, respectively, using a crossing threshold equal to -70 dBm. This crossing threshold was useful for quantifying the effects of band-limiting on temporal characteristics of UWB signals, because it is high enough to avoid significant contribution from the measurement system noise floor and low enough to discern pulses and gated signals given the described measurement conditions.

Table 4 summarizes the effects of band-limiting on the temporal characteristics of the DP and DS signals. DP-01 and DP-02 pulses were resolved because T_{pulse} was significantly greater than $1/B_{DTV}$. As expected for these signals, band-limiting lengthened pulse widths, $BD > w$, and increased fractional on-times, $\zeta_{DTV} = BD/(BD + BI) > \zeta$. Notice that *BI* for DP-01 was greater than T_{pulse} due to dithering. *BD* and *BI* are less meaningful estimates when pulses are not resolved in the limiting bandwidth B_{DTV}, because there are no on- and off-times to distinguish. This was the case for DS signals, DP-03, and DP-04, whose crossing statistics resembled those of GN-01, i.e., *BI* was invariably 0.02 µs, and the variability in *BD* had little effect on $\zeta_{DTV} \approx 1$.

Table 4. Measured Temporal Characteristics of DP and DS Signals Band-Limited to B_{DTV}

Type	Index	Pulse Parameters			Band-Limited Metrics		
		w (µs)	T_{pulse} (µs)	ζ	BD (µs)	BI (µs)	ζ_{DTV}
DP	01	0.000094	10.0	9.4×10^{-6}	0.22	11.24	0.02
	02		1.0	9.4×10^{-5}	0.20	0.91	0.18
	03		0.1	9.4×10^{-4}	2.26	0.02	0.99
	04		0.01	9.4×10^{-3}	8.46	0.02	1.00
DS	01	0.00058	0.000758	0.77	7.40	0.02	1.00
	02		0.00227	0.26	8.36	0.02	1.00
	03		0.00455	0.13	8.10	0.02	1.00
	04		0.000758	0.77	9.03	0.02	1.00
	05		0.00909	0.064	11.22	0.02	1.00
	06		0.000758	0.77	3.71	0.02	0.99
GN	01	N/A	N/A	1.00	6.92	0.02	1.00

2.3.2. Amplitude Analysis

Amplitudes of the DP and DS signals were characterized with amplitude probability distributions, which give the probability that the signal amplitude exceeds a certain value. In this report, *APD*s are plotted on Rayleigh graphs where Rayleigh-distributed amplitudes of complex-Gaussian noise appear as a negatively-sloped, straight line. The sorting method, documented in Appendix D of Part 1 of this report series, was used to estimate and plot *APD*s of 131,072 samples that are free of correlation introduced by the measurement system bandwidth and band-limiting in post-measurement processing.

Figures 17 and 18 provide composite *APD* plots of measured DP and DS signals, respectively. The upper bound of the shaded region is the average power of the VSA noise, approximately -79.7 dBm in B_{DTV}. Notice that measured average powers, indicated in the legends, were proportional to ζ. Band-limiting had profound effects on the *APD*s of the DP and DS signals. For signals with $T_{pulse} > 1/B_{DTV}$, a step-like *APD* occurred, where higher amplitudes corresponded to elongated pulses and lower amplitudes corresponded to system noise observable during the shortened off-times between pulses. DP-01 and DP-02 band-limited to B_{DTV} have step-like *APD*s. For signals with $T_{pulse} \leq 1/B_{DTV}$ a negatively-sloped, straight *APD* can occur, corresponding to Rayleigh-distributed amplitudes due to elongated pulses overlapping each other. DS-01 and DS-02 band-limited to B_{DTV} have Rayleigh-distributed *APD*s.

Table 5 summarizes measured peak-to-average ratio and *APD* characteristics for the band-limited DS and DP signals. *APD* characteristics are labeled RAYL for Rayleigh-distributed amplitudes or RP for resolved pulses. More specifically, RP designates a step-like *APD* whose amplitude falls below the average power of the VSA noise at least 10% of the time. Notice that measured *P/A*s of the DS signals were 0 – 3 dB less than *P/A* of GN-01.

Table 5. Measured Amplitude Characteristics of DP and DS Signals Band-Limited to B_{DTV}

Type	Index	*P/A* (dB)	*APD*
DP	01	23.5	RP
	02	13.8	RP
	03	5.4	
	04	8.1	
DS	01	9.5	RAYL
	02	9.0	RAYL
	03	8.1	
	04	6.6	
	05	6.6	
	06	6.8	
GN	01	9.6	RAYL

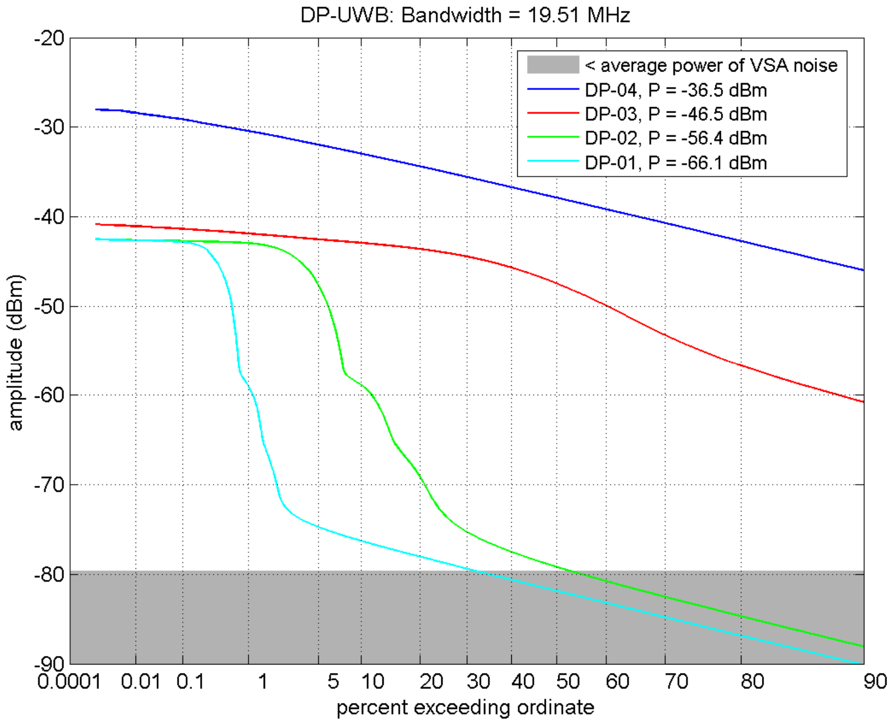

Figure 17. *APD*s of DP signals band-limited to B_{DTV}.

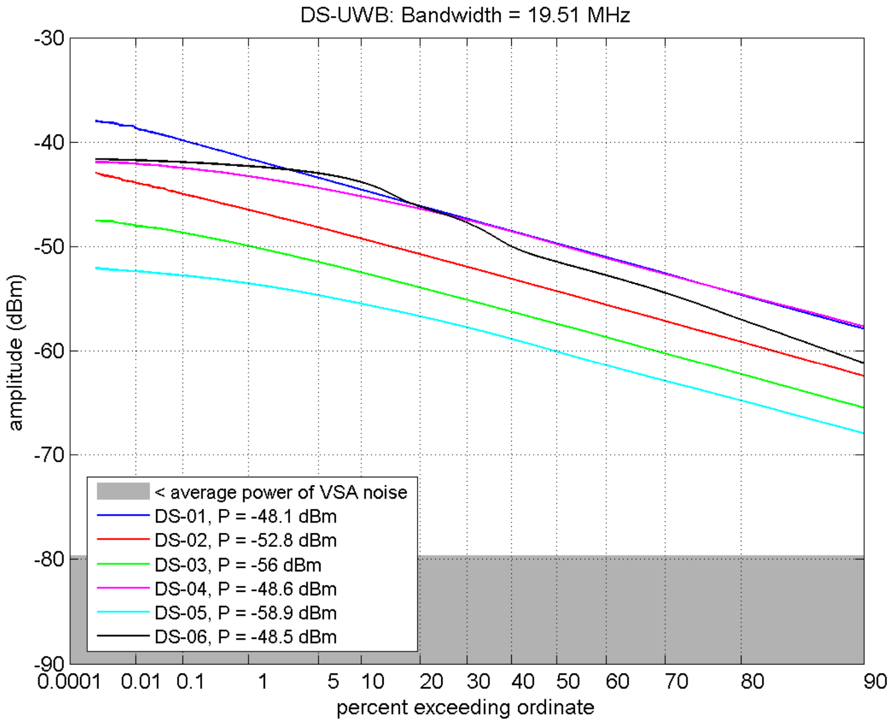

Figure 18. *APD*s of DS signals band-limited to B_{DTV}.

2.3.3. Spectral Analysis

Spectral characteristics of the DP and DS signals were characterized with the power spectral density, which represents the average power present per unit bandwidth as a function of frequency. Appendix A provides theoretical analyses of the *PSD* for DP and DS signals. In short, *PSD*s of the DP signals have discrete and continuous components that depend on the pulse spectrum and the dither function, while *PSD*s of the DS signals have only a continuous component that depends on the pulse spectrum and the code word spectrum.

*PSD*s were calculated from VSA measurements by averaging squared spectrum magnitudes of 500 rectangular-windowed, non-overlapping blocks of signal data. The periodic nature of the signals required that the block size be an integer multiple of the pulse period. To have the same Δf, the block size must also be a common integer multiple of all pulse periods. For the DP signals, these requirements were satisfied with a block size equal to 100 µs, which corresponds to $\Delta f = 10.0$ kHz. For the DS signals, these requirements were satisfied with a block size equal to 90.9 µs, which corresponds to $\Delta f = 11.0$ kHz.

Figures 19 – 20 provide *PSD*s of the DP and DS signals, respectively, in the frequency band of the DTV victim receiver, i.e., 0 Hz on the plots corresponds to 3820 MHz. The victim receiver RRC filter was not applied to the data in post-measurement processing. The measured *PSD*s of DP signals, DS-01, DS-02, DS-03, DS-04, and DS-05 were flat over the DTV frequency band. In contrast and in agreement with Figure A-6, the *PSD* of DS-06 was not flat due to the code word spectrum. Notice that the measured power densities of the DP and DS signals were proportional to ζ. Also, the spectral line at 0 Hz, most prevalent in DP-01, was due to VSG local-oscillator feed-through. The influence of the VSG local-oscillator feed-through on test results was discussed in Appendix C of Part 1 of this report series.

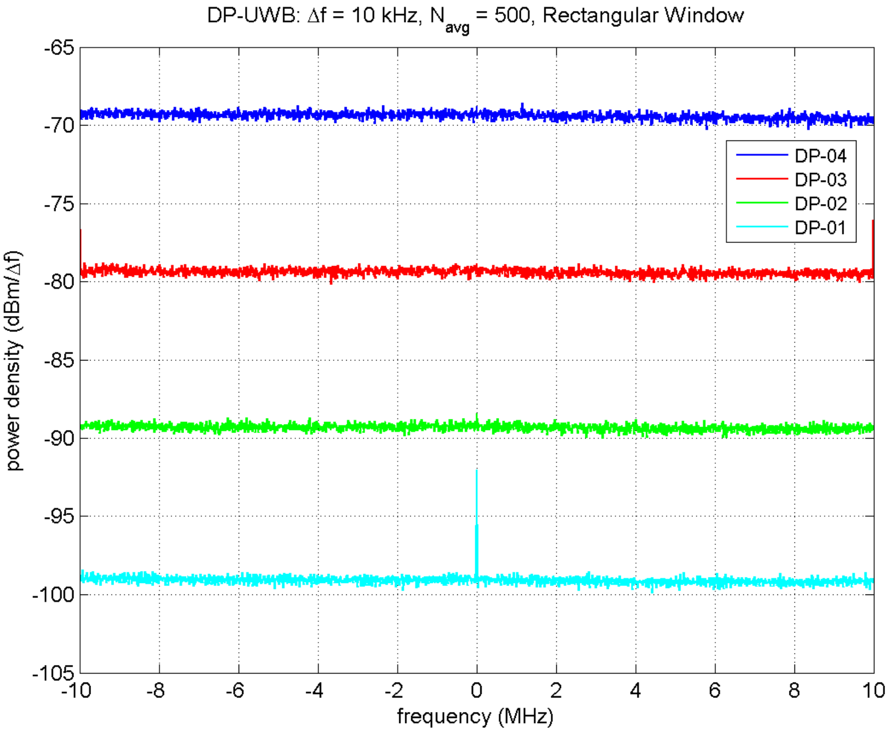

Figure 19. *PSD*s of DP signals.

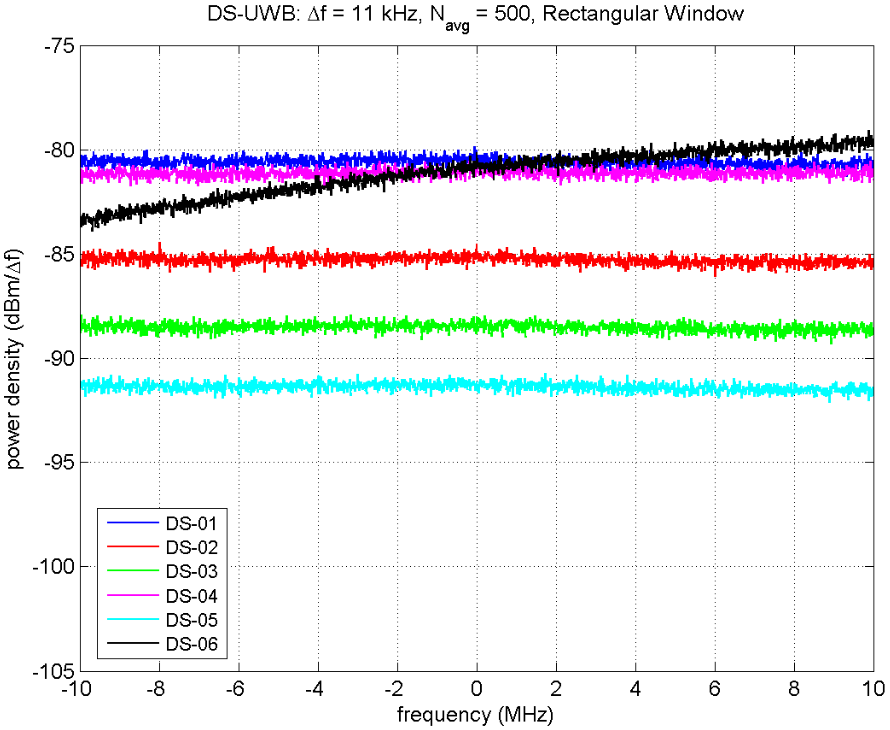

Figure 20. *PSD*s of DS signals.

3. MB INTERFERENCE

This section provides DTV susceptibility test results and characterization measurements for MB interference.

3.1. Gating Parameters

MB-OFDM achieves its ultra-wide bandwidth by simultaneously modulating 122 tones spaced 4.125 MHz apart. MB signals frequency-hop between bands according to a specified time-frequency code, which defines the number of bands (*b*) and the number of dwells (*d*) the signal stays in each band. From the perspective of a victim receiver operating within a single band, MB signals have two gating processes associated with (1) hopping and (2) insertion of zero-prefix and guard-intervals in each MB symbol. Each MB symbol is comprised of a zero-prefix (ZP), data block, and guard interval (GI); the MB symbol period is the sum of its constituents, i.e., $T_{OFDM} = T_{ZP} + T_{DATA} + T_{GI}$, where T_{ZP} = 60.6 ns, T_{DATA} = 242.4 ns, and T_{GI} = 9.5 ns.

Table 6 provides the MB parameters and corresponding gating parameters, i.e., on-time (τ_{on}), off-time (τ_{off}), and fractional on-time (ζ), considered in this report; these parameters also apply to GN(MB) gated-noise signals. Fractional on-time is calculated exactly as $\zeta = T_{DATA} / bT_{OFDM}$. On- and off-times are calculated as $\tau_{on} = dT_{OFDM} - T_{ZP} - T_{GI}$ and $\tau_{off} = (b - 1)dT_{OFDM} + T_{ZP} + T_{GI}$, respectively. These expressions ignore $T_{ZP} + T_{GI}$ between consecutive MB symbols and therefore are approximate in the multiple-dwell, i.e., $d > 1$, cases. This is necessary for later comparisons to *BD* and *BI* metrics and is justified for this experiment because $T_{ZP} + T_{GI}$ = 70.1 ns is comparable to the reciprocal bandwidth of the victim receiver, i.e., $1/B_{DTV}$ = 51.3 ns. Figure 21 illustrates gating parameters for MB-03.

Table 6. MB Gating Parameters

Type	Index	MB Parameters		Gating Parameters		
		b	*d*	τ_{on} (µs)	τ_{off} (µs)	ζ
MB, GN(MB)	01	1	N/A	0.24	0.07	0.776
	02	3	1	0.24	0.70	0.259
	03	3	2	0.55	1.32	0.259
	04	7	1	0.24	1.95	0.111
	05	7	2	0.55	3.82	0.111
	06	7	6	1.80	11.32	0.111
	07	13	1	0.24	3.82	0.060
	08	13	2	0.55	7.57	0.060
	09	13	12	3.68	45.07	0.060

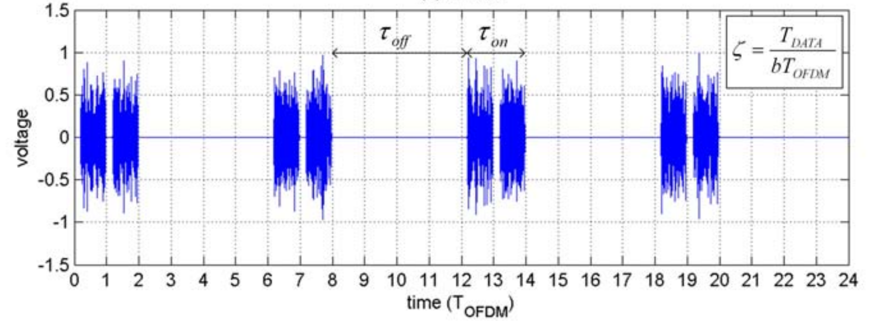

(a) MB-03

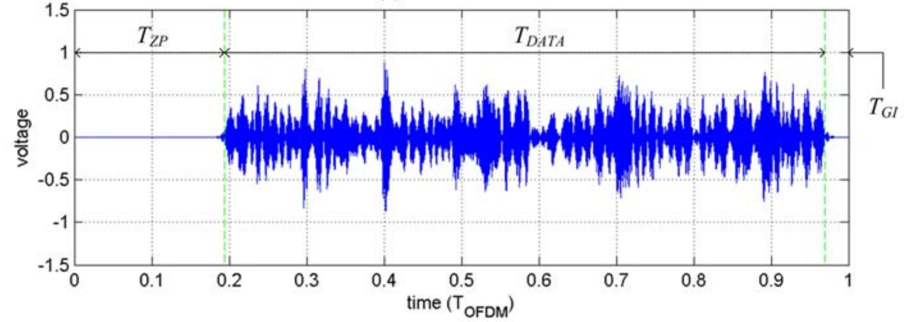

(b) MB-OFDM Word

Figure 21. Simulated MB-03 transmitting random data (T_{OFDM} = 312.5 ns).

3.2. DTV Susceptibility to MB Interference

Results of the DTV susceptibility tests for MB interference are described in this section. Post-Reed-Solomon segment error rate and pre-Viterbi bit error rate are plotted versus the ratio of average interference power to average noise power. Additionally, DTV susceptibility and FEC performance metrics, i.e., INR_{TOV} and BER_{TOV}, are plotted versus $1/\zeta$ in dB.

3.2.1. DTV Signal Quality as a Function of Interference Average Power

In this subsection, *SER* and *BER* are plotted versus *INR* for DTV susceptibility to MB interference. Figures 22 – 27 provide composite plots of measured *SER* and *BER* as a function of *INR*. Each page is dedicated to a single *SNR*, each plot is dedicated to a specific range of *d*, and each curve represents a specific value of *b*. Figures 22, 24, and 26 provide composite plots of *SER*, while Figures 23, 25, and 27 provide composite plots of *BER*. For each plot, GN-01 and MB-01 results are provided as a reference.

The following are general comments regarding the shift, separation, and slope of *SER* and *BER* curves. Both *SER* and *BER* shifted toward greater *INR* with increasing *SNR*. *SER* curves with fixed *SNR* and τ_{on} show increased separation (from GN-01) with decreasing ζ. Likewise, all *SER* curves with fixed *SNR* and ζ exhibit increased separation with increasing τ_{on}. *SER* curves were generally steeper than corresponding *BER* curves. For sufficiently small ζ, slopes of the *SER* curves were not as steep as higher-ζ cases. These observations are similar to those discussed in Appendix A of Part 2 of this report series for GN(MB) gated-noise interference.

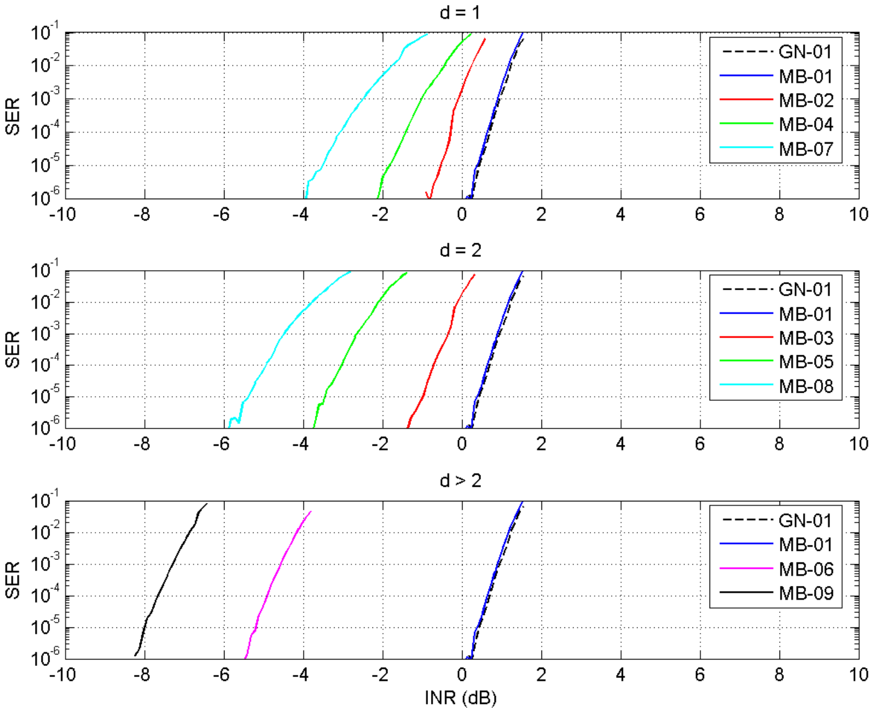

Figure 22. *SER* versus *INR* for a DTV channel operating at *SNR* = 9 dB and exposed to MB interference.

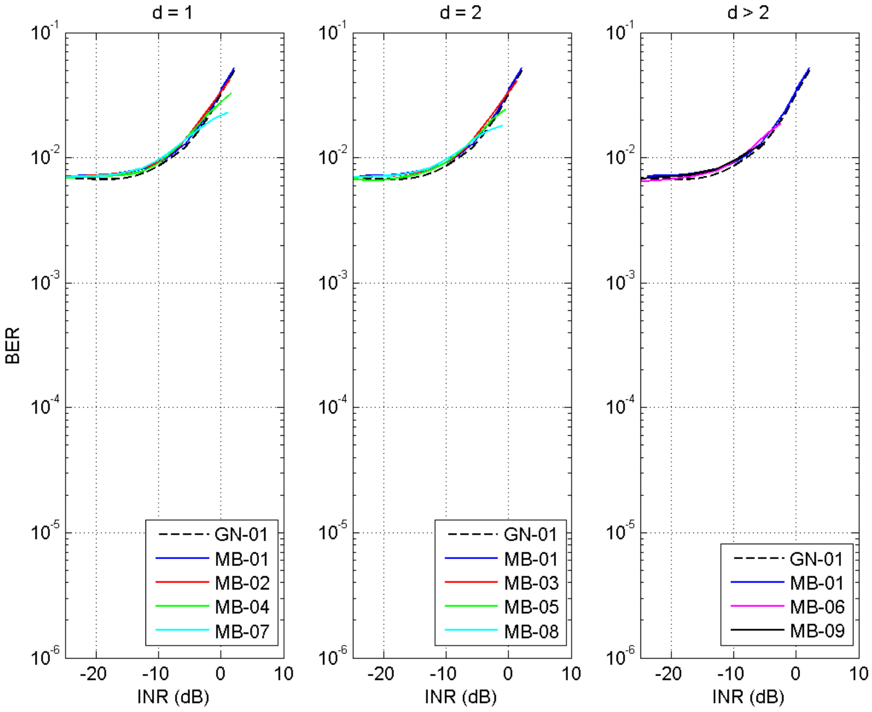

Figure 23. *BER* versus *INR* for a DTV channel operating at *SNR* = 9 dB and exposed to MB interference.

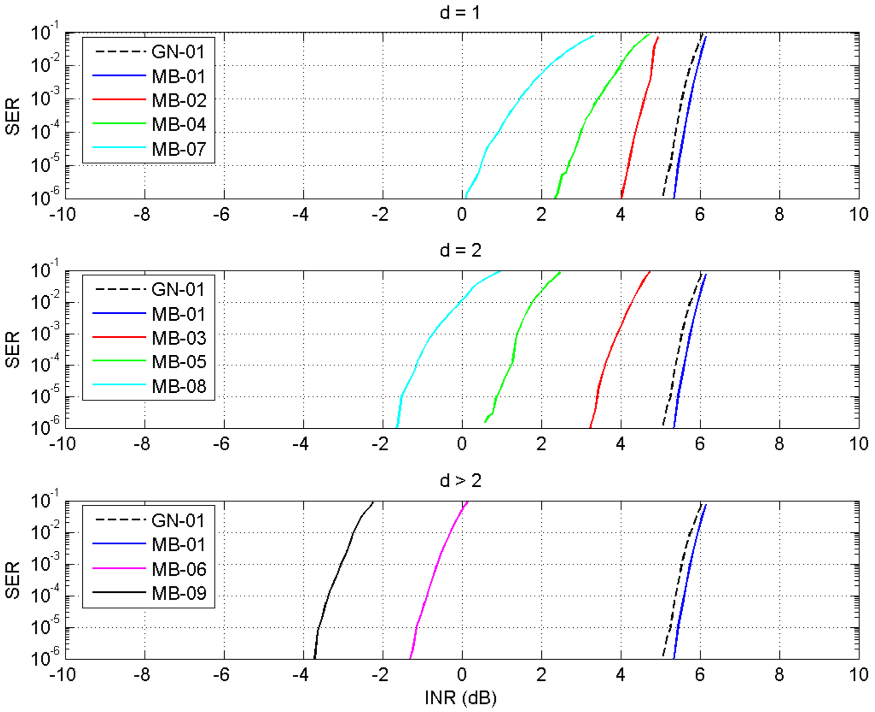

Figure 24. *SER* versus *INR* for a DTV channel operating at *SNR* = 12 dB and exposed to MB interference.

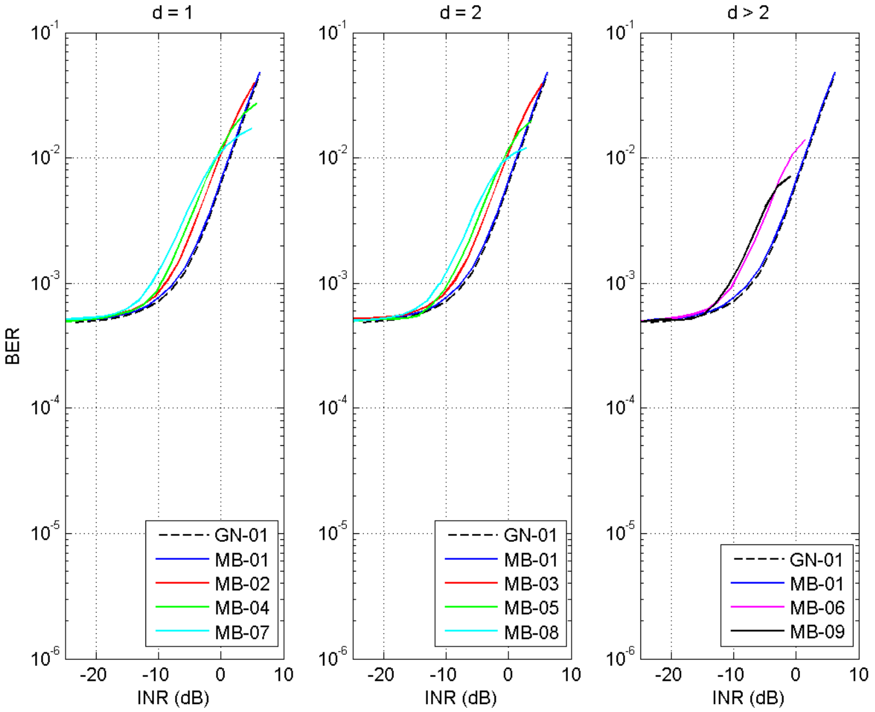

Figure 25. *BER* versus *INR* for a DTV channel operating at *SNR* = 12 dB and exposed to MB interference.

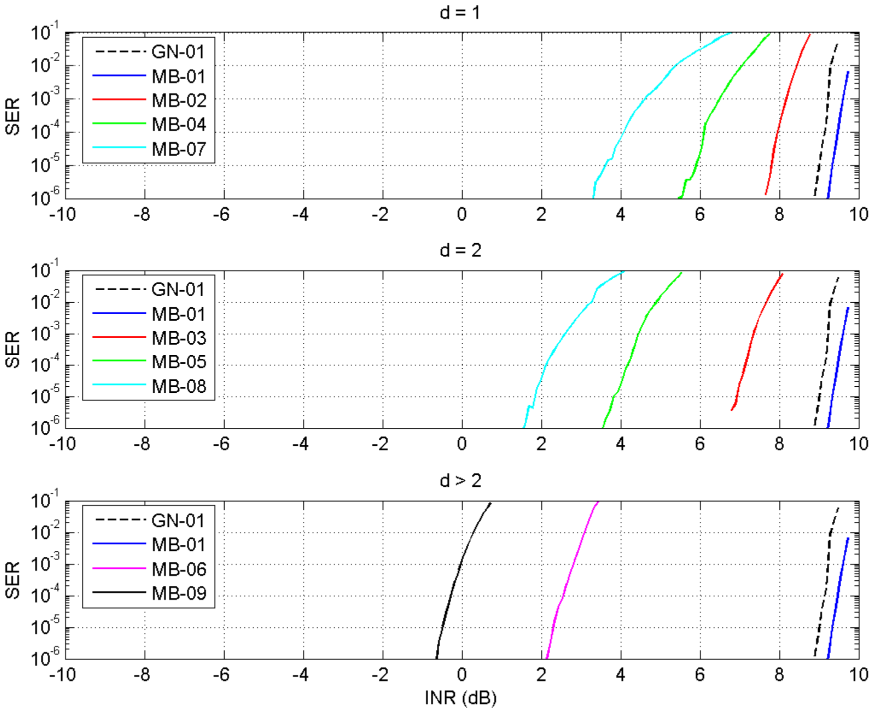

Figure 26. *SER* versus *INR* for a DTV channel operating at *SNR* = 15 dB and exposed to MB interference.

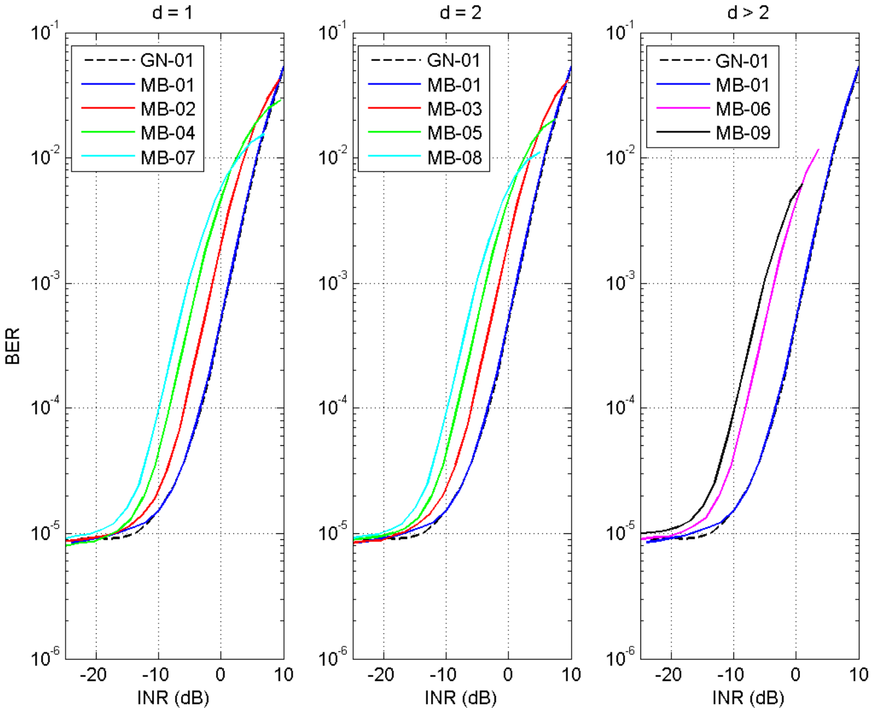

Figure 27. *BER* versus *INR* for a DTV channel operating at *SNR* = 15 dB and exposed to MB interference.

3.2.2. DTV Susceptibility as a Function of Fractional On-Time

Table 7 summarizes INR_{TOV} and BER_{TOV} results for MB interference; GN(MB) results from Part 2 of this report series are included for comparison purposes. Differences between INR_{TOV} of corresponding MB and GN(MB) results were less than 1 dB.

Table 7. Measured DTV Susceptibility and FEC Performance for MB Interference

Type	Index	SNR = 9 dB		SNR = 12 dB		SNR = 15 dB	
		INR_{TOV} (dB)	BER_{TOV}	INR_{TOV} (dB)	BER_{TOV}	INR_{TOV} (dB)	BER_{TOV}
MB	01	0.6	0.039	5.6	0.041	9.5	0.043
	02	-0.3	0.032	4.4	0.032	8.0	0.034
	03	-0.7	0.030	3.6	0.028	7.1	0.029
	04	-1.4	0.024	3.0	0.021	6.1	0.021
	05	-3.0	0.019	1.2	0.015	4.2	0.014
	06	-4.9	0.015	-0.9	0.010	2.6	0.010
	07	-3.1	0.018	0.9	0.013	4.1	0.021
	08	-4.9	0.015	-1.1	0.009	2.1	0.009
	09	-7.7	0.011	-3.4	0.006	-0.3	0.005
GN(MB)	01	0.5	0.037	5.2	0.036	8.5	0.036
	02	-0.7	0.030	3.7	0.027	7.0	0.028
	03	-0.9	0.028	3.5	0.025	6.5	0.025
	04	-1.9	0.022	2.3	0.018	5.8	0.019
	05	-3.2	0.018	0.8	0.013	4.2	0.013
	06	-5.0	0.015	-1.2	0.009	2.3	0.009
	07	-3.3	0.016	0.7	0.012	4.3	0.011
	08	-5.1	0.014	-1.1	0.009	2.3	0.008
	09	-7.4	0.011	-3.3	0.005	-0.3	0.005
GN	01	0.7	0.038	5.4	0.038	9.2	0.038

Figures 28 – 33 plot INR_{TOV} and BER_{TOV} versus $1/\zeta$ in dB, where $b = \{1, 3, 7, 13\}$ correspond to $\zeta = \{0.776, 0.259, 0.111, 0.060\}$ and $10\log(1/\zeta) = \{1.10, 5.87, 9.55, 12.2\}$ dB. The horizontal dashed reference line in each INR_{TOV} plot corresponds to DTV susceptibility to Gaussian noise interference. In terms of average interference power, the DTV receiver was generally more susceptible to MB signals than Gaussian noise. This is observed in Figures 28, 30, and 32 where INR_{TOV} was lower for MB-02 – MB-09 than for GN-01. Additionally, the MB results demonstrated that DTV susceptibility was dependent on temporal parameters of the interfering signal. For MB-01, τ_{off} was comparable to $1/B_{DTV} = 51.3$ ns, and DTV susceptibility was similar to that of Gaussian noise and independent of τ_{on} and ζ. For MB-02 – MB-09, however, τ_{off} was significantly greater than $1/B_{DTV}$, and DTV susceptibility was clearly dependent on τ_{on} and ζ. More specifically, for fixed SNR and τ_{on}, DTV susceptibility increased with decreasing ζ. Likewise, for fixed SNR and ζ, DTV susceptibility increased with increasing τ_{on}.

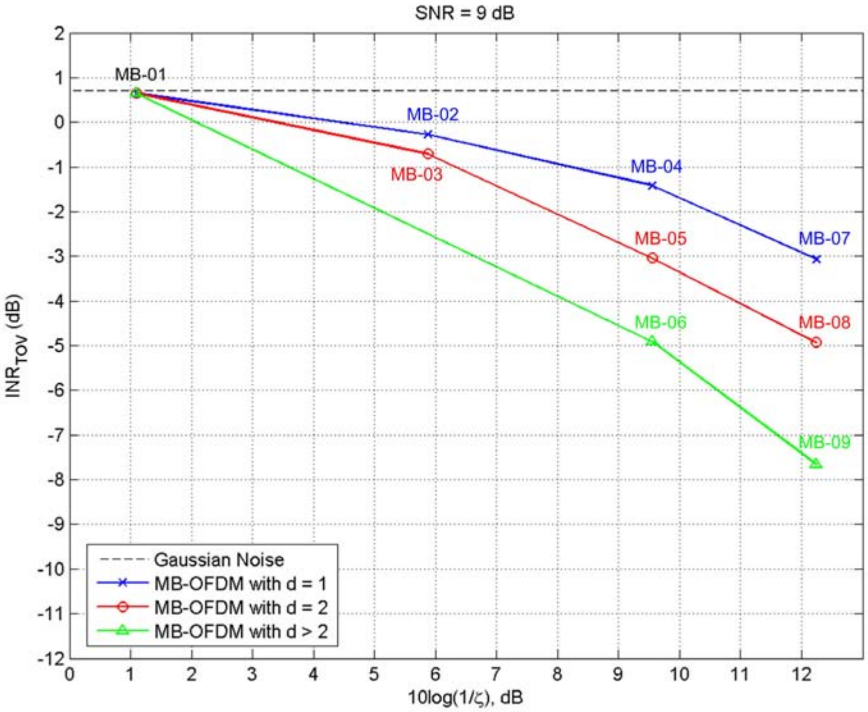

Figure 28. *INR_{TOV}* versus 10log(1/ζ) for a DTV channel operating at *SNR* = 9 dB and exposed to MB interference.

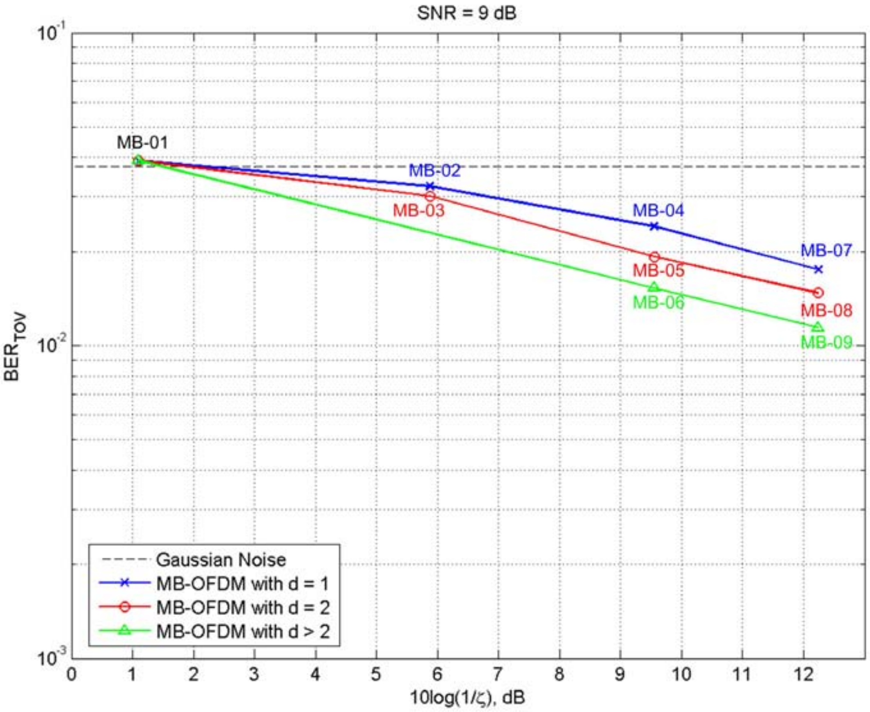

Figure 29. *BER_{TOV}* versus 10log(1/ζ) for a DTV channel operating at *SNR* = 9 dB and exposed to MB interference.

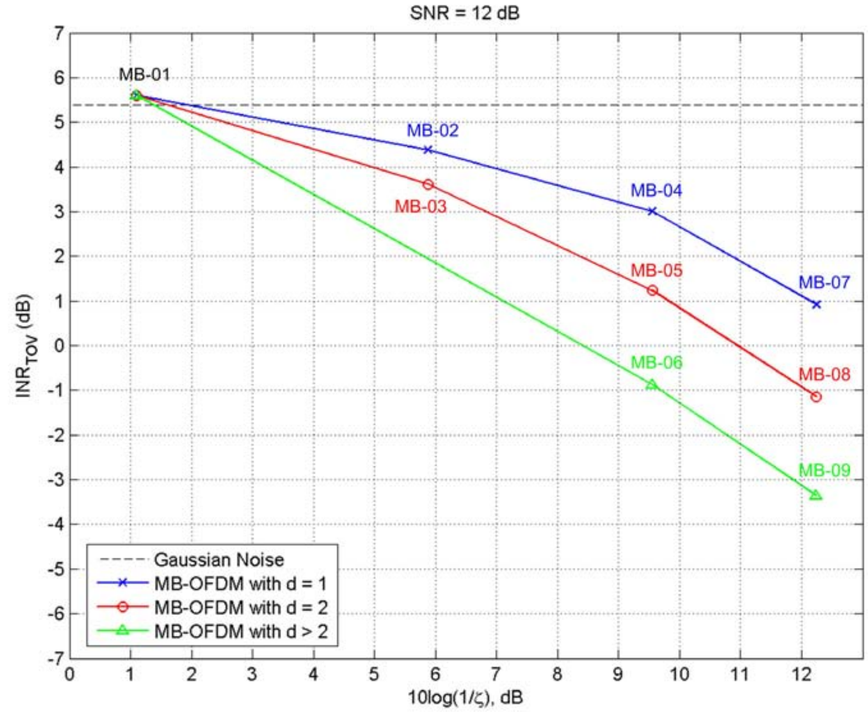

Figure 30. INR_{TOV} versus 10log(1/ζ) for a DTV channel operating at SNR = 12 dB and exposed to MB interference.

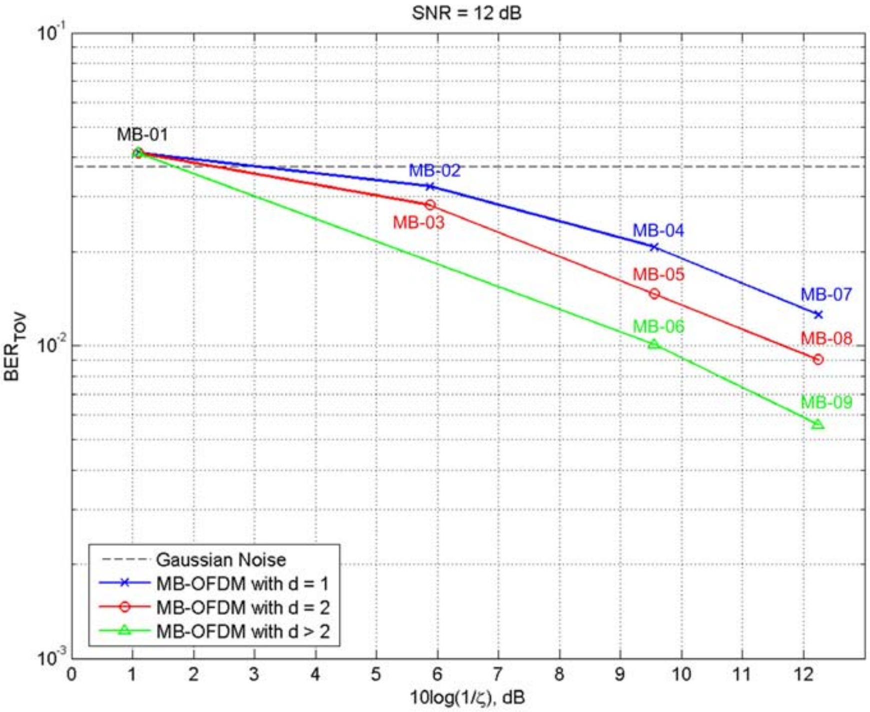

Figure 31. BER_{TOV} versus 10log(1/ζ) for a DTV channel operating at SNR = 12 dB and exposed to MB interference.

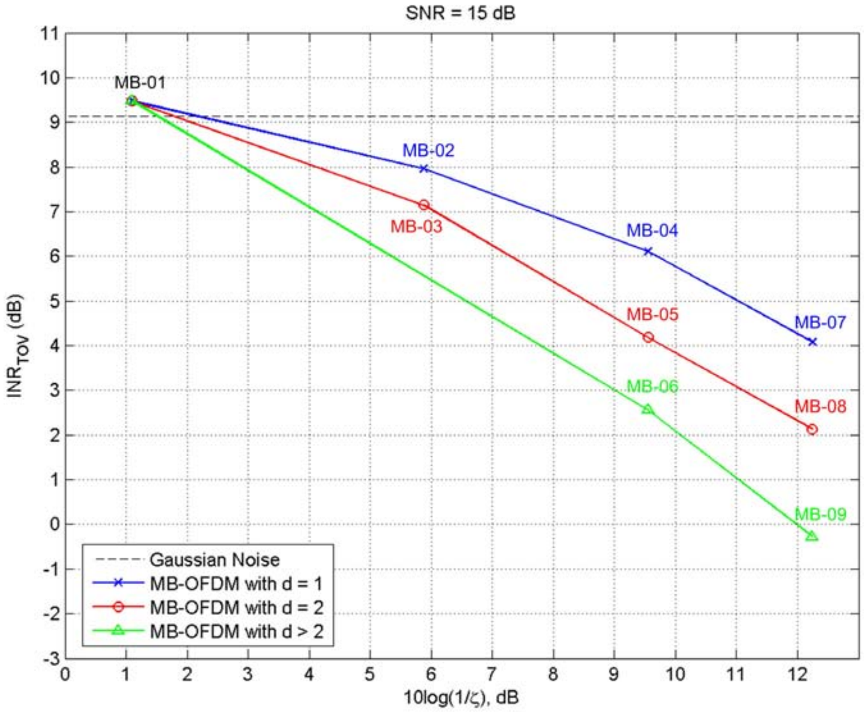

Figure 32. *INR_{TOV}* versus 10log(1/ζ) for a DTV channel operating at *SNR* = 15 dB and exposed to MB interference.

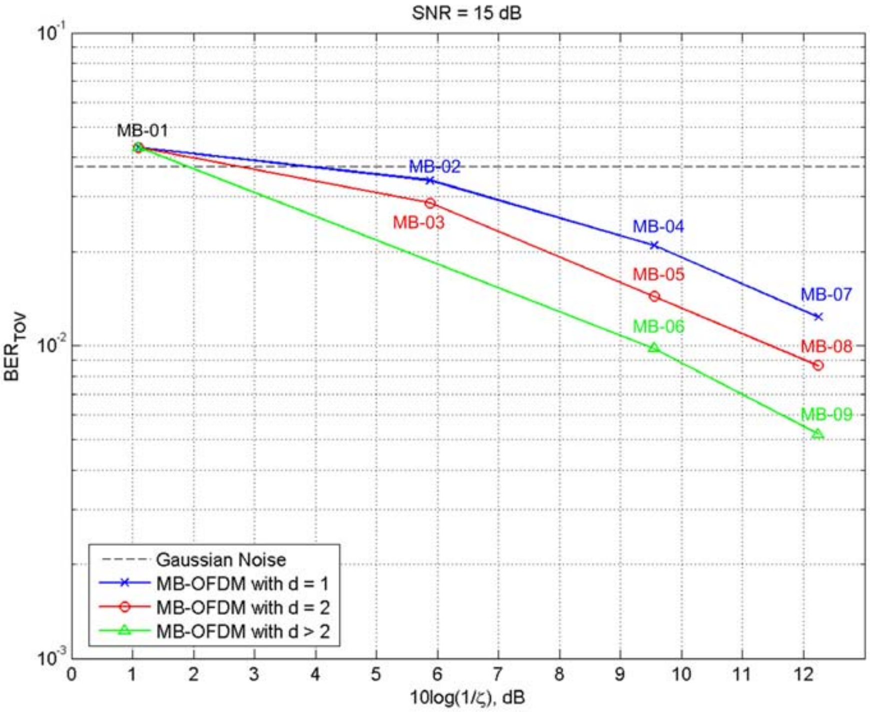

Figure 33. *BER_{TOV}* versus 10log(1/ζ) for a DTV channel operating at *SNR* = 15 dB and exposed to MB interference.

3.3. Characterization of MB Signals

Characterization of MB signals was accomplished via temporal, amplitude, and spectral analyses. This section provides band-limited signal characterization results for the B_{DTV} = 19.51-MHz DTV receiver RRC filter.

3.3.1. Temporal Analysis

Table 8 summarizes the effects of band-limiting on the temporal characteristics of MB signals. As expected, band-limiting lengthened on-times, $BD > \tau_{on}$, shortened off-times, $BI < \tau_{off}$, and increased fractional on-times, $\zeta_{DTV} > \zeta$. BD and BI approached the respective gating parameters only when τ_{on} and τ_{off} were significantly larger than $1/B_{DTV}$. Notice that measured MB temporal characteristics are identical to those of the GN(MB) signals.

Table 8. Measured Temporal Characteristics of MB Signals Band-Limited to B_{DTV}

Index	Gating Parameters			MB			GN(MB)		
	τ_{on} (µs)	τ_{off} (µs)	ζ	BD (µs)	BI (µs)	ζ_{DTV}	BD (µs)	BI (µs)	ζ_{DTV}
01	0.24	0.07	0.776	3.7	0.0	1.00	3.7	0.0	1.00
02	0.24	0.70	0.259	0.4	0.6	0.40	0.4	0.6	0.40
03	0.55	1.32	0.259	0.7	1.2	0.37	0.7	1.2	0.37
04	0.24	1.95	0.111	0.4	1.8	0.18	0.4	1.8	0.18
05	0.55	3.82	0.111	0.7	3.7	0.16	0.7	3.7	0.16
06	1.80	11.32	0.111	1.9	11.2	0.15	1.9	11.2	0.15
07	0.24	3.82	0.060	0.4	3.7	0.10	0.4	3.7	0.10
08	0.55	7.57	0.060	0.7	7.4	0.09	0.7	7.4	0.09
09	3.68	45.07	0.060	2.5	44.9	0.05	2.5	44.9	0.05

3.3.2. Amplitude Analysis

Figures 34 and 35 provide composite *APD* plots of measured single- and multi-dwell MB signals, respectively. Notice that measured average powers, indicated in the legends, were proportional to ζ. Band-limiting had profound effects on the *APD*s of the MB signals. For MB-01, τ_{off} was less than or comparable to $1/B_{DTV}$ and a negatively-sloped, relatively straight *APD* occurred. For MB-02 – MB-09, τ_{off} exceeded $1/B_{DTV}$ and a step-like *APD* occurred where higher amplitudes corresponded to MB interference during elongated on-times and lower amplitudes corresponded to system noise observable during shortened off-times. This was most pronounced for MB-08 and MB-09.

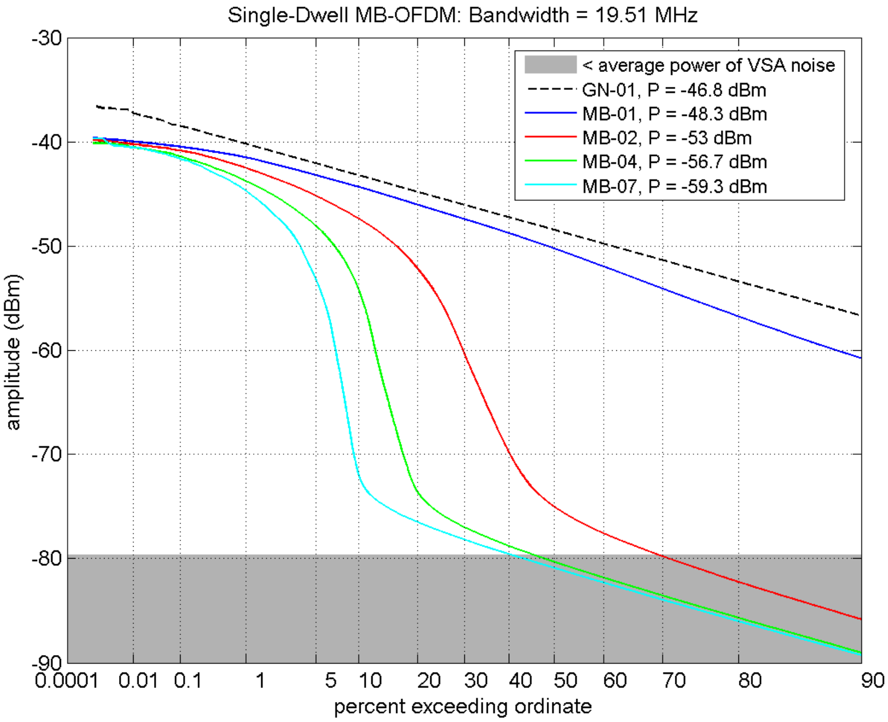

Figure 34. *APD*s of single-dwell MB signals band-limited to B_{DTV}.

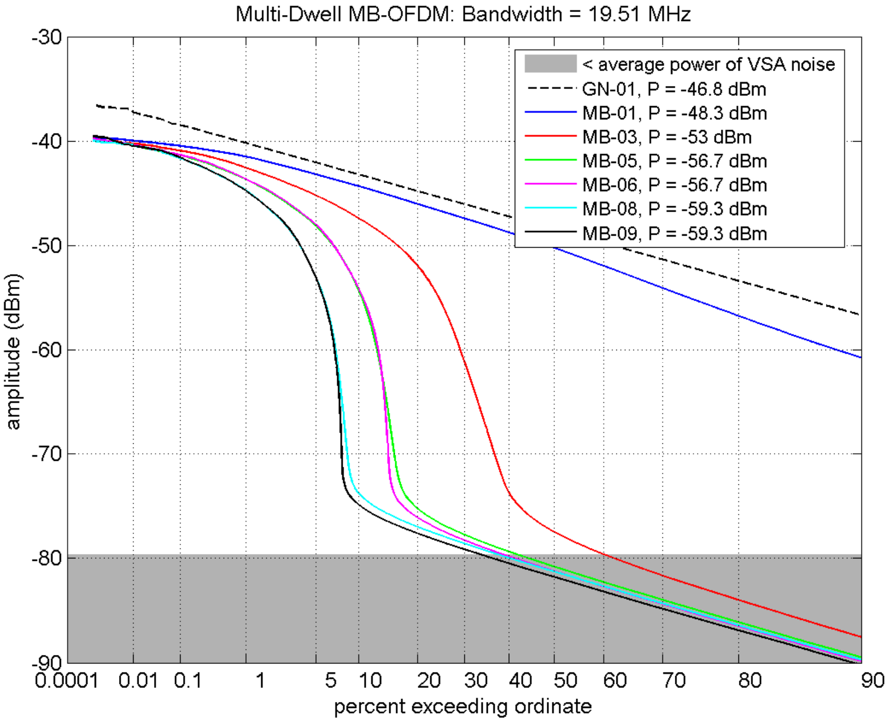

Figure 35. *APD*s of multi-dwell MB signals band-limited to B_{DTV}.

Table 9 summarizes measured *P/A* and *APD* characteristics for the MB signals band-limited to B_{DTV}. *APD* characteristics are labeled RG for resolved gating, i.e., step-like *APD* whose amplitude falls below the average power of the VSA noise at least 10% of the time. Notice that measured *P/A*s of the MB signals were 1 – 2 dB less than the *P/A* of corresponding GN(MB) signals.

Table 9. Measured Amplitude Characteristics of MB Signals Band-Limited to B_{DTV}

Index	MB		GN(MB)	
	P/A (dB)	*APD*	*P/A* (dB)	*APD*
01	8.3		10.5	
02	12.8	RG	14.7	RG
03	12.8	RG	14.6	RG
04	16.2	RG	18.0	RG
05	16.4	RG	17.9	RG
06	16.3	RG	17.8	RG
07	18.7	RG	20.2	RG
08	18.9	RG	20.1	RG
09	18.8	RG	19.9	RG

3.3.3. Spectral Analysis

Figures 36 and 37 provide measured *PSD*s of the single- and multi-dwell MB signals, respectively, over the VSA bandwidth. In Figure 37, the *PSD* of MB-05 is directly beneath MB-06. To compute the *PSD*, 500 blocks of length = 170.6 µs (Δf = 5.9 kHz) were averaged. Measured MB *PSD*s were flat across the band of interest, and measured power density was proportional to ζ. Differences between measured MB and GN(MB) *PSD*s were negligible. Also, the spectral line at 0 Hz was due to VSG local-oscillator feed-through. The influence of the VSG local-oscillator feed-through on test results was discussed in Appendix C of Part 1 of this report series.

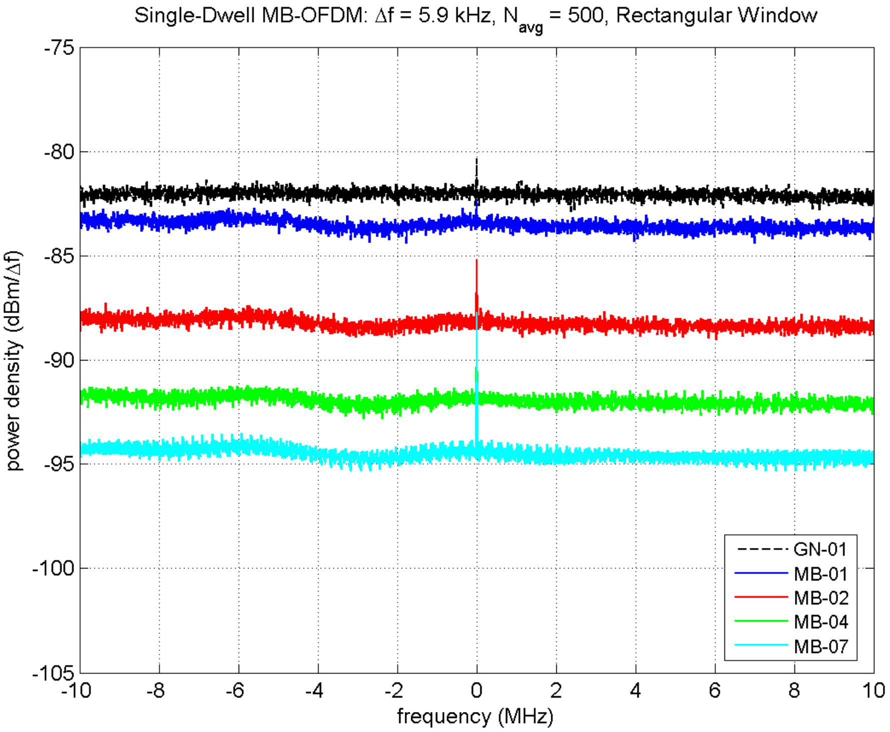

Figure 36. *PSD*s of single-dwell MB signals.

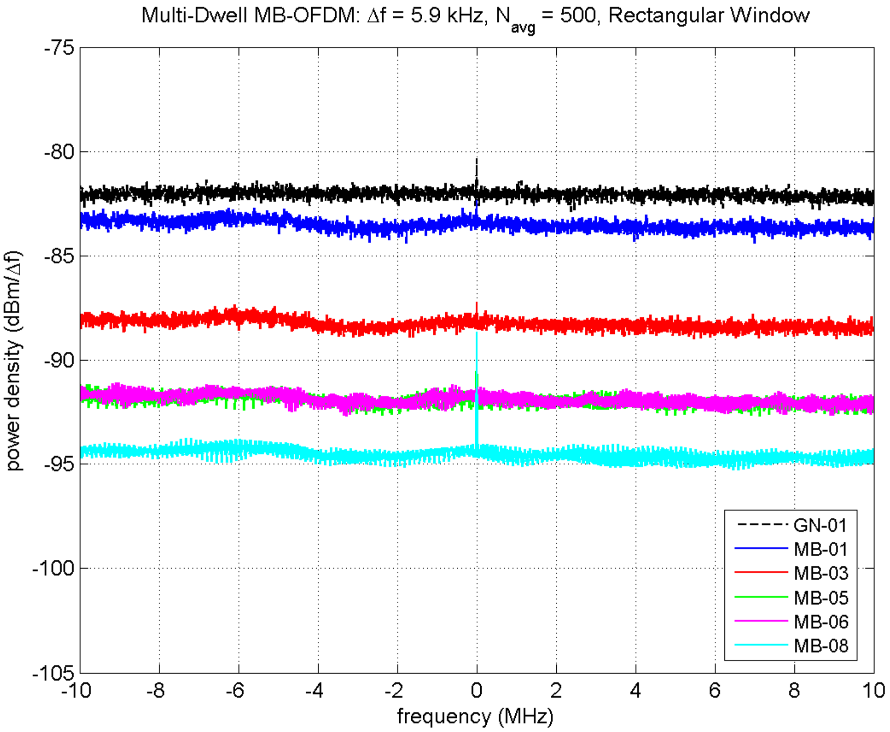

Figure 37. *PSD*s of multi-dwell MB signals.

4. CONCLUSION

The primary objective of this experiment was to measure and evaluate the susceptibility of a C-band satellite DTV receiver to UWB interference. The secondary objective was to determine if DTV susceptibility could be predicted from measured signal characteristics. A final objective was to determine if continuous and gated Gaussian noise could be used to emulate DS and MB signals, respectively, in susceptibility tests. Each of these objectives are addressed in these concluding remarks.

4.1. Signal Sets of Common DTV Susceptibility Behavior

The primary objective of this experiment was to measure and evaluate the susceptibility of a DTV victim receiver to UWB interference. INR_{TOV} is our primary DTV susceptibility metric, i.e., DTV susceptibility increases as INR_{TOV} decreases and conversely decreases as INR_{TOV} increases. Table 10 provides ΔINR_{TOV} for the UWB signals ranked from least to most susceptible, where ΔINR_{TOV} is normalized to the INR_{TOV} of Gaussian noise. Notice that variation with SNR does not affect ranking, and for all signals except DP-01 SNR variation is minimal. Superimposed upon this ranking is categorization into three signal sets distinguished by their distance from the INR_{TOV} of Gaussian noise, i.e., Set 1 is defined as $-0.5 \text{ dB} \leq \Delta INR_{TOV} \leq 0.5 \text{ dB}$, Set 2 is defined as $\Delta INR_{TOV} < -0.5$ dB, and Set 3 is defined as $\Delta INR_{TOV} > 0.5$ dB.

Table 10. Ranked DTV Susceptibility relative to Gaussian Noise Degradation

Rank	Signal	ΔINR_{TOV} (dB)			Set
		SNR = 9 dB	SNR = 12 dB	SNR = 15 dB	
1	DP-01	9.5	15.0	16.1	3
2	DP-03	0.3	0.4	0.5	1
3	MB-01	-0.1	0.2	0.3	
4	DS-03	0.2	0.3	-0.1	
5	DS-04	-0.1	0.3	0.1	
6	DS-05	-0.1	0.3	0.1	
7	DP-04	0.2	0.2	-0.2	
8	GN-01	0.0	0.0	0.0	
9	DS-01	-0.1	0.1	0.0	
10	DS-02	-0.2	0.2	-0.1	
11	DS-06	-0.5	-0.2	-0.3	
12	MB-02	-1.0	-1.0	-1.2	2
13	DP-02	-1.5	-1.2	-1.1	
14	MB-03	-1.4	-1.8	-2.0	
15	MB-04	-2.1	-2.4	-3.0	
16	MB-05	-3.7	-4.2	-5.0	
17	MB-07	-3.8	-4.5	-5.1	
18	MB-06	-5.6	-6.3	-6.6	
19	MB-08	-5.6	-6.5	-7.0	
20	MB-09	-8.4	-8.8	-9.4	

Signals in Set 1 are for all practical purposes equivalent to Gaussian noise in terms of DTV susceptibility. Signals in Set 2 have INR_{TOV} measurably below that of Gaussian noise and consequently are more deleterious to DTV reception. DP-01 is the only signal in Set 3; its INR_{TOV} is considerably greater than that of Gaussian noise and therefore is the most benign to DTV reception. Demarcation of Sets 1 and 3 is relatively straightforward as they are separated by a wide margin. Demarcation of Sets 1 and 2, however, is slightly more subjective. For example, INR_{TOV} of MB-02 is merely 1.0 – 1.2 dB below that of Gaussian noise.

During this experiment, there was interest in understanding the effects of UWB interference on the DTV forward error correction, consisting of a Viterbi decoder, convolutional byte de-interleaver, and Reed-Solomon decoder. Having access only to pre-Viterbi *BER* and post-Reed-Solomon *SER*, the FEC was regarded as a black box whose performance was evaluated by the average number of bit errors it corrected. In particular, FEC performance was deemed good when it achieved $SER_{TOV} = 10^{-4}$ from a relatively high BER_{TOV}. Interestingly in Sets 1 and 2, poor FEC performance, i.e., low BER_{TOV}, was correlated with high DTV susceptibility, i.e., low INR_{TOV}. Inspection of MB-01 and MB-09 in Table 7 (SNR = 12 dB), for example, shows that BER_{TOV} decreased from 0.041 to 0.006 as INR_{TOV} decreased from 5.6 dB to -3.4 dB. As was pointed out in Section 2.2.2, DP-01 in Set 3 did not correlate in the same way. Disregarding this exception, the correlation between BER_{TOV} and INR_{TOV} indicates that FEC plays a strong role in susceptibility. The effects of UWB interference on FEC performance is a topic for further study.

4.2. Summary of Measured Signal Characteristics

UWB signal characterization measurements were performed in the DTV victim signal bandwidth. Measured UWB signals were subjected to temporal, amplitude, and spectral analyses. Temporal analyses used *BD* and *BI* statistics and corresponding ζ_{DTV} estimates. Amplitude analyses used the *APD* and *P/A*. Finally, spectral analyses focused on the *PSD*.

Temporal analyses of DP and DS signals showed that band-limiting elongated pulse width, w. This was evident in Table 4, which demonstrates that $BD > w$ and $\zeta_{DTV} > \zeta$. For signals with T_{pulse} less than or comparable to $1/B_{DTV}$, elongated pulses overlapped and the subsequent *APD* and *P/A* approached Rayleigh amplitude statistics. For signals with T_{pulse} significantly greater than $1/B_{DTV}$, elongated pulses remained distinct and a step-like *APD* occurred with correspondingly high *P/A*.

Similar results were observed with the MB signals; in these cases, however, band-limiting elongated on-time, τ_{on}, and shortened off-time, τ_{off}. These changes were evident in Table 8, which demonstrated $BD > \tau_{on}$, $BI < \tau_{off}$, and $\zeta_{DTV} > \zeta$. For signals with τ_{off} less than or comparable to $1/B_{DTV}$, elongated on-times overlapped and the subsequent *APD* and *P/A* approached Rayleigh amplitude statistics. For signals with τ_{off} significantly greater than $1/B_{DTV}$, elongated on-times remained distinct and a step-like *APD* occurred with correspondingly high *P/A*.

Spectral analyses of DP, DS, and MB signals revealed flat power spectral densities like white Gaussian noise. A notable exception to this was DS-06 whose *PSD* sloped several dB over the DTV signal bandwidth. Theoretical analysis demonstrated that this was due to the DS code word spectral characteristics. Further comments on spectral analyses for bandwidths other than B_{DTV} can be found in Section 4.4.

4.3. Correlations Between DTV Susceptibility and Signal Characteristics

The second objective of this experiment was to determine if DTV susceptibility could be predicted from measured signal characteristics. Indeed, in Part 2 of this report series it was found that DTV susceptibility to gated noise interference could not be predicted by interference power alone. It was demonstrated that DTV susceptibility was also dependent on the temporal parameters of the gated noise signals, i.e., τ_{on}, τ_{off}, and ζ. In this section, the analysis is taken one step further by plotting DTV susceptibility versus the band-limited metrics *BD*, *BI*, ζ_{DTV}, and *P/A*.

Figures 38 and 39 summarize the temporal metrics of the UWB signals and illustrate how DTV susceptibility, i.e., ΔINR_{TOV}, depends on these metrics. Figure 38 provides *BI* versus *BD* of the UWB signals, and Figure 39 provides ΔINR_{TOV} as a function of ζ_{DTV}. In both plots, contours are drawn around the DTV susceptibility sets identified in Section 4.1. Signals within Set 1 have short $BI < 1/B_{DTV}$ and a wide range of longer *BD*. For these signals, the pulse period or gating off-time is less than $1/B_{DTV}$, and band-limiting caused overlapping. This either preserved or created signal characteristics that resembled continuous noise as evidenced by ζ_{DTV} near unity. Hence, INR_{TOV} for signals within Set 1 resembles that of Gaussian noise. Signals within Set 2 have a wide range of $BI > 1/B_{DTV}$ and *BD*. For these signals, the pulse period or gating off-time is greater than or comparable to $1/B_{DTV}$, and band-limiting did not create a continuous interference signal as evidenced by ζ_{DTV} ranging from 0.05 to 0.4. The wide range of *BD* and *BI* for signals within Set 2 caused a correspondingly wide range of ΔINR_{TOV} below that of Gaussian noise, where the DTV receiver was most susceptible to signals with long *BD* and *BI*, e.g., MB-09, and least susceptible to signals with short *BD* and *BI*, e.g., MB-02 and DP-02. DP-01 in Set 3 has long $BI >> 1/B_{DTV}$. For this signal, *BD* is much less than *BI* making ζ_{DTV} small. Hence, the victim receiver was exposed to interference the least amount of time, and ΔINR_{TOV} is significantly greater than that of Gaussian noise.

Contours drawn around signals within the DTV susceptibility sets, defined by ΔINR_{TOV} alone, persist as regions when plotted against the temporal metrics *BD*, *BI*, and ζ_{DTV}. These findings suggest that DTV susceptibility categorization can be predicted from a priori knowledge of these band-limited metrics. Results suggest that UWB signals with ζ_{DTV} close to unity will generate interference much like Gaussian noise. Further, results suggest that UWB signals with ζ_{DTV} approaching zero will generate benign interference. Finally, results suggest that UWB signals with $0.05 \leq \zeta_{DTV} \leq 0.4$ are likely to generate a range of interference effects more deleterious than Gaussian noise interference, which requires more knowledge to determine the specific impact on the victim receiver. For example, Figure 39 shows the signals clustering horizontally with those having the same number of bands. Within these clusters, signals are differentiated vertically by their dwell. Understanding this dependence on dwell required the in-depth study of the effects of gated noise on-time given in Part 2 of this report series.

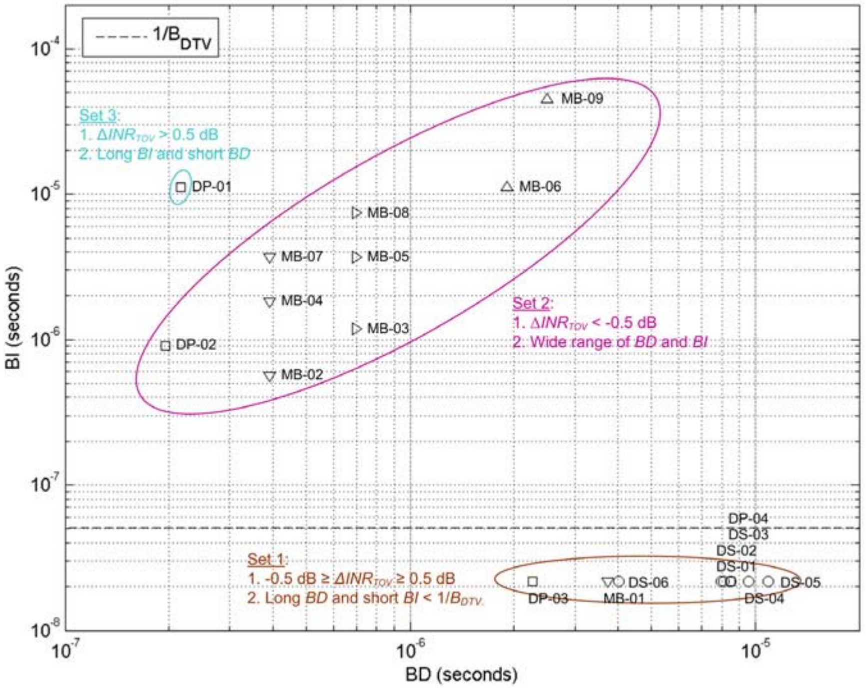

Figure 38. *BI* versus *BD* of UWB interference. Contours are drawn around signals within the same DTV susceptibility set.

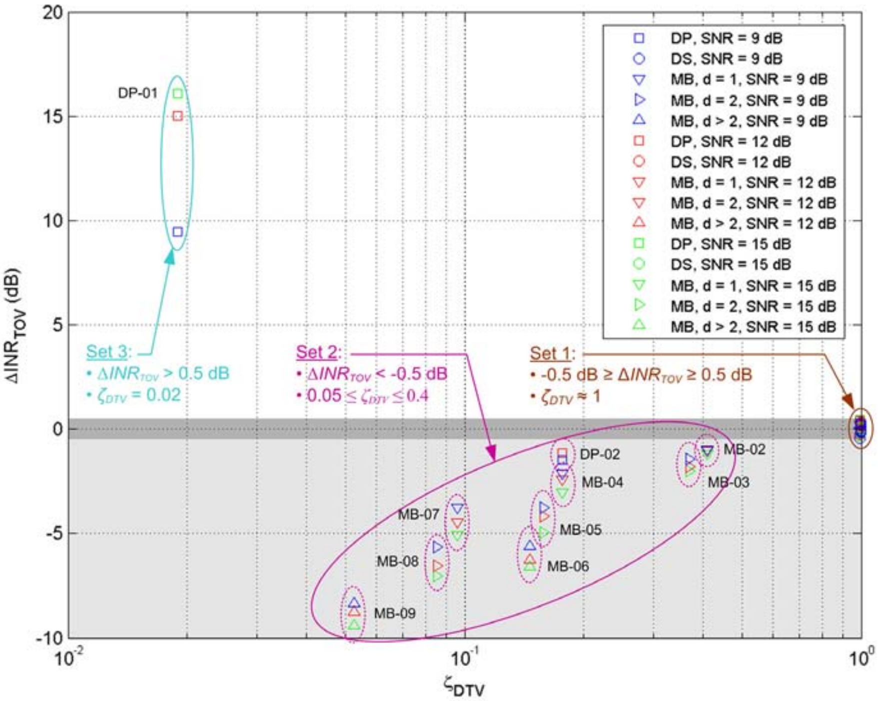

Figure 39. ΔINR_{TOV} versus ζ_{DTV} of UWB interference. Contours are drawn around signals within the same DTV susceptibility set.

Figure 40 provides ΔINR_{TOV} versus *P/A* with contours drawn around the DTV susceptibility sets. Signals within Set 1 are in a horizontal line in the range $5.4\text{ dB} \le P/A \le 9.6\text{ dB}$, which indicates that the peaks of these signals have negligible effect on ΔINR_{TOV}. Signals within Set 2 follow a downward trend in the range $12.8\text{ dB} \le P/A \le 18.9\text{ dB}$, which indicates that DTV susceptibility increases with increasing *P/A*. Exact determination of the *P/A* transitions between Sets 1 and 2 and Sets 2 and 3 requires further investigation.

Contours drawn around the signals within the DTV susceptibility signal sets, defined by ΔINR_{TOV} alone, persist as regions when plotted against *P/A*. This suggests that DTV susceptibility categorization can be predicted from a priori knowledge of the *P/A* metric. Results suggest that UWB signals with $5.4\text{ dB} \le P/A \le 9.6\text{ dB}$ will generate interference much like Gaussian noise. Further, results suggest that UWB signals with exceedingly high *P/A* will generate benign interference. Finally, results suggest that UWB signals with $12.8\text{ dB} \le P/A \le 18.9\text{ dB}$ are likely to generate a range of interference effects more deleterious than Gaussian noise interference, which requires more knowledge to determine the specific impact on the victim receiver.

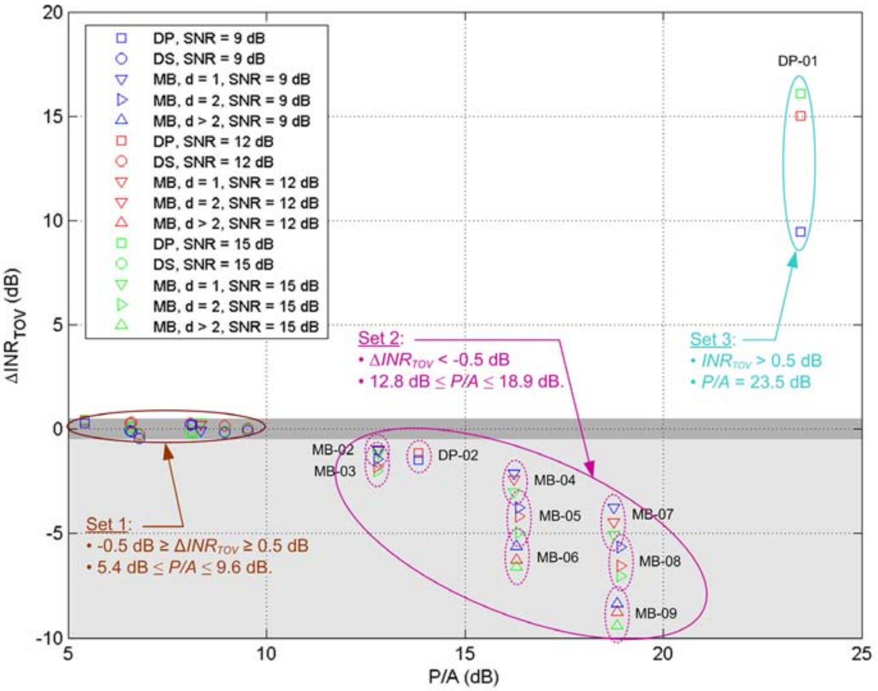

Figure 40. ΔINR_{TOV} versus *P/A* of UWB interference. Contours are drawn around signals within the same DTV susceptibility set.

In Section 4.1, it was mentioned that ΔINR_{TOV} varied slightly with *SNR* in Sets 1 and 2. This variation manifests itself as vertical displacement of ΔINR_{TOV} with *SNR* in Figures 39 and 40. Displacement of *BD*, *BI*, ζ_{DTV}, and *P/A* with *SNR* are not applicable since these metrics were derived from RF measurements. Hence, horizontal displacement of *BD* and vertical displacement of *BI* in Figure 38, horizontal displacement of ζ_{DTV} in Figure 39, and horizontal displacement of *P/A* in Figure 40 do not exist.

4.4. UWB Signal Emulation

As stated previously, the last objective of this study was to determine whether continuous and gated noise could be used to emulate DS and MB signals, respectively, in these and other susceptibility tests. This objective is important since gated noise is easier to implement and analyze than the UWB signals.

The main body of this report provided temporal, amplitude, and spectral analyses for each of the signals band-limited to B_{DTV}. With two exceptions, these analyses demonstrated that DS signals are similar to Gaussian noise. First, *P/A*s of the DS signals were 0 – 3 dB less than *P/A* of Gaussian noise. Consequently, *APD*s of the DS signals deviated slightly from Rayleigh. Second, the *PSD* of DS-06 sloped several dB over the DTV signal bandwidth in contrast to the flat spectrum of white Gaussian noise. This slope was attributed to the spectrum of the direct sequence codeword. Similarly, these analyses showed that gated noise was similar to MB signals with the exception that the *P/A* was 1 – 2 dB less than those of GN(MB).

The similarities were also present in the DTV susceptibility results, which were nearly identical for comparative signals. Hence, it appears reasonable to substitute continuous and gated noise signals for DS and MB signals, respectively, when replicating this experiment.

APD statistics as a function of frequency in Section B.4, however, suggest that GN(MB) signals cannot be used in place of MB signals for susceptibility tests on victim receivers with narrower bandwidths. These statistics show significant variation as a function of frequency when the signal is band-limited to 1.0 and 0.1 MHz. *APD* statistics versus frequency in the 1-MHz bandwidth case have a distinct periodic lobing pattern. *APD* statistics versus frequency in the 0.1-MHz bandwidth case have a distinct periodic spiking pattern centered at the pilot tone frequency. These features are not present in the GN(MB) signals and require further analysis.

5. REFERENCES

[1] "First Report and Order in the matter of ET Docket 98-153 (Revision of Part 15 of the Commission's Rules Regarding Ultra-Wideband Transmission Systems)," *FCC 02-48*, adopted Feb. 14, 2002, released Apr. 22, 2002.

[2] W.A. Kissick, Ed., "The temporal and spectral characteristics of ultrawideband signals," NTIA Report 01-383, Jan. 2001.

[3] J.R. Hoffman, M.G. Cotton, R.J. Achatz, R.N. Statz, and R.A. Dalke, "Measurements to determine potential interference to GPS receivers from ultrawideband transmission systems," NTIA Report 01-384, Feb. 2001.

[4] J.R. Hoffman, M.G. Cotton, R.J. Achatz, and R.N. Statz, "Addendum to NTIA Report 01-384: Measurements to determine potential interference to GPS receivers from ultrawideband transmission systems," NTIA Report 01-389, Sep. 2001.

[5] J.R. Hoffman, E.J. Haakinson, and Y. Lo, "Measurements to determine potential interference to public safety radio receivers from ultrawideband transmission systems," NTIA Report 03-402, Apr. 2003.

[6] M. Cotton, R. Achatz, J. Wepman, and B. Bedford, "Interference potential of ultrawideband signals: Part 1 – Procedures to characterize ultrawideband emissions and measure interference susceptibility of C-band satellite digital television receivers," NTIA Report TR-05-419, Feb. 2005.

[7] M. Cotton, R. Achatz, J. Wepman, and P. Runkle, "Interference potential of ultrawideband signals: Part 2 – Measurement of gated-noise interference to C-band satellite digital television receivers," NTIA Report TR-05-429, Aug. 2005.

[8] J.C. Whitaker, "Digital television transmission systems," Ch. 13 in *Standard Handbook of Video and Television Engineering*, J.C. Whitaker, Ed., New York, NY: McGraw-Hill, 2000.

[9] F. Sanders, "Measurements of pulsed co-channel interference in a 4-GHz digital Earth station receiver," NTIA Report 02-393, May 2002.

APPENDIX A: THEORETICAL *PSD* OF DP AND DS SIGNALS

A general expression for the power spectral density (*PSD*) of ultrawideband (UWB) signals using a fixed time-base dither was provided in Section 3 of [2]. This section provides the derivation of the expression and uses it to evaluate the *PSD* of DP and DS signals.

UWB signals that modulate pulses to convey binary data can be expressed as

$$u(t) = \sum_{n=-\infty}^{\infty} \alpha_{0n} y_0(t - nT - \beta_n) + \alpha_{1n} y_1(t - nT - \beta_n) = \sum_{n=-\infty}^{\infty} \sum_{k=0}^{1} \alpha_{kn} y_k(t - nT - \beta_n) \quad , \qquad \text{(A-1)}$$

where y_k is the channel symbol, e.g., y_0 represents a zero and y_1 represents a one, T is the nominal symbol period, n is the symbol period index, and β_n is a random variable that defines the dithering as described by the dither function $q(\beta)$. α_{kn} chooses the appropriate symbol for each information bit according to

$$\alpha_{kn} = \begin{cases} 1 - a_n & (k = 0) \\ a_n & (k = 1) \end{cases} \qquad \text{and} \qquad a_n = \begin{cases} 0 & (\text{with probability } \xi_0) \\ 1 & (\text{with probability } \xi_1 = 1 - \xi_0) \end{cases} \quad .$$

This formulation can be altered to map any two distinct information bit values, e.g., {1, -1}, with no change in the final *PSD* expressions. Note that a_n and β_n are independent and identically distributed (iid).

The *PSD* is the Fourier transform of the autocorrelation function, i.e., $R_{uu}(t_1,t_2) = \mathrm{E}\{u(t_1)u^*(t_2)\}$, where the expectation operator, defined as $\mathrm{E}\{X\} = \int xq(x)dx$, is distributive and for independent random variables the expectation of the product is equal to the product of the individual expectations. The complex conjugate * can be dropped because $u(t)$ is a real function, and the autocorrelation function is expressed as

$$R_{uu}(t_1,t_2) = \mathrm{E}\{u(t_1)u(t_2)\} = \mathrm{E}\left\{ \sum_{n,m} \sum_{k,l} \alpha_{kn}\alpha_{lm} y_k(t_1 - nT - \beta_n) y_l(t_2 - mT - \beta_m) \right\} \quad .$$

Note that summations involving n and/or m imply a range $\pm\infty$, summations involving k and/or l imply a range from 0 to 1, and integrals with unspecified limits imply the limits $\pm\infty$.

Evaluation of $R_{uu}(t_1, t_2)$ involves summation of the function

$$\gamma_{nm}(t_1,t_2) = \sum_{k,l} \mathrm{E}\{\alpha_{kn}\alpha_{lm}\} \mathrm{E}\{y_k(t_1 - nT - \beta_n) y_l(t_2 - mT - \beta_m)\} \quad ,$$

where the expectation was moved inside the summation operators and split into the product of expectations of the independent random variables. The expectation of the product of the channel symbols is difficult to simplify in a meaningful way. To avoid this difficulty, the following variable is introduced

$$\hat{\gamma}_{nm}(t_1,t_2) = \sum_{k,l} \mathrm{E}\{\alpha_{kn}\}\mathrm{E}\{\alpha_{lm}\}\mathrm{E}\{y_k(t_1 - nT - \beta_n)\}\mathrm{E}\{y_l(t_2 - mT - \beta_m)\} \quad .$$

$\sum_{n \neq m} \gamma_{nm}(t_1,t_2) = \sum_{n \neq m} \hat{\gamma}_{nm}(t_1,t_2)$ because the symbols are independent in different symbol periods. However, $\sum_{n} \gamma_{nn}(t_1,t_2) \neq \sum_{n} \hat{\gamma}_{nn}(t_1,t_2)$ because the symbols are not independent in the same symbol period. Since both quantities are easily evaluated along the diagonal, $\sum_{n} \hat{\gamma}_{nn}(t_1,t_2)$ is subtracted and $\sum_{n} \gamma_{nn}(t_1,t_2)$ is added to formulate the expression in a way that can be evaluated analytically, i.e.,

$$R_{uu}(t_1,t_2) = \sum_{n,m} \gamma_{nm}(t_1,t_2) = \sum_{n,m} \hat{\gamma}_{nm}(t_1,t_2) + \sum_{n} \left[\gamma_{nn}(t_1,t_2) - \hat{\gamma}_{nn}(t_1,t_2)\right] \quad . \qquad \text{(A-2)}$$

As will be demonstrated, this approach has the added benefit of distinguishing between the discrete and continuous spectra of the resulting *PSD*.

Consider the first term of equation (A-2), $\sum_{n,m} \hat{\gamma}_{nm}(t_1,t_2)$. E{$\alpha_{kn}$} is evaluated as

$$\mathrm{E}\{\alpha_{1n}\} = \mathrm{E}\{a_n\} = (0)\xi_0 + (1)\xi_1 = \xi_1$$

$$\mathrm{E}\{\alpha_{0n}\} = \mathrm{E}\{1 - a_n\} = \mathrm{E}\{1\} - \mathrm{E}\{a_n\} = \xi_0 \quad .$$

Hence, E{α_{kn}} = ξ_k is independent of *n* and can be moved outside $\sum_{n}$, yielding

$$\sum_{n,m} \hat{\gamma}_{nm}(t_1,t_2) = \left[\sum_{k} \xi_k \sum_{n} \mathrm{E}\{y_k(t_1 - nT - \beta_n)\}\right]\left[\sum_{l} \xi_l \sum_{m} \mathrm{E}\{y_l(t_2 - mT - \beta_m)\}\right] \quad .$$

Expanding the expectation into integral form and introducing $\phi_k(t) = \sum_{n} y_k(t - nT)$ gives

$$\sum_{n} \mathrm{E}\{y_k(t - nT - \beta_n)\} = \sum_{n} \int y_k(t - nT - \beta)q(\beta)d\beta = \int \phi_k(t - \beta)q(\beta)d\beta = (\phi_k * q)(t) \quad ,$$

where $*$ is the convolutional operator. Defining the function $\psi(t) = \sum_{k} \xi_k \phi_k(t)$ gives

$$\sum_{n,m} \hat{\gamma}_{nm}(t_1,t_2) = \left[(\psi * q)(t_1)\right]\left[(\psi * q)(t_2)\right] \quad , \qquad \text{(A-3)}$$

where the periodic function $\psi(t)$ can be expressed as a Fourier series

$$\psi(t) = \sum_m \Psi_m e^{j2\pi mt/T} \quad , \qquad \Psi_m = \frac{1}{T}\int_{-T/2}^{T/2} \psi(t) e^{-j2\pi mt/T} dt \quad .$$

This allows for the convolution in equation (A-3) to be expressed as

$$\begin{aligned}(\psi * q)(t) &= \int \sum_m \Psi_m e^{j2\pi m(t-\beta)/T} q(\beta) d\beta = \sum_m \Psi_m e^{j2\pi mt/T} \int q(\beta) e^{-j2\pi m\beta/T} d\beta \\ &= \sum_m \Psi_m Q\left(\frac{m}{T}\right) e^{j2\pi mt/T} \quad ,\end{aligned}$$

where Q is the Fourier transform of q. The Fourier coefficients in terms of ξ_k and y_k are

$$\Psi_m = \frac{1}{T}\sum_k \xi_k \int y_k(t') e^{-j2\pi mt'/T} dt' = \frac{1}{T}\sum_k \xi_k Y_k\left(\frac{m}{T}\right) \quad ,$$

where change of variable, $t' = t - nT$, was used to simplify and Y_k is the Fourier transform of y_k. Substitution into equation (A-3) and changing the independent variables to $\tau = t_2 - t_1$ and $t = t_2$ yields

$$\sum_{n,m} \hat{\gamma}_{nm}(\tau, t) = \frac{1}{T^2}\sum_{n,m}\left[\sum_k \xi_k Y_k\left(\frac{n}{T}\right)\right]\left[\sum_k \xi_k Y_k\left(\frac{m}{T}\right)\right] Q\left(\frac{n}{T}\right) Q\left(\frac{m}{T}\right) e^{j2\pi[(m+n)t - m\tau]/T} \quad . \tag{A-4}$$

The next term in equation (A-2) to be considered is

$$\begin{aligned}\sum_n \hat{\gamma}(t_1, t_2) &= \sum_{k,l} \xi_k \xi_l \sum_n \left(\int y_k(t_1 - nT - \beta) q(\beta) d\beta\right)\left(\int y_l(t_2 - nT - \beta) q(\beta) d\beta\right) \\ &= \sum_{k,l} \xi_k \xi_l \iint Y_k(f_1) Y_l(f_2) Q(f_1) Q(f_2) \left[\sum_n e^{-j2\pi(f_1 + f_2)nT}\right] e^{j2\pi(f_1 t_1 + f_2 t_2)} df_1 df_2 \quad ,\end{aligned}$$

where $\int y_k(t - nT - \beta) q(\beta) d\beta = \int Y_k(f) Q(f) e^{-j2\pi fnT} e^{j2\pi ft} df$.

The term in square brackets may be expressed as the sum of delta functions using the identity

$$\sum_n e^{-j2\pi fnT} = \frac{1}{T}\sum_n \delta\left(f - \frac{n}{T}\right) \quad . \tag{A-5}$$

Simple evaluation of the f_2 integral, changing the independent variables to $\tau = t_2 - t_1$ and $t = t_2$, and consolidating the k and l terms yields

$$\begin{aligned}\sum_n \hat{\gamma}_{nn}(t_1, t_2) &= \frac{1}{T}\sum_n e^{j2\pi nt/T}\int\left[\sum_k \xi_k Y_k(f)\right]\left[\sum_l \xi_l Y_l\left(\frac{n}{T} - f\right)\right]Q(f)Q\left(\frac{n}{T} - f\right)e^{-j2\pi f\tau}df \\ &= \frac{1}{T}\sum_n e^{j2\pi nt/T}\left[\left(\sum_k \xi_k y_k(\tau)\right) * \left(\sum_l \xi_l y_l(-\tau)e^{j2\pi n\tau/T}\right)\right] * \left[q(\tau) * \left(q(-\tau)e^{j2\pi n\tau/T}\right)\right] \quad ,\end{aligned} \tag{A-6}$$

where $\int Y_k\left(\frac{n}{T} - f\right)e^{j2\pi f\tau}df = y_k(-\tau)e^{j2\pi n\tau/T}$.

The last term to be evaluated in equation (A-2) is

$$\sum_n \gamma_{nn}(t_1, t_2) = \sum_n \sum_{k,l} \mathrm{E}\{\alpha_{kn}\alpha_{kn}\}\mathrm{E}\{y_k(t_1 - nT - \beta_n)y_l(t_2 - nT - \beta_n)\} \quad .$$

$\mathrm{E}\{\alpha_{kn}\alpha_{ln}\}$ is independent of n, that is

$$\mathrm{E}\{\alpha_{1n}\alpha_{1n}\} = \mathrm{E}\{a_n^2\} = (0)^2\xi_0 + (1)^2\xi_1 = \xi_1$$

$$\mathrm{E}\{\alpha_{0n}\alpha_{0n}\} = \mathrm{E}\{(1 - a_n)^2\} = \mathrm{E}\{1\} - 2\mathrm{E}\{a_n\} + \mathrm{E}\{a_n^2\} = \xi_0$$

$$\mathrm{E}\{\alpha_{0n}\alpha_{1n}\} = \mathrm{E}\{\nu_{1n}\nu_{0n}\} = \mathrm{E}\{(1 - a_n)a_n\} = \mathrm{E}\{a_n\} - \mathrm{E}\{a_n^2\} = 0 \quad .$$

Hence, $\mathrm{E}\{\alpha_{kn}\alpha_{ln}\} = \xi_k\delta_{kl}$, where δ_{kl} is the Kronecker delta function. Expanding the expectation into integral form, taking the double Fourier transform, and consolidating n and β terms yields

$$\begin{aligned}\sum_n \gamma_{nn}(t_1, t_2) &= \sum_k \xi_k \sum_n \int y_k(t_1 - nT - \beta)y_k(t_2 - nT - \beta)q(\beta)d\beta \\ &= \sum_k \xi_k \iint Y_k(f_1)Y_k(f_2)\left[\sum_n e^{-j2\pi(f_1+f_2)nT}\right]\left[\int q(\beta)e^{-j2\pi(f_1+f_2)\beta}d\beta\right]e^{j2\pi(f_1t_1+f_2t_2)}df_1df_2 \quad .\end{aligned}$$

Utilizing equation (A-5) to evaluate the f_2 integral, changing independent variables to $\tau = t_2 - t_1$ and $t = t_2$, rearranging terms, and recognizing the Fourier transform with respect to τ yields

$$\begin{aligned}\sum_n \gamma_{nn}(\tau, t) &= \frac{1}{T}\sum_n e^{j2\pi nt/T}Q\left(\frac{n}{T}\right)\int\sum_k \xi_k Y_k(f)Y_k\left(\frac{n}{T} - f\right)e^{-j2\pi f\tau}df \\ &= \frac{1}{T}\sum_n e^{j2\pi nt/T}Q\left(\frac{n}{T}\right)\sum_k \xi_k y_k(\tau) * \left(y_k(-\tau)e^{j2\pi n\tau/T}\right) \quad .\end{aligned} \tag{A-7}$$

Equations (A-2), (A-4), (A-6), and (A-7) combine to give an expression for the autocorrelation function in terms of τ and t. The statistics for $R_{uu}(\tau, t)$ are periodic with period T. Such processes are commonly referred to as cyclostationary. For these processes, it is useful to calculate the average over all possible observation times within a period. The time average over one period is denoted as follows

$$\left\langle R_{uu}(\tau)\right\rangle = \frac{1}{T}\int_0^T R_{uu}(\tau,t)dt \quad .$$

Evaluating this integral involves the integral identity

$$\frac{1}{T}\int_0^T e^{j2\pi kt/T}dt = \begin{cases} 1 & (k=0) \\ 0 & (\text{otherwise}) \end{cases} \quad ,$$

where k is an integer. Hence, the time average of equation (A-4) is non-zero only for $n = -m$, and the time average of equations (A-6) and (A-7) are non-zero only for $n = 0$. The time-average autocorrelation function reduces to

$$\begin{aligned}\left\langle R_{uu}(\tau)\right\rangle = {} & \frac{1}{T^2}\sum_n \left|\sum_k \xi_k Y_k\left(\frac{n}{T}\right)\right|^2 \left|Q\left(\frac{n}{T}\right)\right|^2 e^{j2\pi n\tau/T} \\ & + \frac{1}{T}\left\{\sum_k \xi_k y_k(\tau) * y_k(-\tau) - \left[\left(\sum_k \xi_k y_k(\tau)\right) * \left(\sum_k \xi_k y_k(-\tau)\right)\right] * \left[q(\tau) * q(-\tau)\right]\right\} \quad ,\end{aligned}$$

where $Q(0)$ is the integrated probability density function $q(\beta)$ equal to 1.

Finally, taking the Fourier transform of $\left\langle R_{uu}(\tau)\right\rangle$ yields

$$\begin{aligned}\left\langle S_{uu}(f)\right\rangle = \mathrm{FT}\left\{\left\langle R_{uu}(\tau)\right\rangle\right\} = {} & \frac{1}{T^2}\left|\sum_k \xi_k Y_k(f)\right|^2 \left|Q(f)\right|^2 \sum_n \delta\left(f - \frac{n}{T}\right) \\ & + \frac{1}{T}\left\{\sum_k \xi_k \left|Y_k(f)\right|^2 - \left|\sum_k \xi_k Y_k(f)\right|^2 \left|Q(f)\right|^2\right\} \quad , \qquad \text{(A-8)}\end{aligned}$$

which is comprised of discrete and continuous components that depend on the symbol spectrum and the Fourier transform of the density function used to randomize the signal.

A.1. DP-UWB

For DP signals, $q(\beta)$ is uniformly distributed (and more importantly symmetric); hence, the signal can be expressed according to the general expression (A-1). The DP channel symbol y_1 is a time advanced version of y_0 defined as

$$y_1\left(t+\frac{\beta_{max}T}{2}\right)=y_0(t)\equiv p_{DP}(t) \quad ,$$

where β_{max} is the dither fraction and $p_{DP}(t)$ is the pulse shape. Assuming equiprobable DP information bits, i.e., $\xi_k = ½$, and knowing that time shift translates to a phase shift in the frequency domain results in

$$\sum_k \xi_k \left|Y_k(f)\right|^2 = \frac{1}{2}\left[\left|\int p_{DP}(t)e^{-j2\pi ft}dt\right|^2 + \left|e^{j\pi f\beta_{\max}T}\int p_{DP}(t)e^{-j2\pi ft}dt\right|^2\right] = \left|P_{DP}(f)\right|^2$$

$$\left|\sum_k \xi_k Y_k(f)\right|^2 = \frac{1}{4}\left|P_{DP}(f)\right|^2\left|1+e^{j\pi f\beta_{max}T}\right|^2 = \frac{1}{2}\left|P_{DP}(f)\right|^2\left[1+\cos(\pi f\beta_{max}T)\right] \quad .$$

Substitution in equation (A-8) yields

$$\begin{aligned}\left\langle S_{uu}(f)\right\rangle &= \frac{1}{2T^2}\left|P_{DP}(f)Q(f)\right|^2\left[1+\cos\left(\pi f\beta_{max}T\right)\right]\sum_n \delta\left(f-\frac{n}{T}\right)\\ &+\frac{1}{T}\left|P_{DP}(f)\right|^2\left\{1-\frac{\left|Q(f)\right|^2\left[1+\cos\left(\pi f\beta_{max}T\right)\right]}{2}\right\} \quad .\end{aligned}$$

Figures A-1 – A-4 illustrate the power spectral densities of DP-01 – DP-04, respectively. The magnitudes of the spectra were normalized to the peak of the continuous spectrum. For DP-01 – DP-04, $q(\beta)$ is uniformly distributed over half of the pulse period. Consequently, $\beta_{max} = 0.5$ and $Q(f) = \text{sinc}(\pi\beta_{max}Tf)$. This sinc function has nulls at frequencies equal to $2k/T$ ($k = \pm1, \pm2, \ldots$), which zeros out every other spectral line and causes the spacing between discrete spectral lines to be $2/T$. In these plots, the vertical shaded regions in the top plots correspond to the DTV channel displayed in the bottom plots. Notice that in all cases the spectral lines were either below the continuous spectrum or outside the DTV channel.

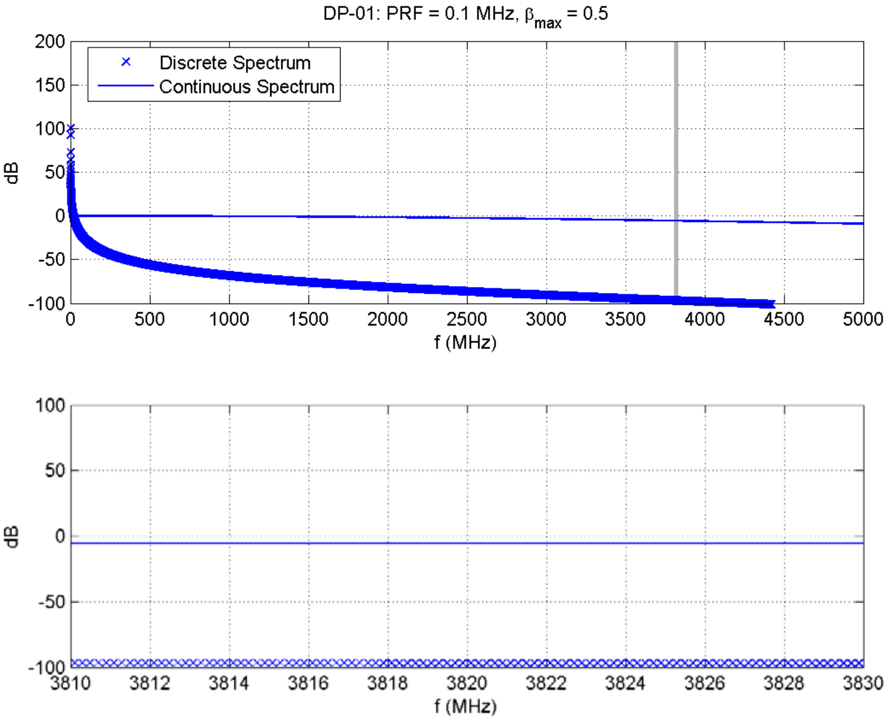

Figure A-1. Theoretical discrete and continuous spectra of DP-01.

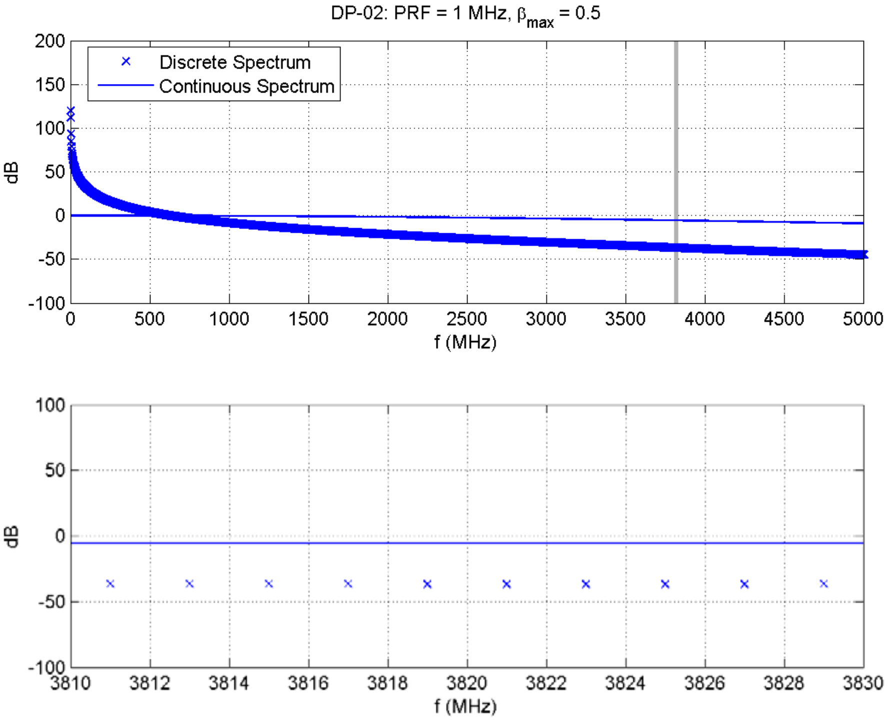

Figure A-2. Theoretical discrete and continuous spectra of DP-02.

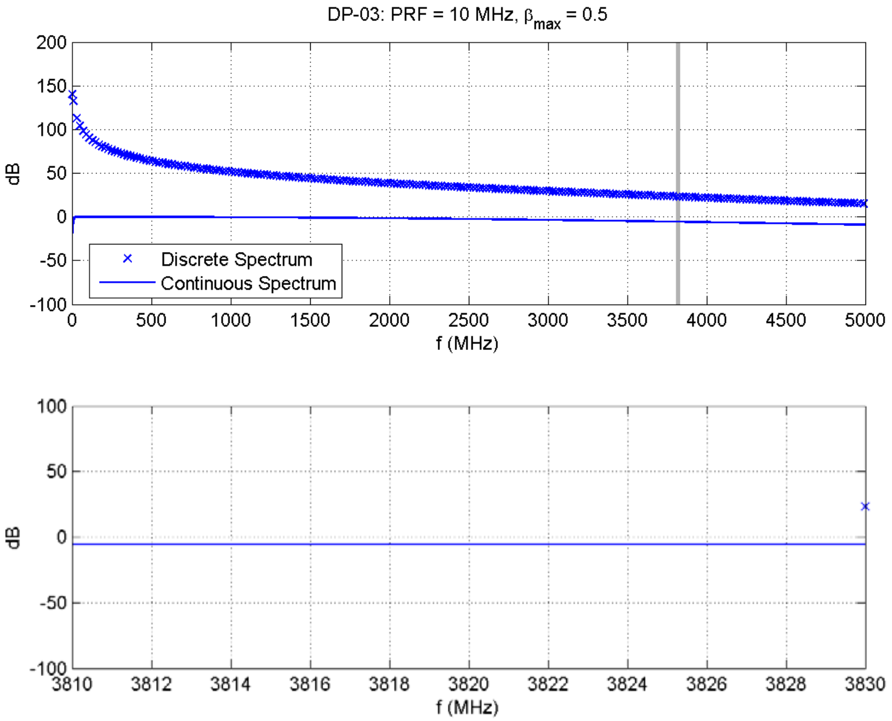

Figure A-3. Theoretical discrete and continuous spectra of DP-03.

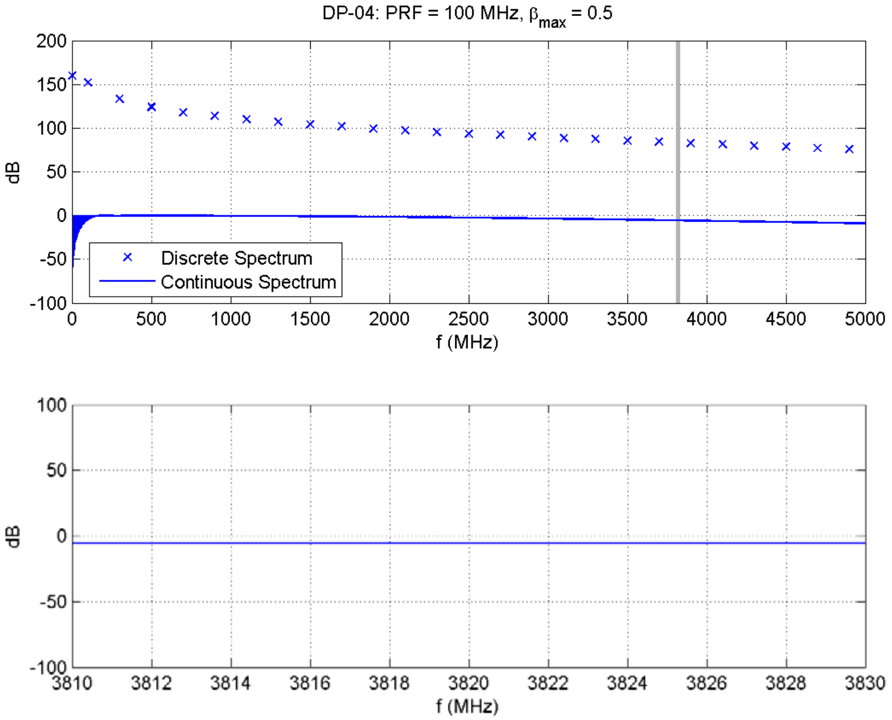

Figure A-4. Theoretical discrete and continuous spectra of DP-04.

A.2. DS-UWB

DS channel symbols are not dithered, i.e., $Q(f) = \mathrm{FT}\{q(\beta)\} = \mathrm{FT}\{\delta(0)\} = 1$. They are defined as the convolution of a codeword and the DS pulse shape (p_{DS}), i.e.,

$$-y_1(t) = y_0(t) \equiv \sum_{l=0}^{L-1} c_l \, p_{DS}(t - lT_{chip}) \quad ,$$

where L is the codeword length with values of {1, 3, 6, 12, or 24}, c_l is the l^{th} codeword chip with values {-1, 0, 1}, and T_{chip} is the chip period. Assuming DS information bit values are equiprobable, the negative relation between y_1 and y_0 makes

$$\left| \sum_k \xi_k Y_k(f) \right|^2 = \frac{1}{2} \int \left[y_0(t) + (-y_0(t)) \right] e^{-j2\pi f t} dt = 0 \quad ,$$

and causes the discrete component of the DS-UWB *PSD* to be zero. The other sum in equation (A-7) evaluates to

$$\begin{aligned} \sum_k \xi_k \left| Y_k(f) \right|^2 &= \left| \sum_{l=0}^{L-1} c_l \int p_{DS}(t - lT_{chip}) e^{-j2\pi f t} dt \right|^2 \\ &= \left| P_{DS}(f) \right|^2 \left| \sum_{l=0}^{L-1} c_l e^{-j2\pi f l T_{chip}} \right|^2 \\ &= \left| P_{DS}(f) \right|^2 \left| C(f) \right|^2 \quad , \end{aligned}$$

and substitution into equation (A-8) yields

$$\left\langle S_{uu}(f) \right\rangle = \frac{1}{T} \left| P_{DS}(f) \right|^2 \left| C(f) \right|^2 \quad .$$

Figures A-5 and A-6 illustrate $|C(f)|$ for DS-04 and DS-06, respectively. In these plots, the magnitudes of the spectra were normalized to their peak, and the vertical shaded regions in the top plots correspond to the DTV channel displayed in the bottom plots. Notice the resemblance between the $|C(f)|$ and the measured *PSD* of DS-06 illustrated in Section 2.3.3. This agreement is because $|P_{DS}(f)|$ is flat over the frequency range 3.7 – 4.2 GHz as illustrated in Figure 3 of Part 1 [6]. Not shown in this appendix are frequency flat sparse codes for DS-01, DS-02, DS-03, and DS-05, which produce the flat measured *PSD*s shown in Section 2.3.3.

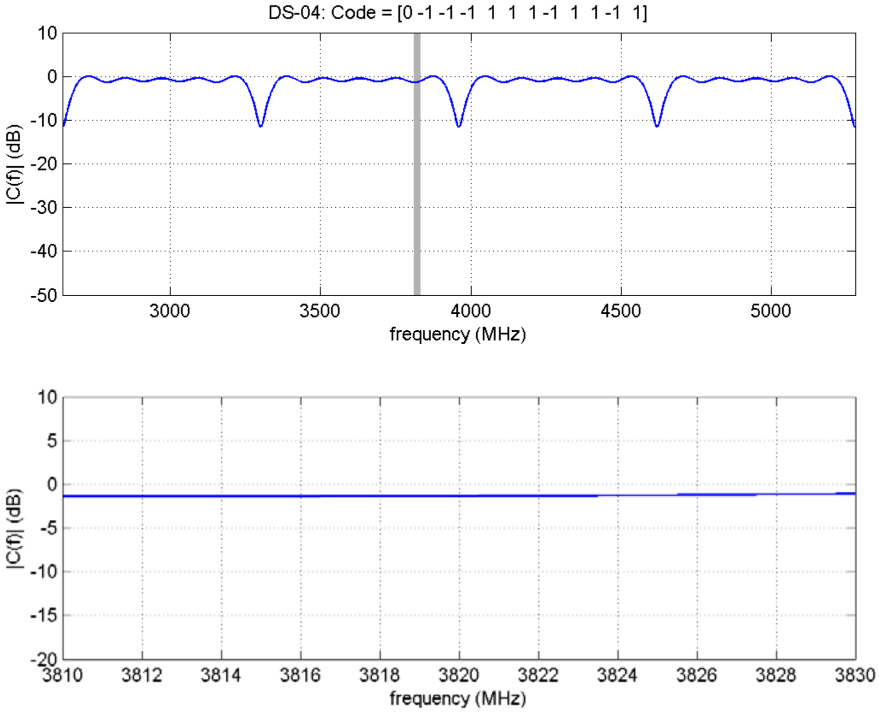

Figure A-5. |*C*(*f*)| of the DS-04 code word.

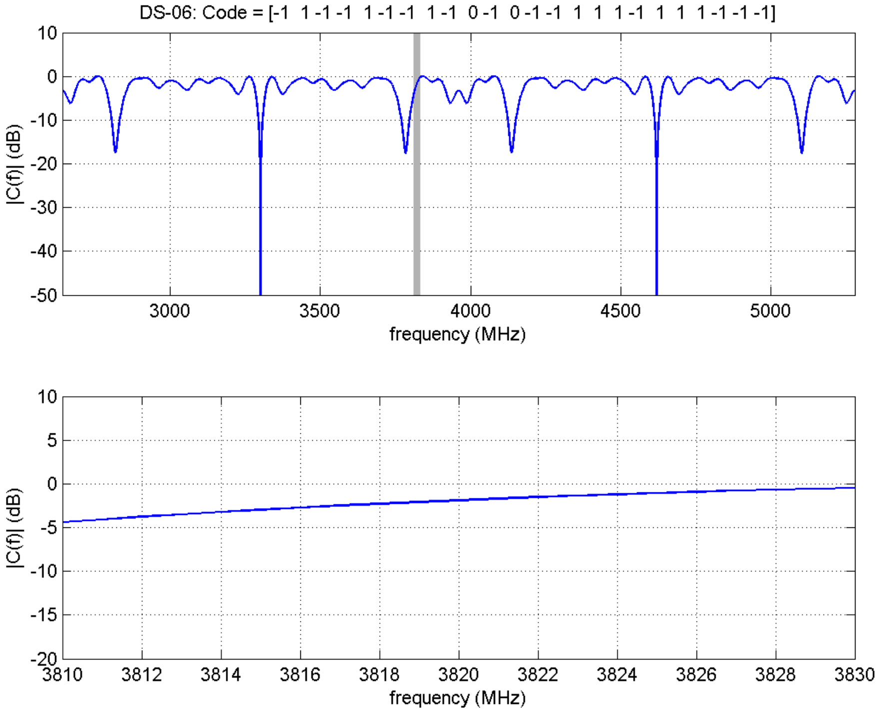

Figure A-6. |*C*(*f*)| of the DS-06 code word.

APPENDIX B. CHARACTERIZATION MEASUREMENTS

This appendix provides a thorough description of the measurement procedures and processing used to characterize the ultrawideband (UWB) signals. It provides an extensive set of temporal, amplitude, and spectral analysis results that support Sections 2.3 and 3.3.

B.1. Measurement Setup

The UWB signals were measured under optimal conditions at the radio frequency (RF) output of the vector signal generator (VSG) as described in Figure B-1. Measurements at RF were made with the vector signal analyzer (VSA) and digital oscilloscope (DO).

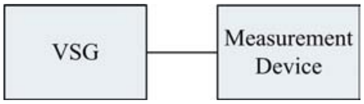

Figure B-1. Setup for RF signal characterization measurements.

Prototype DS and MB devices were made available for these tests; however, we chose to generate simulated signals with a VSG to have more control over modulation parameters and test conditions. Prototype DS and MB signals were characterized to verify corresponding VSG signals. Characteristics of the prototype DS signals matched those of the VSG DS signals. General characteristics of the prototype MB signals resembled those of the VSG MB signals. However, differences attributed to local-oscillator (LO) feed-through in the prototype MB signals were observed. Prototype-generated signal characterization measurements are not included in this report.

The VSG was set up with the procedures described in Appendix B of Part 1 [6]. UWB waveforms were created via software simulation, down-conversion to baseband, and decimation to the sampling frequency of the VSG. In order to ensure optimal use of the analog-to-digital converters in the VSG, DP and DS signals were normalized according to their maximum values shown in Table B-1. In contrast, MB-02 – MB-09 were normalized by the maximum value of MB-01 from which they were derived. In the composite plots of Section 2.3, discrepancies due to different normalization factors were removed so the relative average powers are proportional to T_{pulse}. Plots in this appendix, however, were not adjusted according to the individual normalization factors.

VSA instrument settings are summarized in Table B-2. As discussed in Appendix E of Part 1, VSG amplitudes were adjusted to ensure that the dynamic range of the VSA was optimally utilized. Table B-1 provides the VSG amplitudes used for RF signal characterization of DP and DS signals. The VSG amplitude for MB signals was -28.62 dBm.

Table B-1. Maximum Waveform Values and VSG Amplitudes for RF VSA Measurements

Type	Index	Maximum	VSG Amplitude (dBm)
DP	01	0.014	-31.61
	02	0.014	
	03	0.018	
	04	0.053	
DS	01	0.048	-29.86
	02	0.025	-30.71
	03	0.016	-31.62
	04	0.032	-33.31
	05	0.009	-33.61
	06	0.029	-33.23

Table B-2. RF VSA Measurement Settings

Post-Processing Bandwidths (MHz)	Span (MHz)	Number of Samples	Center Frequency (MHz)	Input Range (dBm)
36, 19.51, 10	36	> 360,000	3820	-30
1	4.5	> 450,000		
0.1	0.5625	> 562,500		

DO measurements at the maximum sample rate, i.e., 20 GSps, provided real, time-domain representations of RF signals. DO measurements were made with the VSG output level set to a higher value, i.e., 0 dBm, to compensate for low DO sensitivity at the maximum sample rate.

UWB interference signals were also measured at the IF output of the low-noise block downconverter (LNB) with the setup described in Figure 20 of Part 1 with the VSG output level corresponding to INR_{TOV}. The simplified block diagram of the hardware components that affect the IF signal characterization measurements is shown in Figure B-2. Bandpass filter BPF1 has a 1-dB bandwidth equal to 40 MHz.

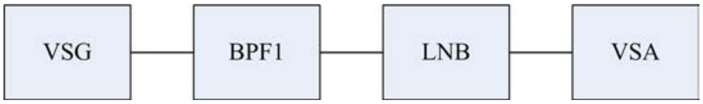

Figure B-2. Simplified setup for IF signal characterization measurements.

Measurements at IF were made with the VSA only. VSA settings for IF measurements were the same as those used for RF measurements described in Table B-2, except the center frequency was set to 1330 MHz.

B.2. Temporal Analysis

Time or crossing statistics are provided via the pulse duration distribution (*PDD*) and the pulse interval distribution (*PID*). *PDD* is presented in terms of the percentage of pulses that exceed various time durations in seconds. It provides statistics on how long a signal crosses and stays above a specified threshold. *PID* gives the probability distribution for the times a signal falls and stays below a threshold. *PDD* and *PID* are plotted on Rayleigh graph where the ordinate is plotted on a log scale. Poisson-distributed crossings with exponentially-distributed *PD* and *PI* values would plot as a straight line on this graph.

Figure B-3 is an illustration of *PD* statistics from VSA measurements of the gated-noise signal, GN-10, i.e., τ_{on} = 1 µs and 50% duty cycle, when the crossing threshold is set to -70 dBm. There are three *PD* categories: non-interrupted on-times in black, interrupted on-times in green, and anomalous spikes in red. Non-interrupted pulse durations are identified by the horizontal portion at low percentiles. Nearly 40% of *PD*s are approximately 1.13 µs corresponding to a τ_{on} slightly broadened by band-limiting.

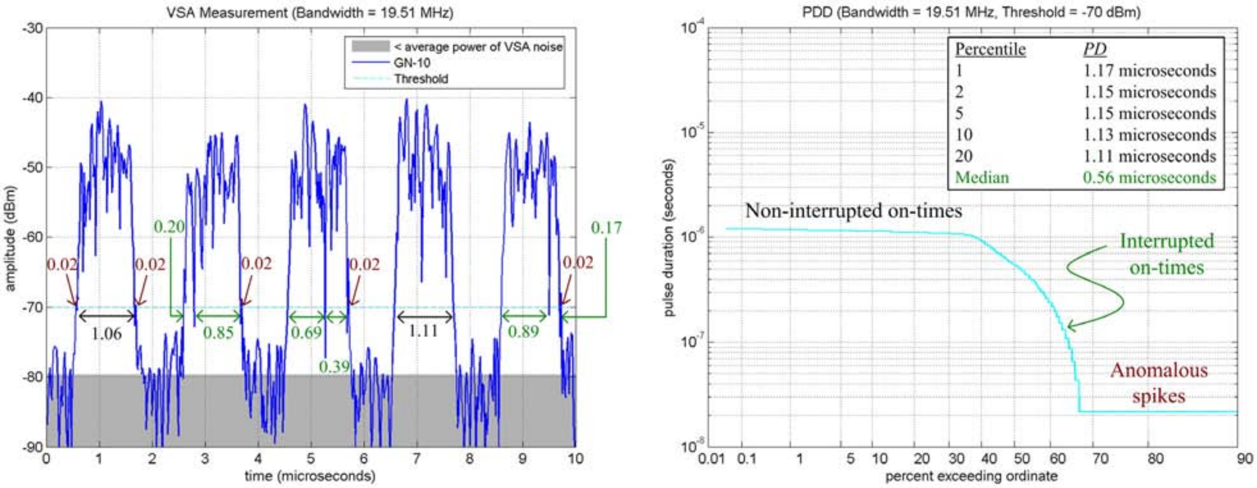

Percentile	PD
1	1.17 microseconds
2	1.15 microseconds
5	1.15 microseconds
10	1.13 microseconds
20	1.11 microseconds
Median	0.56 microseconds

Figure B-3. Pulse duration statistics of gated noise with 50% duty cycle and 1-µs on-time.

Figure B-4 is an illustration of *PI* estimates from VSA measurements of GN-10 when the crossing threshold is set to -70 dBm. Interestingly, the interrupted off-time category is absent because there are negligible disruptions from higher amplitudes. The resulting *PID* is nearly a step function. Similar to the *PD* analysis, non-interrupted *PI* estimates are identified by the horizontal portion at low percentiles.

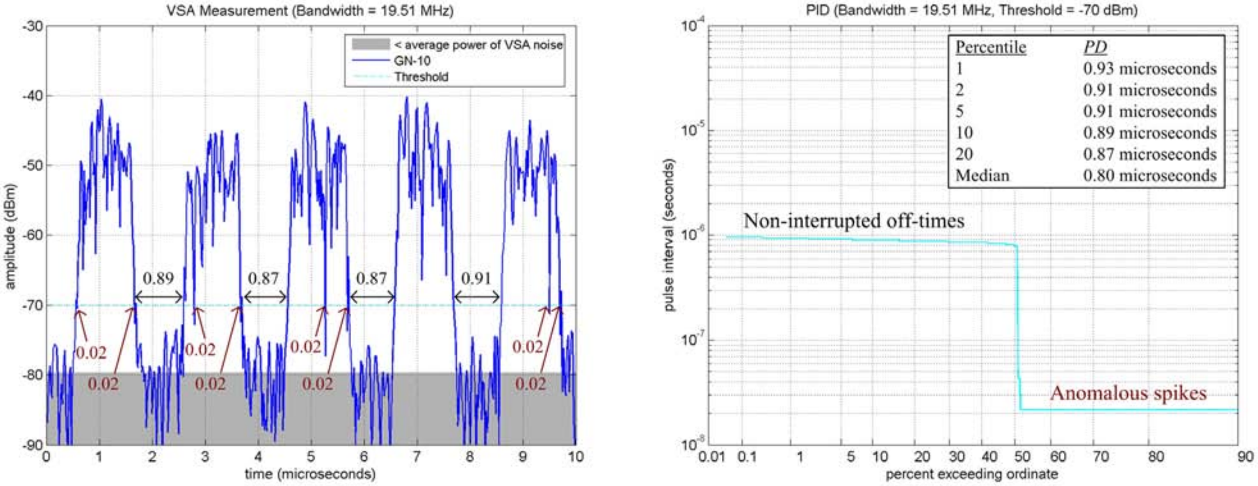

Figure B-4. Pulse interval statistics of gated noise with 50% duty cycle and 1-µs on-time.

Figure B-5 is an illustration of *PI* estimates from VSA measurements of complex Gaussian noise, GN-01, when the crossing threshold is set to -70 dBm. For the given measurement procedure, this choice for the crossing threshold is too low to quantify meaningful time statistics of continuous signals. As illustrated, GN-01 only triggered time statistic estimates at anomalous noise spikes. Therefore, it is useful to provide curves for a range of crossing thresholds.

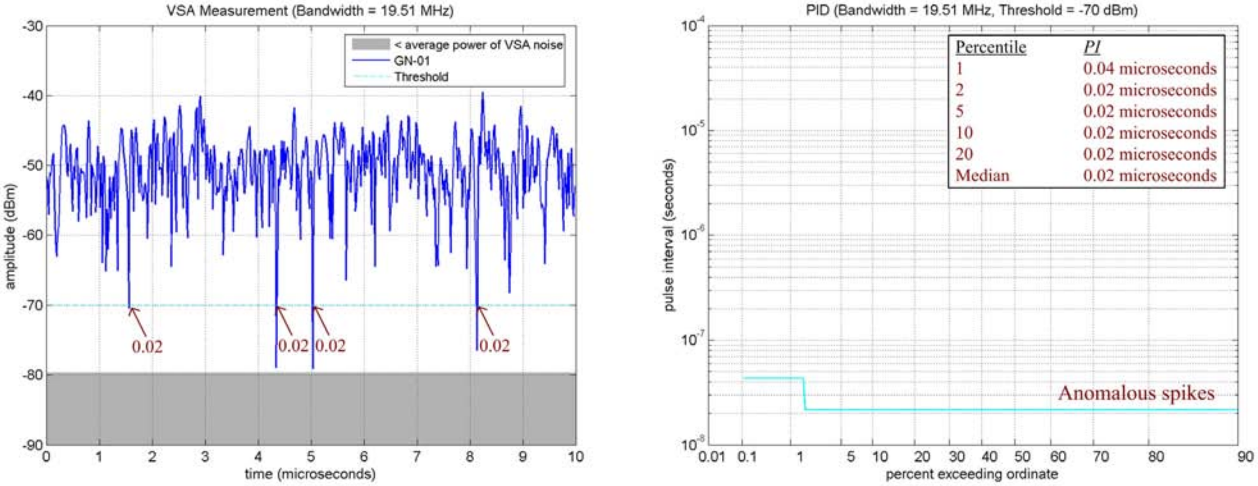

Figure B-5. Pulse interval statistics of complex Gaussian noise.

Figures B-6 – B-24 provide *PDD* and *PID* for the UWB signals when the crossing threshold was set to mean amplitude, -50 dBm, -60 dBm, and -70 dBm. Tenth percentile *PD* and *PI* estimates when the crossing threshold was set to -70 dBm were chosen as meaningful metrics to quantify the on- and off-times of band-limited signals and were specified in the main text as burst duration (*BD*) and burst interval (*BI*), respectively.

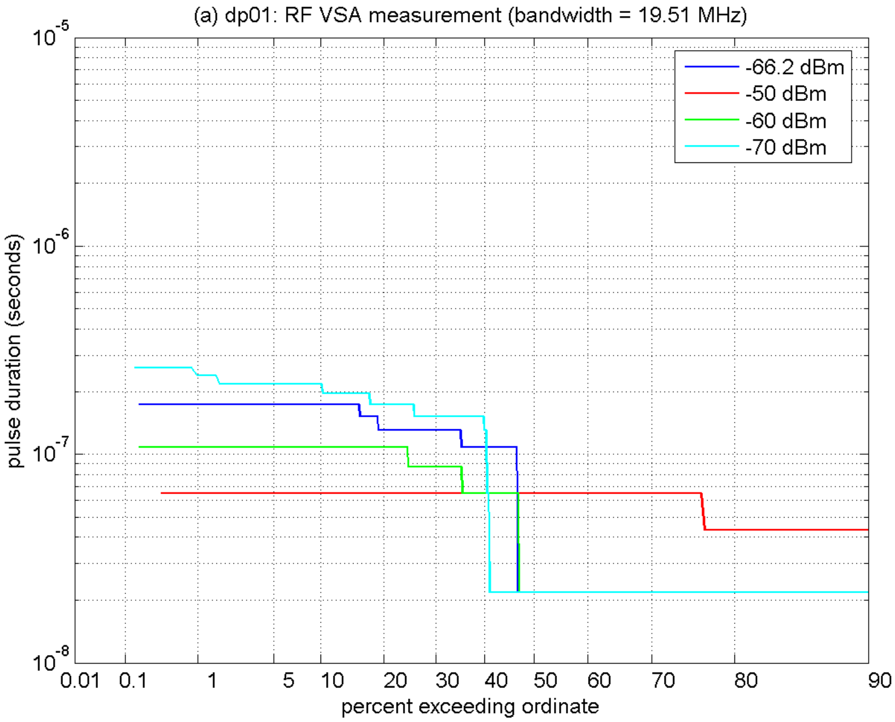

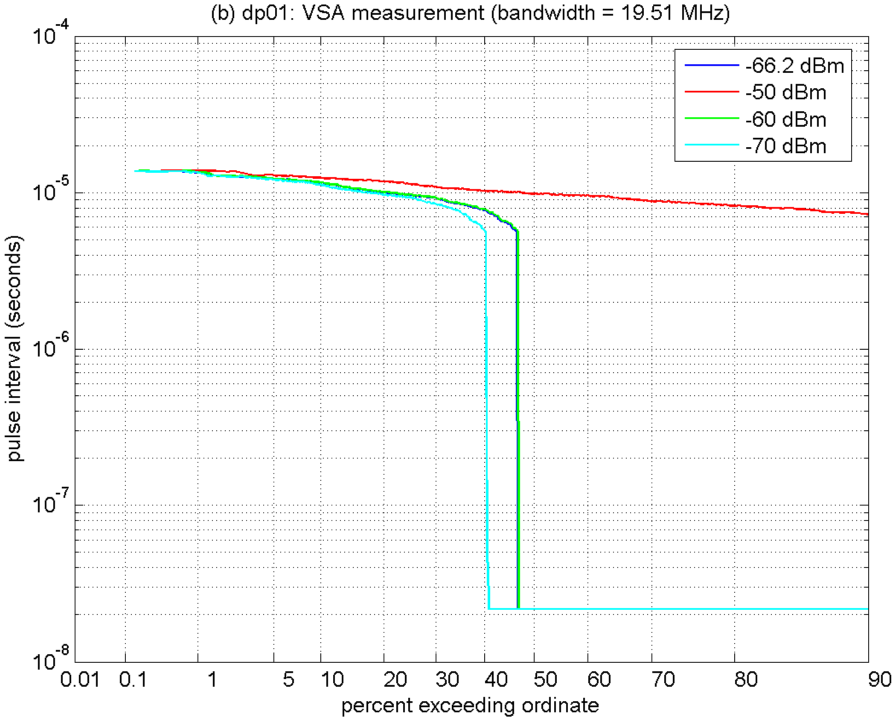

Figure B-6. RF temporal analyses of DP-01 (T_{pulse} = 10,000 ns, w = 0.094 ns, f_D = 0.5).

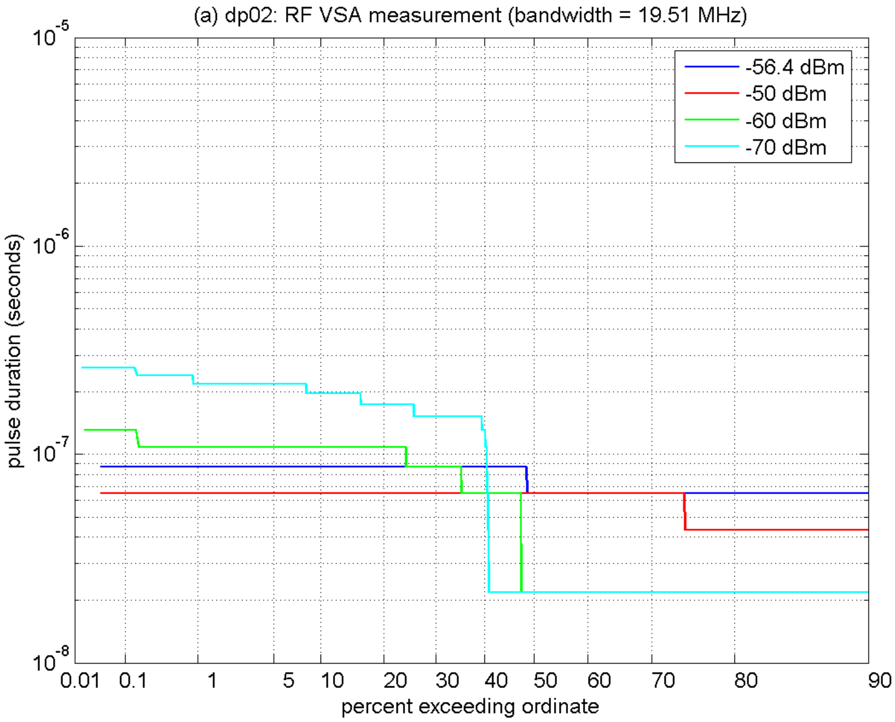
(a) dp02: RF VSA measurement (bandwidth = 19.51 MHz)

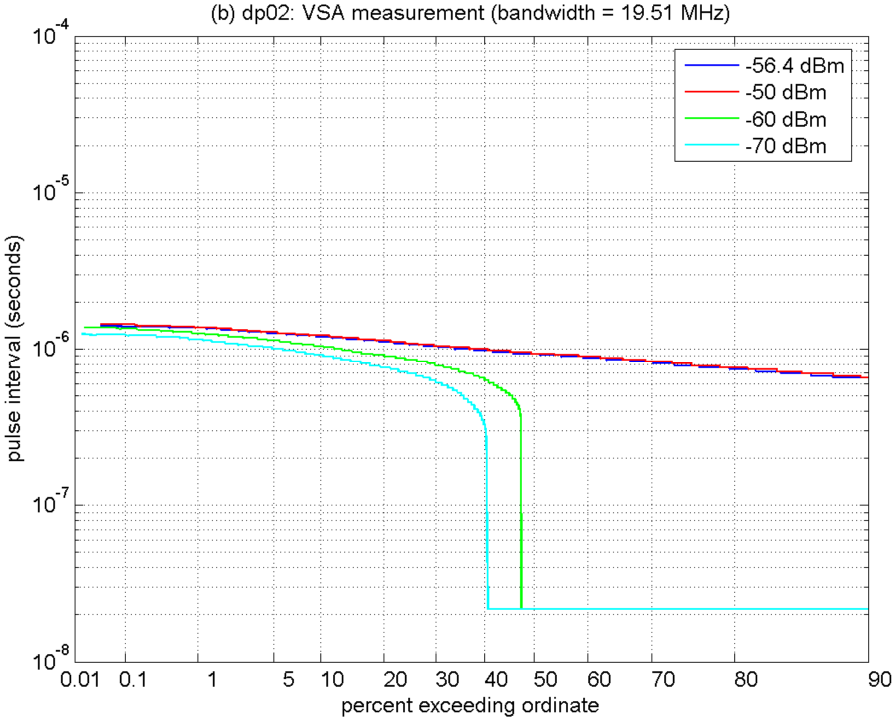
(b) dp02: VSA measurement (bandwidth = 19.51 MHz)

Figure B-7. RF temporal analyses of DP-02 (T_{pulse} = 1000 ns, w = 0.094 ns, f_D = 0.5).

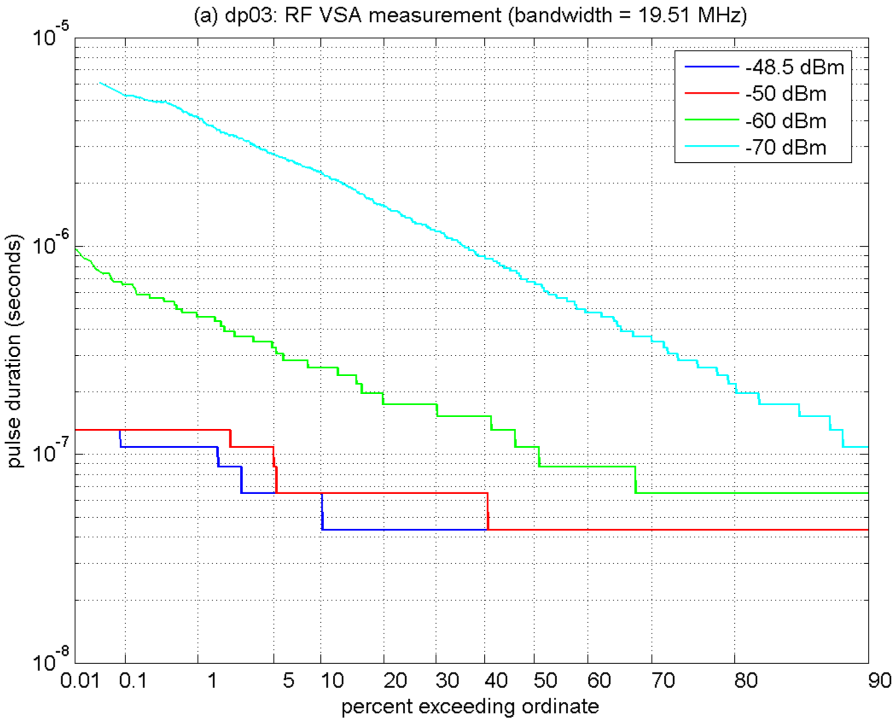

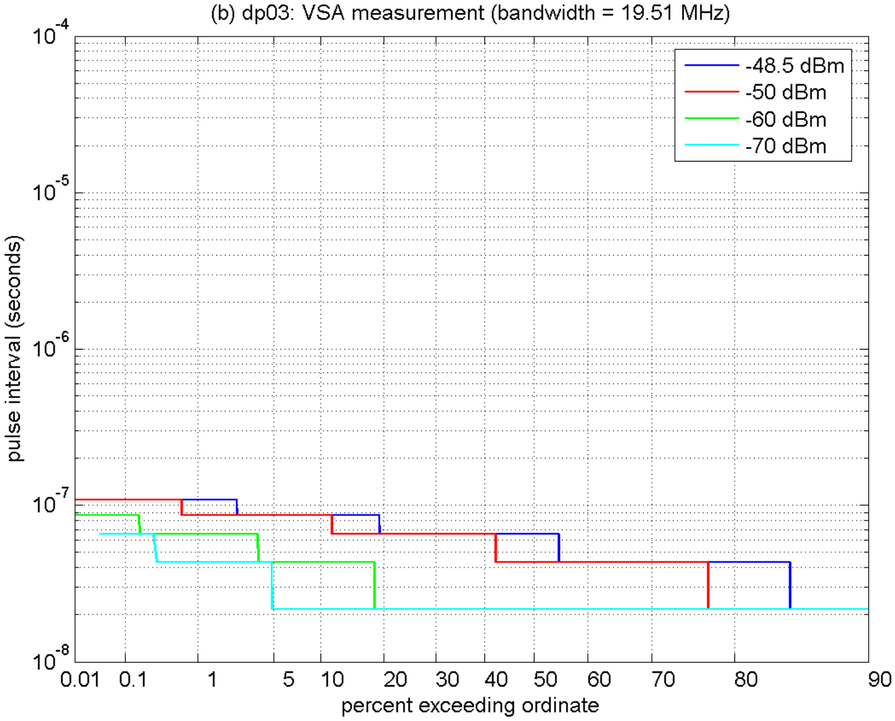

Figure B-8. RF temporal analyses of DP-03 (T_{pulse} = 100 ns, w = 0.094 ns, f_D = 0.5).

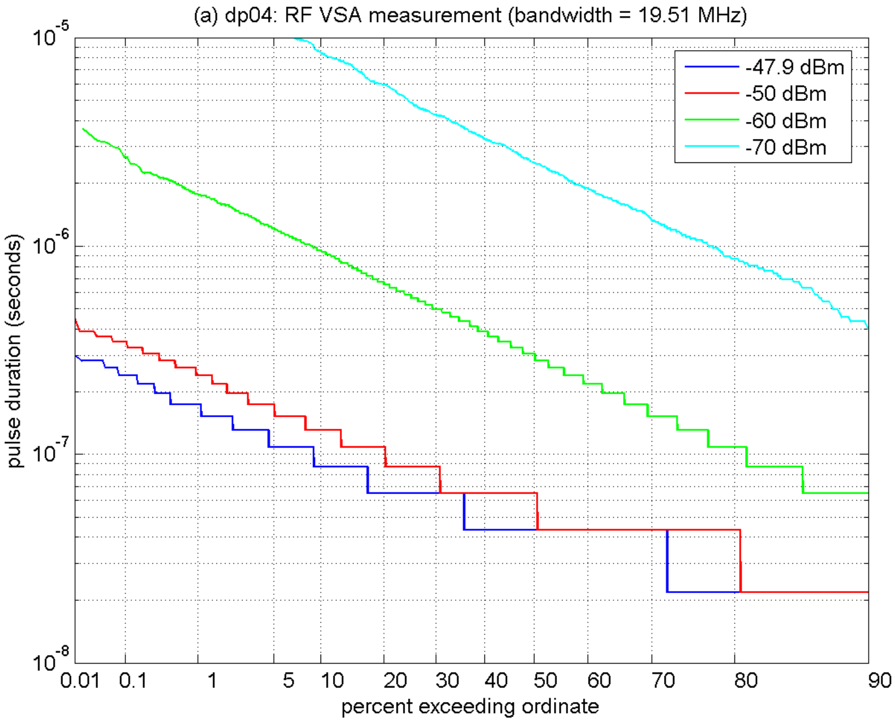

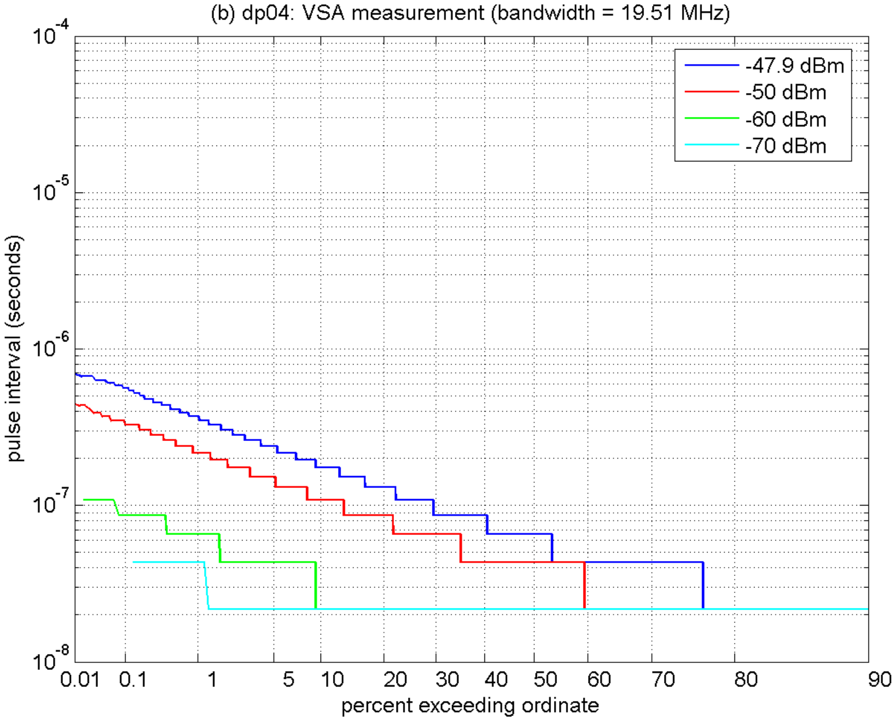

Figure B-9. RF temporal analyses of DP-04 (T_{pulse} = 10 ns, w = 0.094 ns, f_D = 0.5).

(a) ds01: RF VSA measurement (bandwidth = 19.51 MHz)

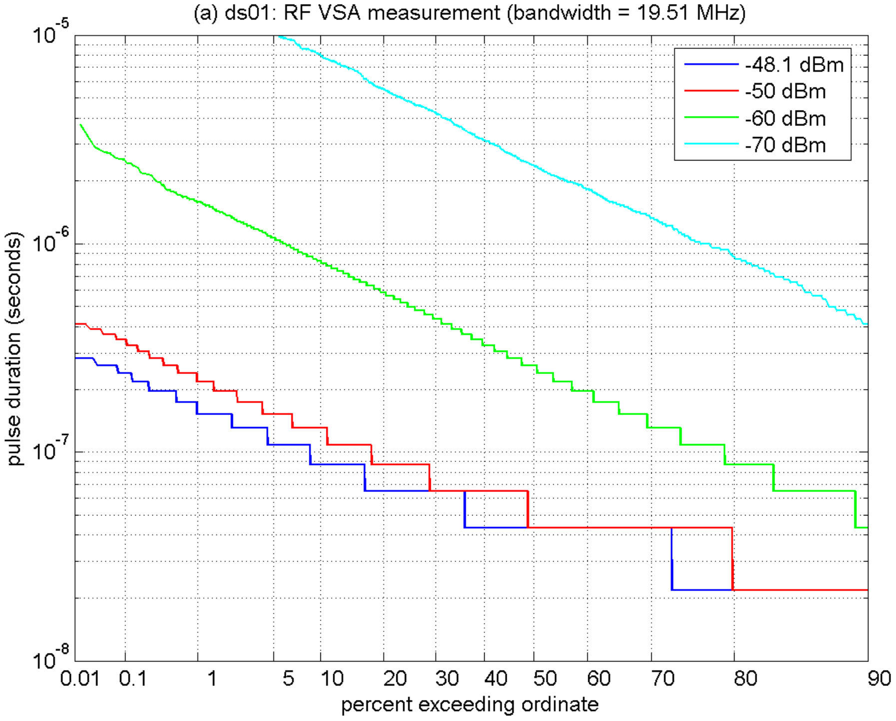

(b) ds01: VSA measurement (bandwidth = 19.51 MHz)

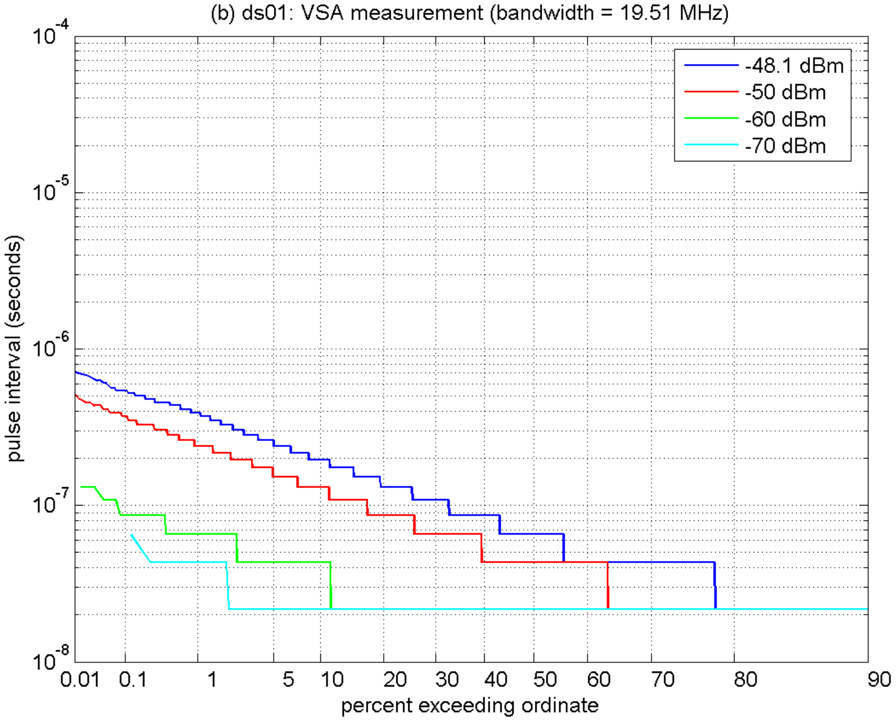

Figure B-10. RF temporal analyses of DS-01 ($L = 1$).

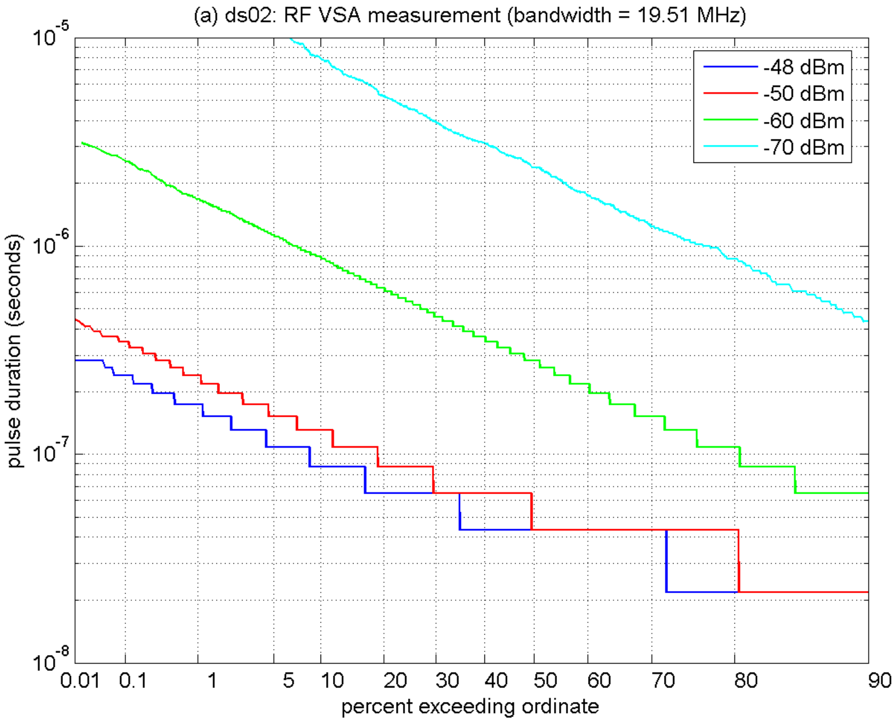

(a) ds02: RF VSA measurement (bandwidth = 19.51 MHz)

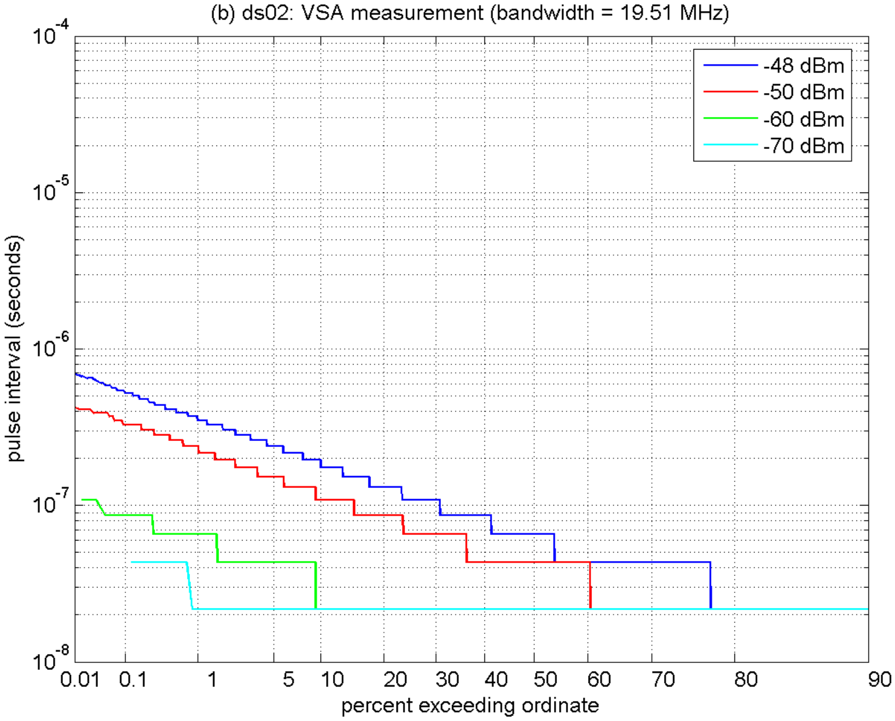

(b) ds02: VSA measurement (bandwidth = 19.51 MHz)

Figure B-11. RF temporal analyses of DS-02 ($L = 3$, sparse code).

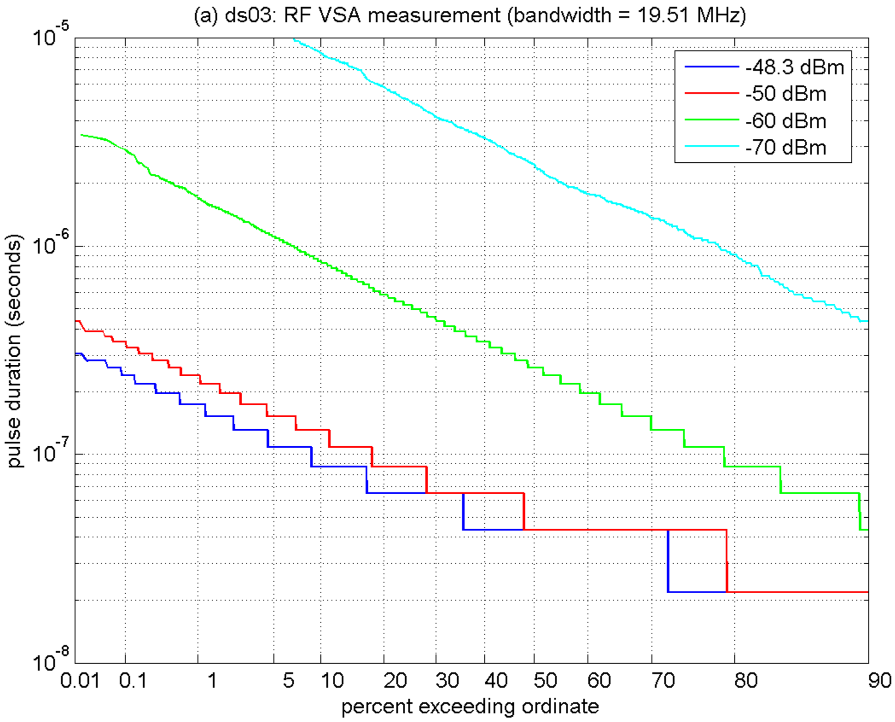
(a) ds03: RF VSA measurement (bandwidth = 19.51 MHz)

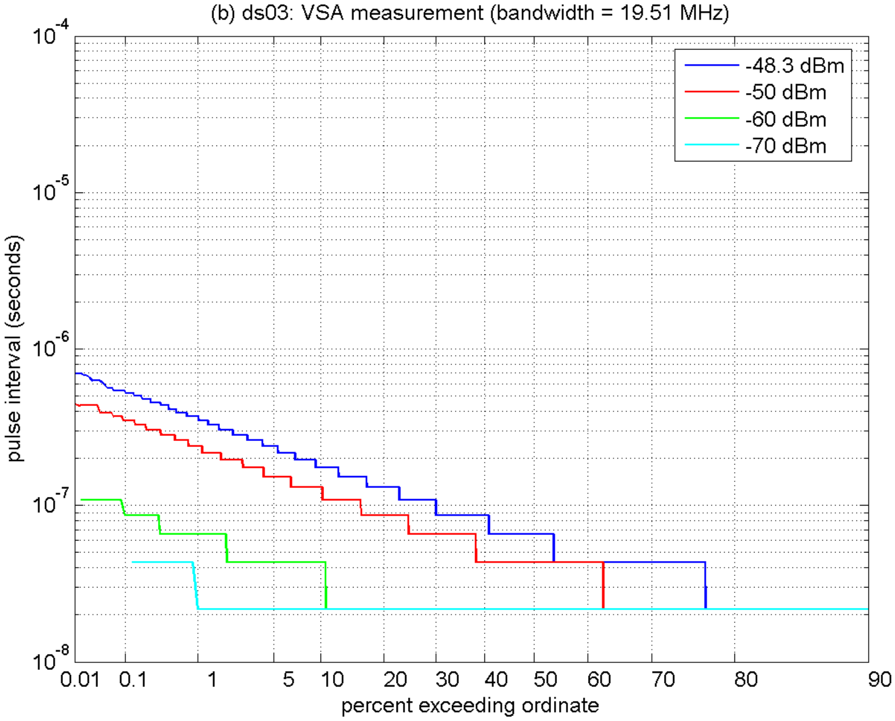
(b) ds03: VSA measurement (bandwidth = 19.51 MHz)

Figure B-12. RF temporal analyses of DS-03 (*L* = 6, sparse code).

(a) ds04: RF VSA measurement (bandwidth = 19.51 MHz)

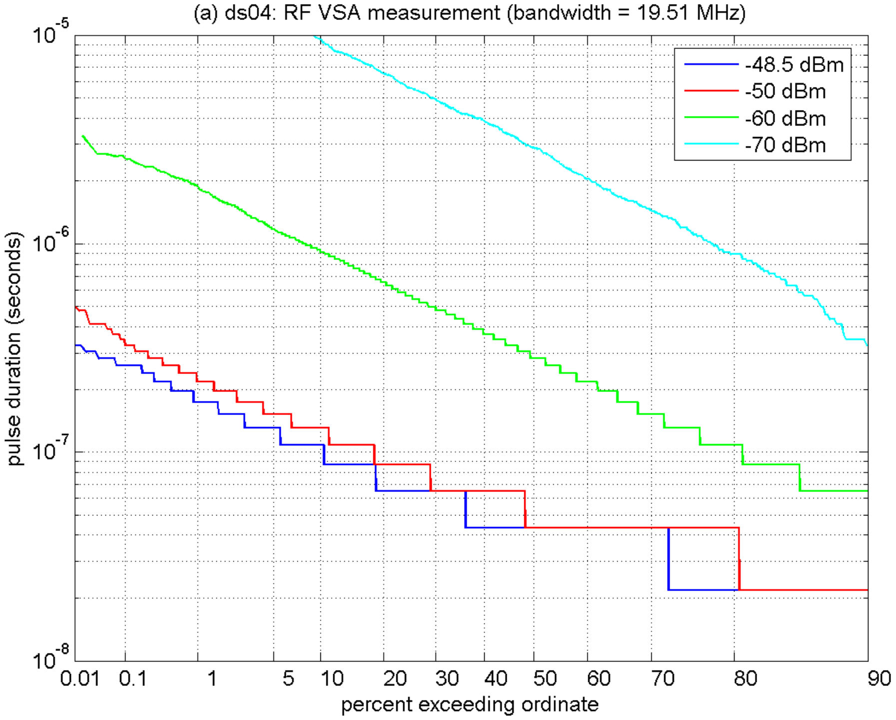

(b) ds04: VSA measurement (bandwidth = 19.51 MHz)

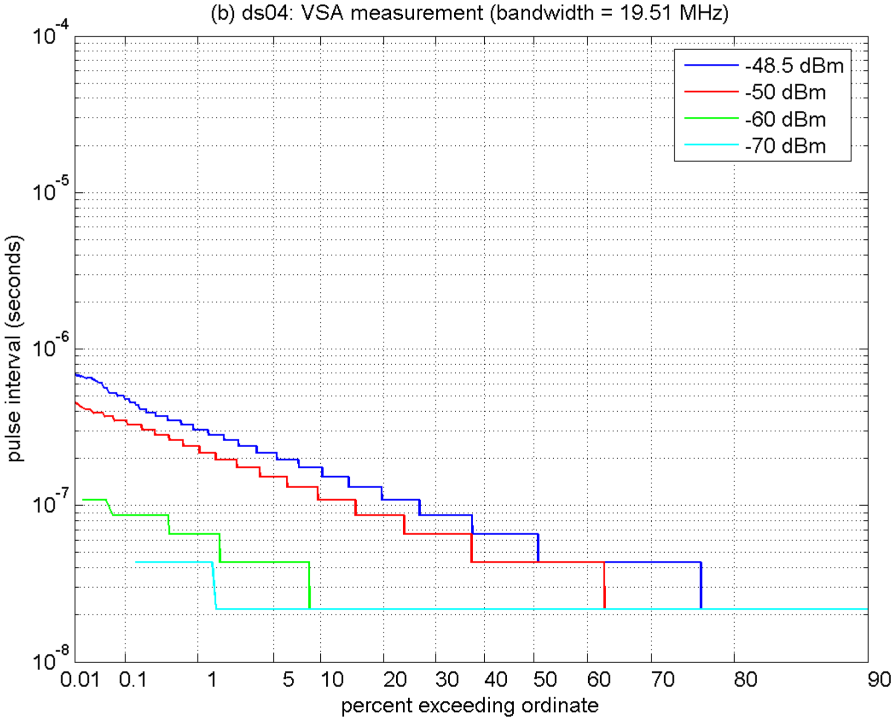

Figure B-13. RF temporal analyses of DS-04 (*L* = 12, DS code).

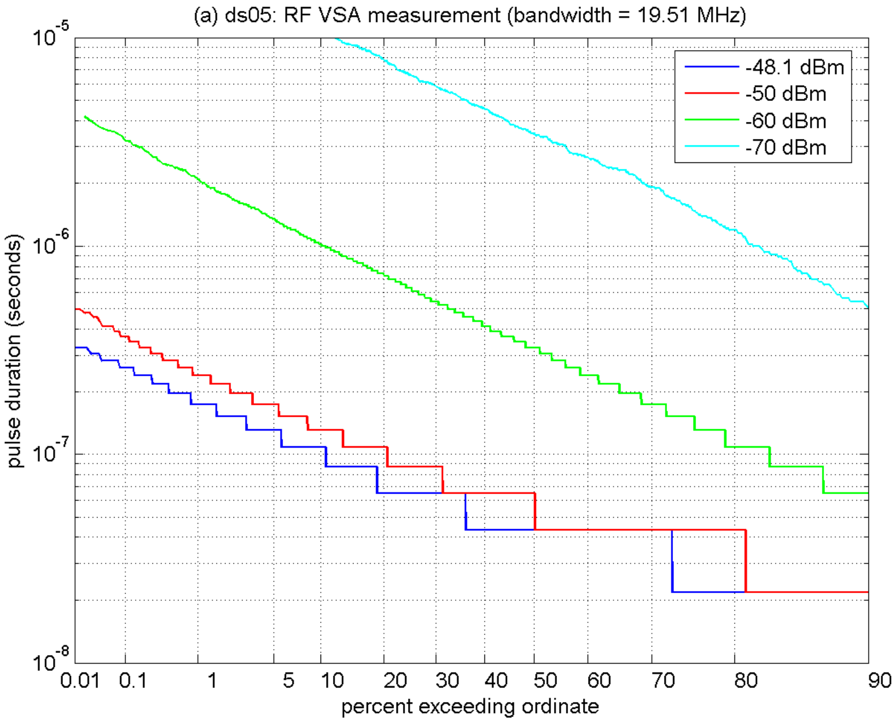

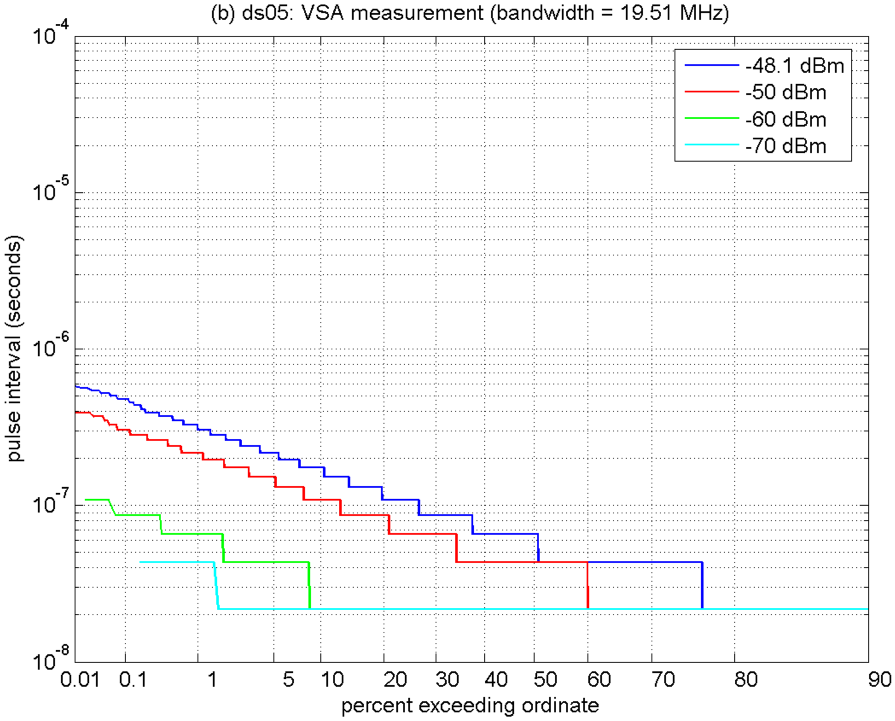

Figure B-14. RF temporal analyses of DS-05 (*L* = 12, sparse code).

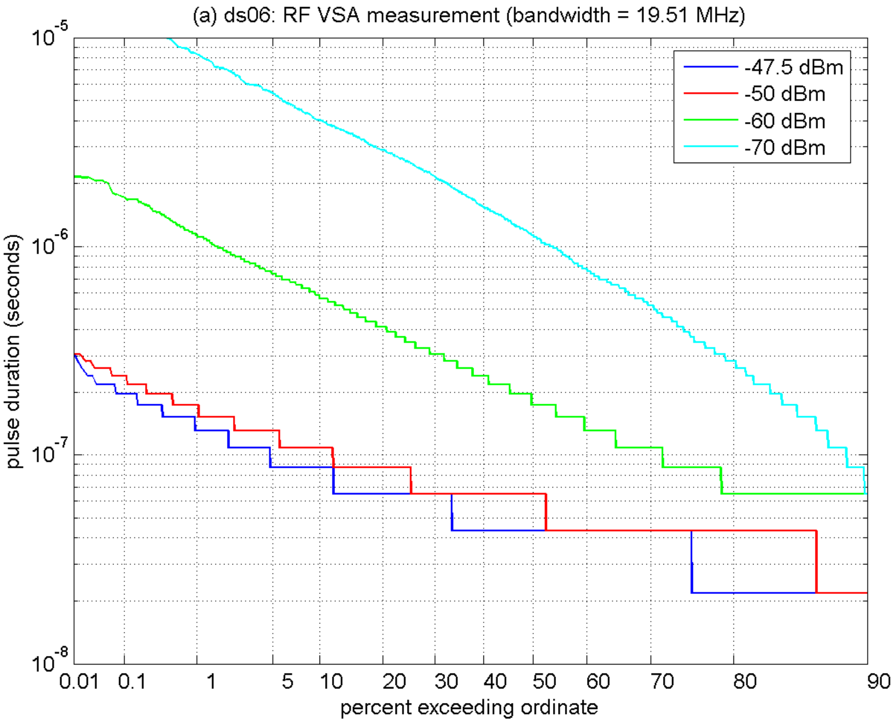

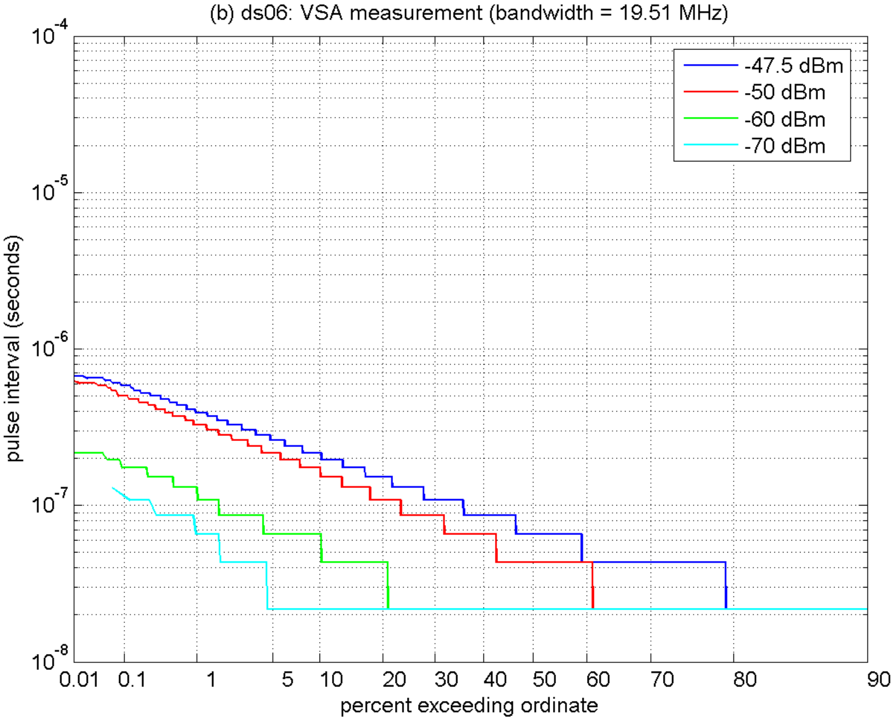

Figure B-15. RF temporal analyses of DS-06 (*L* = 24, DS code).

(a) mb01: RF VSA measurement (bandwidth = 19.51 MHz)

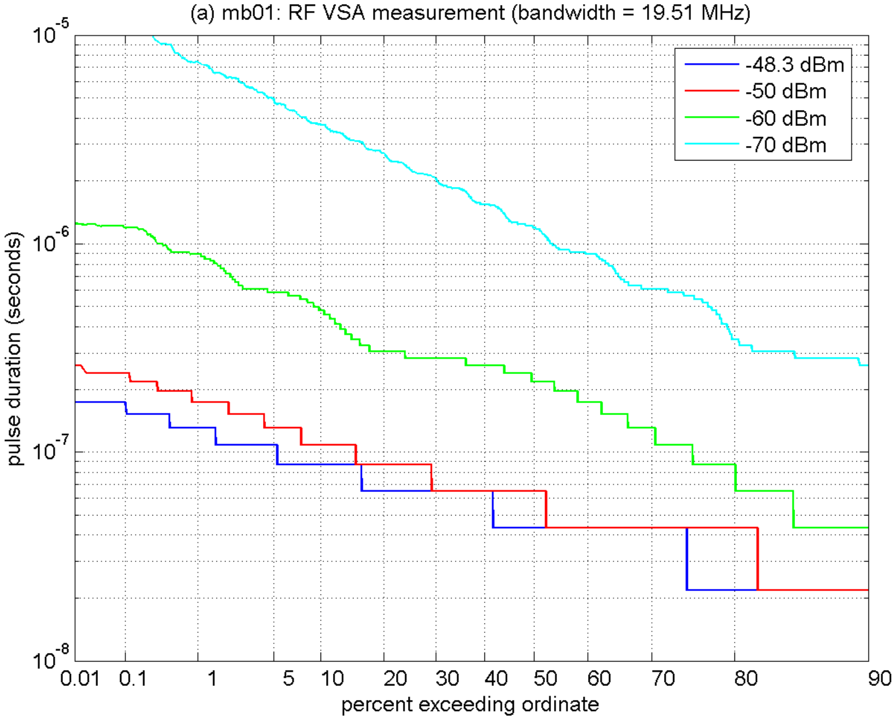

(b) mb01: VSA measurement (bandwidth = 19.51 MHz)

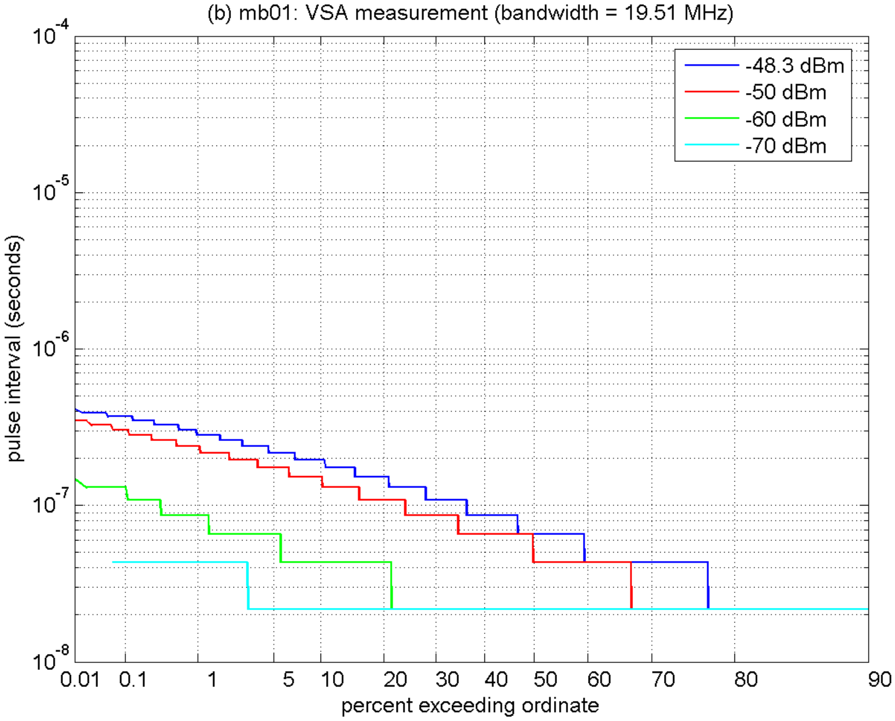

Figure B-16. RF temporal analyses of MB-01 (*b* = 1).

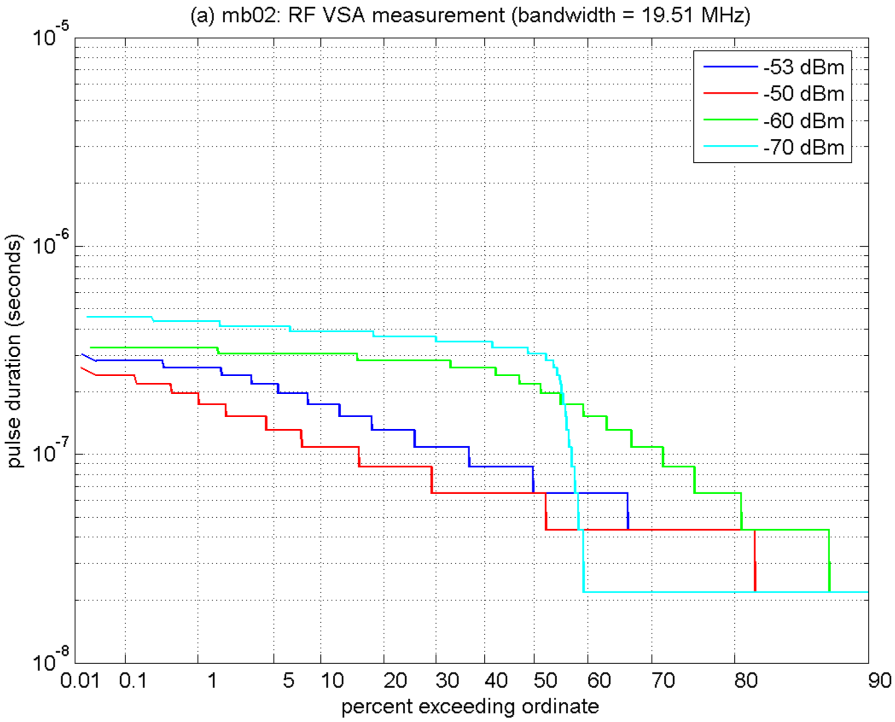

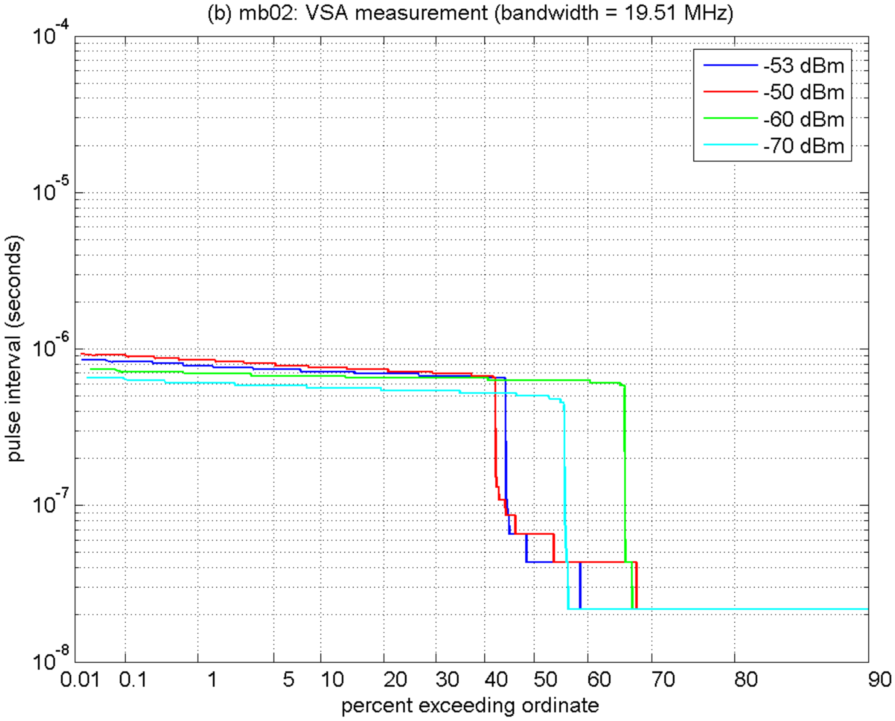

Figure B-17. RF temporal analyses of MB-02 (*b* = 3, *d* = 1).

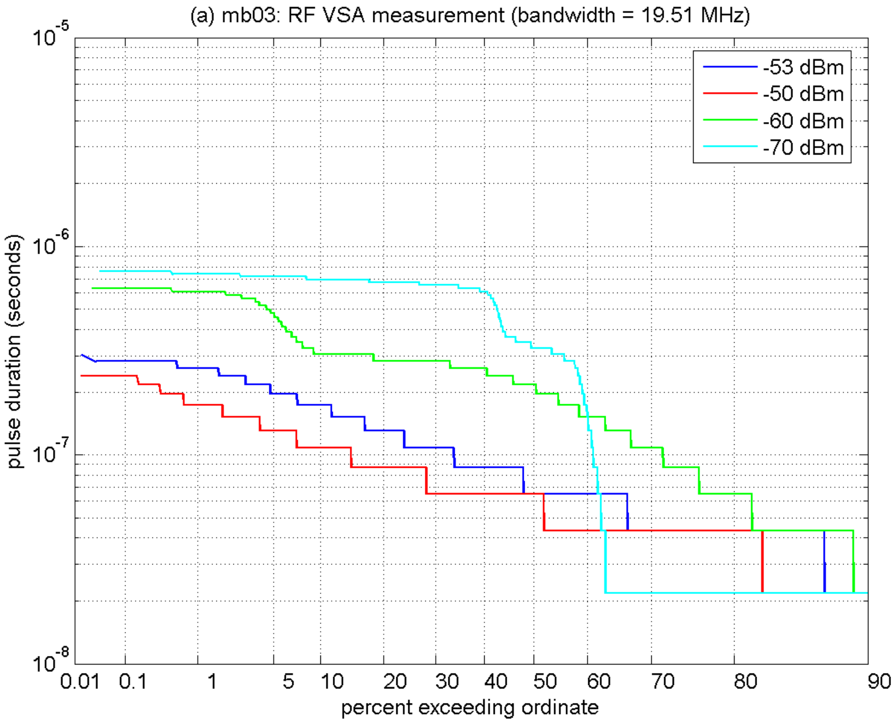

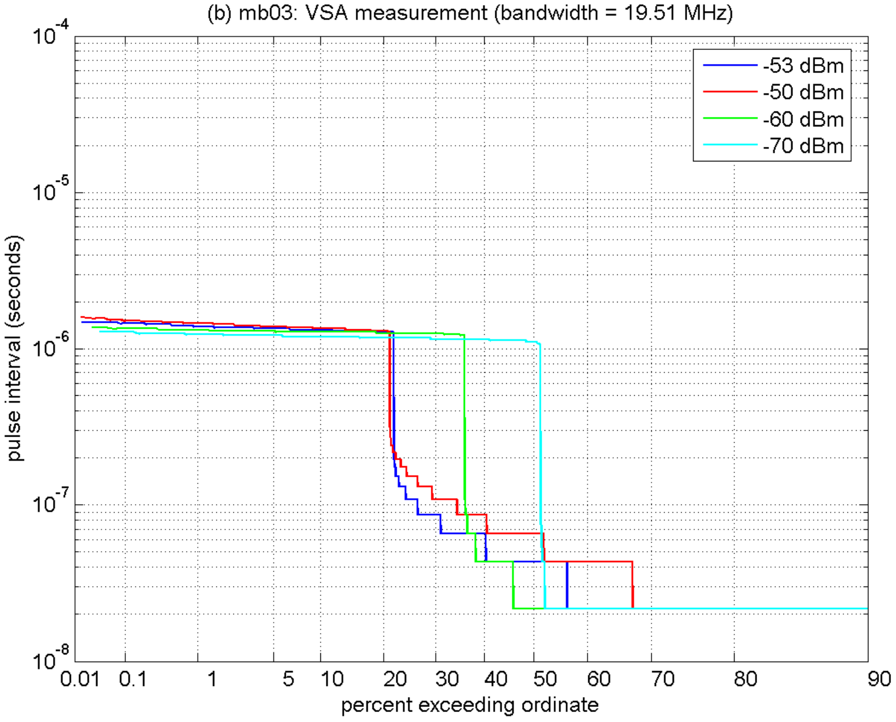

Figure B-18. RF temporal analyses of MB-03 (*b* = 3, *d* = 2).

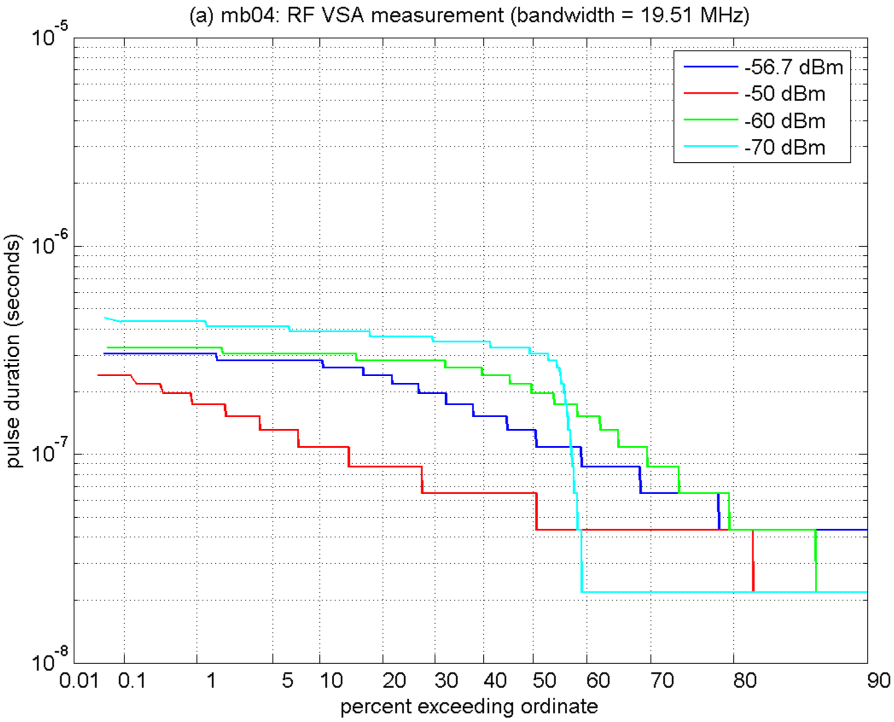

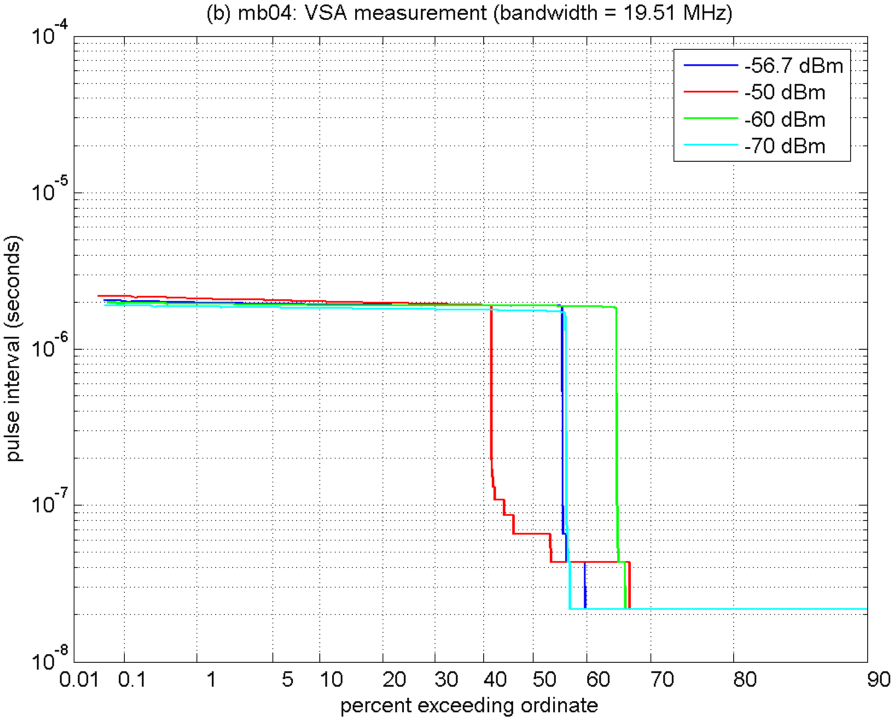

Figure B-19. RF temporal analyses of MB-04 (*b* = 7, *d* = 1).

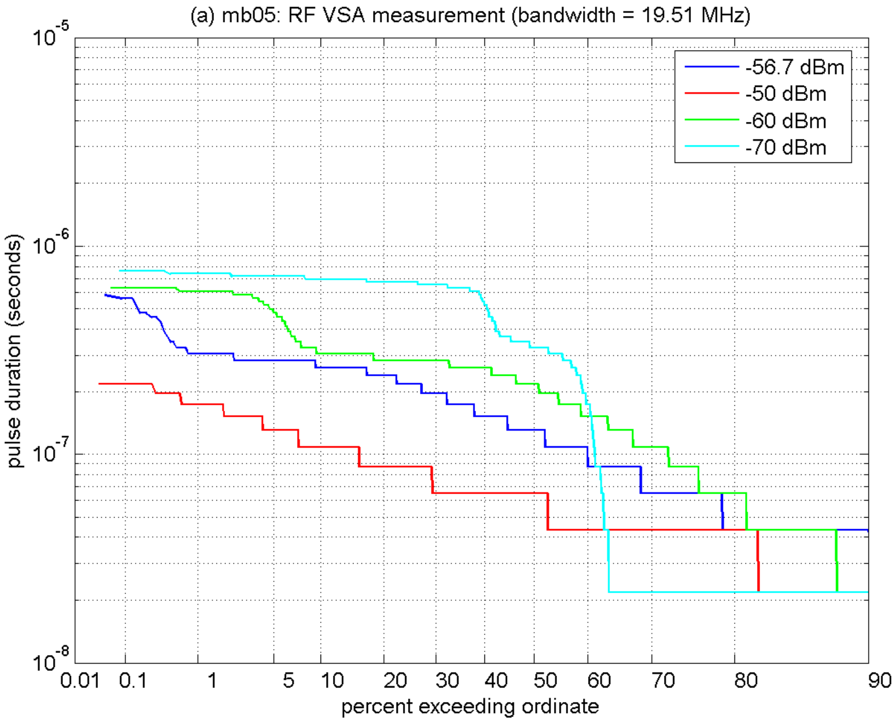

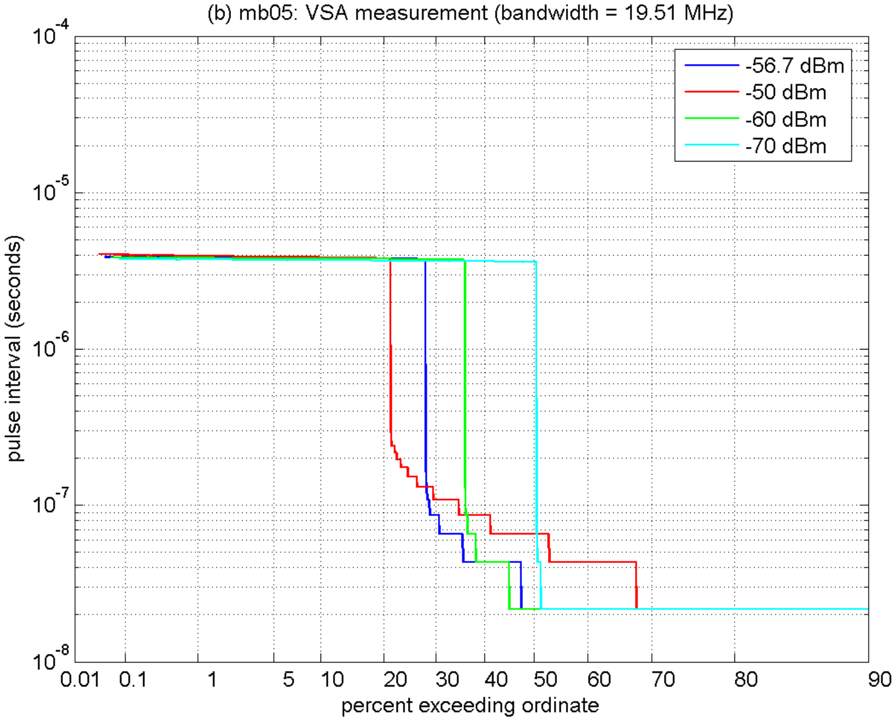

Figure B-20. RF temporal analyses of MB-05 (*b* = 7, *d* = 2).

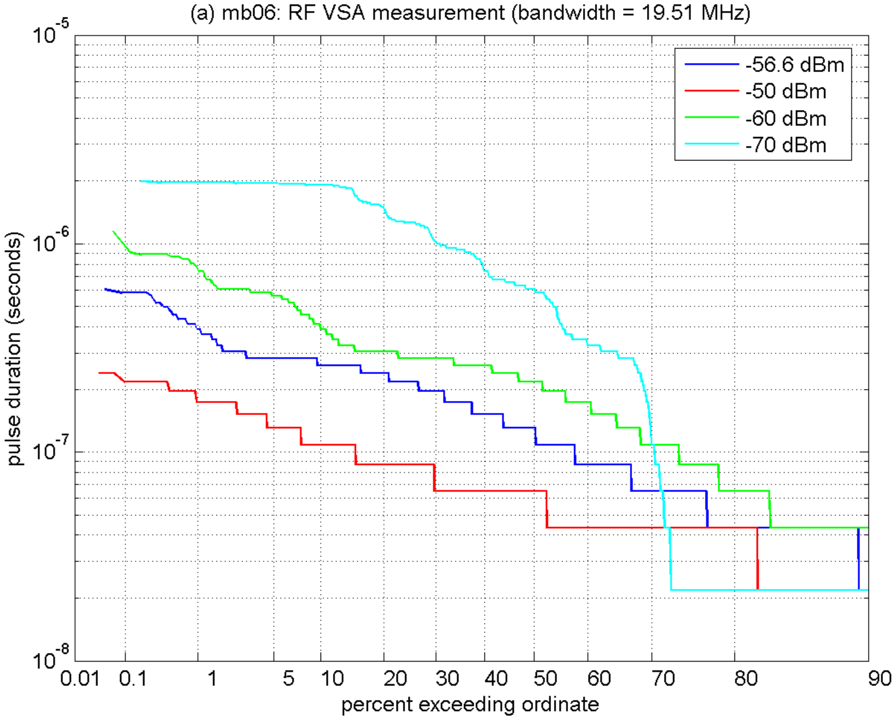

(a) mb06: RF VSA measurement (bandwidth = 19.51 MHz)

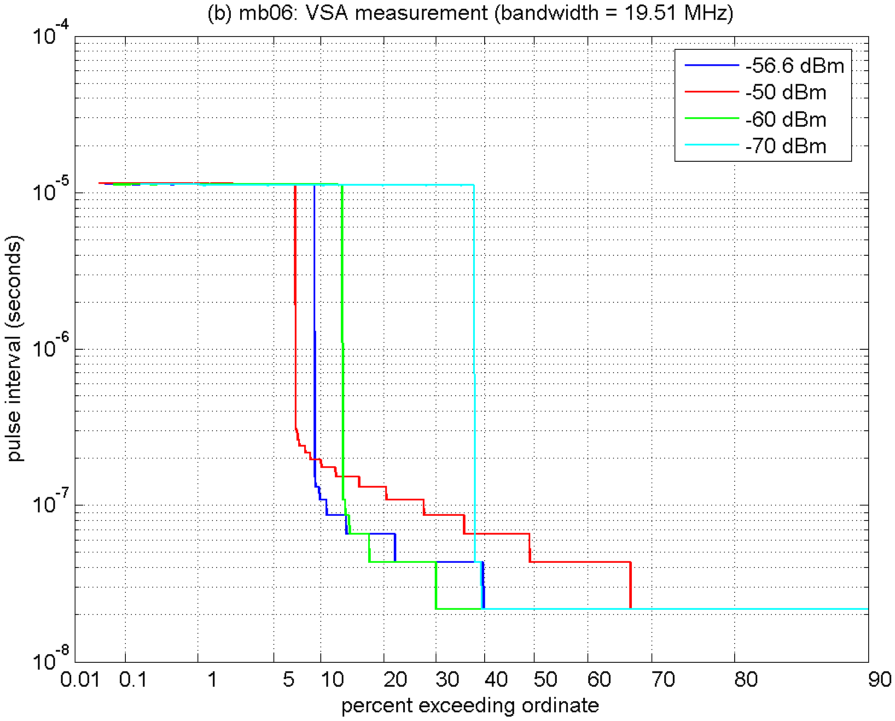

(b) mb06: VSA measurement (bandwidth = 19.51 MHz)

Figure B-21. RF temporal analyses of MB-06 (b = 7, d = 6).

(a) mb07: RF VSA measurement (bandwidth = 19.51 MHz)

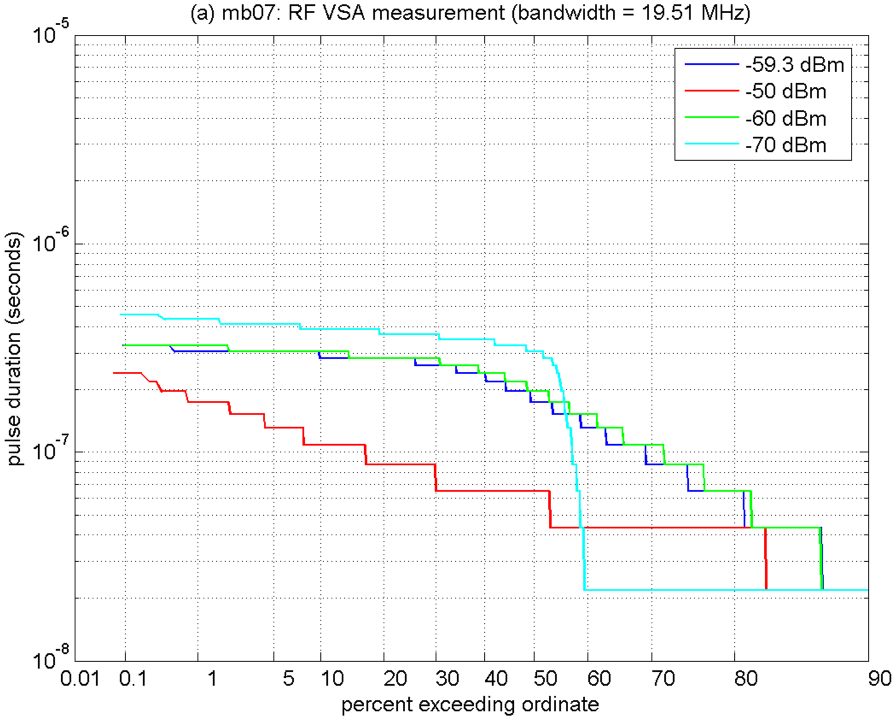

(b) mb07: VSA measurement (bandwidth = 19.51 MHz)

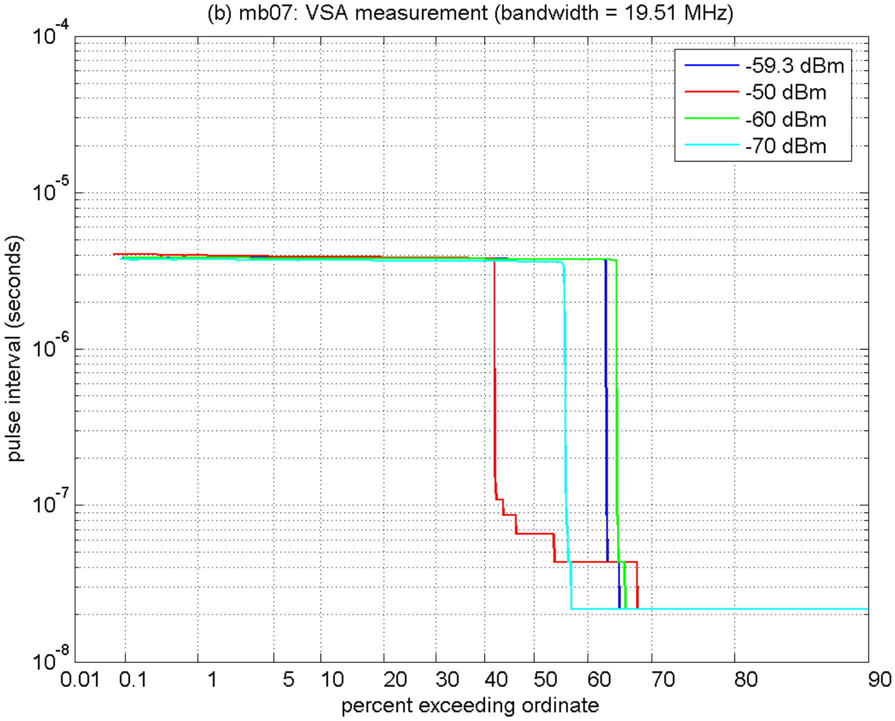

Figure B-22. RF temporal analyses of MB-07 (*b* = 13, *d* = 1).

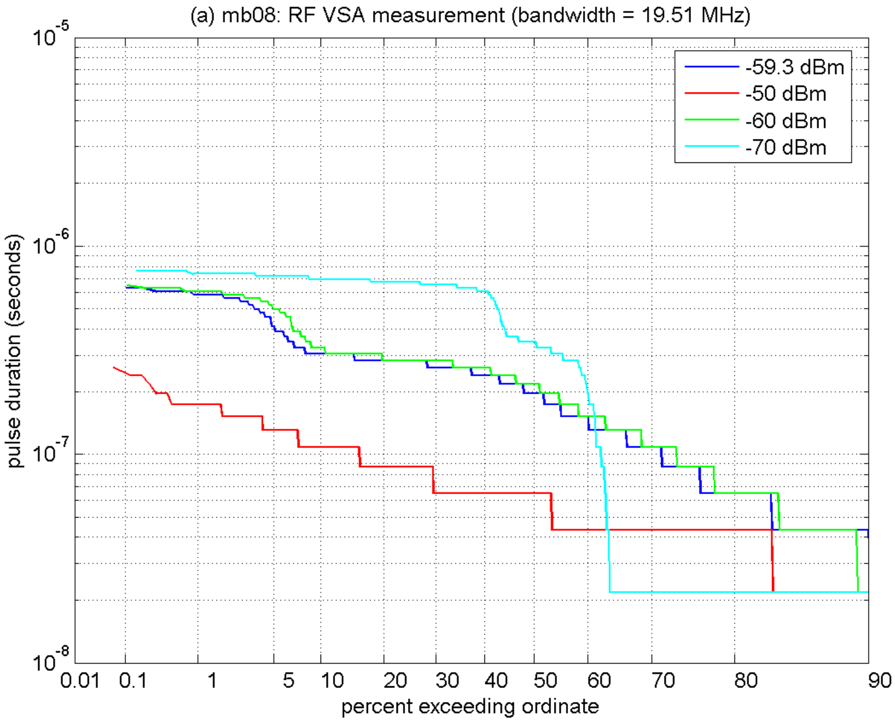

(a) mb08: RF VSA measurement (bandwidth = 19.51 MHz)

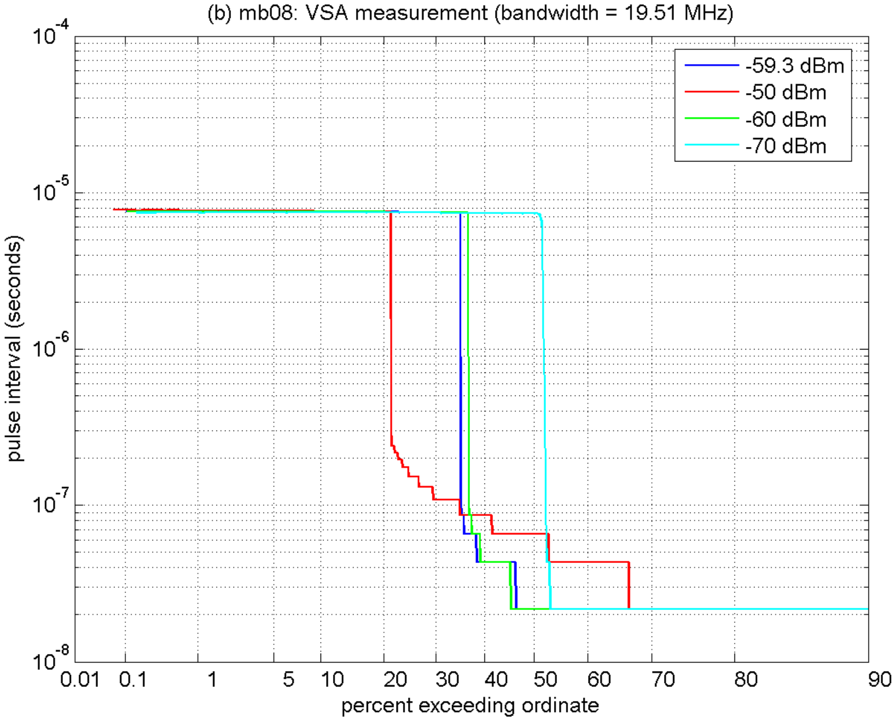

(b) mb08: VSA measurement (bandwidth = 19.51 MHz)

Figure B-23. RF temporal analyses of MB-08 (*b* = 13, *d* = 2).

(a) mb09: RF VSA measurement (bandwidth = 19.51 MHz)

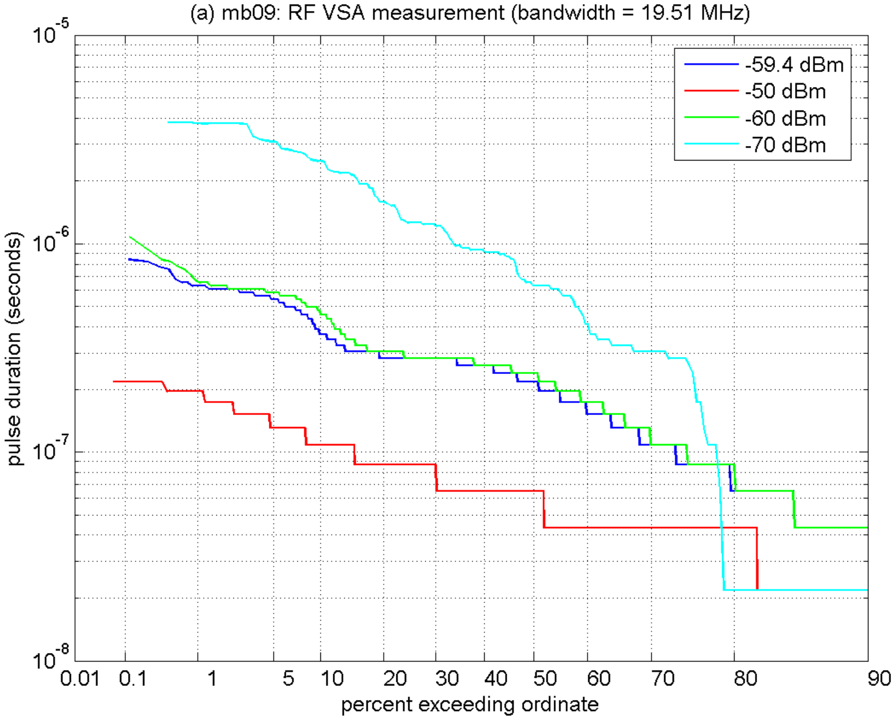

(b) mb09: VSA measurement (bandwidth = 19.51 MHz)

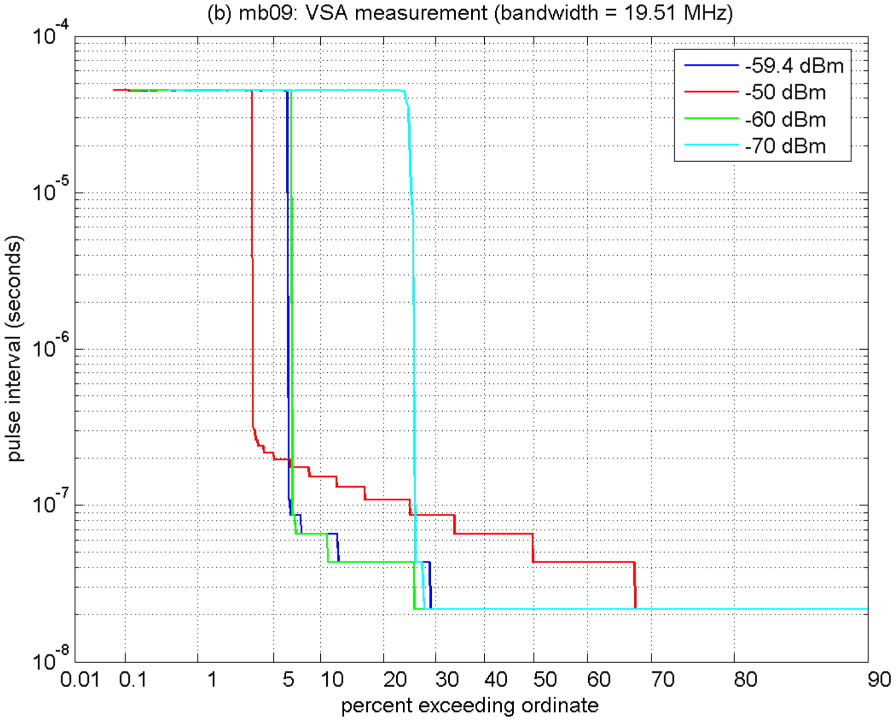

Figure B-24. RF temporal analyses of MB-09 (*b* = 13, *d* = 12).

B.3. Amplitude Analysis

This subsection provides measured time series and amplitude probability distributions (*APD*s) of the UWB signals. Odd numbered plots in Figures B-25 – B-62 provide RF measurement results organized as:

(a) Real time series measured with the DO and amplitude time series measured with the VSA and band-limited to B_{DTV} = 19.51 MHz.
(b) *APD*s measured with the VSA and band-limited to 36, B_{DTV}, 10, 1, and 0.1 MHz.

Even numbered plots in Figures B-25 – B-62 provide IF measurement results organized as:

(a) Amplitude time series measured with the VSA and band-limited to B_{DTV}.
(b) *APD*s measured with the VSA and band-limited to B_{DTV}.

Table B-3 provides peak-to-average (*P/A*) values for the UWB signals measured at RF and band-limited to various bandwidths in post-measurement processing. Table B-4 provides *P/A* values for the UWB signals measured at IF under TOV operational conditions and band-limited to B_{DTV} in post-measurement processing.

Table B-3. Measured RF *P/A* (dB) of UWB Signals Band-Limited to Different Bandwidths[‡]

Type	Index	36.0 MHz	B_{DTV}	10.0 MHz	1.0 MHz	0.1 MHz
DP	01	25.4	23.5	20.6	11.5	6.8
	02	15.7	13.8	11.0	6.1	9.4
	03	7.8	5.4	6.0	9.0	10.1
	04	7.7	8.1	9.0	9.4	9.4
DS	01	9.3	9.5	9.5	9.5	9.5
	02	8.8	9.0	9.5	9.8	9.6
	03	7.8	8.1	8.8	9.9	9.7
	04	6.8	6.6	8.0	9.6	9.6
	05	6.8	6.6	8.0	9.8	9.8
	06	6.6	6.8	8.3	9.5	9.8
MB	01	9.6	8.3	6.9	7.5	9.2
	02	13.5	12.8	11.1	5.6	8.6
	03	13.8	12.8	11.3	7.4	8.7
	04	16.9	16.2	14.7	6.4	8.1
	05	17.1	16.4	14.8	10.8	8.2
	06	17.2	16.3	15.0	14.8	10.0
	07	19.4	18.7	17.3	8.6	7.4
	08	19.4	18.9	17.3	13.3	7.6
	09	19.4	18.8	17.4	17.7	14.9

[‡] Shaded cells highlight Rayleigh-amplitude statistics.

Table B-4. Measured IF *P/A* (dB) of UWB Signals at INR_{TOV} and Band-Limited to B_{DTV} [§]

Type	Index	*SNR* = 9 dB	*SNR* = 12 dB	*SNR* = 15 dB
DP	01	23.4	?	?
	02	13.2	14.0	14.1
	03	8.9	7.9	7.2
	04	9.3	8.9	8.7
DS	01	9.6	9.4	9.4
	02	9.5	9.0	9.1
	03	9.1	8.8	8.6
	04	9.1	8.1	7.8
	05	8.9	8.4	7.7
	06	9.4	8.9	8.4
MB	01	9.6	9.3	9.0
	02	11.7	12.7	12.8
	03	11.9	12.4	12.5
	04	13.6	15.1	15.6
	05	12.8	14.5	15.2
	06	12.4	14.0	15.2
	07	15.0	16.6	17.8
	08	14.0	16.0	17.2
	09	12.7	14.6	16.2

[§] Shaded cells highlight Rayleigh-amplitude statistics. Question marks indicate uncertainty in the measurement due to exceedingly high signal voltages overdriving the VSA.

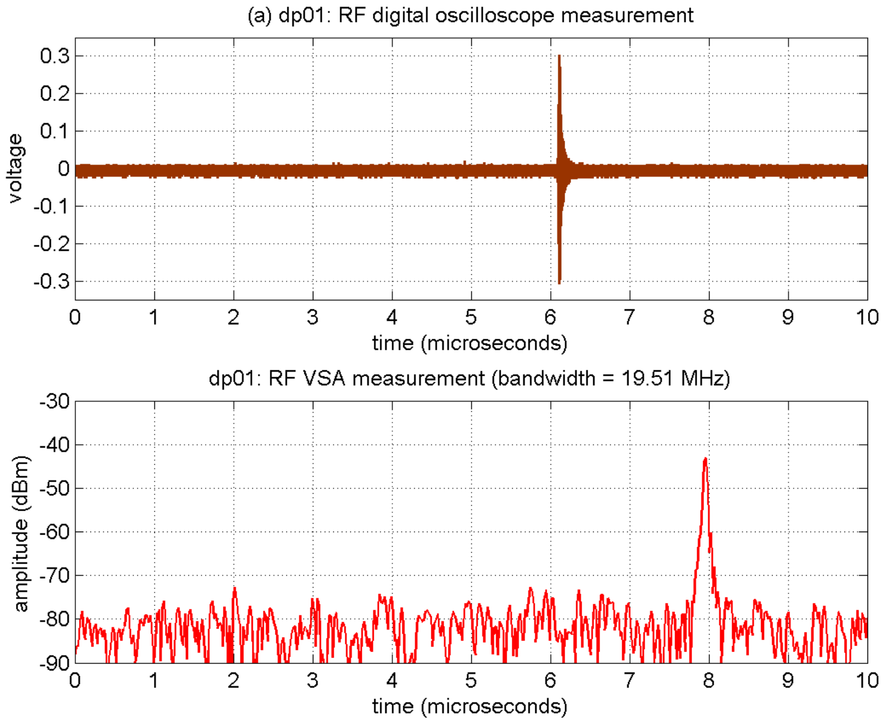

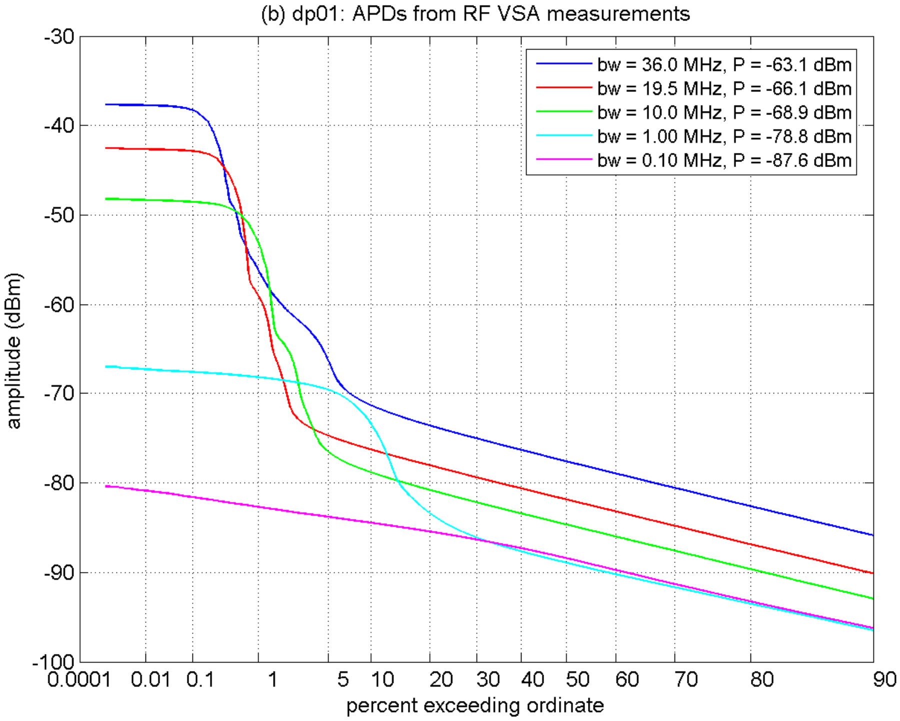

Figure B-25. RF amplitude analyses of DP-01 (T_{pulse} = 10,000 ns, w = 0.094 ns, f_D = 0.5).

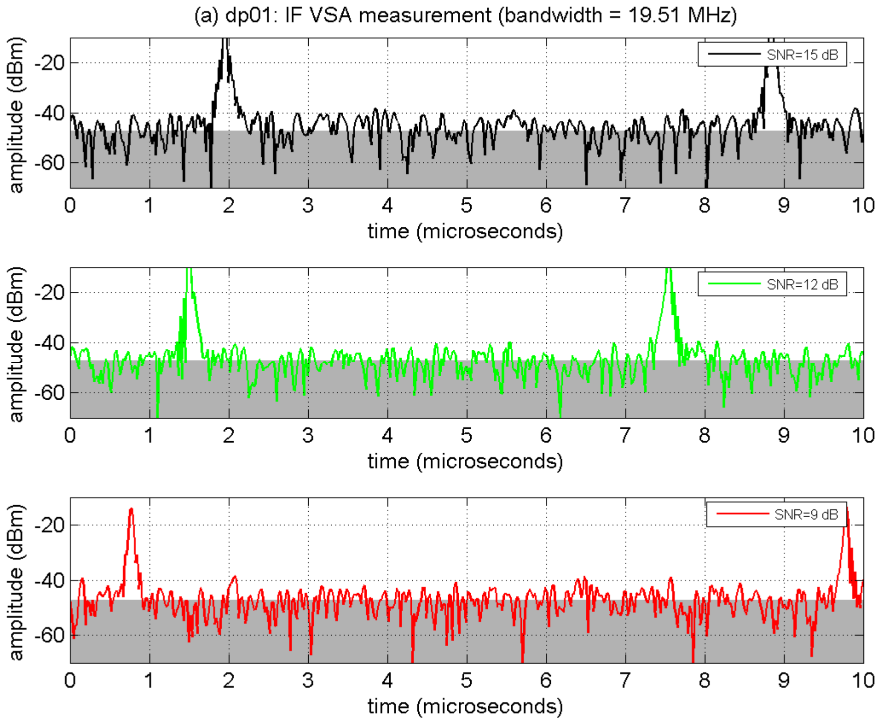

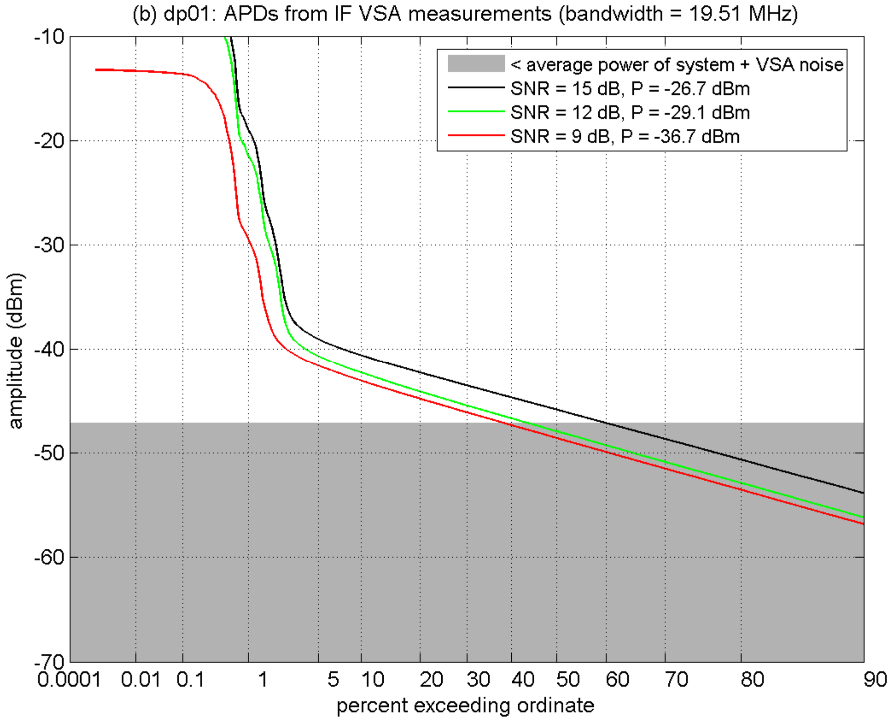

Figure B-26. IF amplitude analyses of DP-01 at INR_{TOV}.

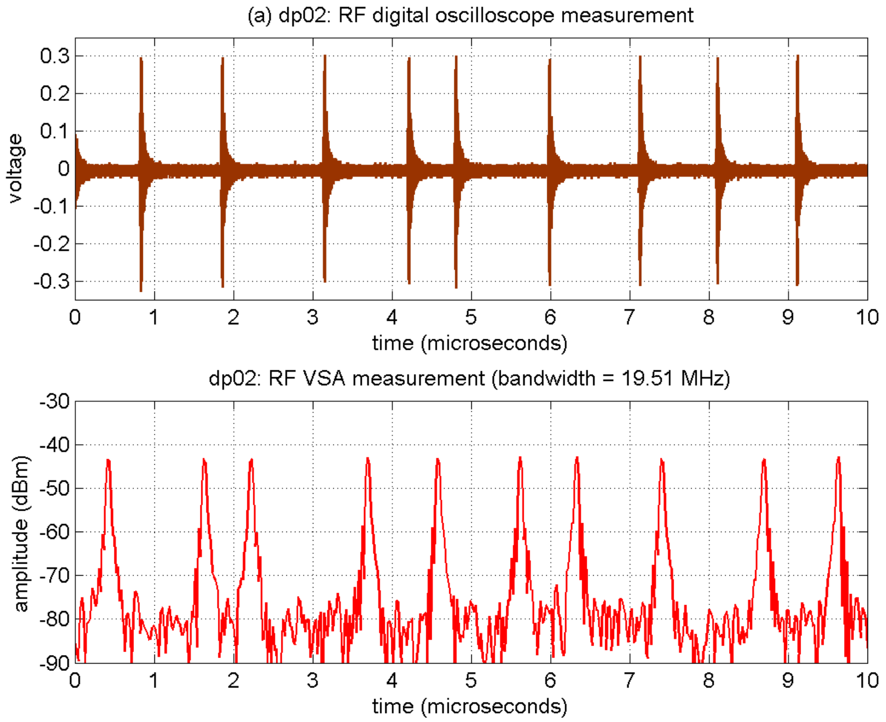

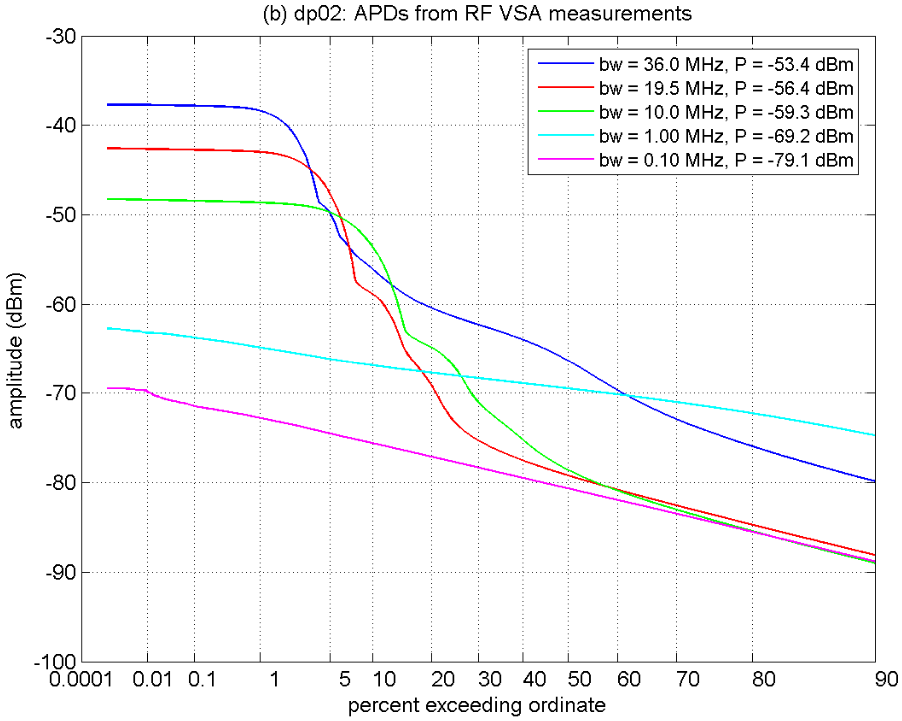

Figure B-27. RF amplitude analyses of DP-02 (T_{pulse} = 1000 ns, w = 0.094 ns, f_D = 0.5).

(a) dp02: IF VSA measurement (bandwidth = 19.51 MHz)

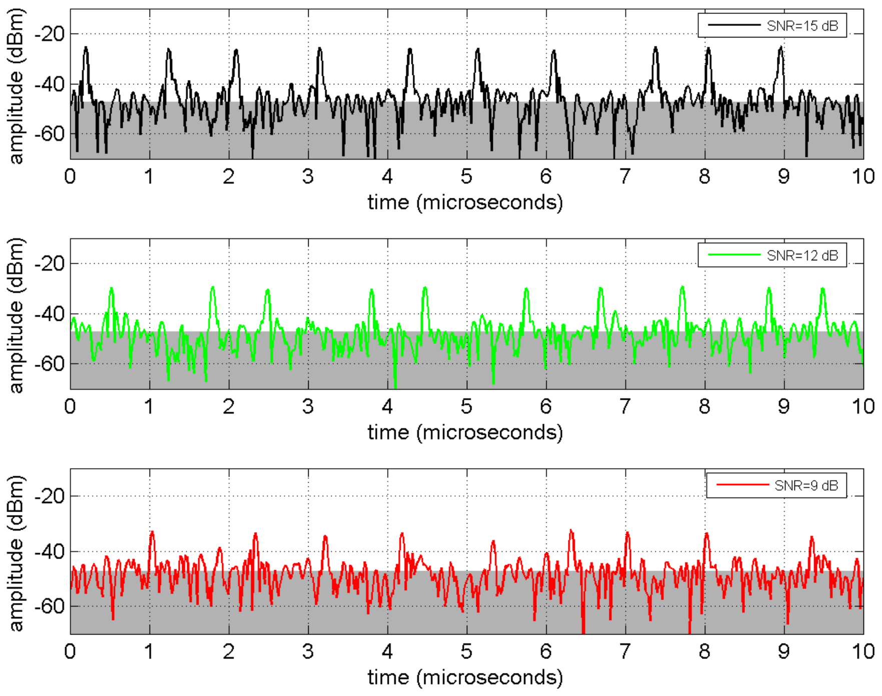

(b) dp02: APDs from IF VSA measurements (bandwidth = 19.51 MHz)

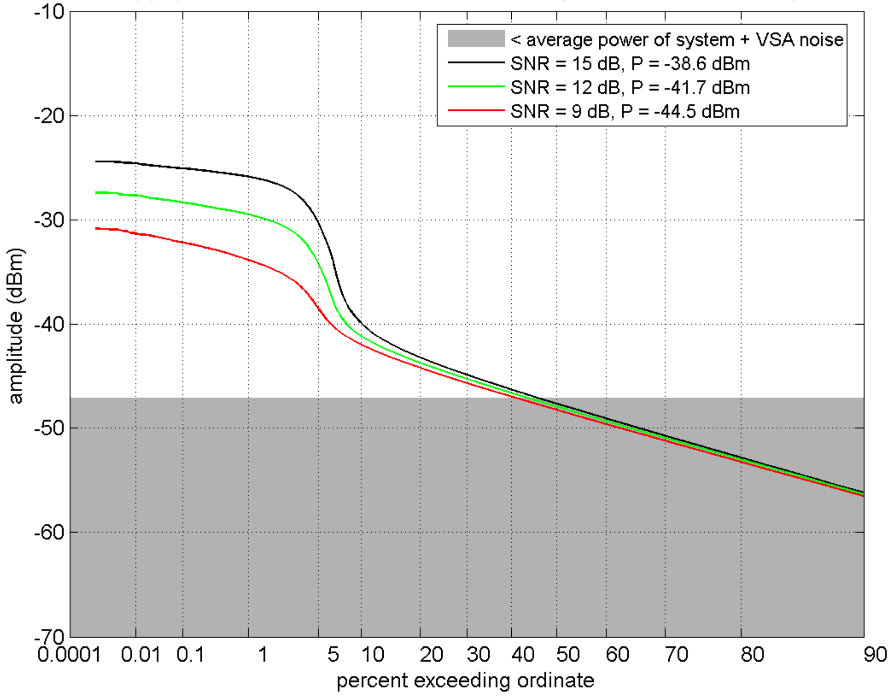

Figure B-28. IF amplitude analyses of DP-02 at INR_{TOV}.

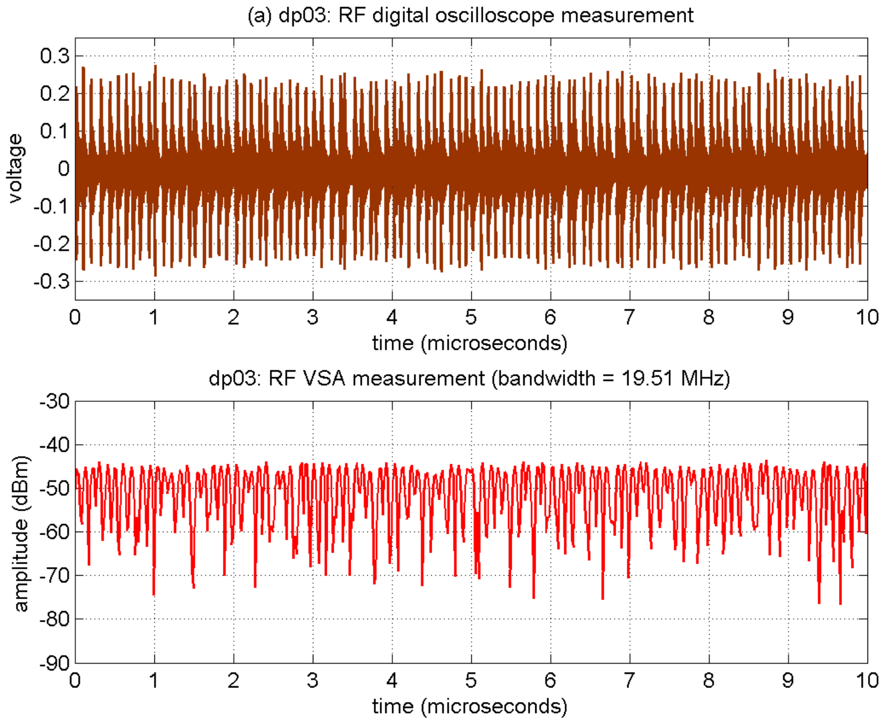

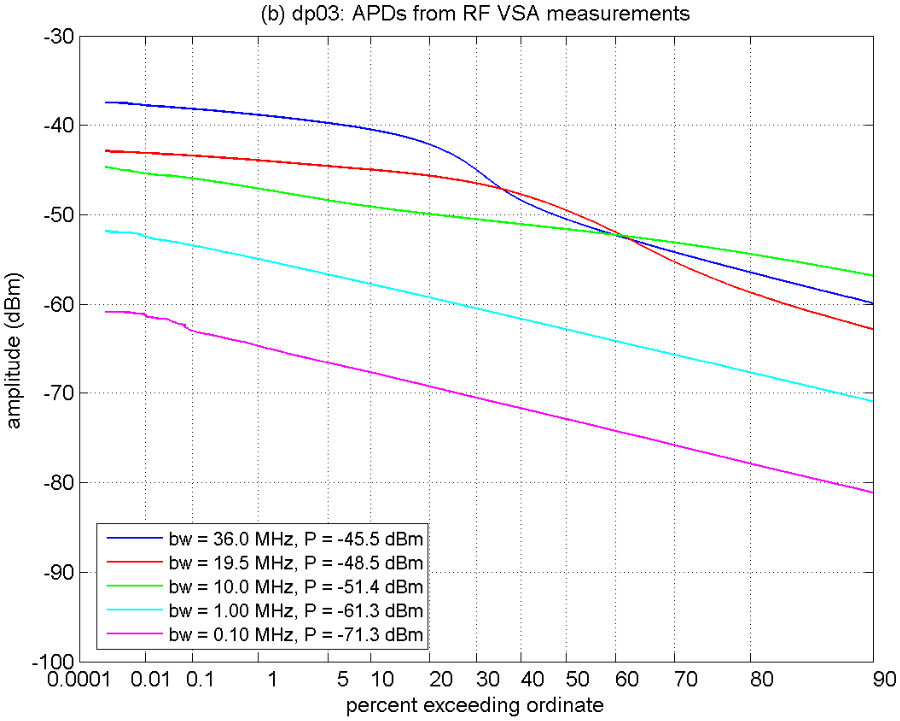

Figure B-29. RF amplitude analyses of DP-03 (T_{pulse} = 100 ns, w = 0.094 ns, f_D = 0.5).

(a) dp03: IF VSA measurement (bandwidth = 19.51 MHz)

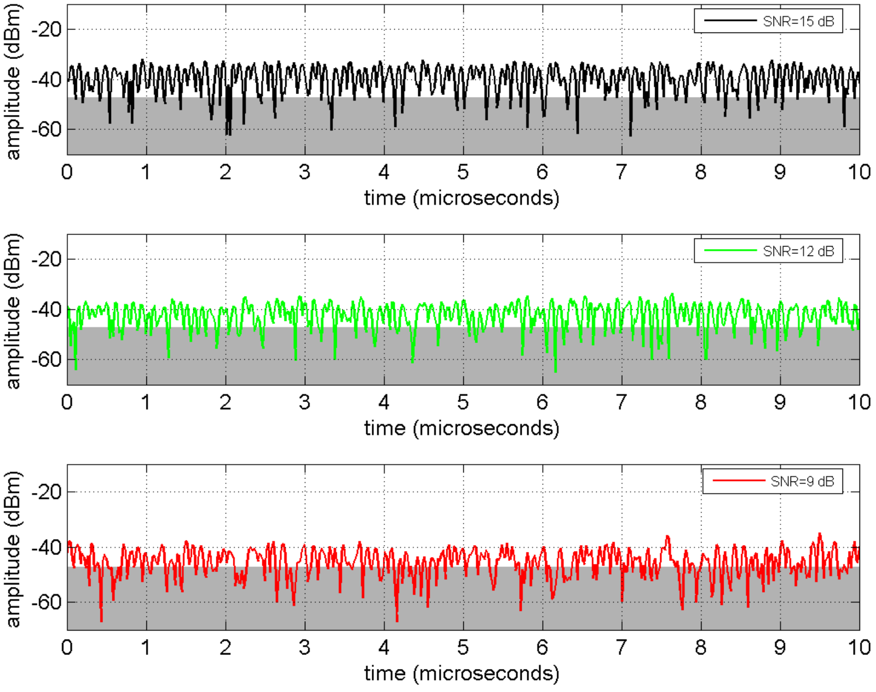

(b) dp03: APDs from IF VSA measurements (bandwidth = 19.51 MHz)

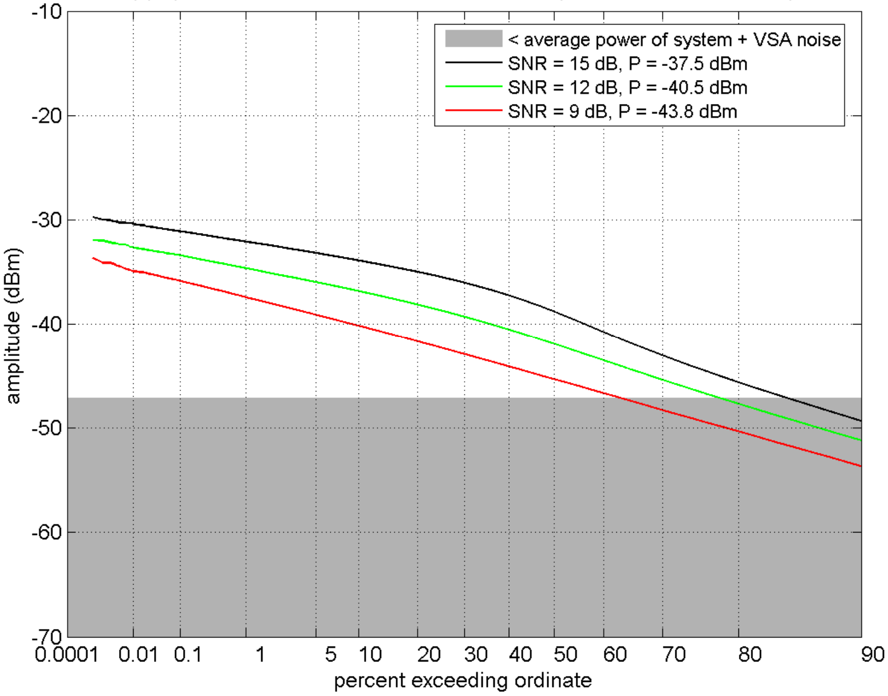

Figure B-30. IF amplitude analyses of DP-03 at INR_{TOV}.

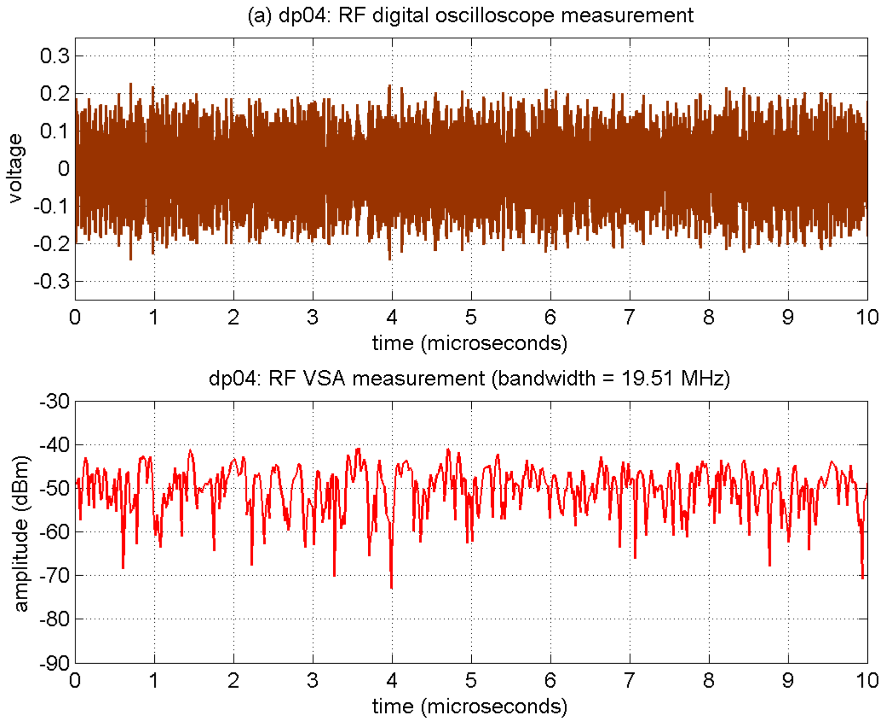

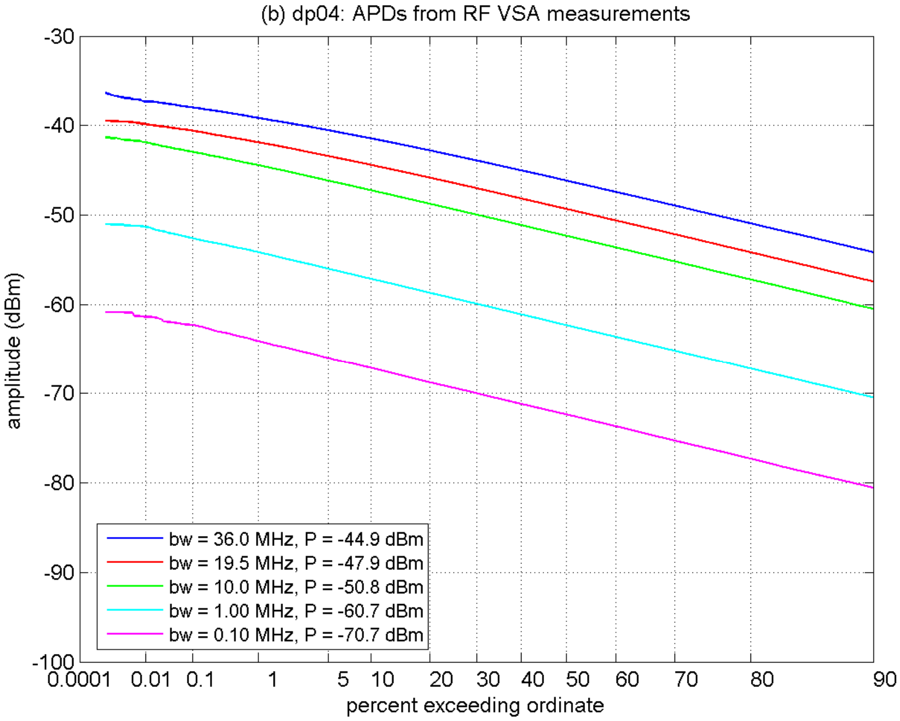

Figure B-31. RF amplitude analyses of DP-04 (T_{pulse} = 10 ns, w = 0.094 ns, f_D = 0.5).

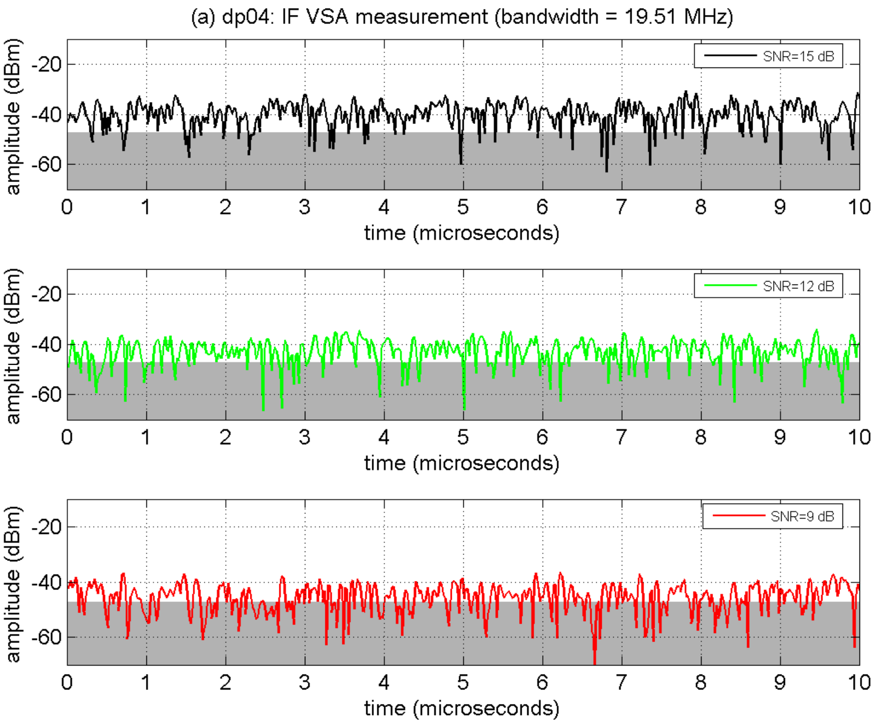

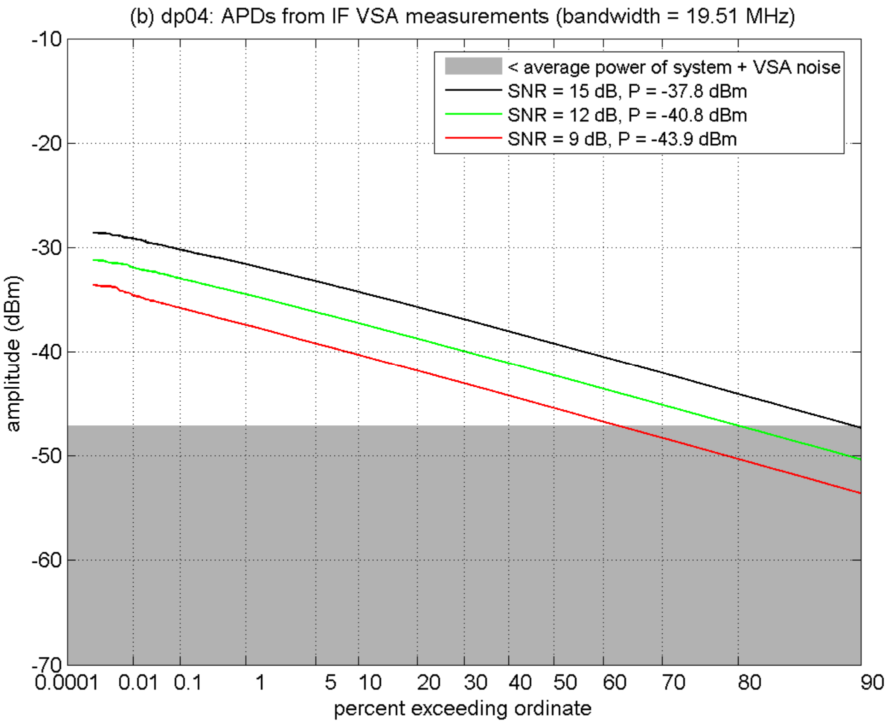

Figure B-32. IF amplitude analyses of DP-04 at INR_{TOV}.

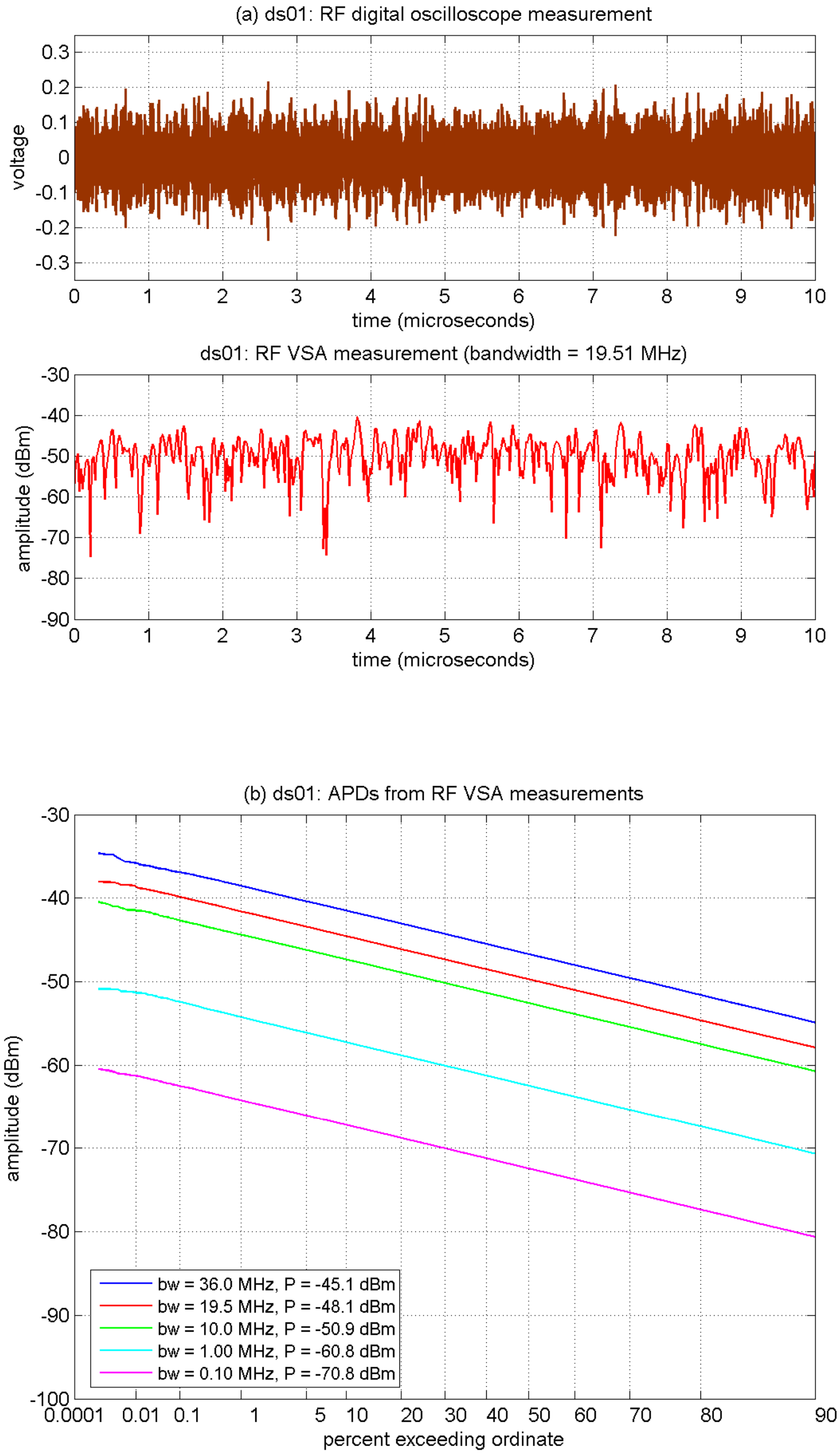

Figure B-33. RF amplitude analyses of DS-01 (L = 1).

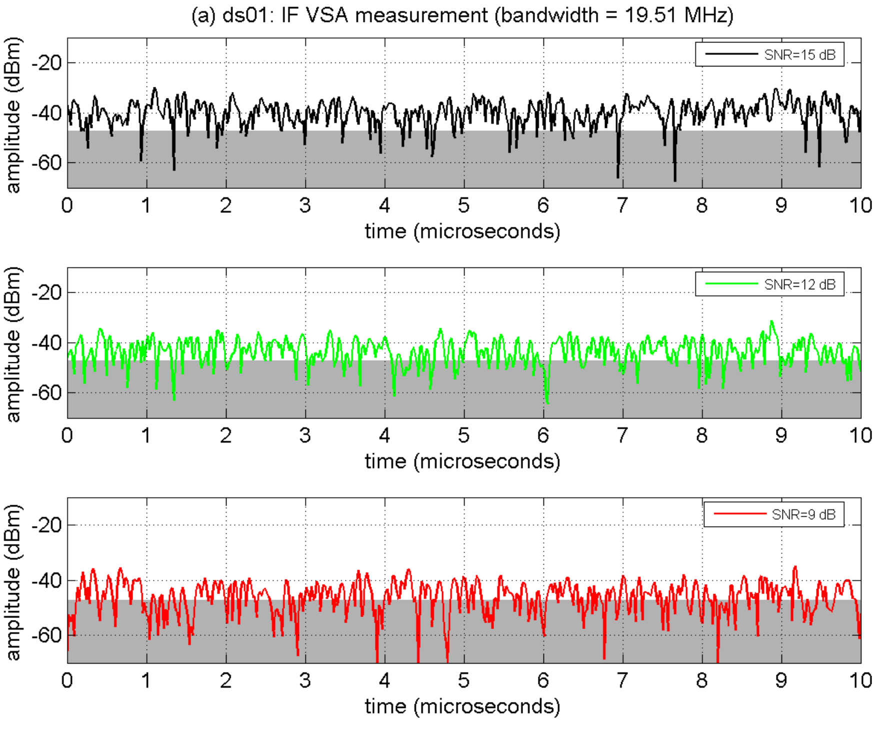
(a) ds01: IF VSA measurement (bandwidth = 19.51 MHz)

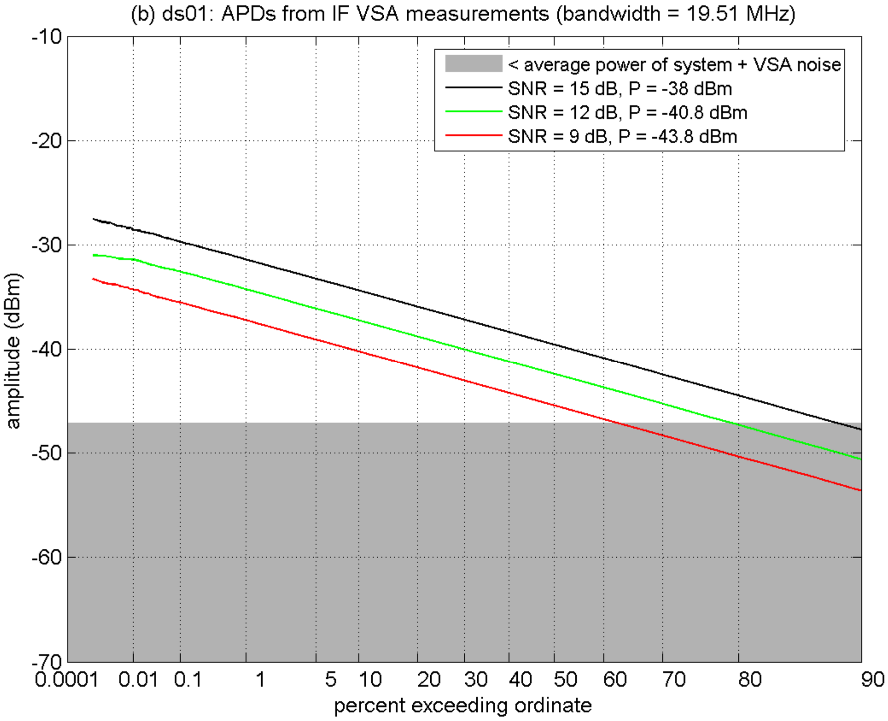
(b) ds01: APDs from IF VSA measurements (bandwidth = 19.51 MHz)

Figure B-34. IF amplitude analyses of DS-01 at INR_{TOV}.

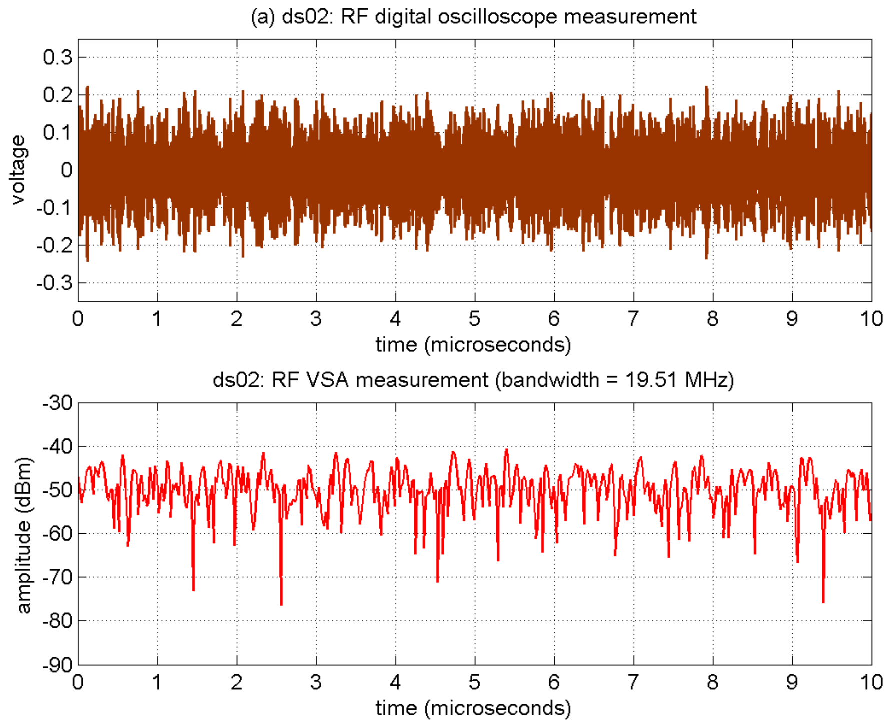

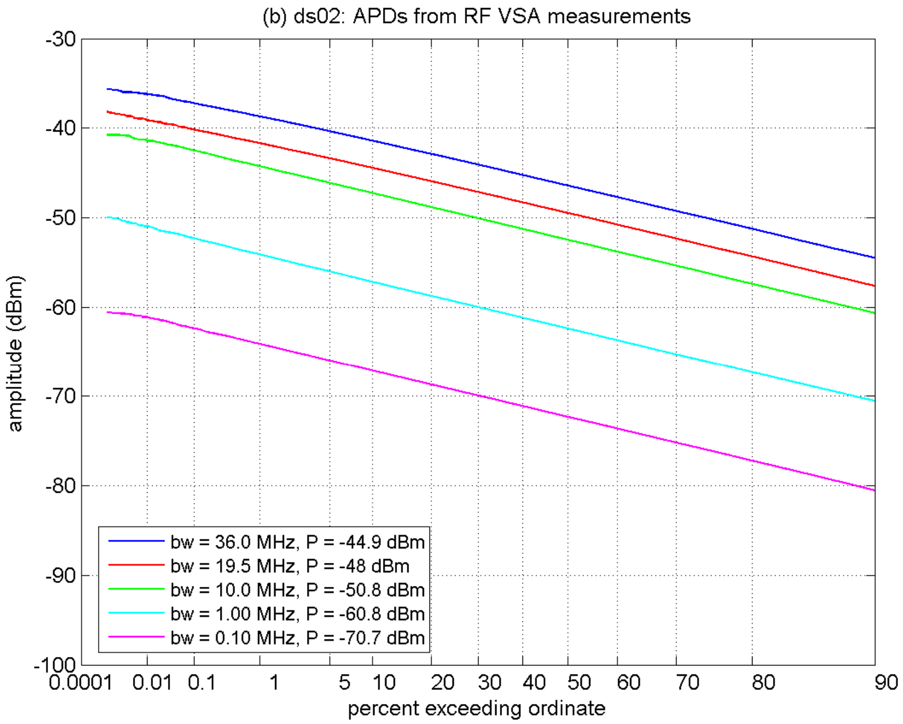

Figure B-35. RF amplitude analyses of DS-02 (*L* = 3, sparse code).

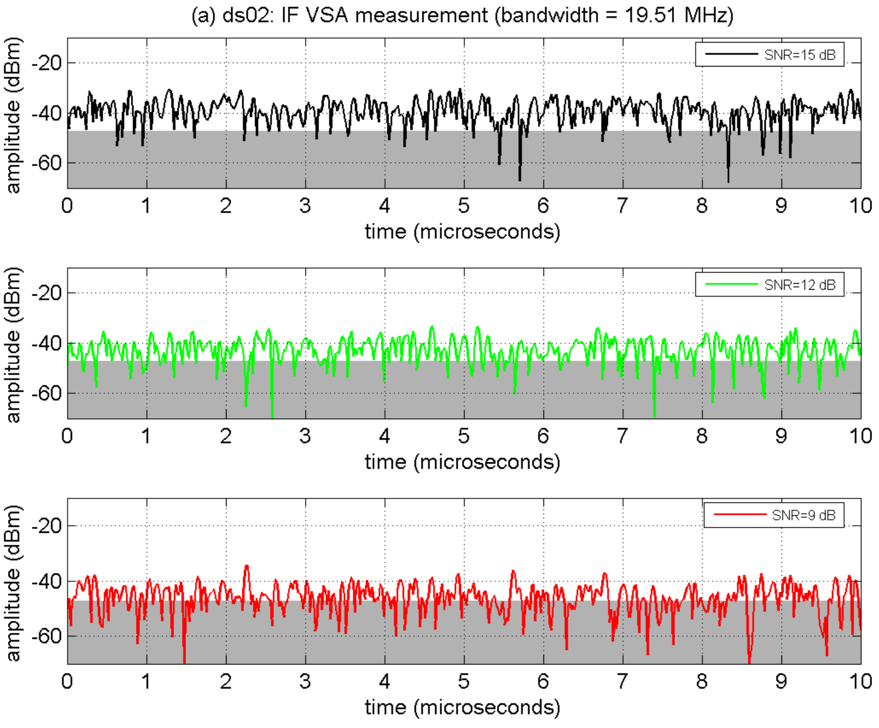

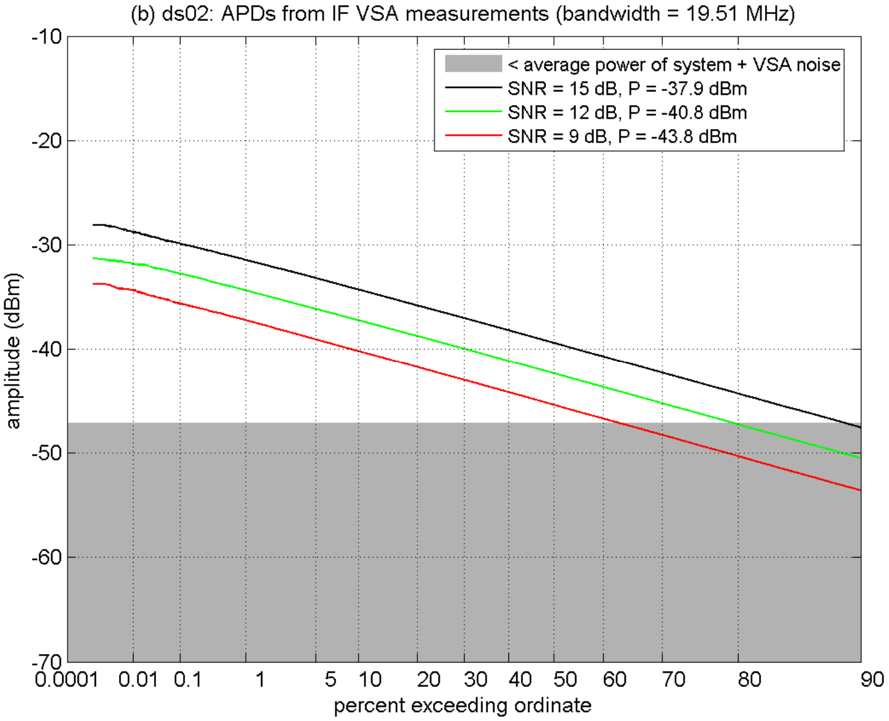

Figure B-36. IF amplitude analyses of DS-02 at INR_{TOV}.

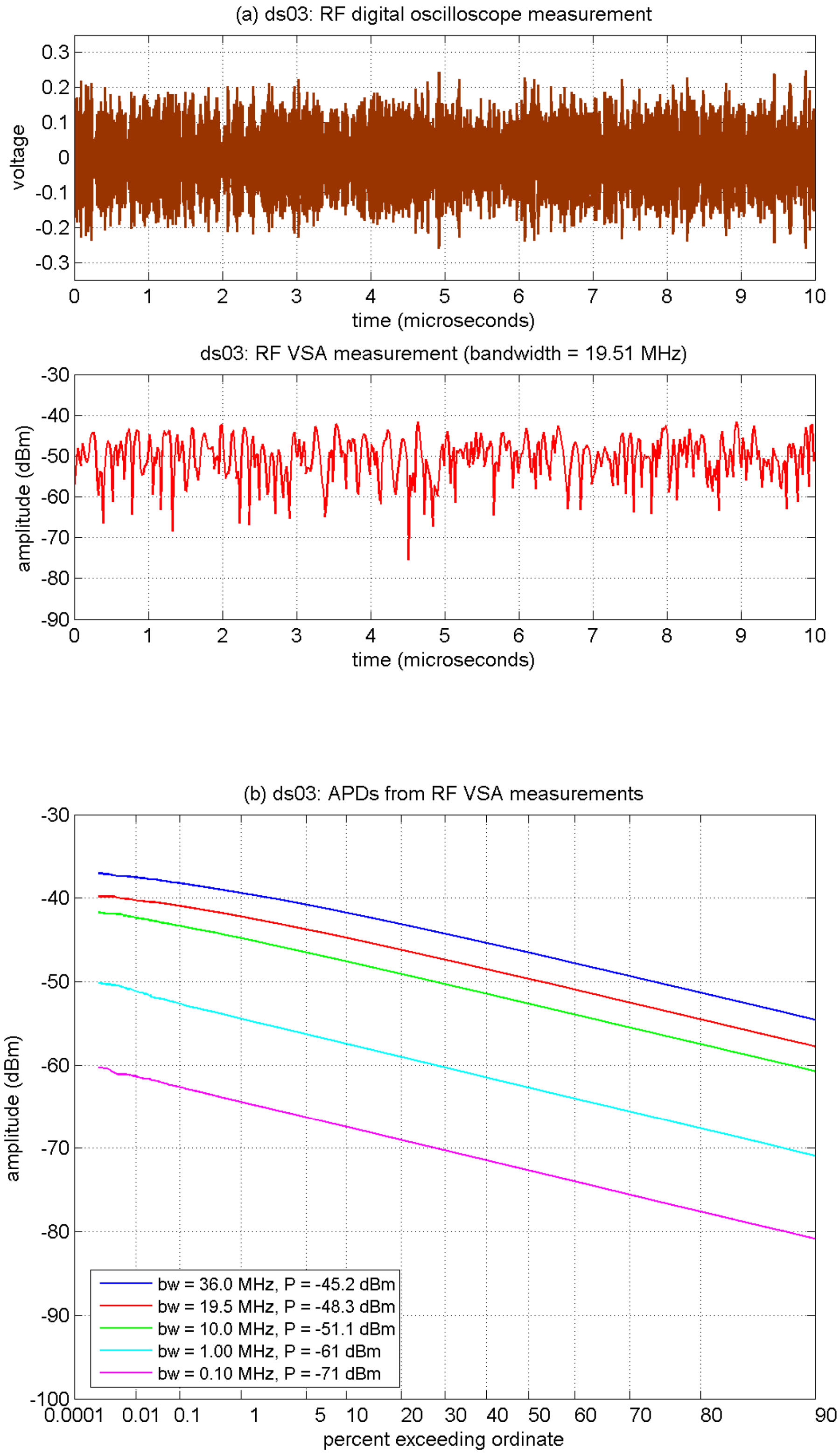

Figure B-37. RF amplitude analyses of DS-03 ($L = 6$, sparse code).

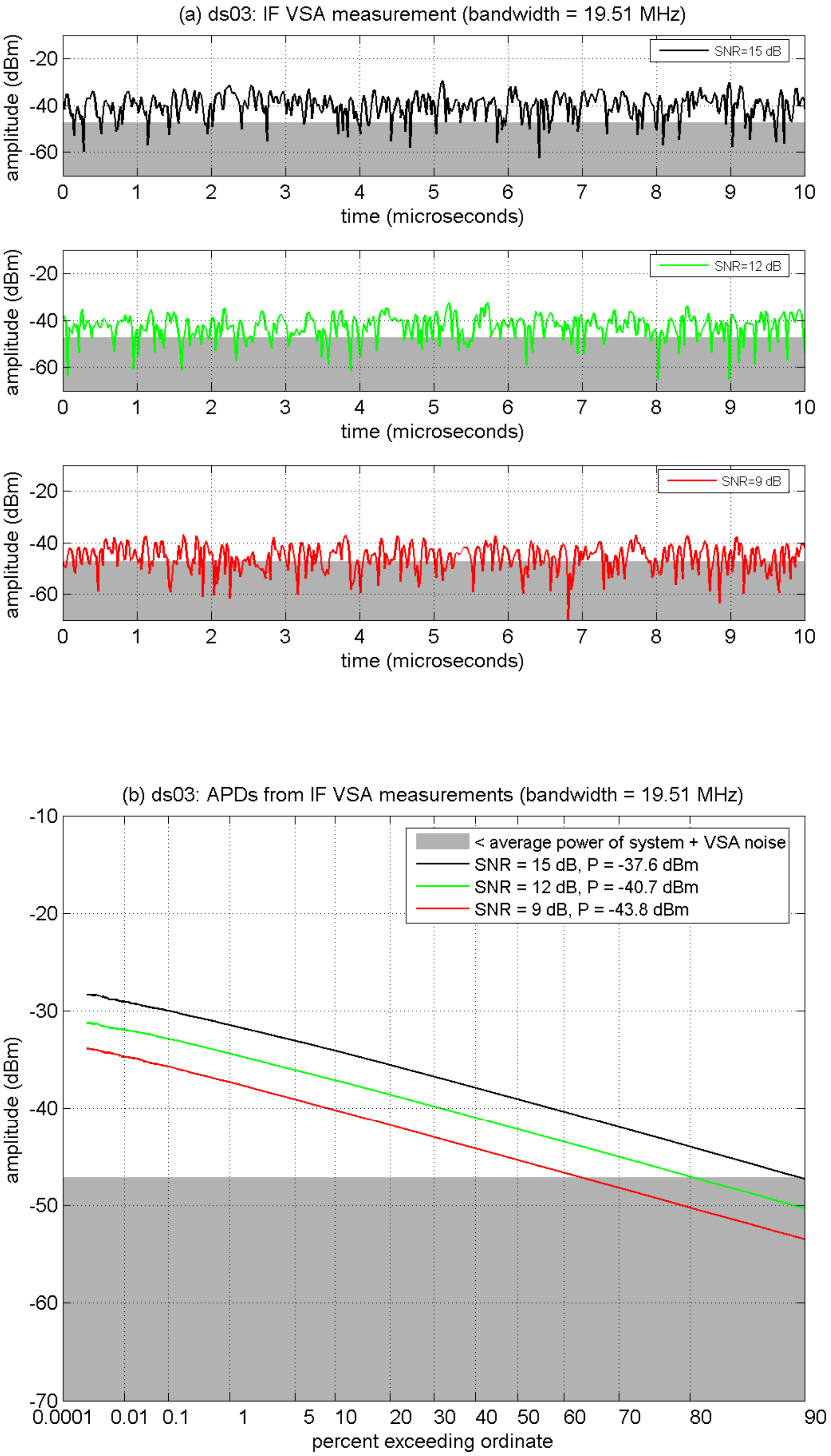

Figure B-38. IF amplitude analyses of DS-03 at INR_{TOV}.

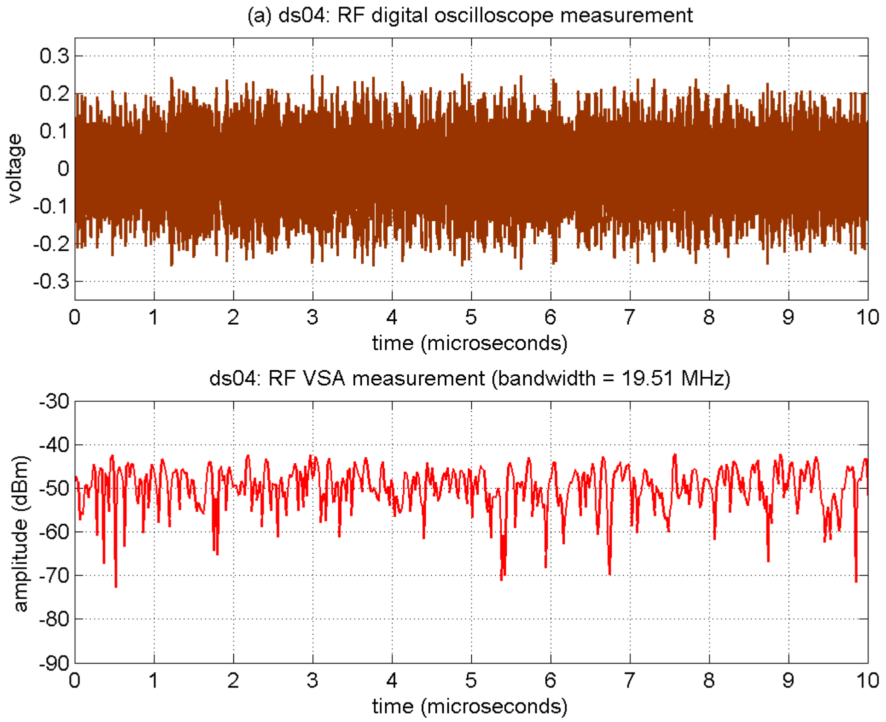

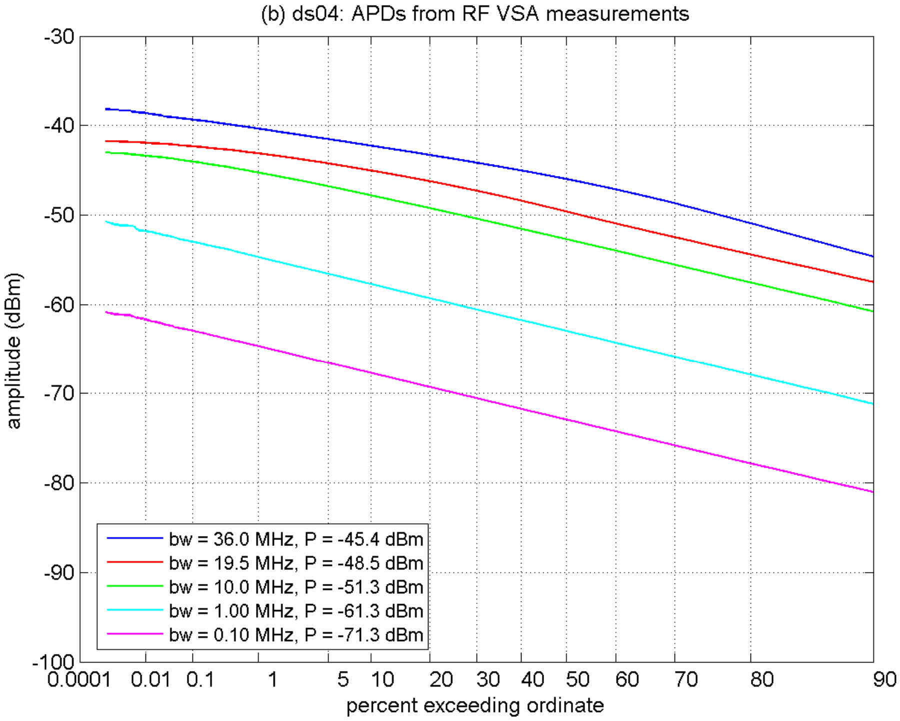

Figure B-39. RF amplitude analyses of DS-04 (*L* = 12, DS code).

(a) ds04: IF VSA measurement (bandwidth = 19.51 MHz)

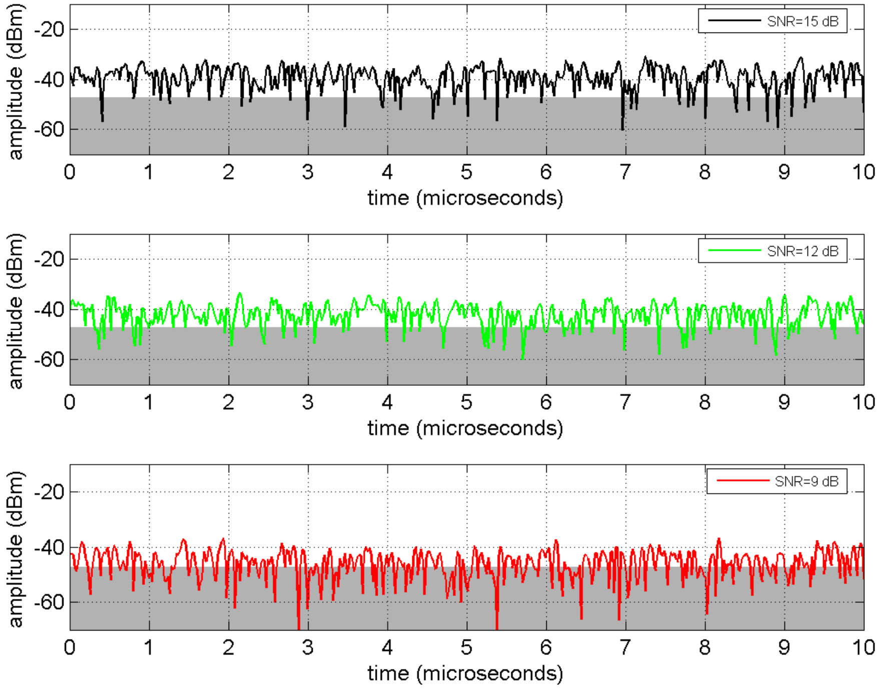

(b) ds04: APDs from IF VSA measurements (bandwidth = 19.51 MHz)

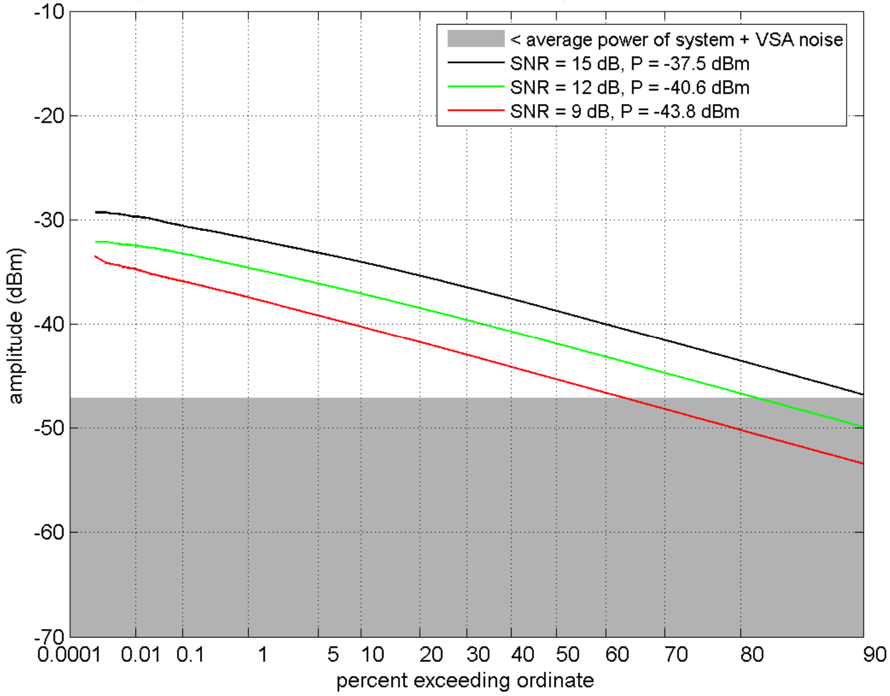

Figure B-40. IF amplitude analyses of DS-04 at INR_{TOV}.

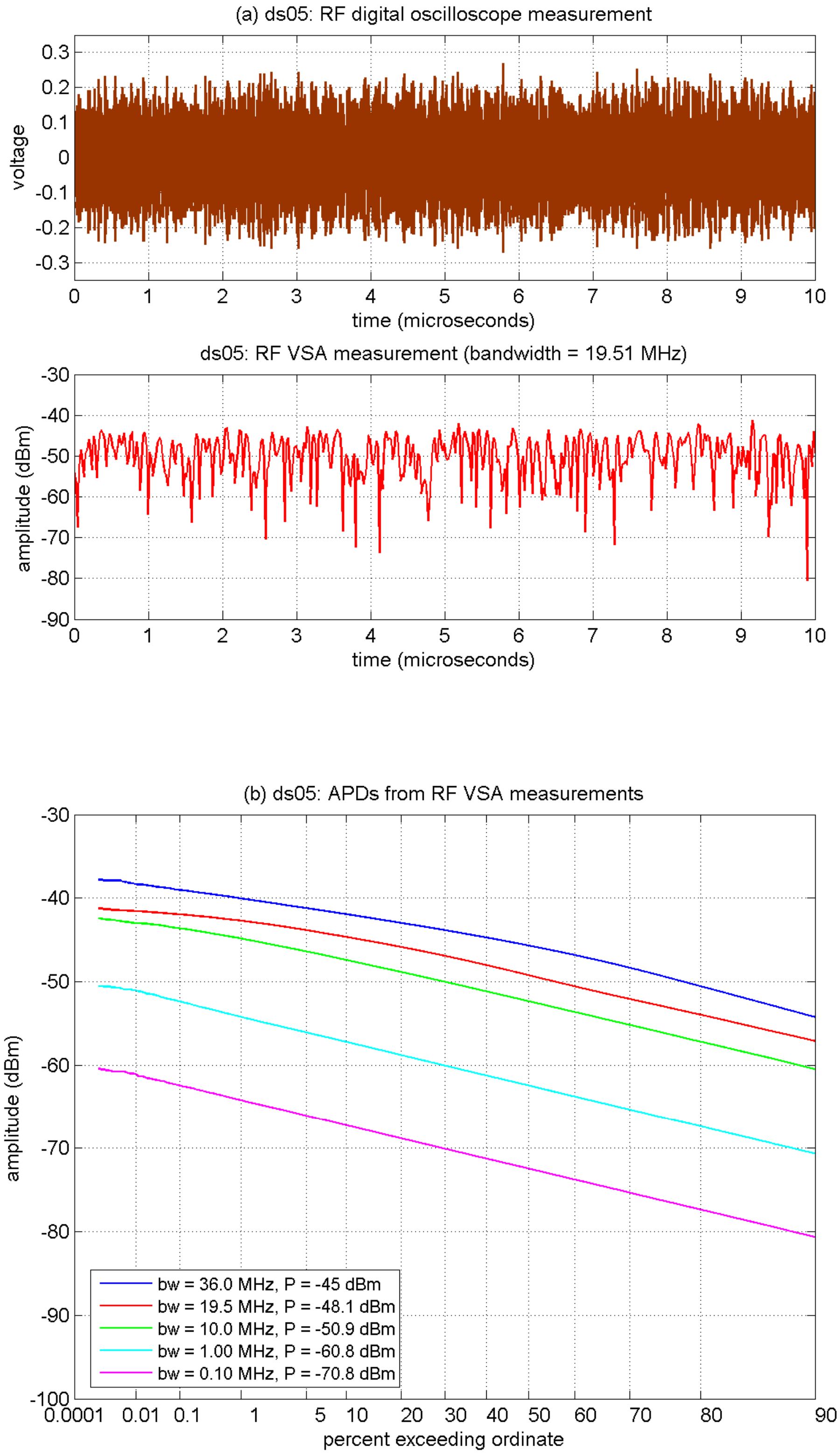

Figure B-41. RF amplitude analyses of DS-05 (*L* = 12, sparse code).

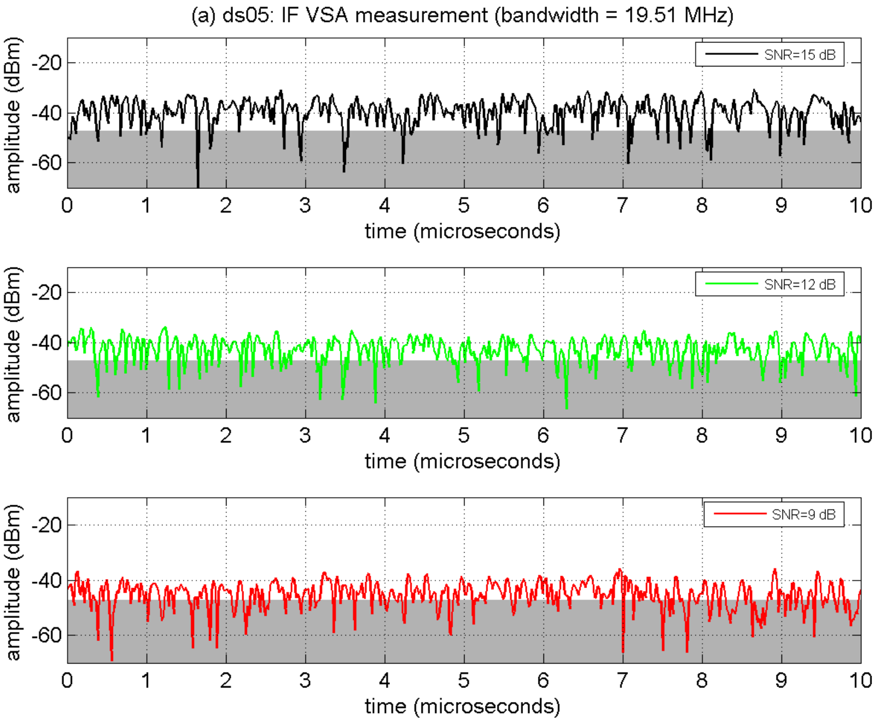

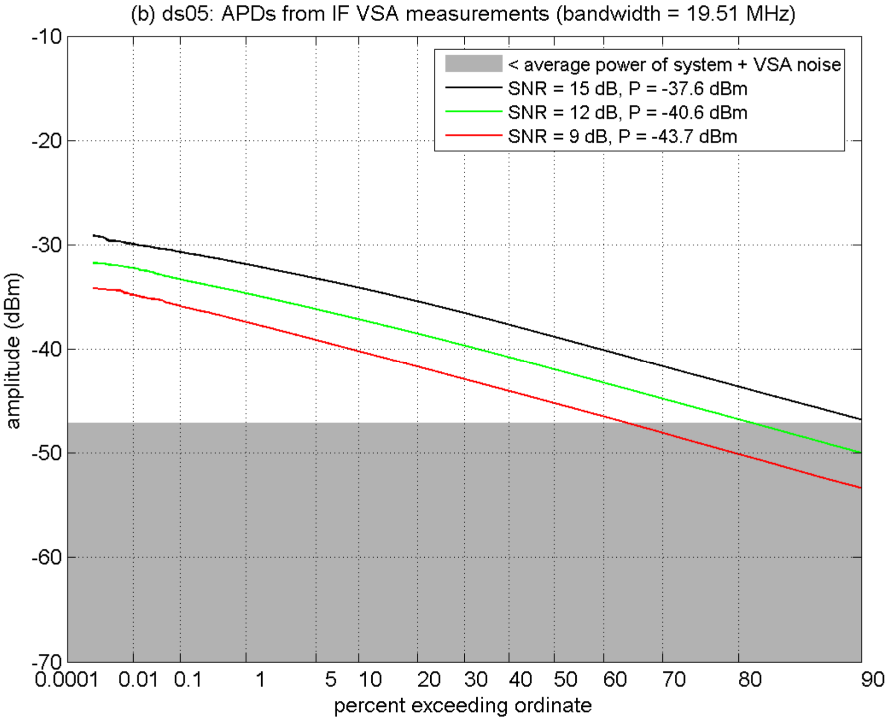

Figure B-42. IF amplitude analyses of DS-05 at INR_{TOV}.

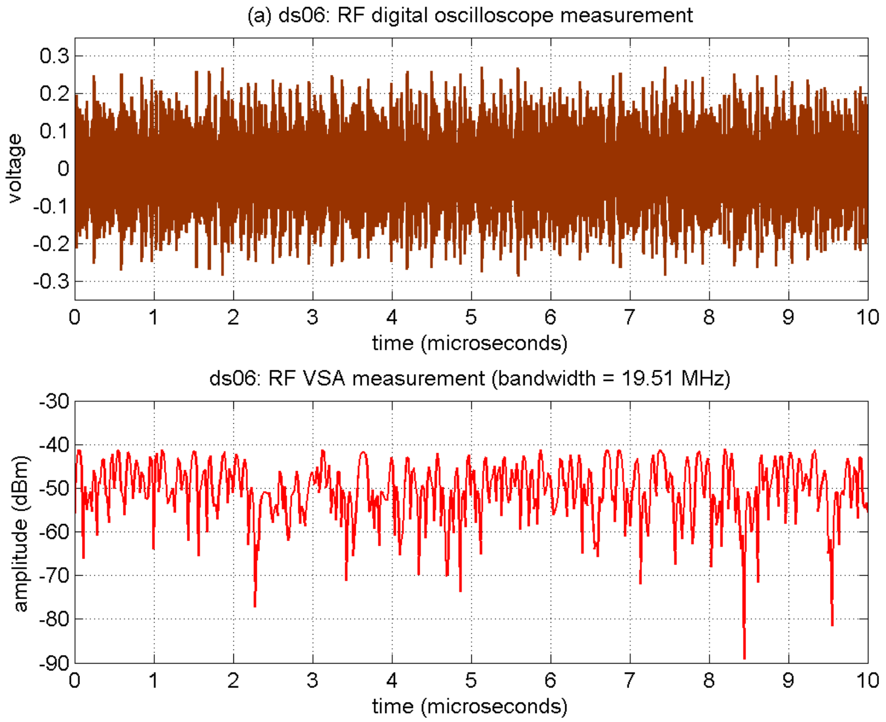
(a) ds06: RF digital oscilloscope measurement

ds06: RF VSA measurement (bandwidth = 19.51 MHz)

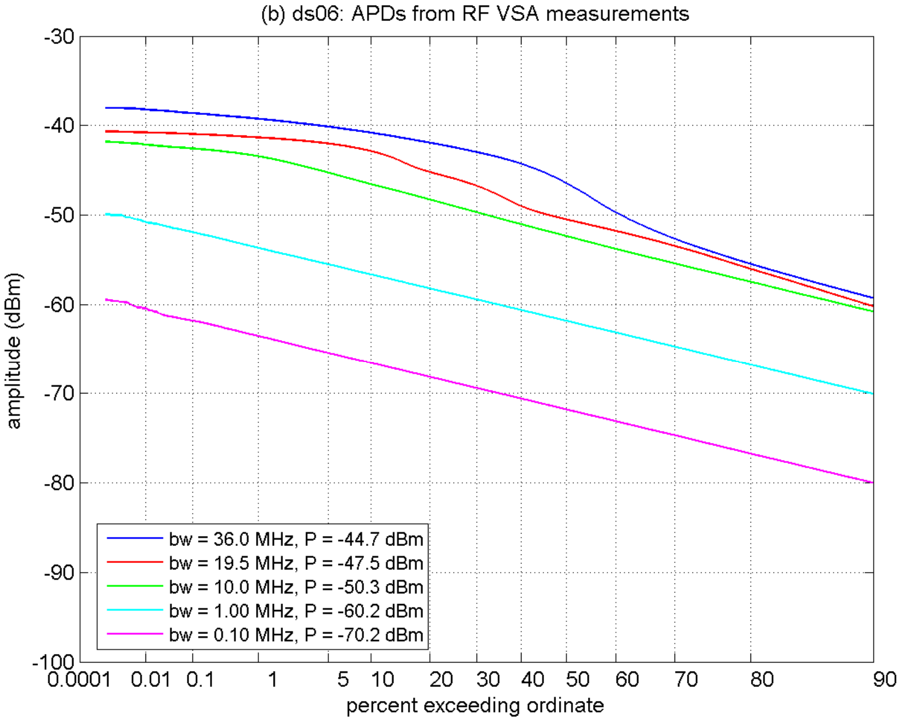
(b) ds06: APDs from RF VSA measurements

Figure B-43. RF amplitude analyses of DS-06 (L = 24, DS code).

(a) ds06: IF VSA measurement (bandwidth = 19.51 MHz)

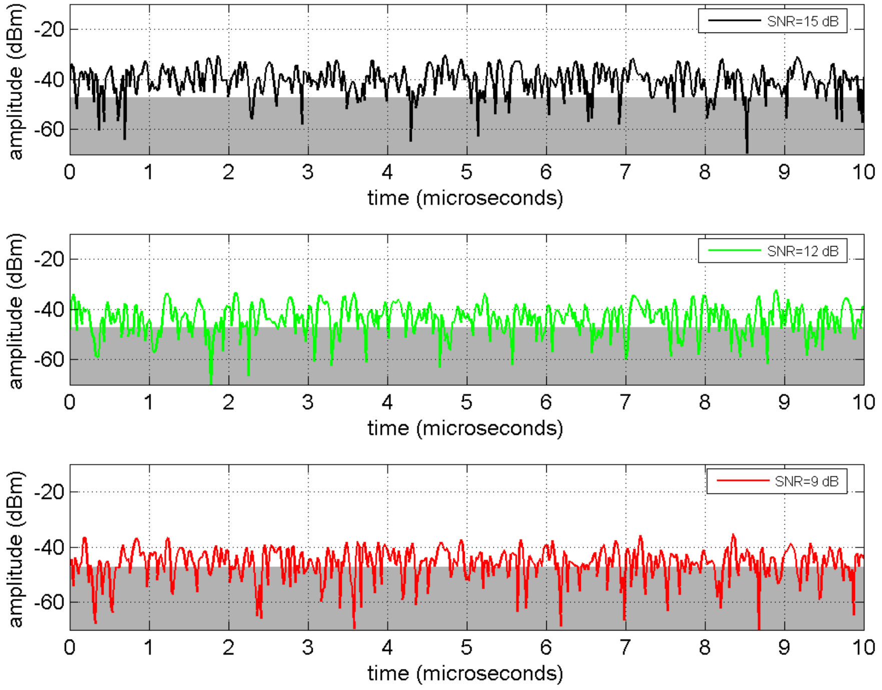

(b) ds06: APDs from IF VSA measurements (bandwidth = 19.51 MHz)

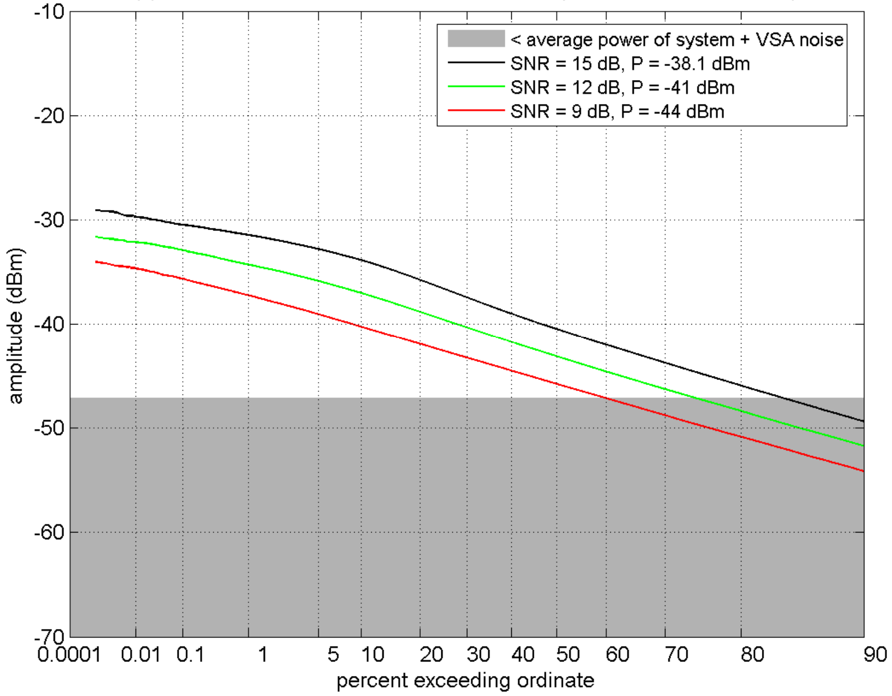

Figure B-44. IF amplitude analyses of DS-06 at *INR*$_{TOV}$.

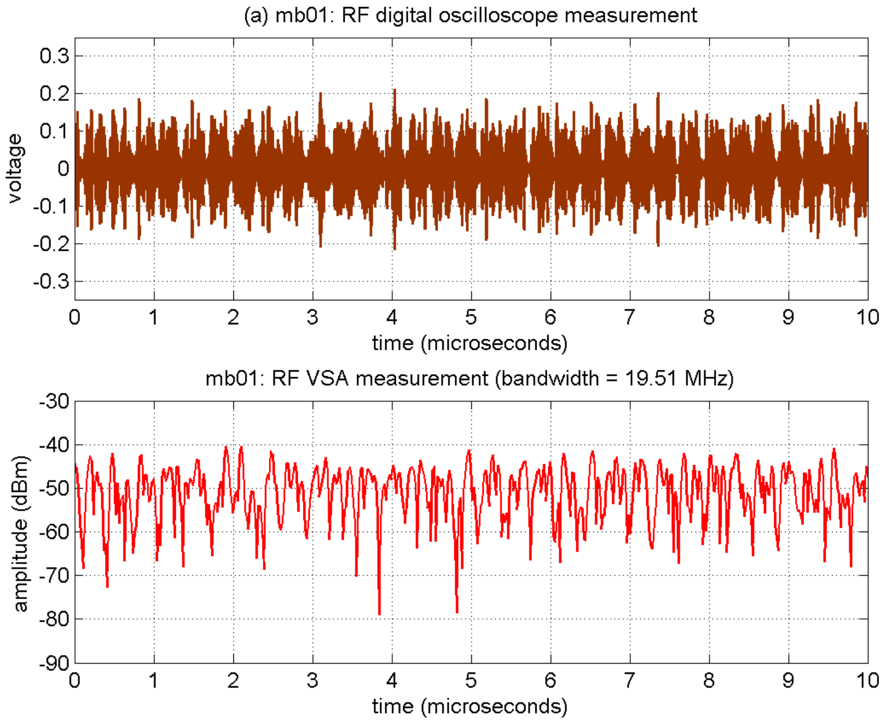

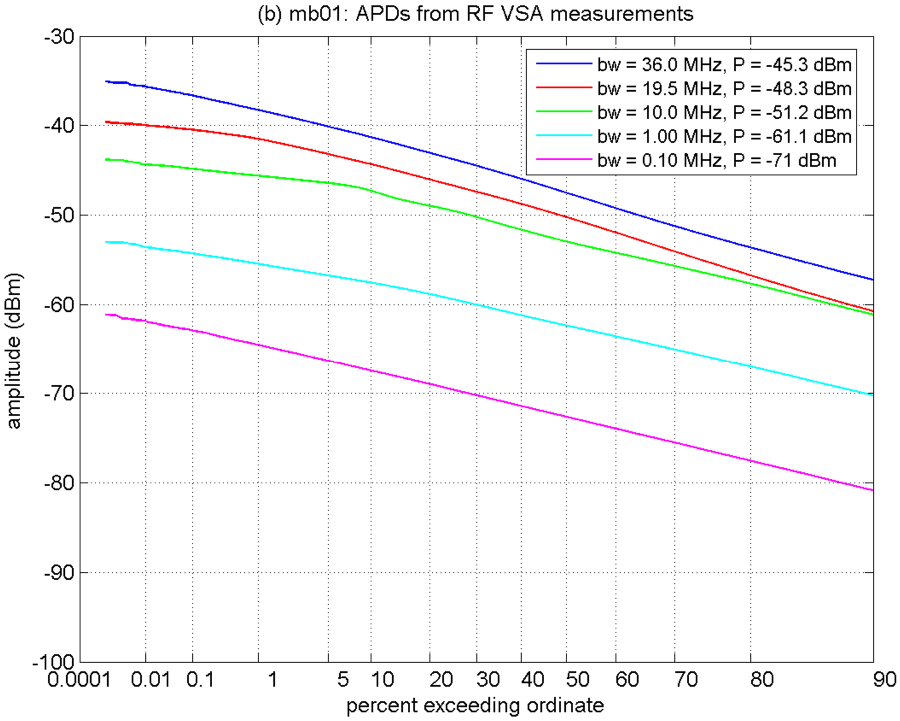

Figure B-45. RF amplitude analyses of MB-01 (*b* = 1).

(a) mb01: IF VSA measurement (bandwidth = 19.51 MHz)

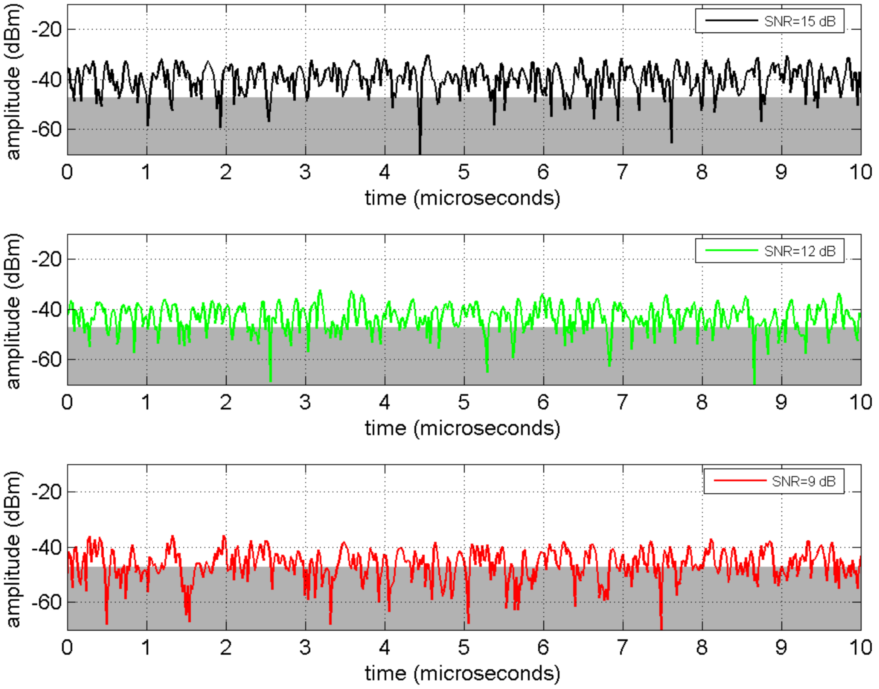

(b) mb01: APDs from IF VSA measurements (bandwidth = 19.51 MHz)

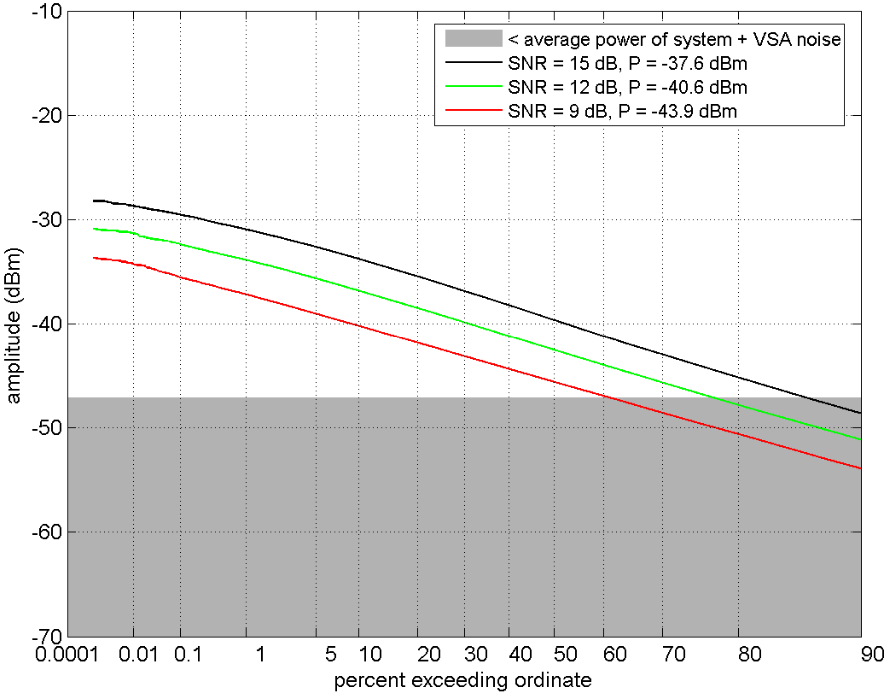

Figure B-46. IF amplitude analyses of MB-01 at INR_{TOV}.

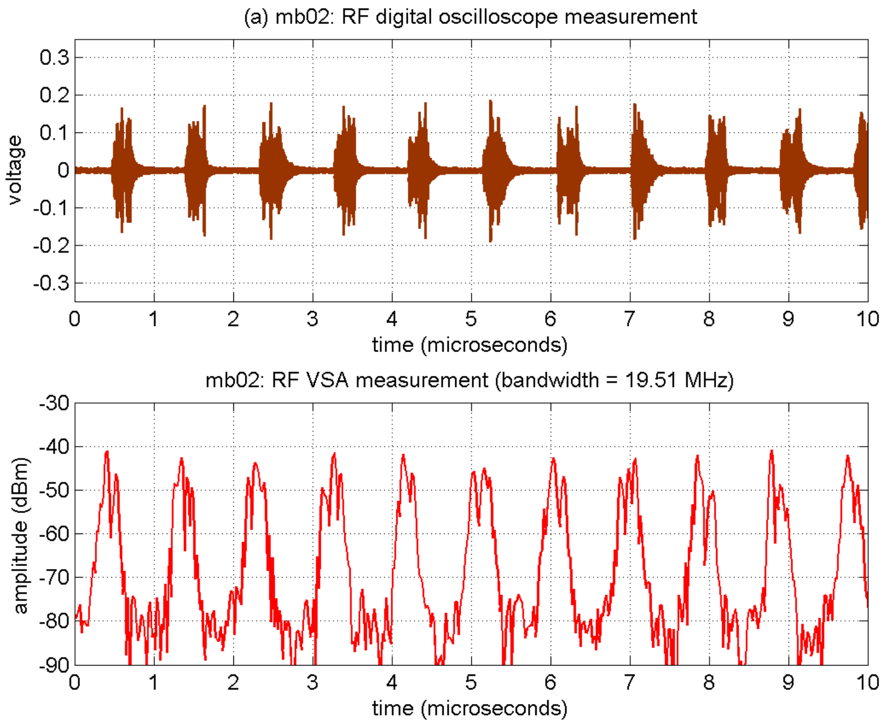

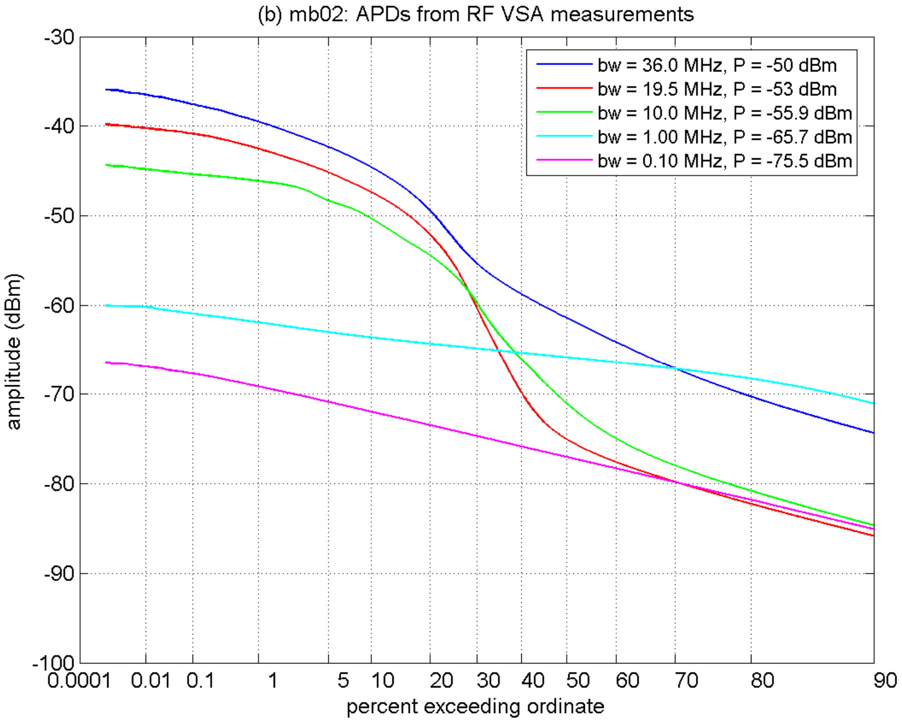

Figure B-47. RF amplitude analyses of MB-02 (*b* = 3, *d* = 1).

(a) mb02: IF VSA measurement (bandwidth = 19.51 MHz)

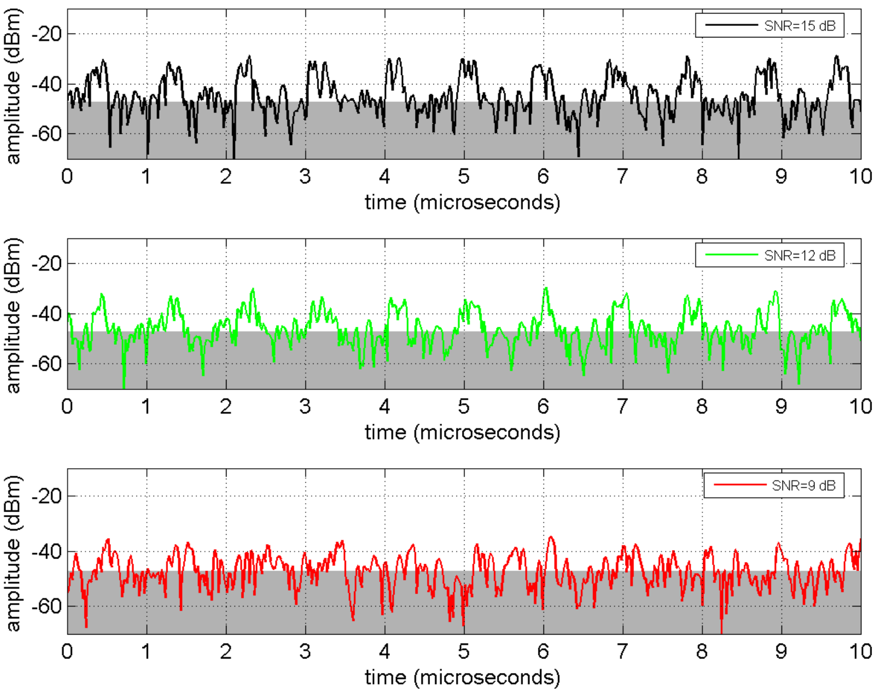

(b) mb02: APDs from IF VSA measurements (bandwidth = 19.51 MHz)

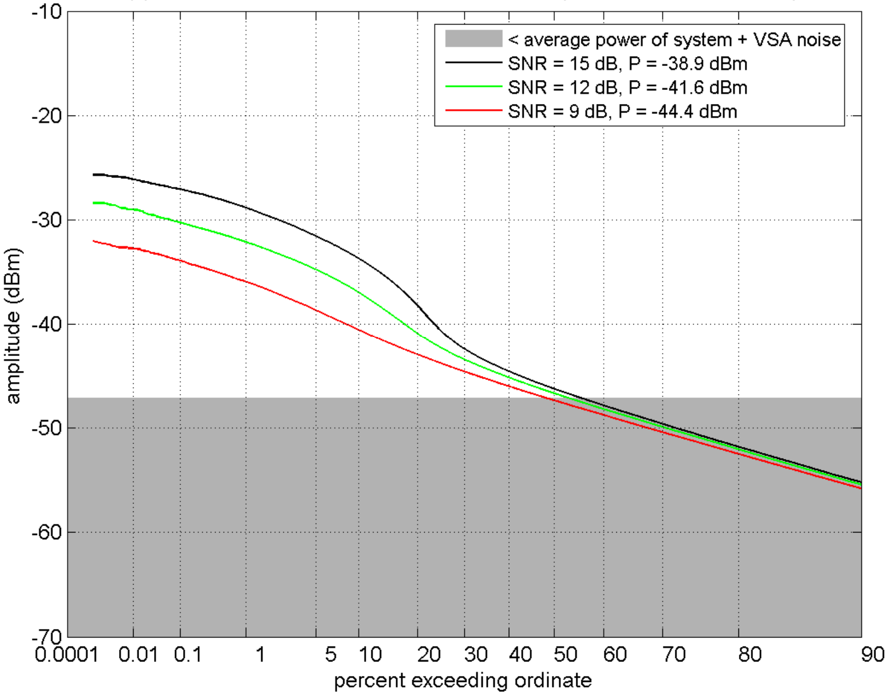

Figure B-48. IF amplitude analyses of MB-02 at INR_{TOV}.

(a) mb03: RF digital oscilloscope measurement

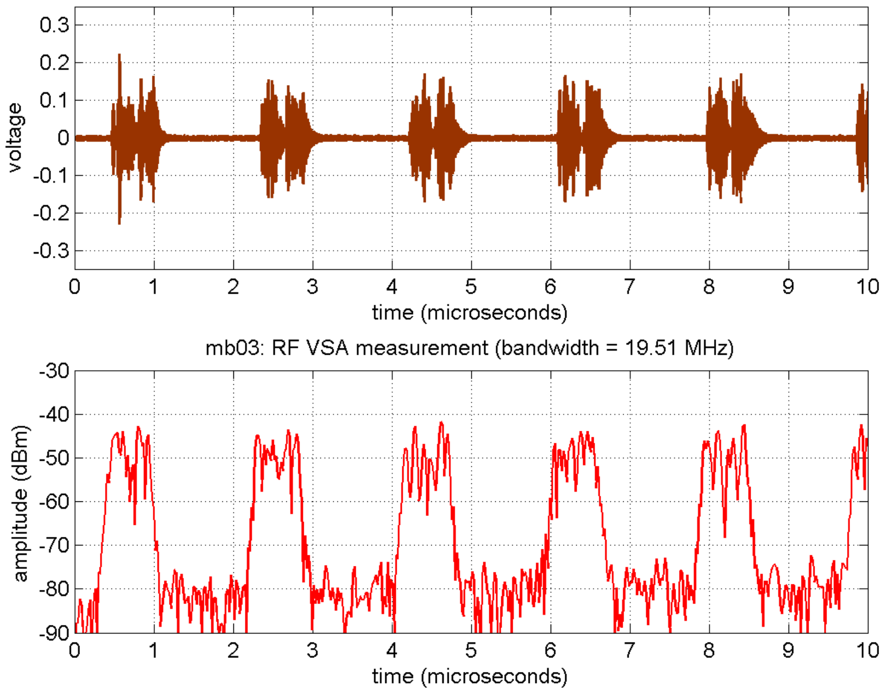

(b) mb03: APDs from RF VSA measurements

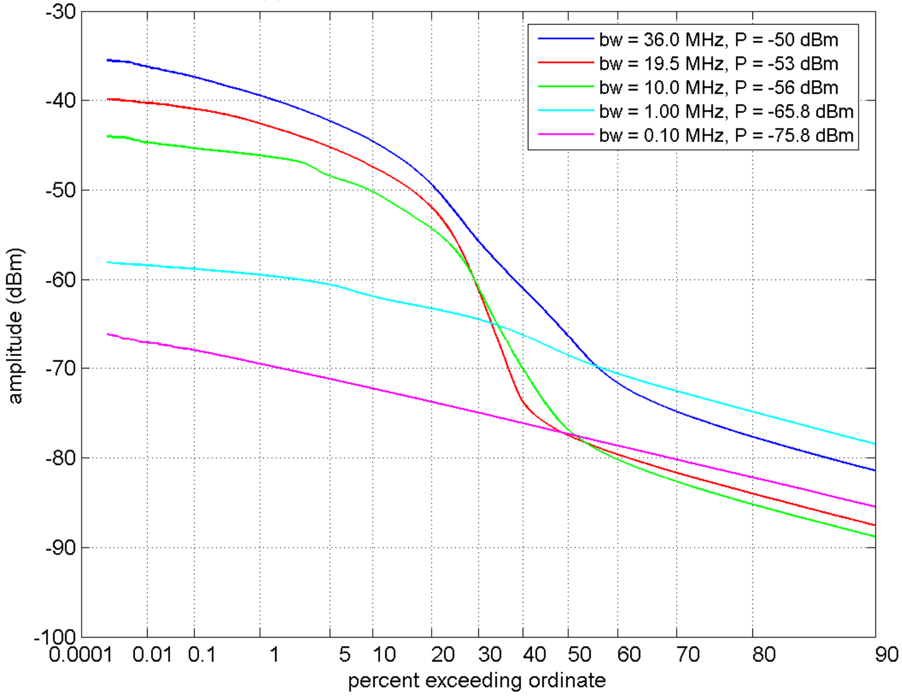

Figure B-49. RF amplitude analyses of MB-03 ($b = 3$, $d = 2$).

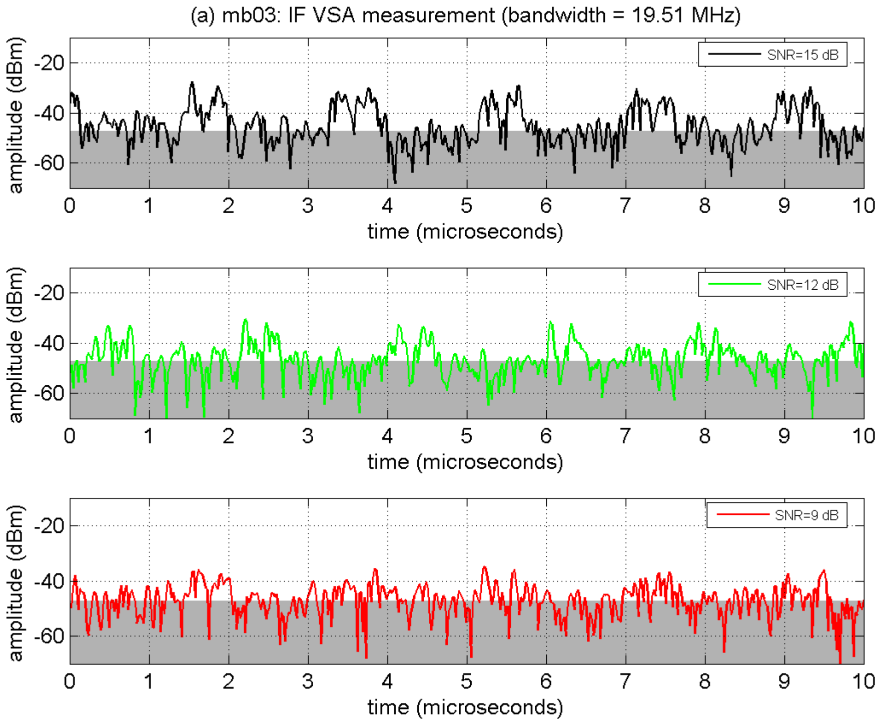

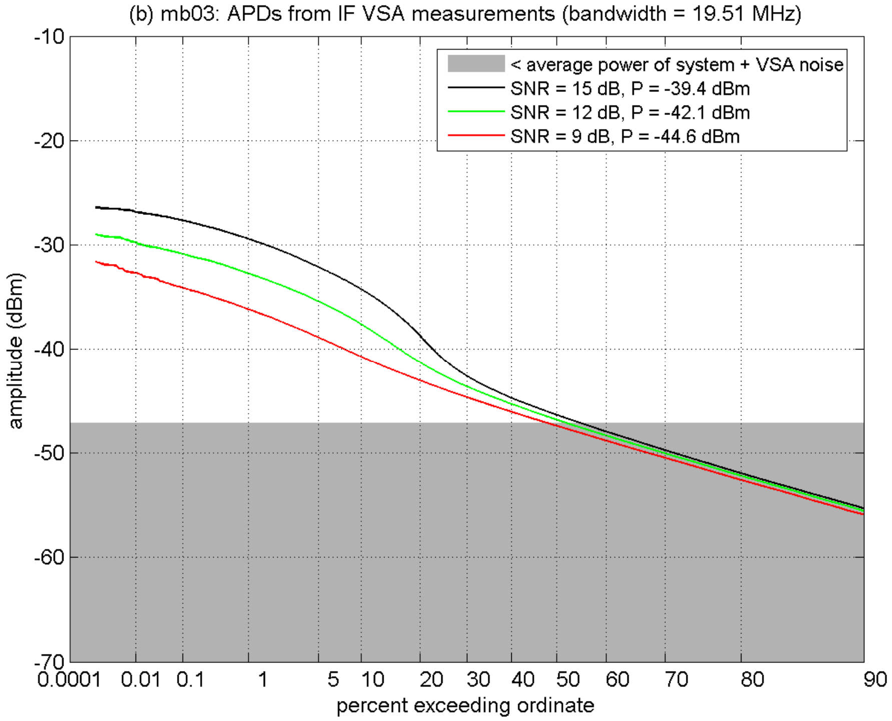

Figure B-50. IF amplitude analyses of MB-03 at INR_{TOV}.

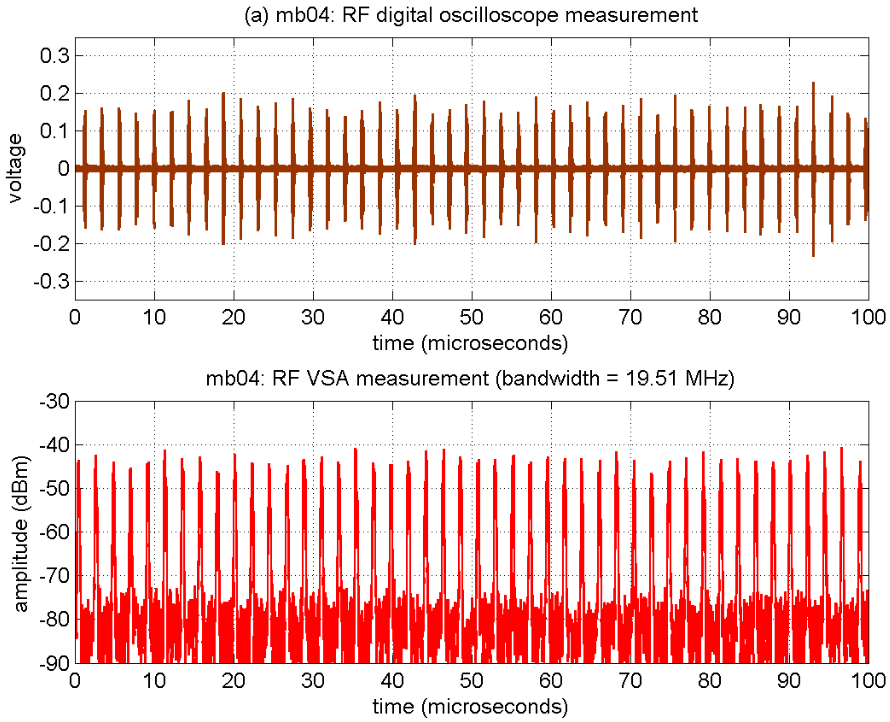
(a) mb04: RF digital oscilloscope measurement

mb04: RF VSA measurement (bandwidth = 19.51 MHz)

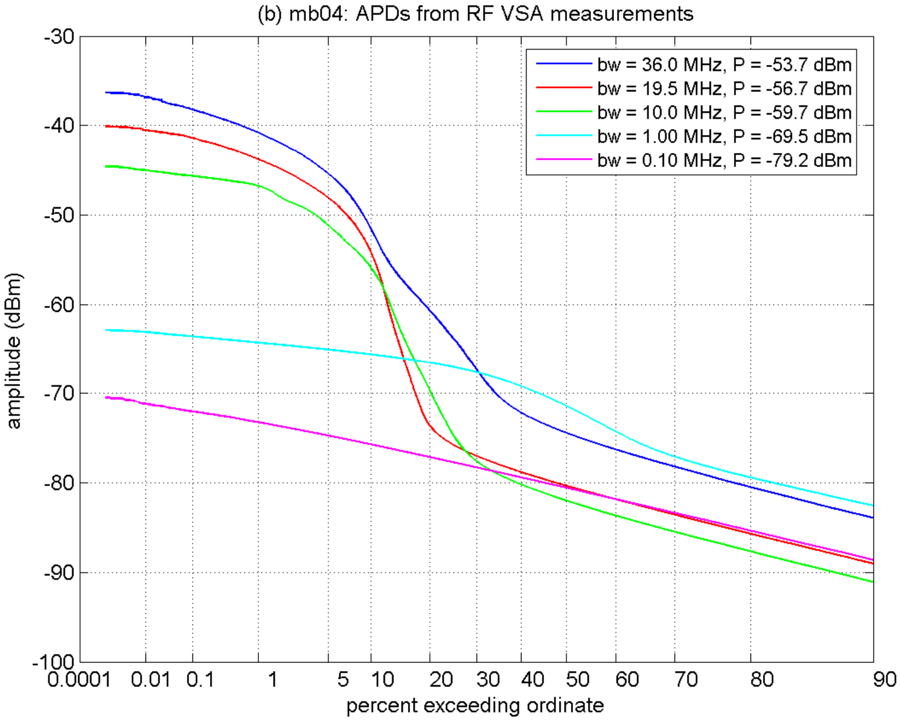
(b) mb04: APDs from RF VSA measurements

Figure B-51. RF amplitude analyses of MB-04 ($b = 7$, $d = 1$).

(a) mb04: IF VSA measurement (bandwidth = 19.51 MHz)

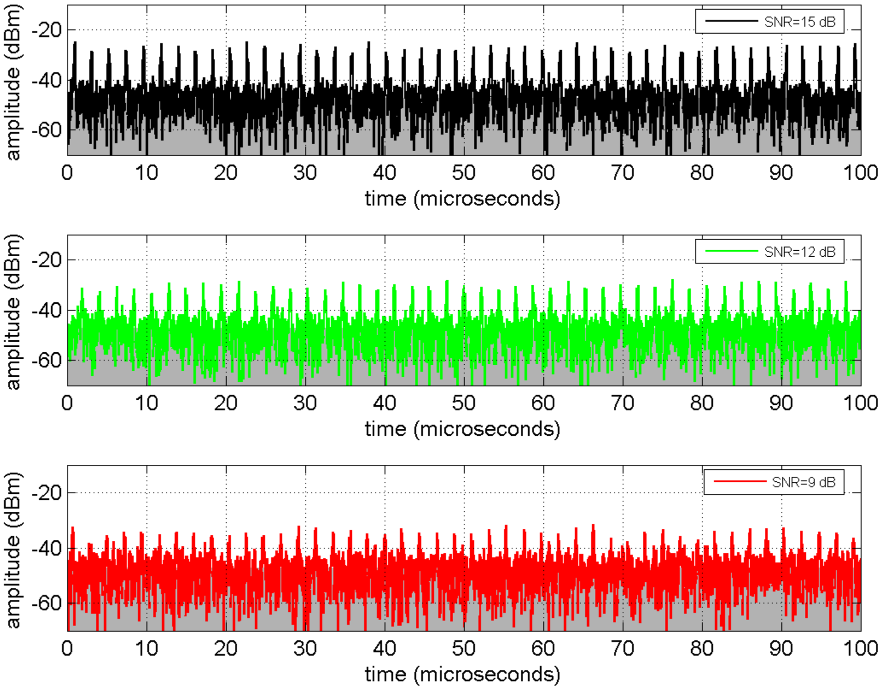

(b) mb04: APDs from IF VSA measurements (bandwidth = 19.51 MHz)

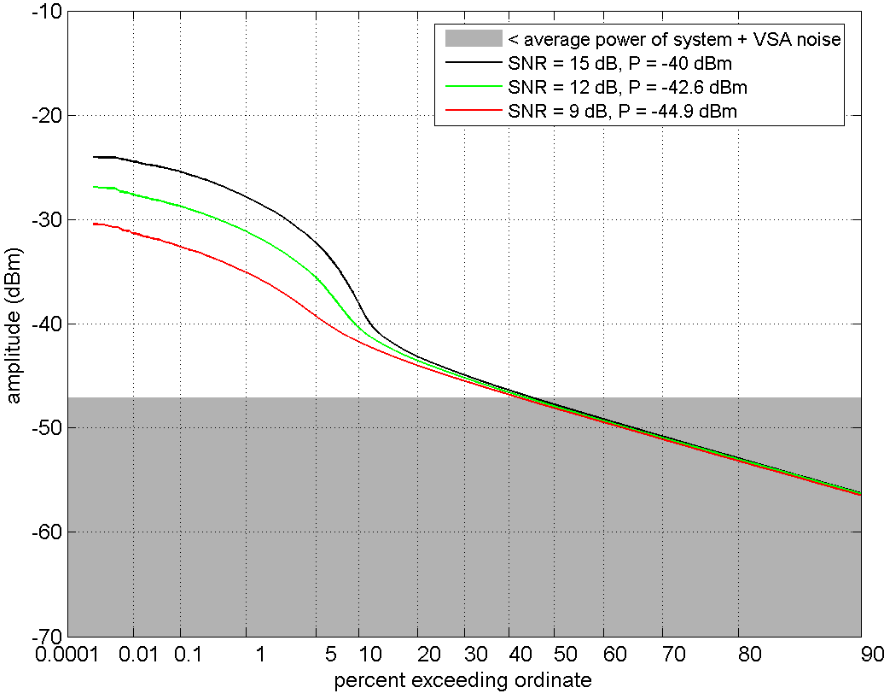

Figure B-52. IF amplitude analyses of MB-04 at INR_{TOV}.

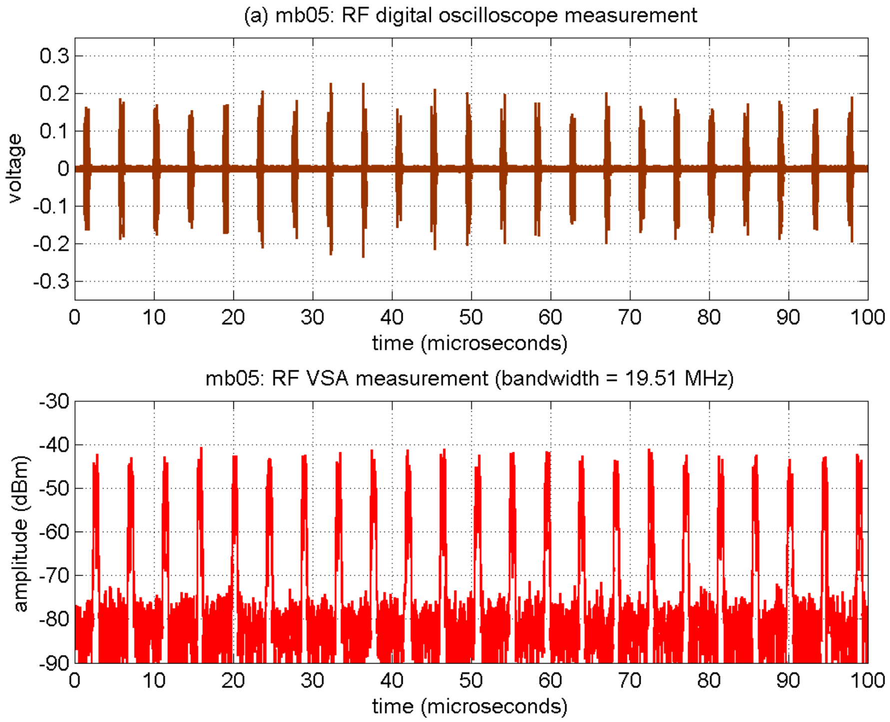

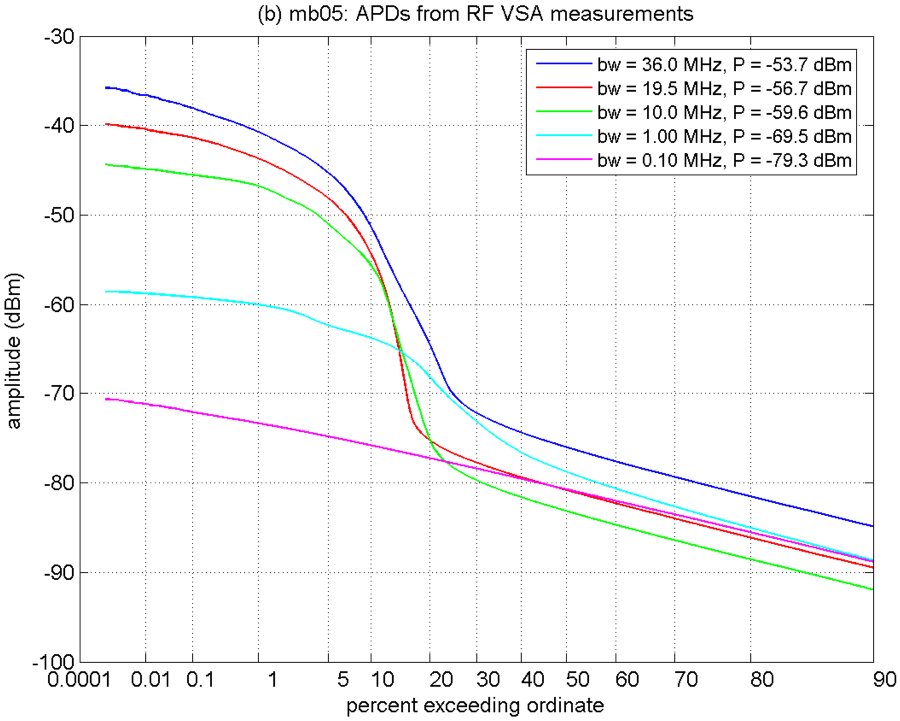

Figure B-53. RF amplitude analyses of MB-05 (b = 7, d = 2).

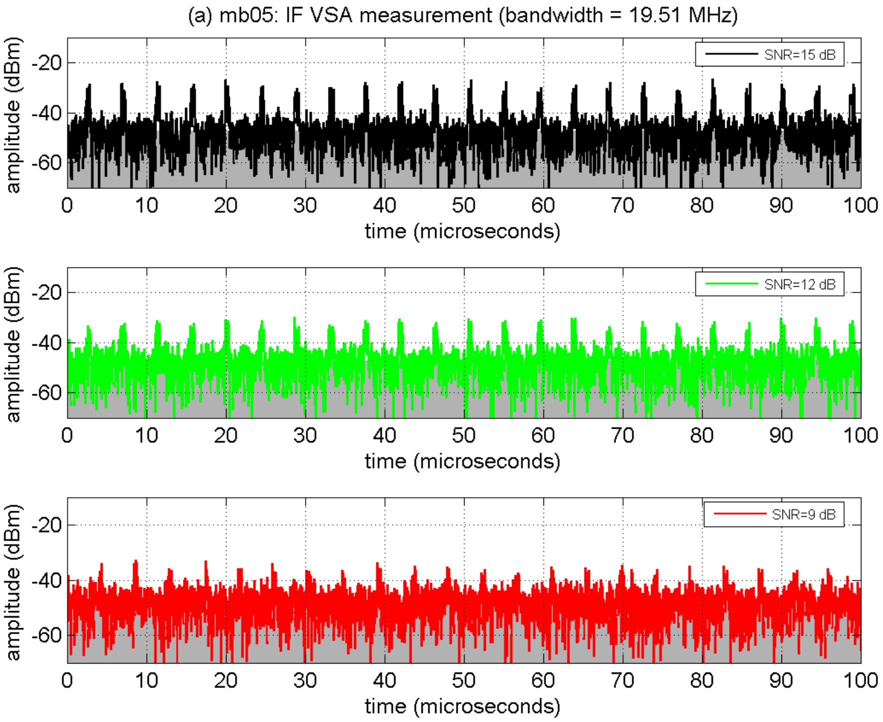
(a) mb05: IF VSA measurement (bandwidth = 19.51 MHz)

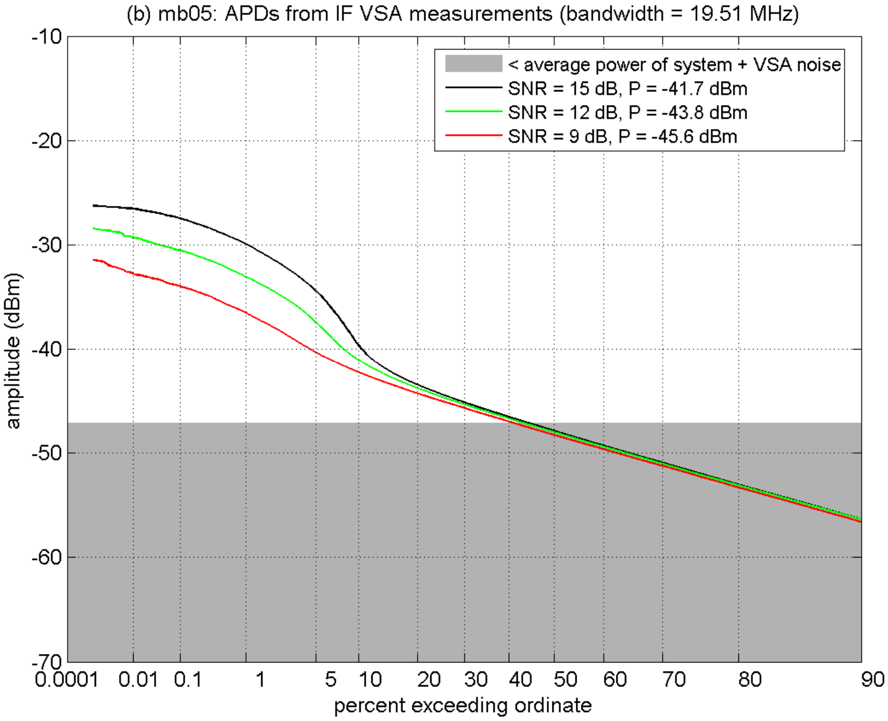
(b) mb05: APDs from IF VSA measurements (bandwidth = 19.51 MHz)

Figure B-54. IF amplitude analyses of MB-05 at INR_{TOV}.

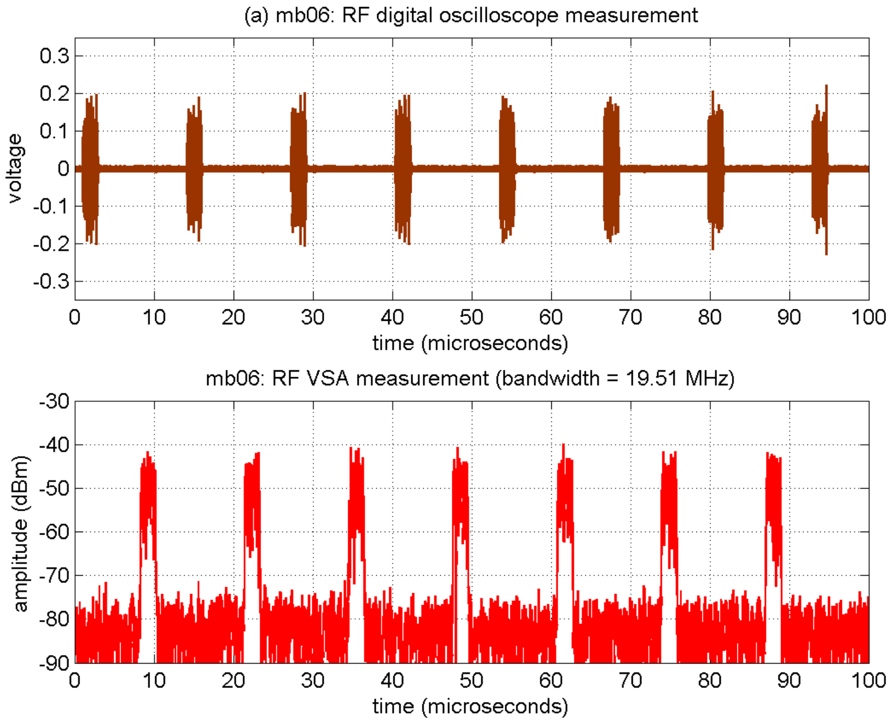

(a) mb06: RF digital oscilloscope measurement

mb06: RF VSA measurement (bandwidth = 19.51 MHz)

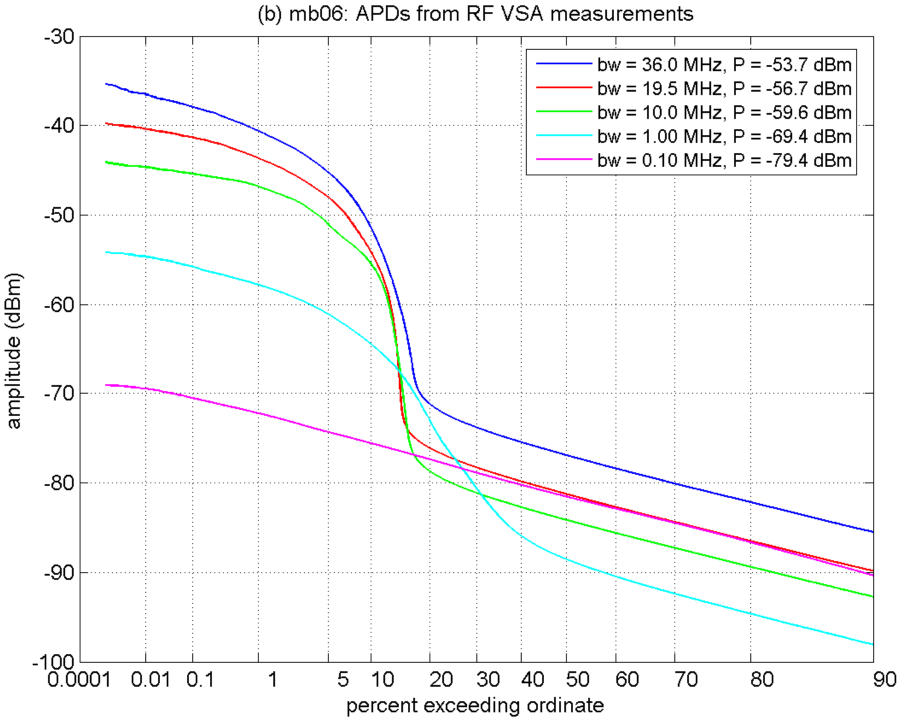

(b) mb06: APDs from RF VSA measurements

Figure B-55. RF amplitude analyses of MB-06 ($b = 7$, $d = 6$).

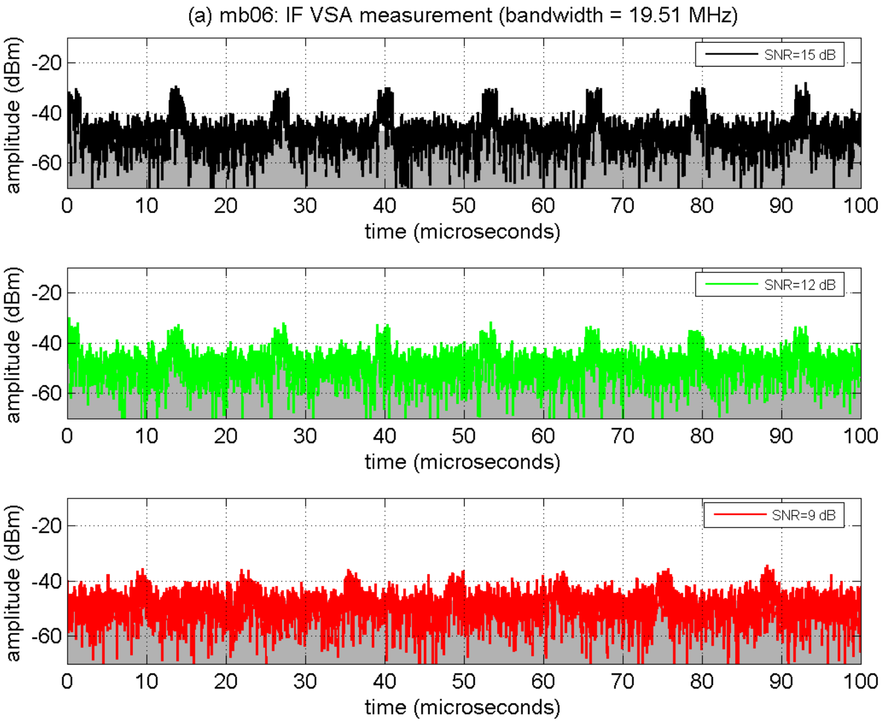

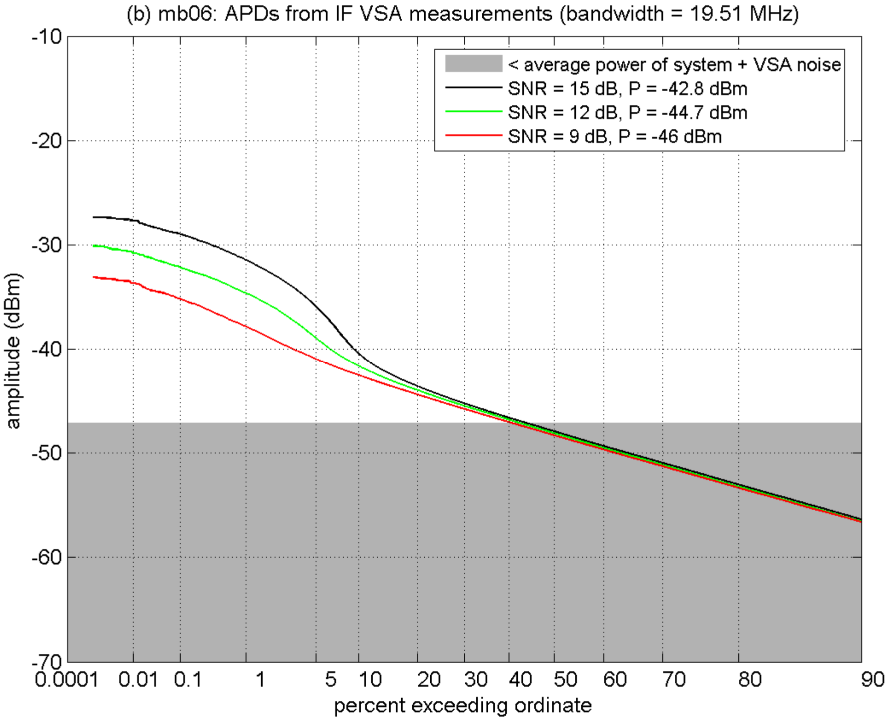

Figure B-56. IF amplitude analyses of MB-06 at INR_{TOV}.

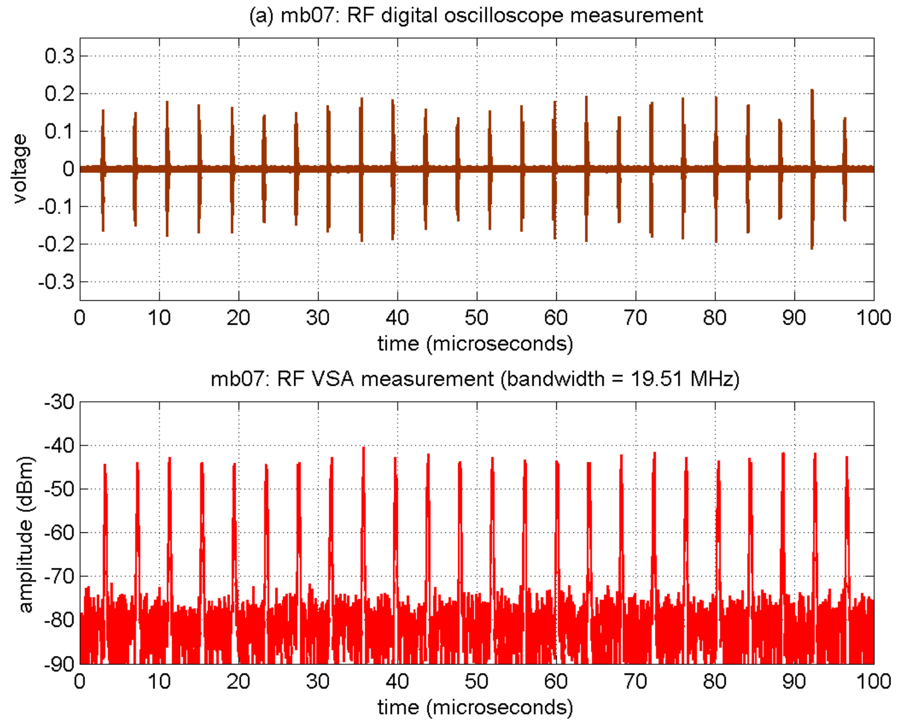

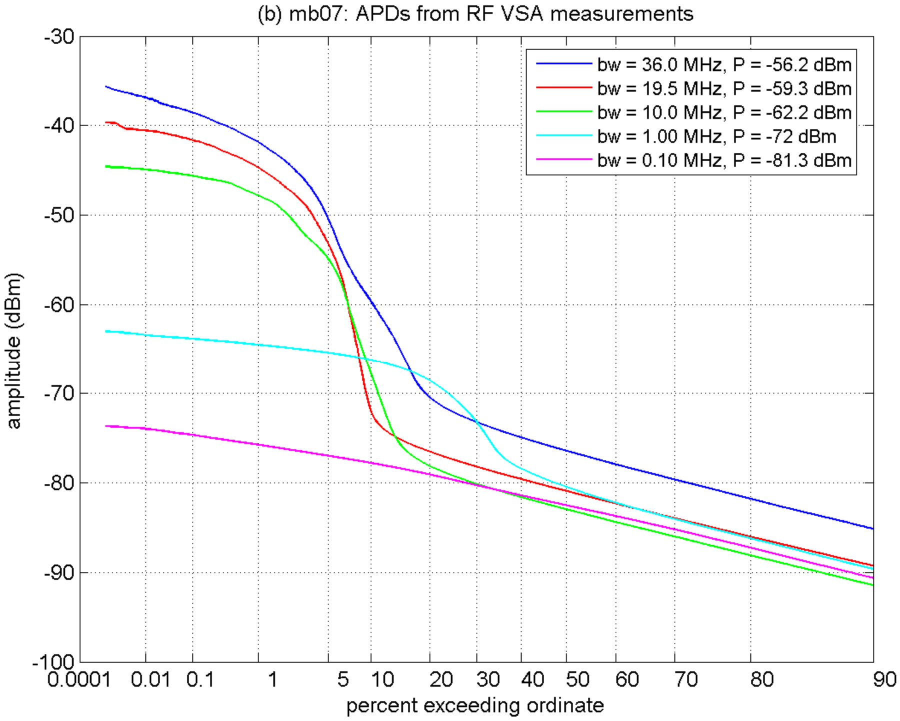

Figure B-57. RF amplitude analyses of MB-07 (b = 13, d = 1).

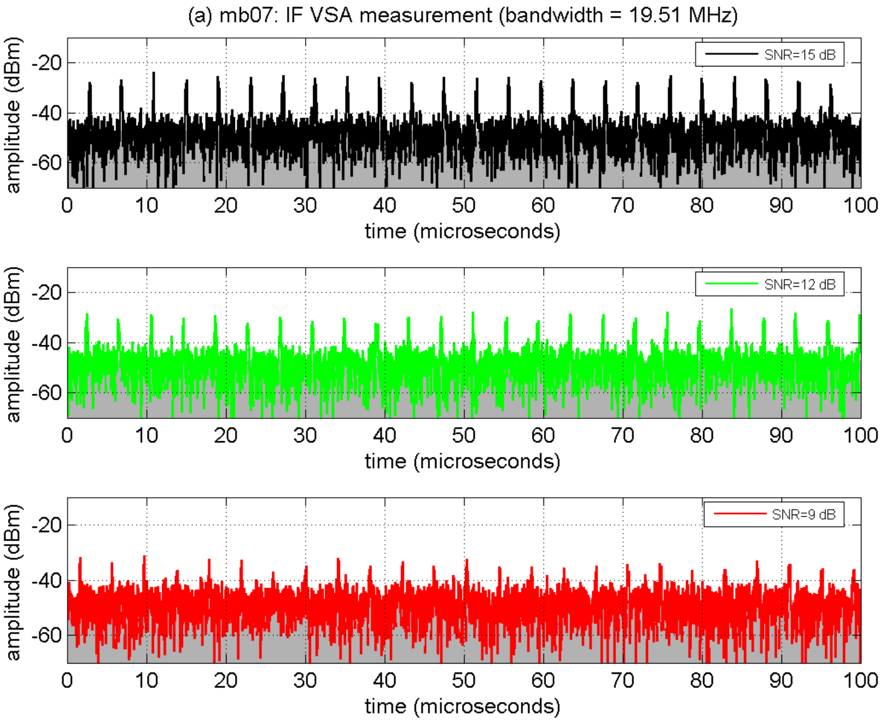
(a) mb07: IF VSA measurement (bandwidth = 19.51 MHz)

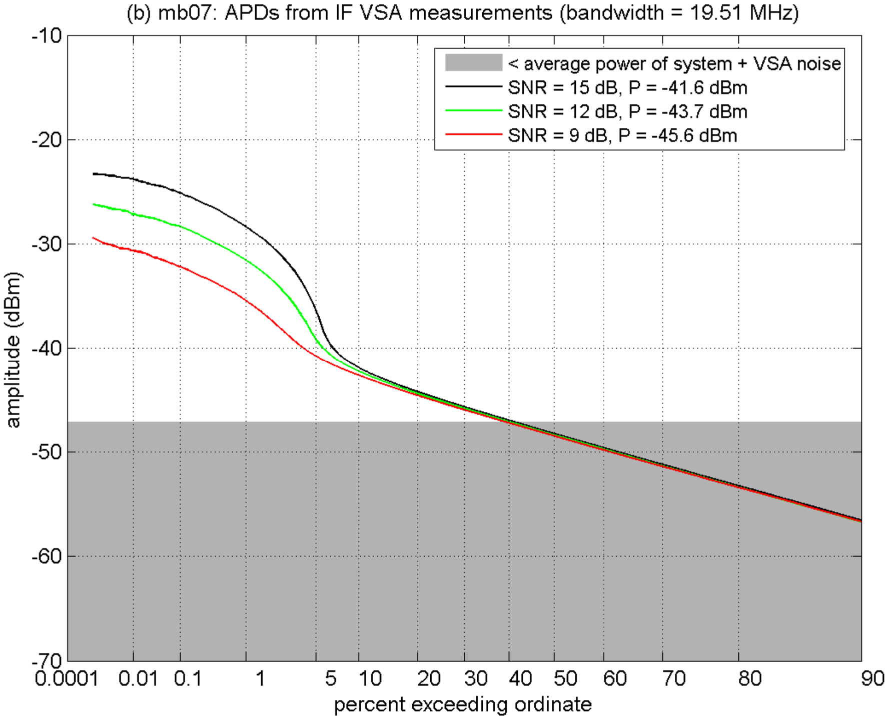
(b) mb07: APDs from IF VSA measurements (bandwidth = 19.51 MHz)

Figure B-58. IF amplitude analyses of MB-07 at INR_{TOV}.

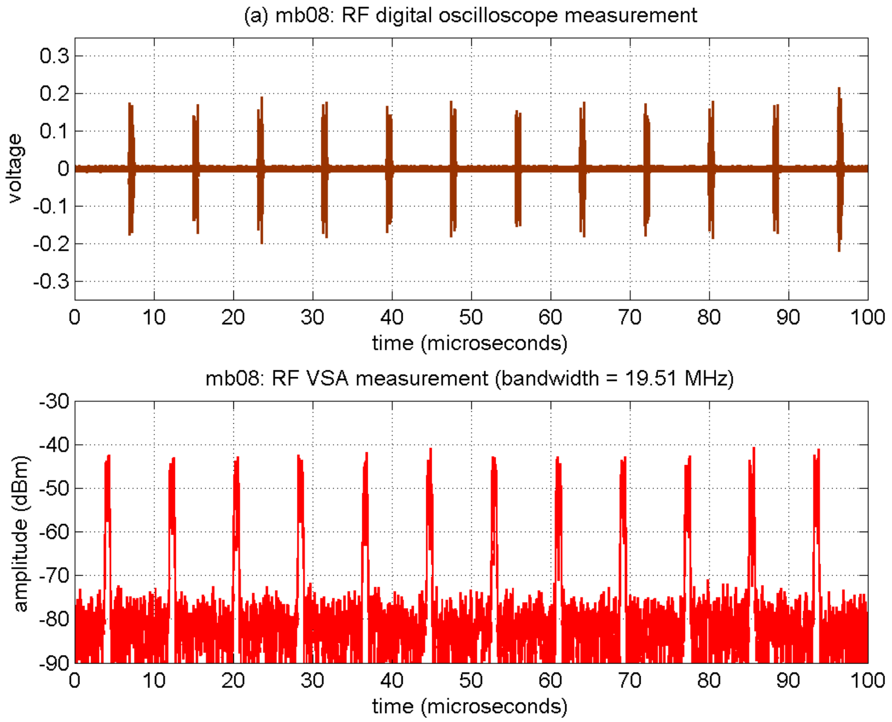

(a) mb08: RF digital oscilloscope measurement

mb08: RF VSA measurement (bandwidth = 19.51 MHz)

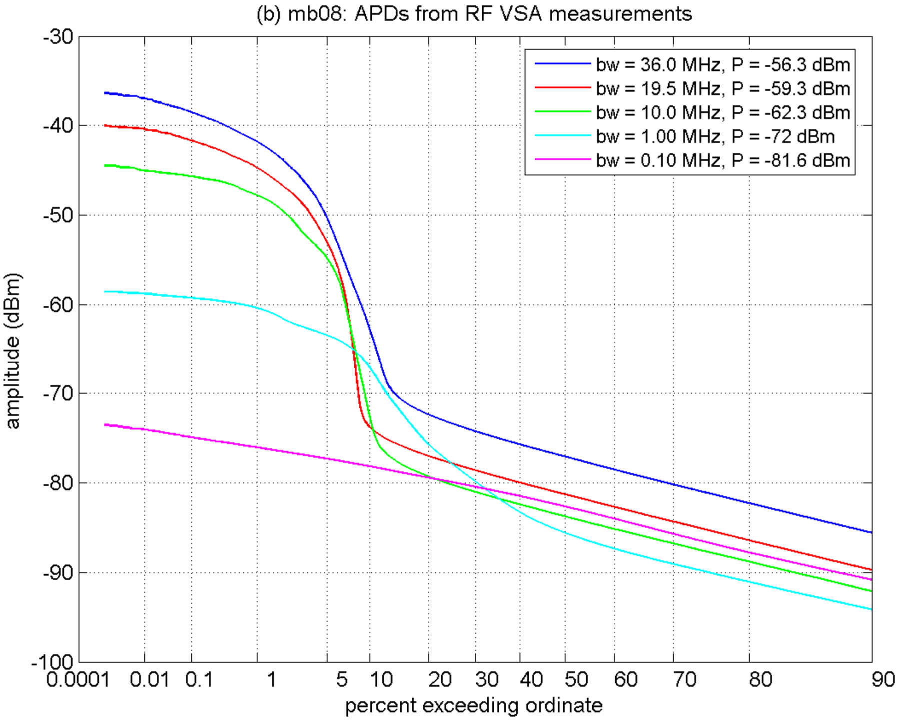

(b) mb08: APDs from RF VSA measurements

Figure B-59. RF amplitude analyses of MB-08 (*b* = 13, *d* = 2).

(a) mb08: IF VSA measurement (bandwidth = 19.51 MHz)

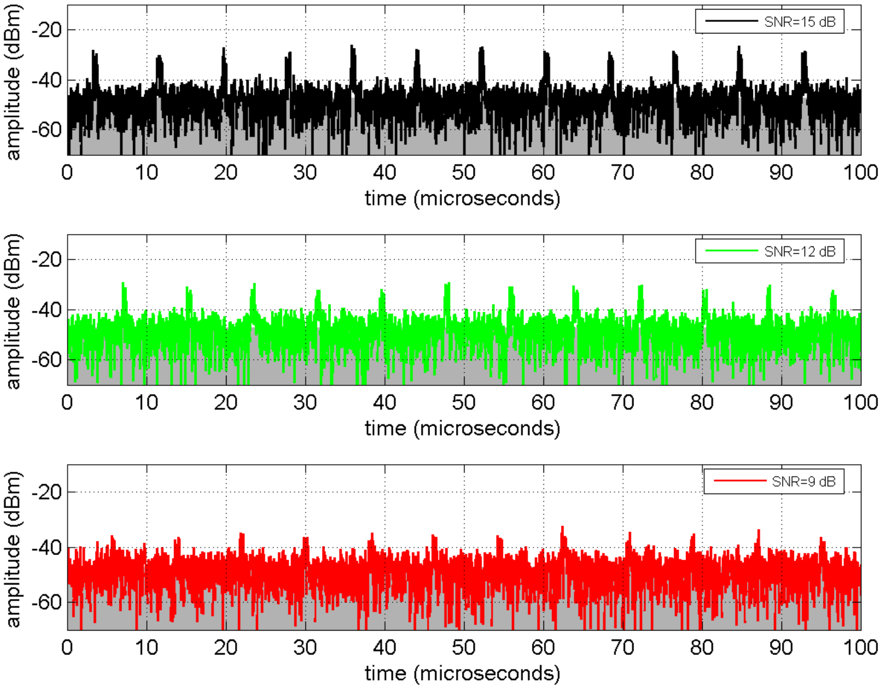

(b) mb08: APDs from IF VSA measurements (bandwidth = 19.51 MHz)

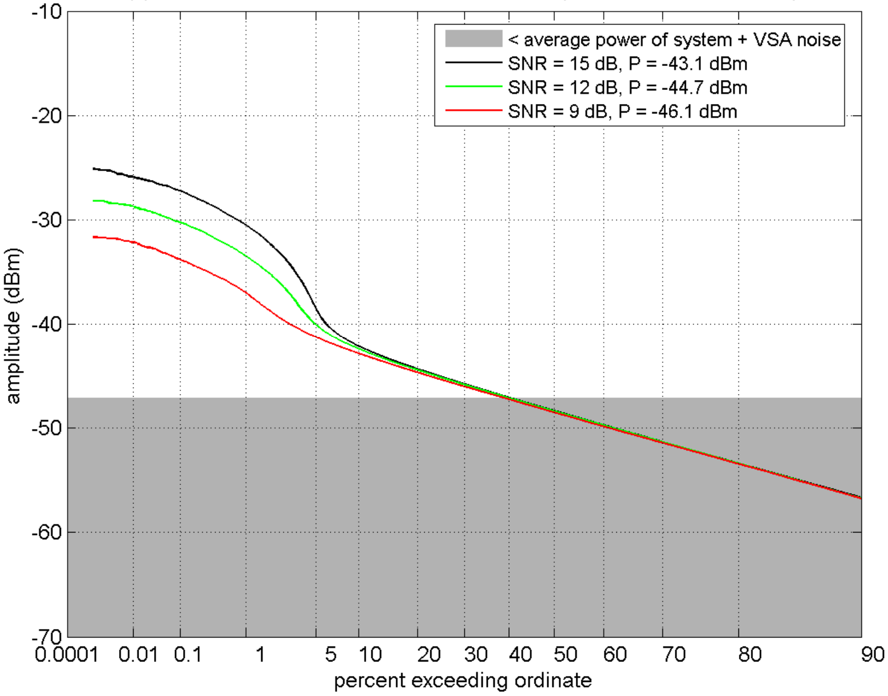

Figure B-60. IF amplitude analyses of MB-08 at INR_{TOV}.

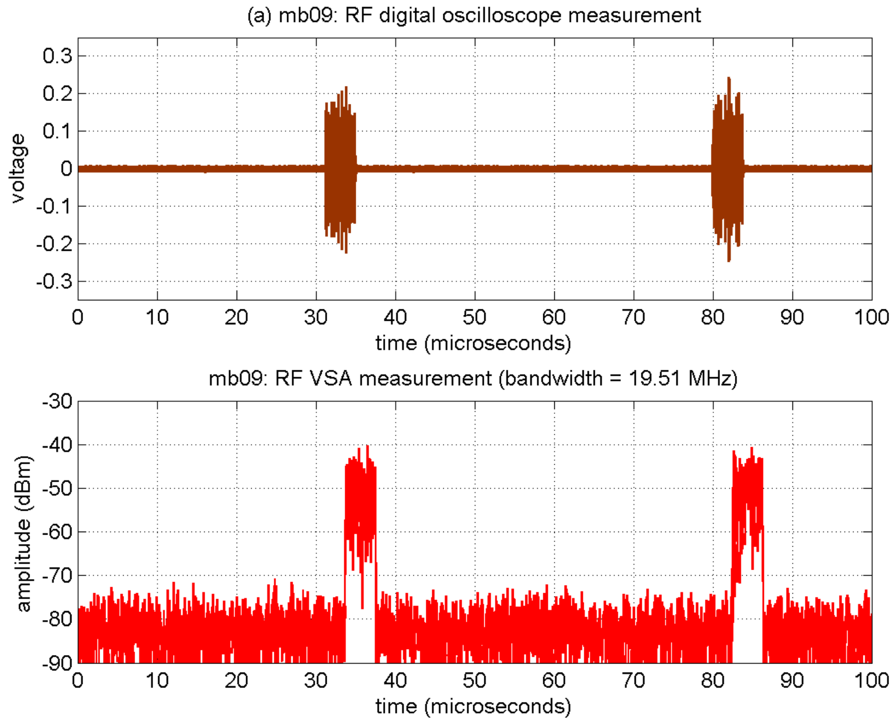

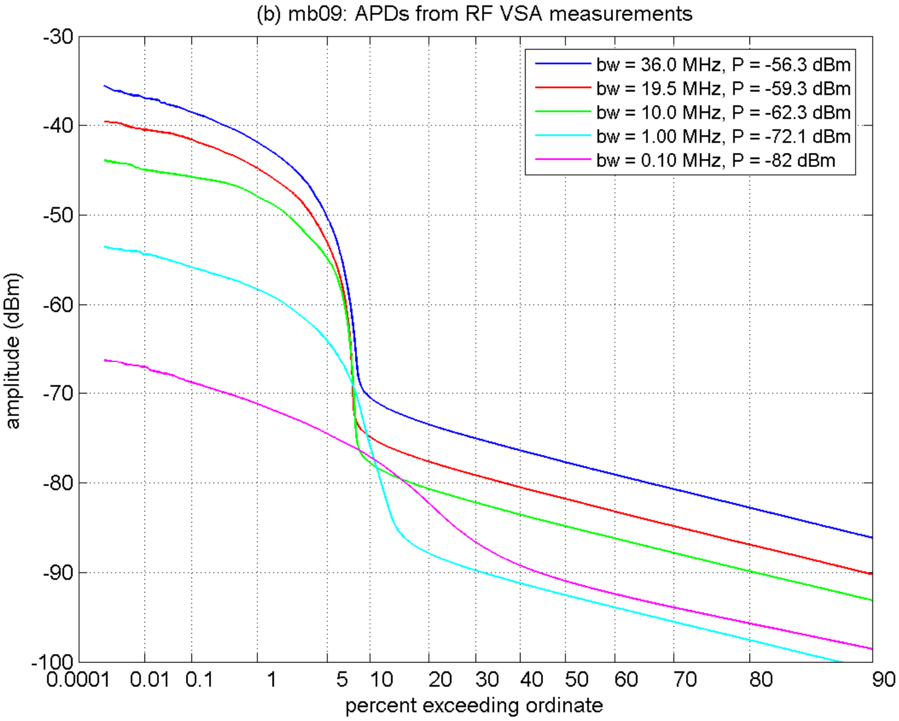

Figure B-61. RF amplitude analyses of MB-09 ($b = 13$, $d = 12$).

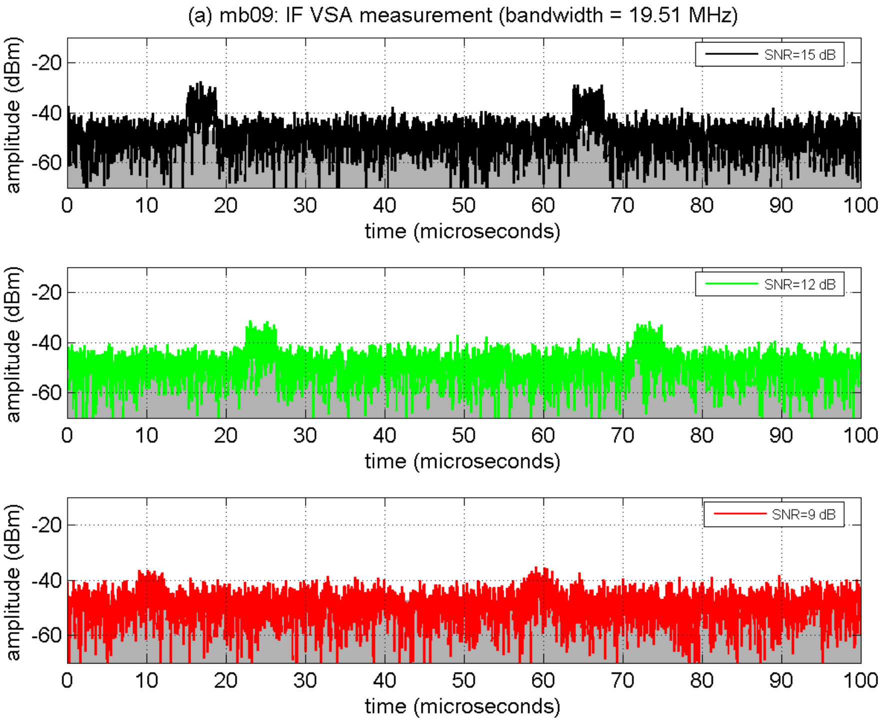
(a) mb09: IF VSA measurement (bandwidth = 19.51 MHz)

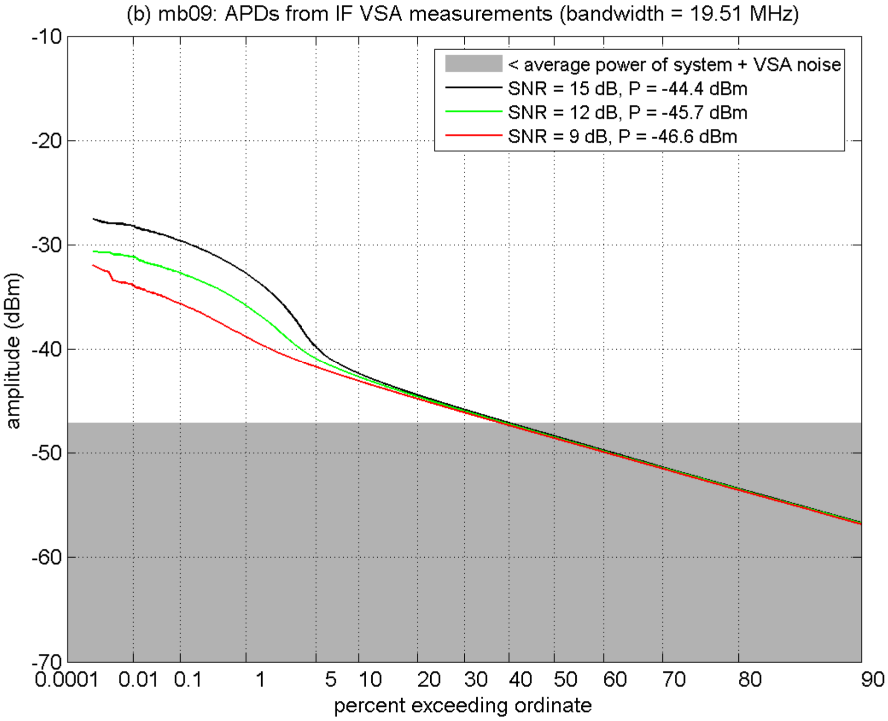
(b) mb09: APDs from IF VSA measurements (bandwidth = 19.51 MHz)

Figure B-62. IF amplitude analyses of MB-09 at INR_{TOV}.

B.4. Spectral Analyses

The spectral analyses provided in this subsection were derived from VSA measurements and intended to emulate the swept spectrum analyzer (SA) measurements described in Table B-5. Complex samples measured in a 36-MHz VSA span were frequency shifted so that the frequency of interest was centered at 0 Hz. Next, the signal was band-limited to a resolution bandwidth (*RBW*) of 1 MHz or 0.1 MHz using a root-raised cosine filter with α = 0.35. Mean, median, and peak statistics were computed for the resulting band-limited complex-baseband data.

Table B-5. Spectrum Analyzer Settings for Characterizing UWB Signals

Center Frequency (MHz)	Span (MHz)	Resolution Bandwidth (MHz)	Video Bandwidth (MHz)	Number of Frequency Steps	Sweep Time (seconds)	Detector
3950	600	1	50	3600	10.8	Rms, peak
3820	40	0.1		2400	72.0	

These *RBW*s are smaller than that of the victim digital television channel; however, results provide mean and peak estimates relevant to possible narrowband circuitry within the receiver. Frequencies of interest spanned the bandwidth of the satellite channel with a frequency step size set to one tenth of *RBW* to ensure that spectrum details were not missed.

Figures B-63 – B-81 provide spectral statistics for the UWB signals: Figures B-63 – B-66 correspond to DP-01 – DP-04, Figures B-67 – B-72 correspond to DS-01 – DS-06, and Figures B-73 – B-81 correspond to MB-01 – MB-09. SA measurements were made and show agreement with the VSA measurement results; SA measurements are not included in this report.

The most notable trend was frequency-dependent variation in the MB peak amplitude statistics. This behavior is related to the location and modulation of the data and pilot tones of the MB signals, and is the primary difference between MB and GN(MB) signals. GN(MB) peak statistics are flat versus frequency as demonstrated theoretically in Section C.2 in Part 2 [7].

A notable example of this trend is MB-02 in a 0.1-MHz *RBW*. The pilot tone in the band of interest, located at -4.375 MHz, caused spikes in the peak spectra at intervals of ½ the reciprocal gating repetition rate, i.e., 0.533 MHz. Although this feature is evident in the 1-MHz *RBW*, the more prominent feature is the cyclic variation of all peak statistics. Interestingly, the nulls in the cyclic variation correspond to center frequencies of the data and pilot tones.

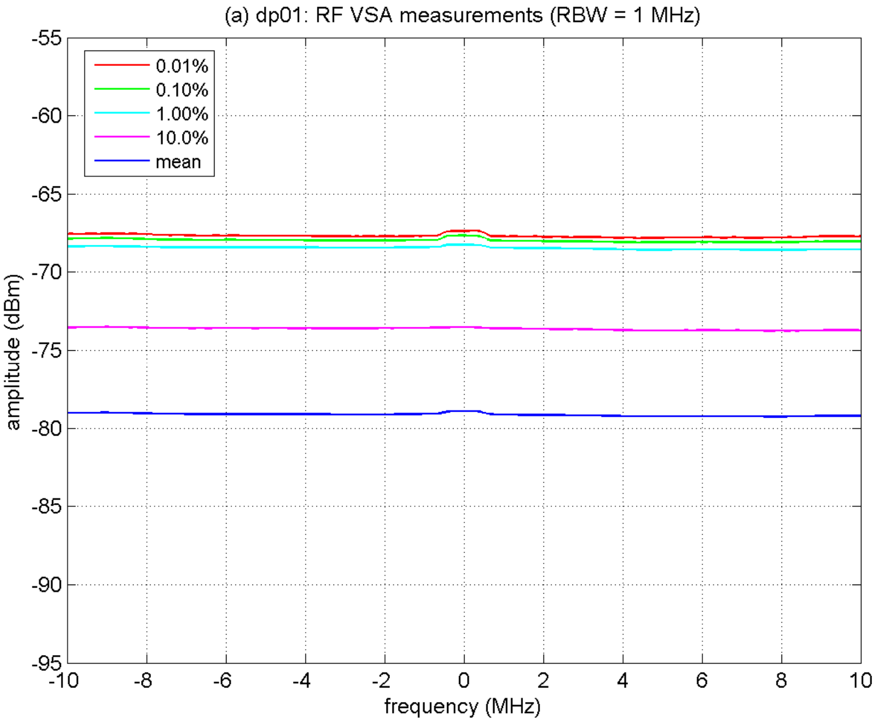

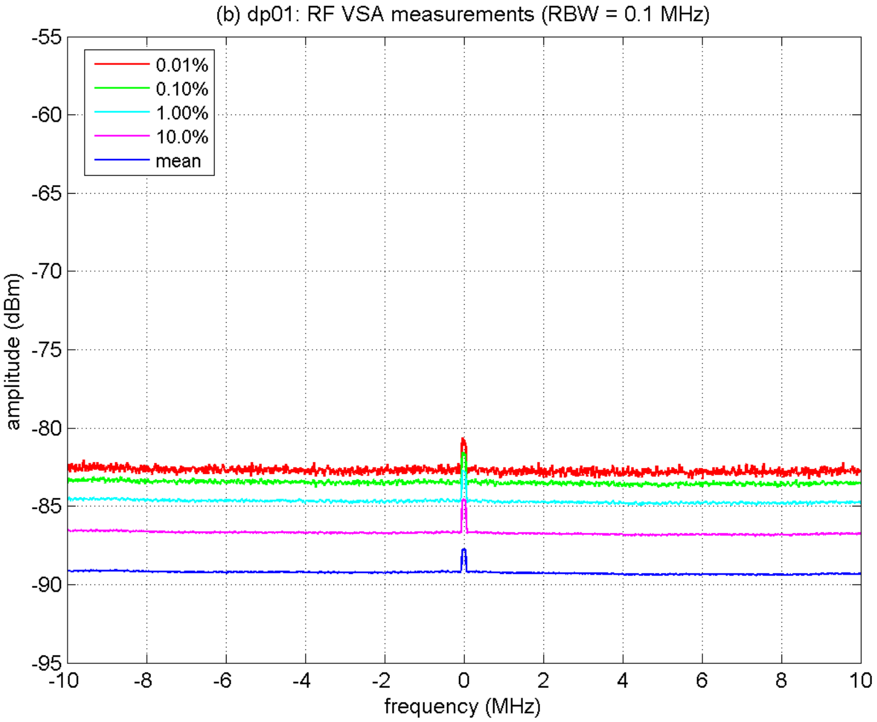

Figure B-63. RF spectral analyses of DP-01 (T_{pulse} = 10,000 ns, w = 0.094 ns, f_D = 0.5).

(a) dp02: RF VSA measurements (RBW = 1 MHz)

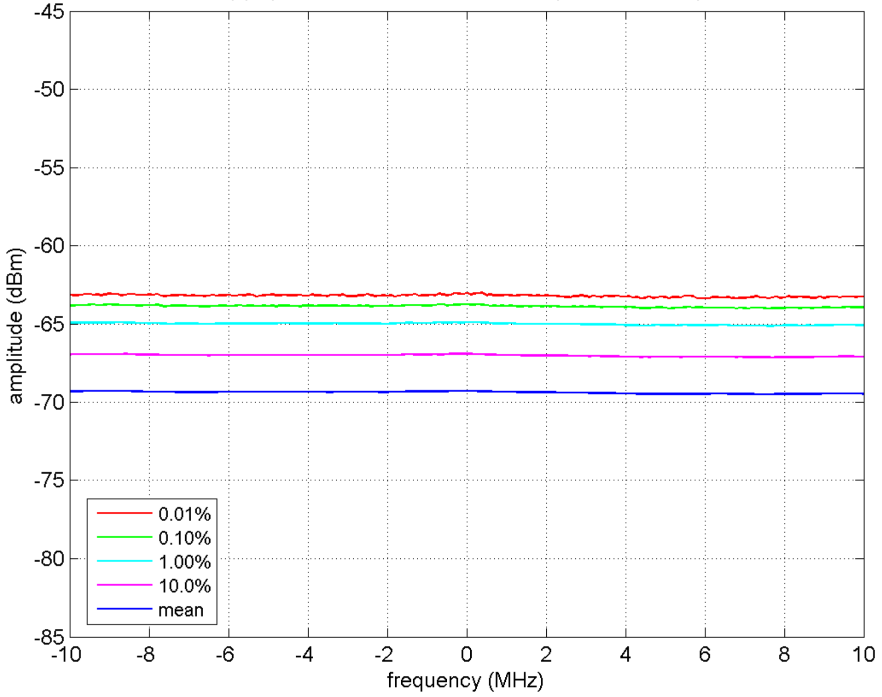

(b) dp02: RF VSA measurements (RBW = 0.1 MHz)

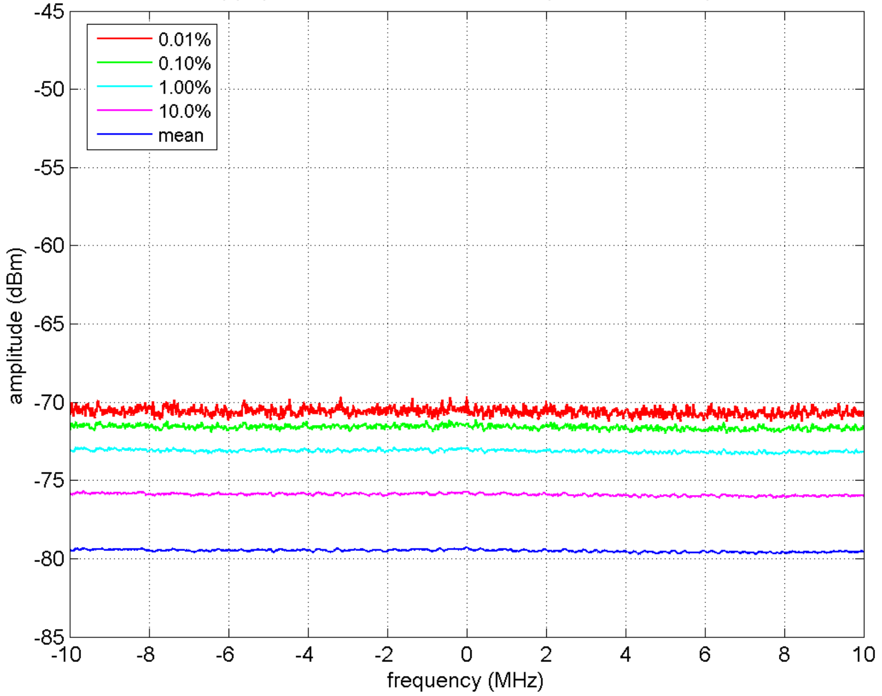

Figure B-64. RF spectral analyses of DP-02 (T_{pulse} = 1000 ns, w = 0.094 ns, f_D = 0.5).

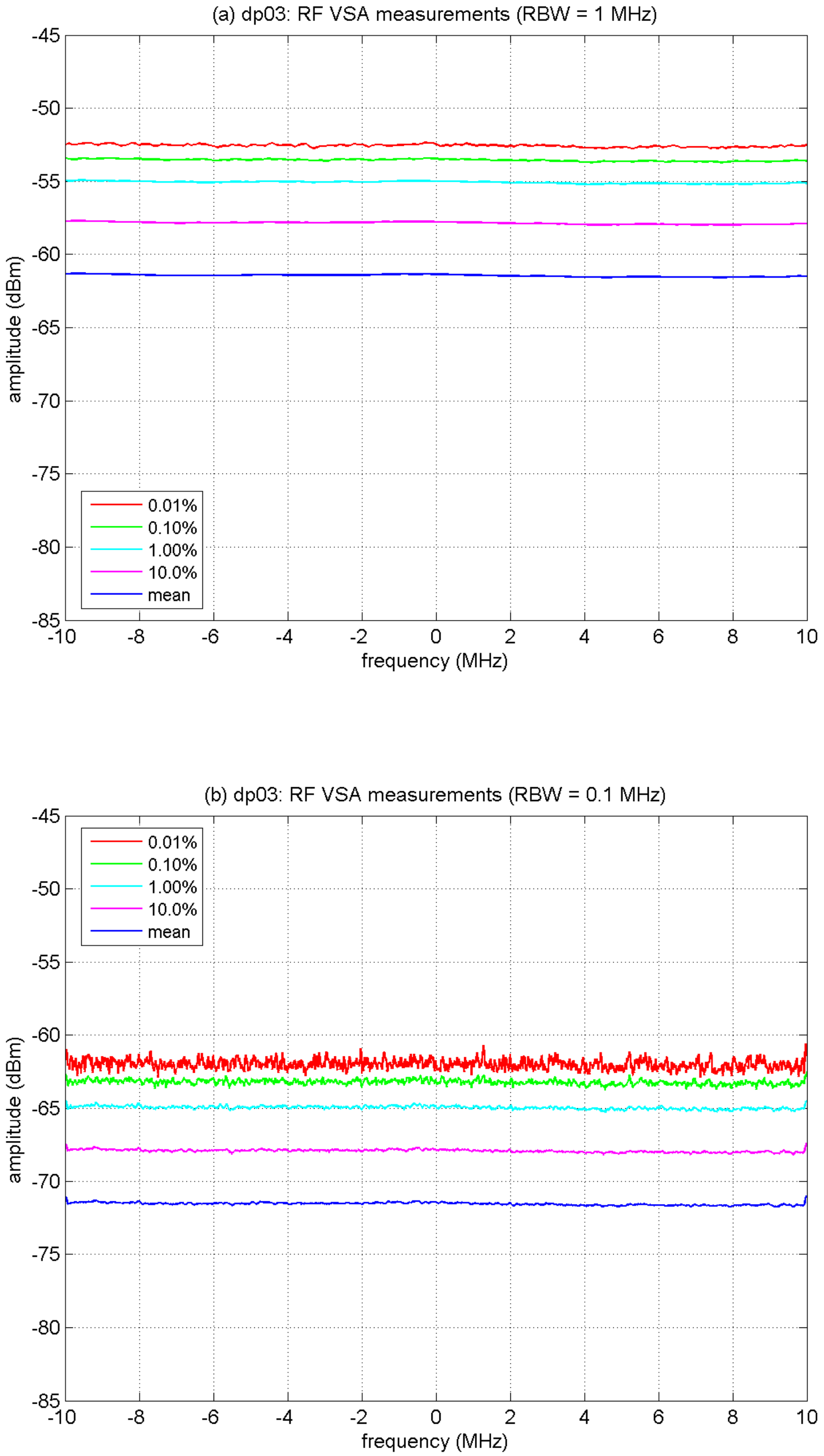

Figure B-65. RF spectral analyses of DP-03 (T_{pulse} = 100 ns, w = 0.094 ns, f_D = 0.5).

(a) dp04: RF VSA measurements (RBW = 1 MHz)

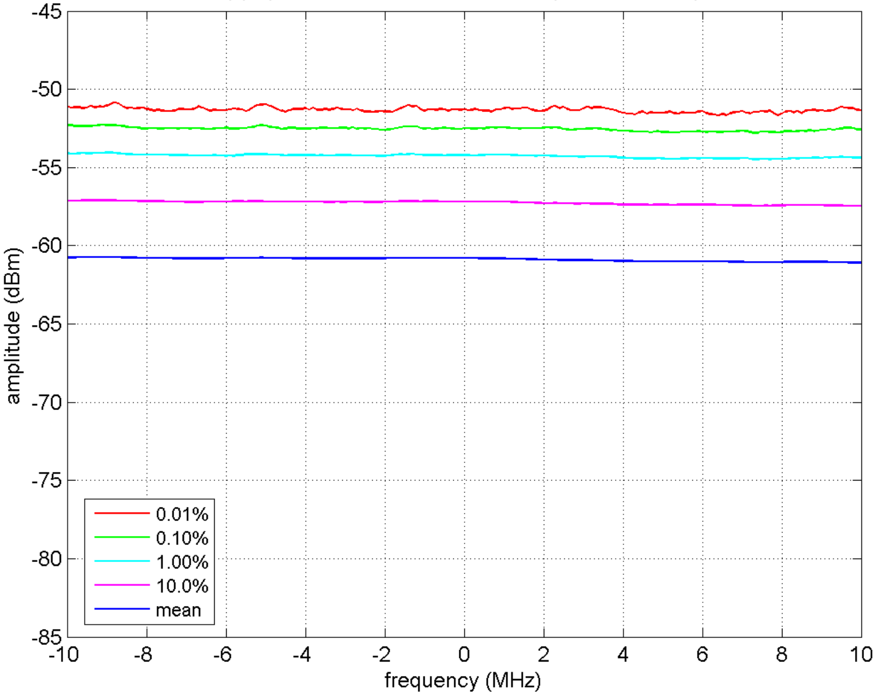

(b) dp04: RF VSA measurements (RBW = 0.1 MHz)

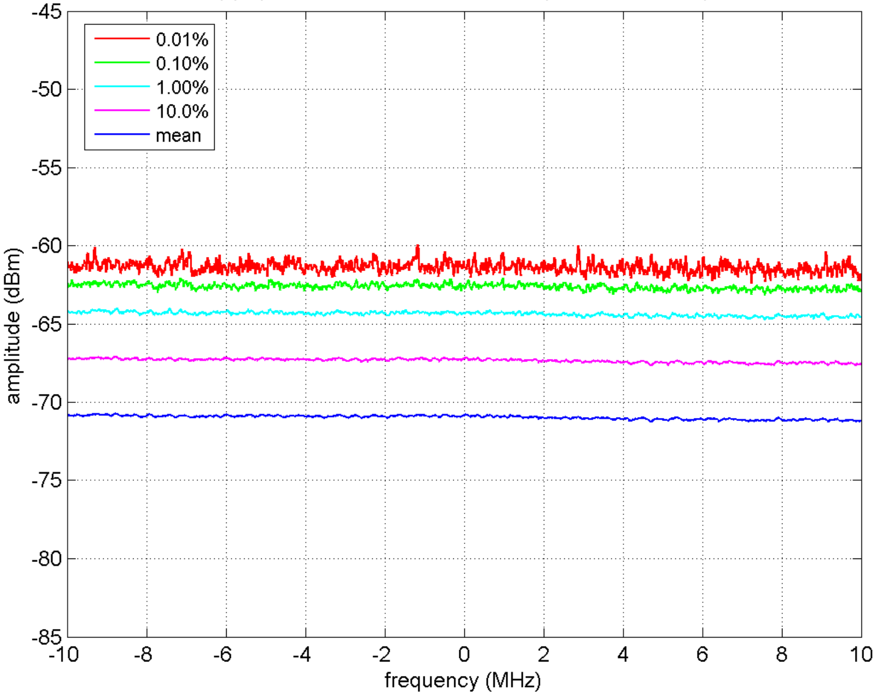

Figure B-66. RF spectral analyses of DP-04 (T_{pulse} = 10 ns, w = 0.094 ns, f_D = 0.5).

(a) ds01: RF VSA measurements (RBW = 1 MHz)

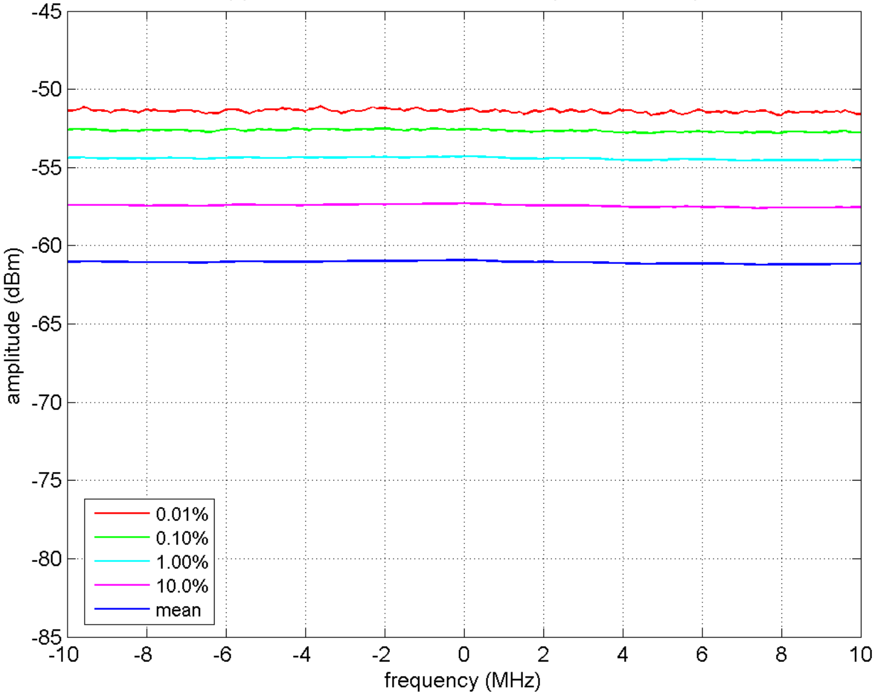

(b) ds01: RF VSA measurements (RBW = 0.1 MHz)

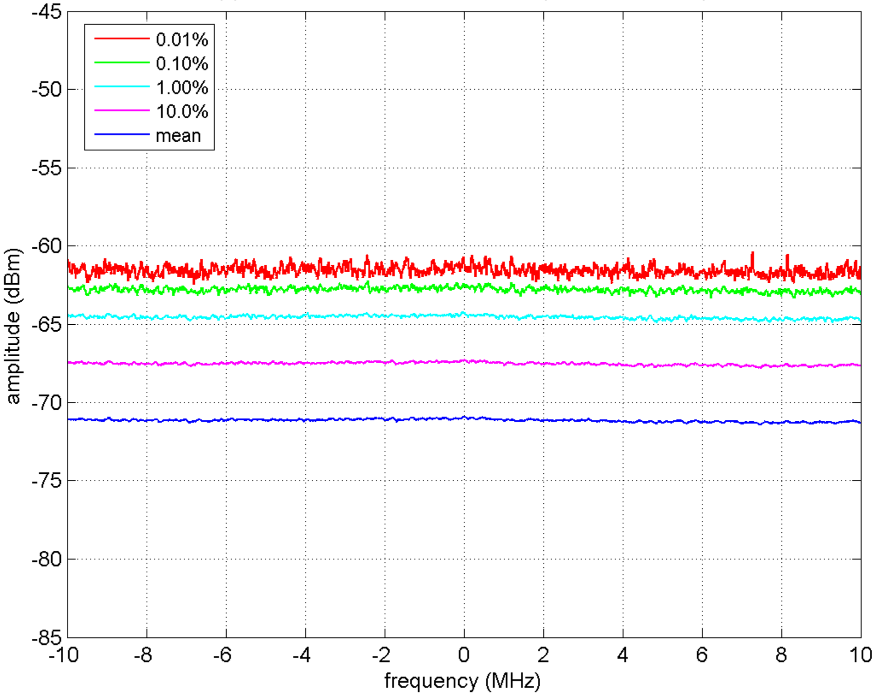

Figure B-67. RF spectral analyses of DS-01 ($L = 1$).

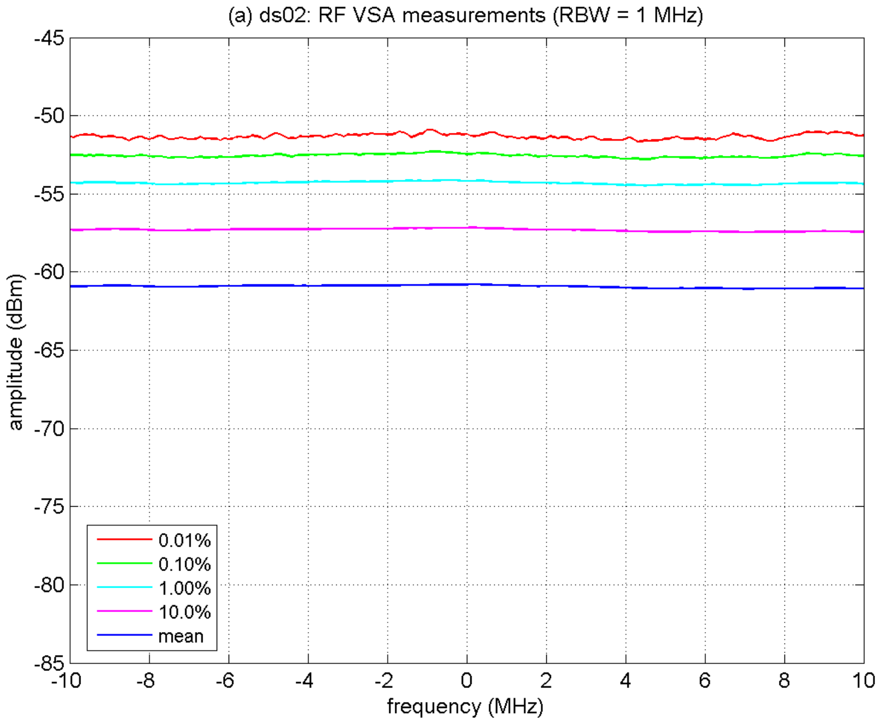
(a) ds02: RF VSA measurements (RBW = 1 MHz)

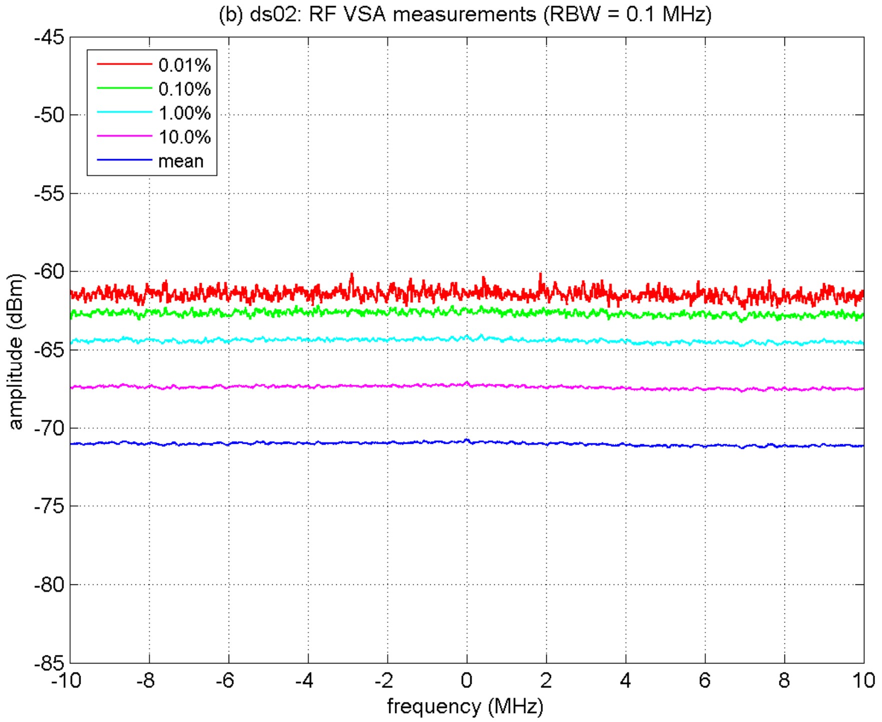
(b) ds02: RF VSA measurements (RBW = 0.1 MHz)

Figure B-68. RF spectral analyses of DS-02 (*L* = 3, sparse code).

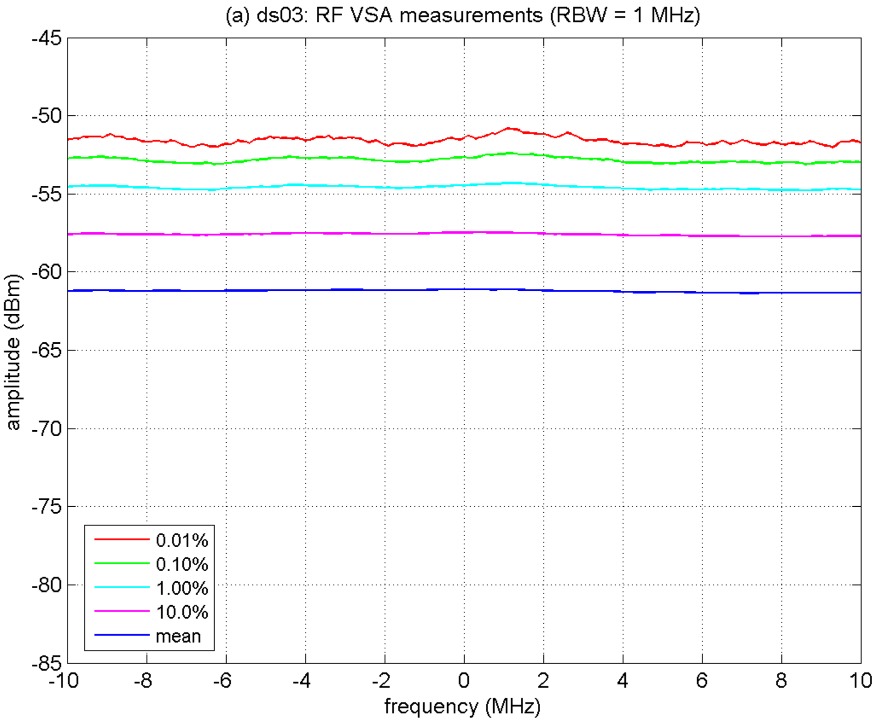

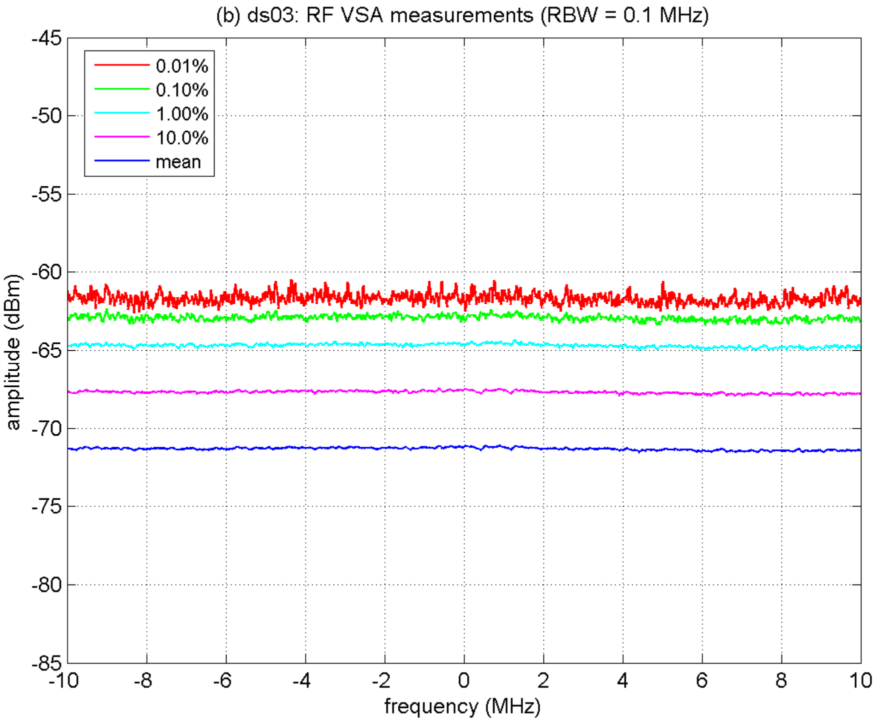

Figure B-69. RF spectral analyses of DS-03 (L = 6, sparse code).

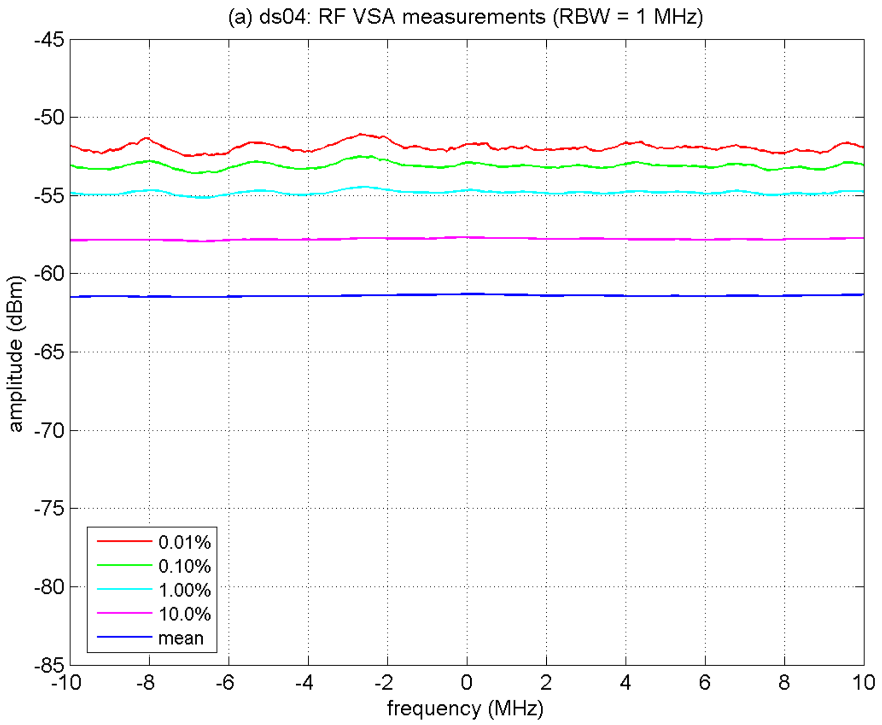
(a) ds04: RF VSA measurements (RBW = 1 MHz)

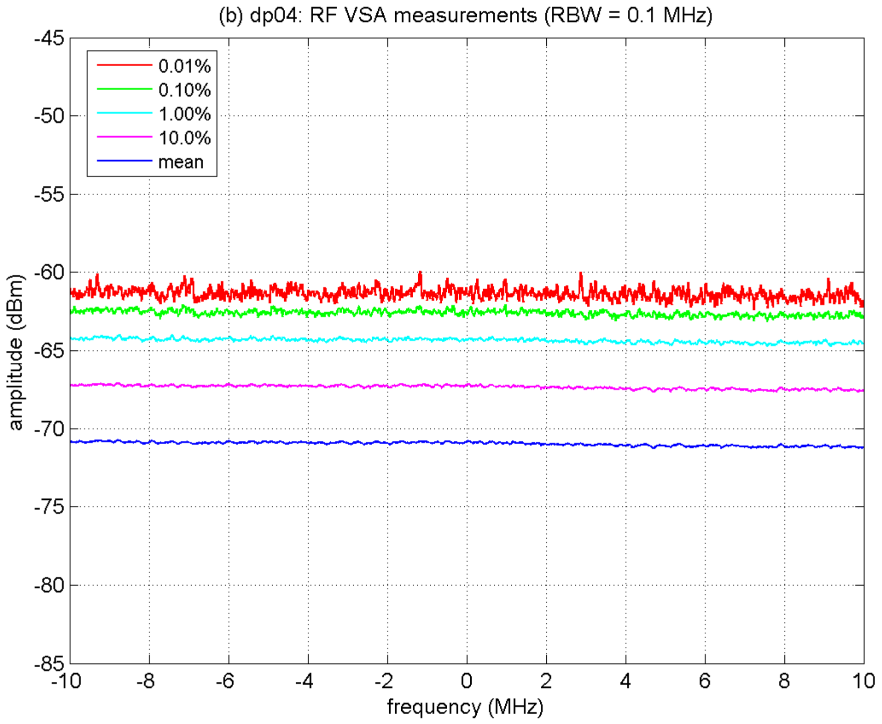
(b) dp04: RF VSA measurements (RBW = 0.1 MHz)

Figure B-70. RF spectral analyses of DS-04 (*L* = 12, DS code).

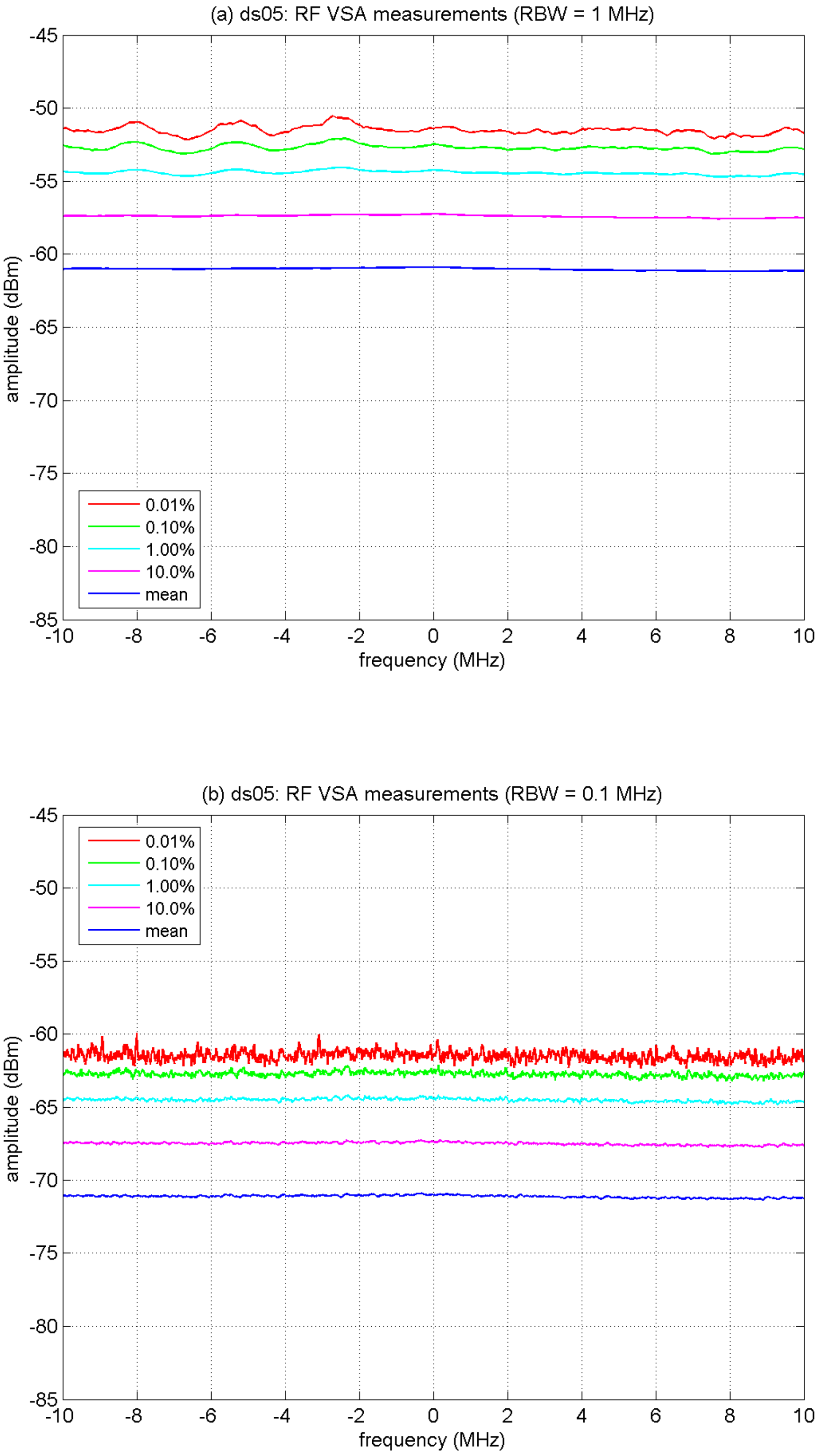

Figure B-71. RF spectral analyses of DS-05 (*L* = 12, sparse code).

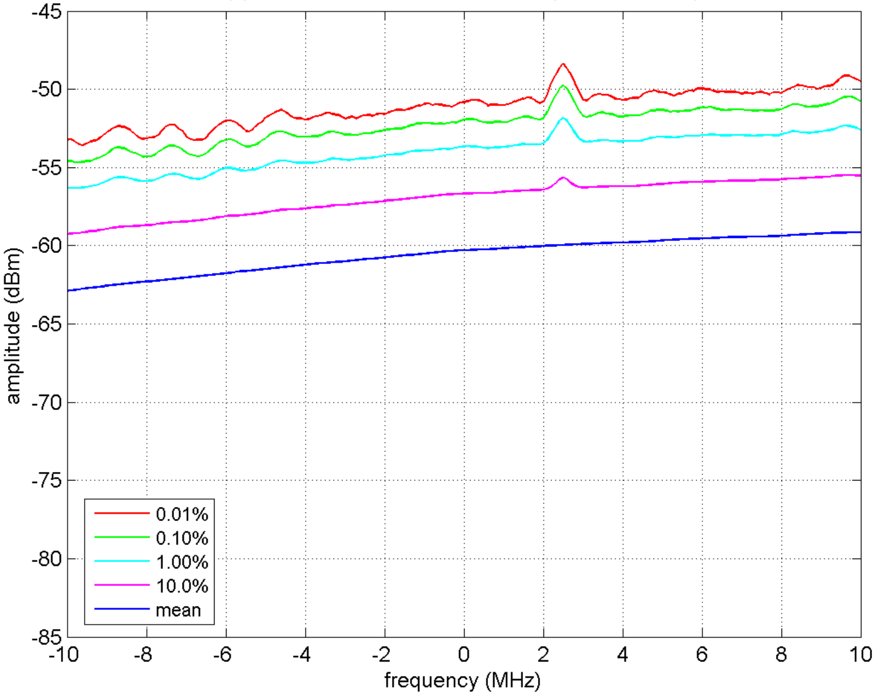
(a) ds06: RF VSA measurements (RBW = 1 MHz)

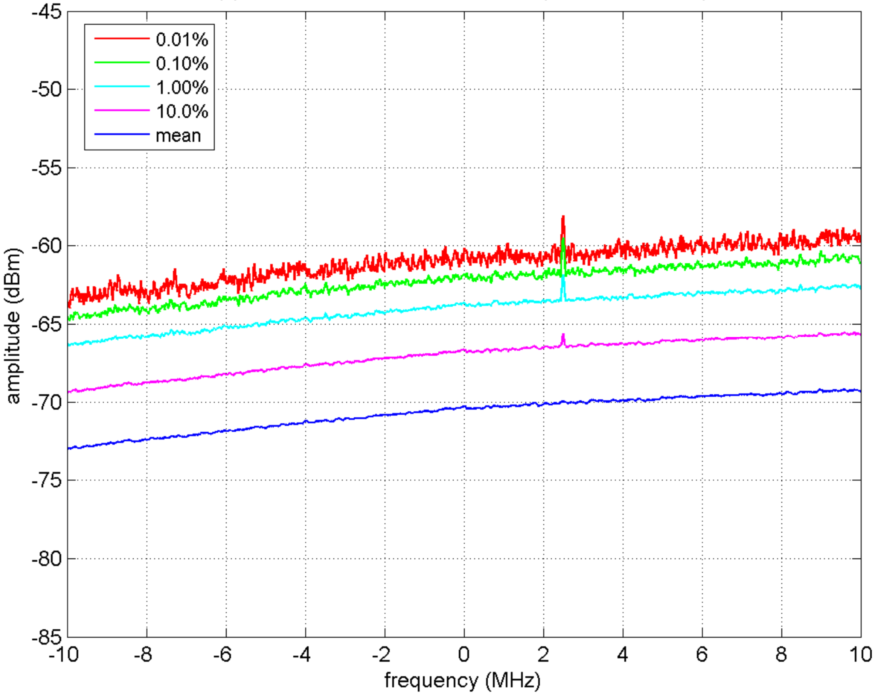
(b) ds06: RF VSA measurements (RBW = 0.1 MHz)

Figure B-72. RF spectral analyses of DS-06 (*L* = 24, DS code).

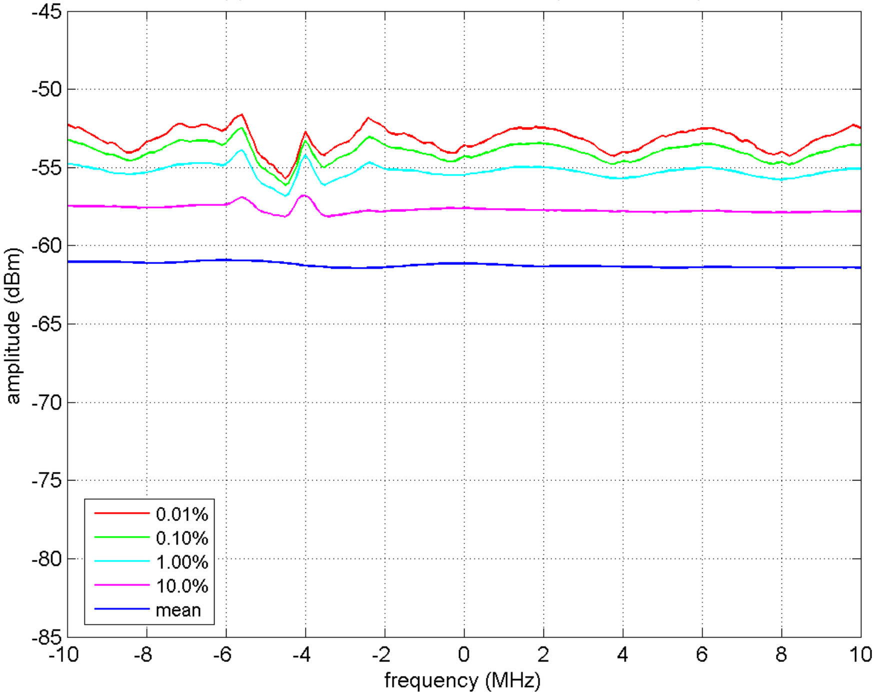
(a) mb01: RF VSA measurements (RBW = 1 MHz)

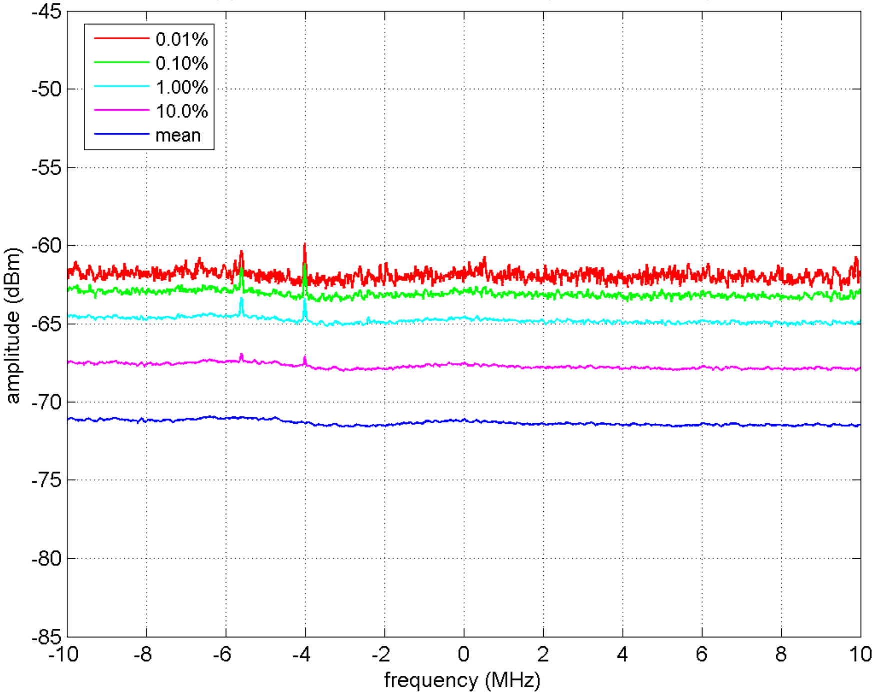
(b) mb01: RF VSA measurements (RBW = 0.1 MHz)

Figure B-73. RF spectral analyses of MB-01 (*b* = 1).

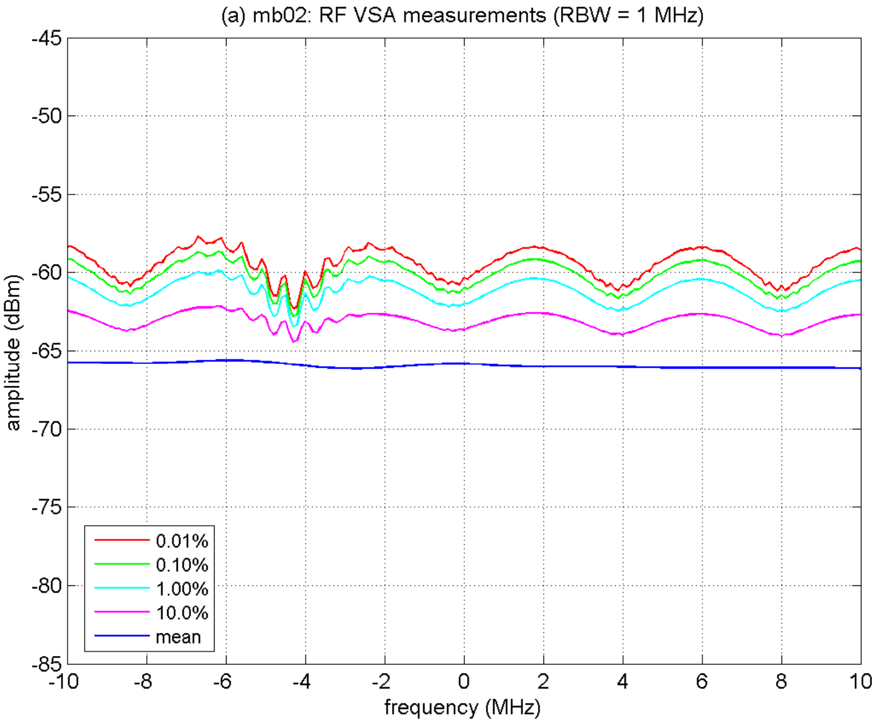

(a) mb02: RF VSA measurements (RBW = 1 MHz)

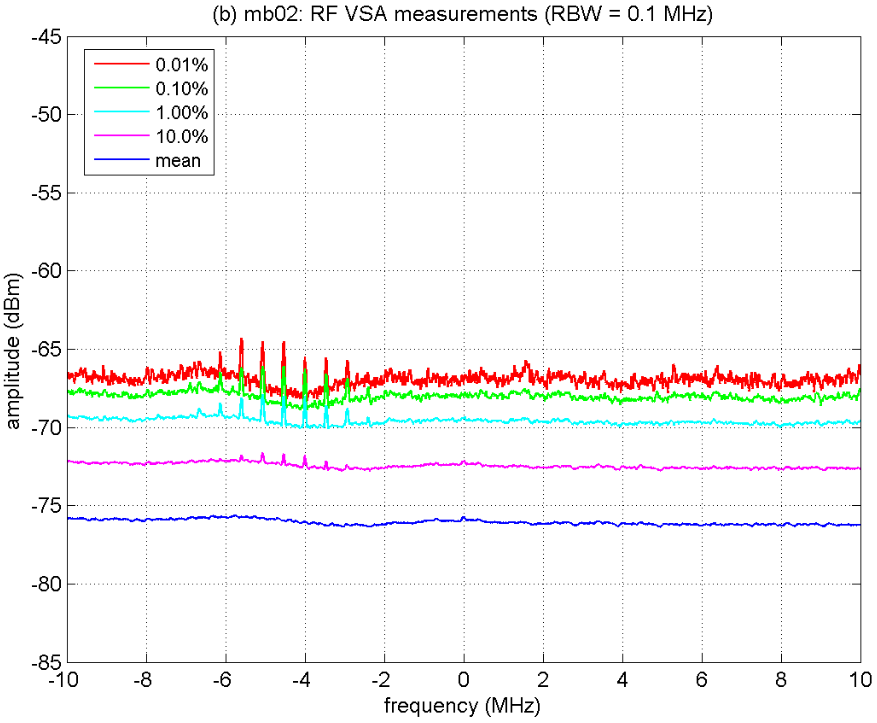

(b) mb02: RF VSA measurements (RBW = 0.1 MHz)

Figure B-74. RF spectral analyses of MB-02 (*b* = 3, *d* = 1).

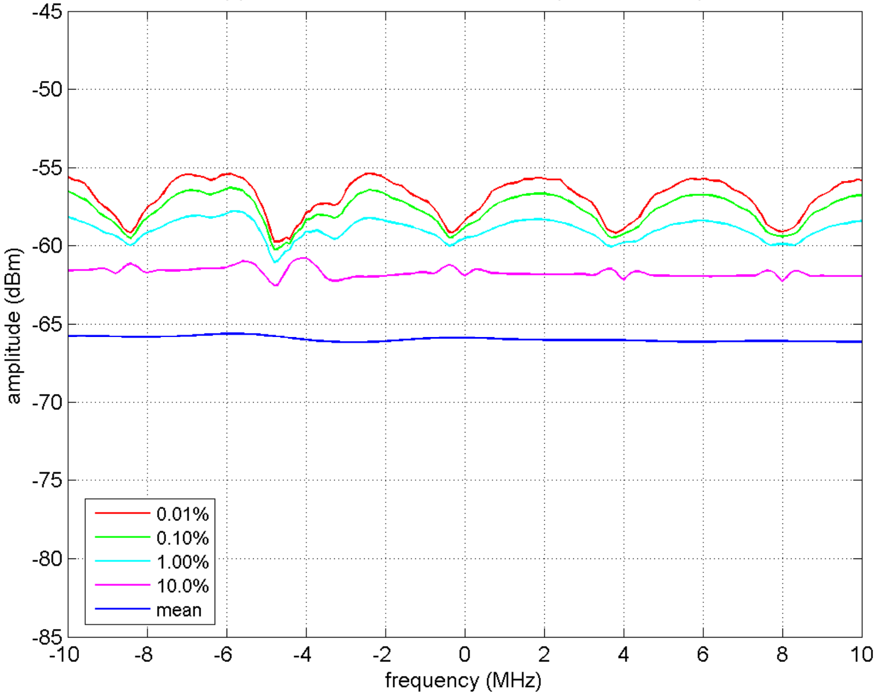
(a) mb03: RF VSA measurements (RBW = 1 MHz)

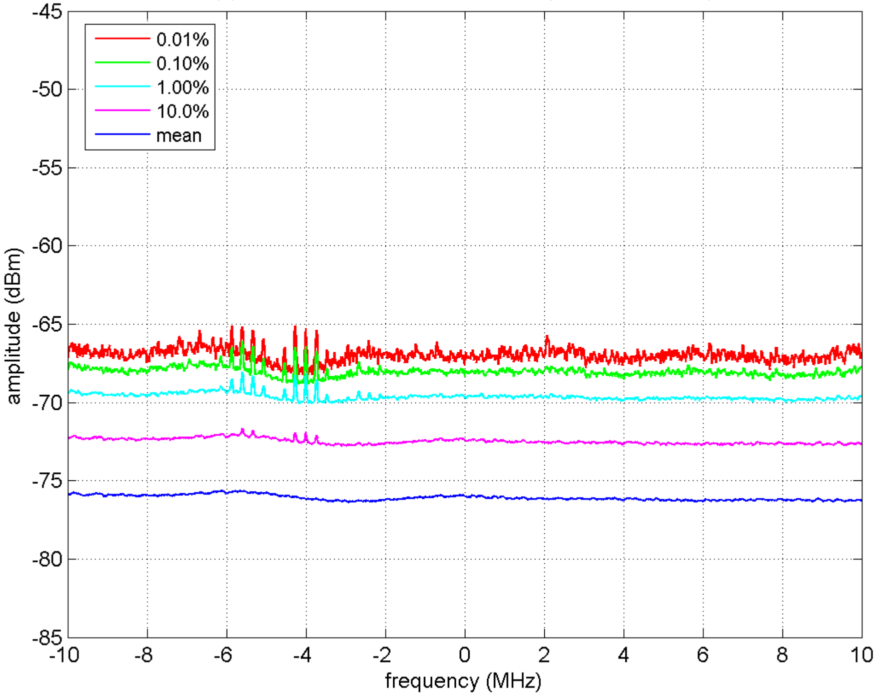
(b) mb03: RF VSA measurements (RBW = 0.1 MHz)

Figure B-75. RF spectral analyses of MB-03 ($b = 3$, $d = 2$).

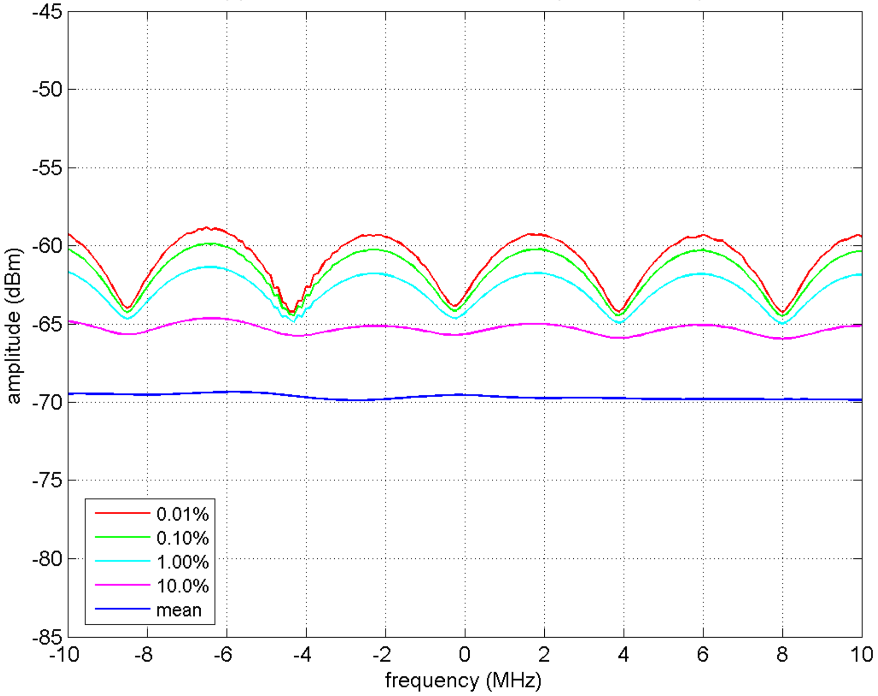

(a) mb04: RF VSA measurements (RBW = 1 MHz)

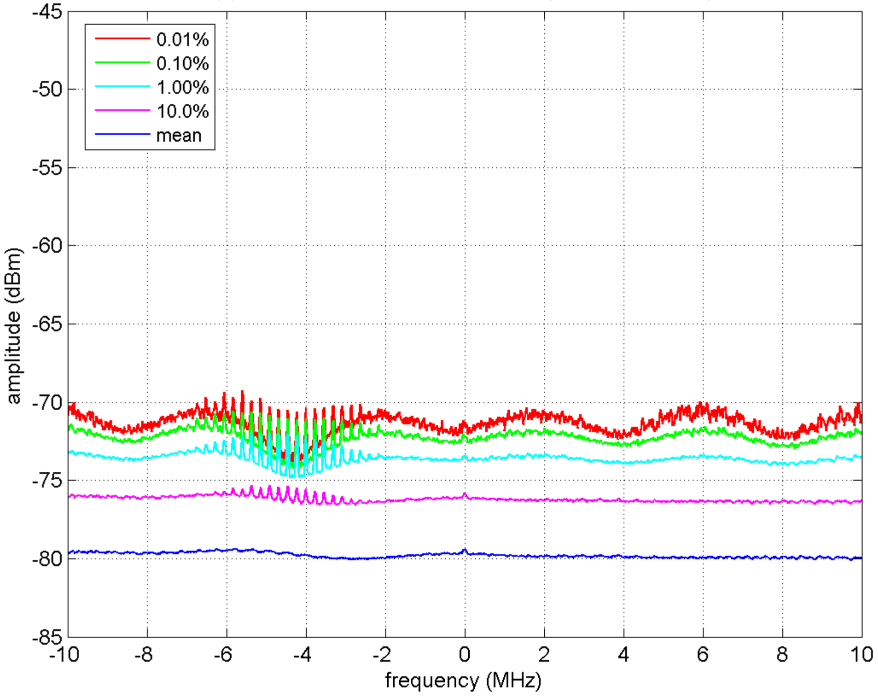

(b) mb04: RF VSA measurements (RBW = 0.1 MHz)

Figure B-76. RF spectral analyses of MB-04 ($b = 7$, $d = 1$).

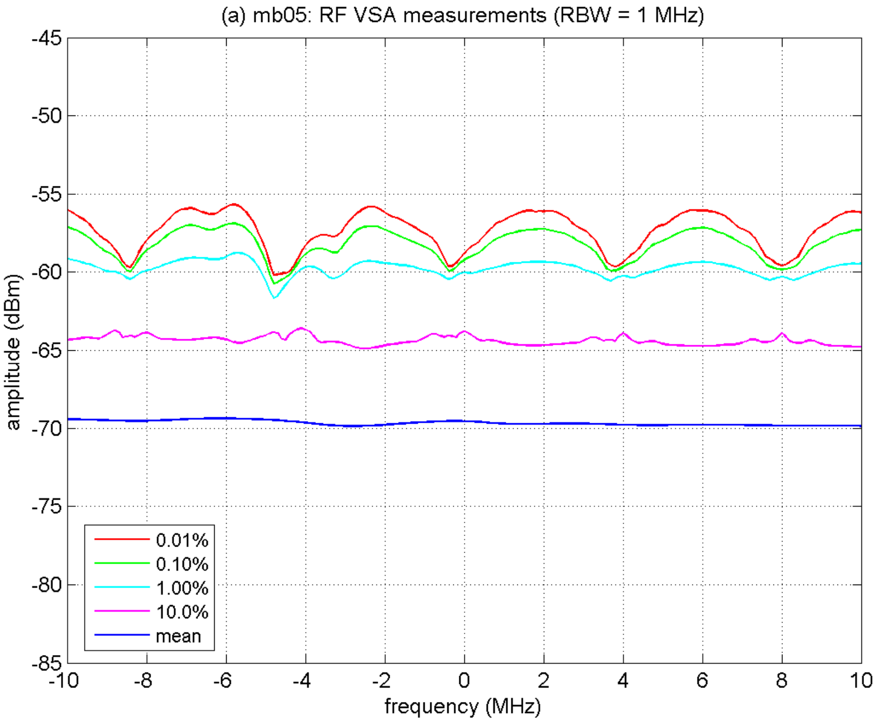

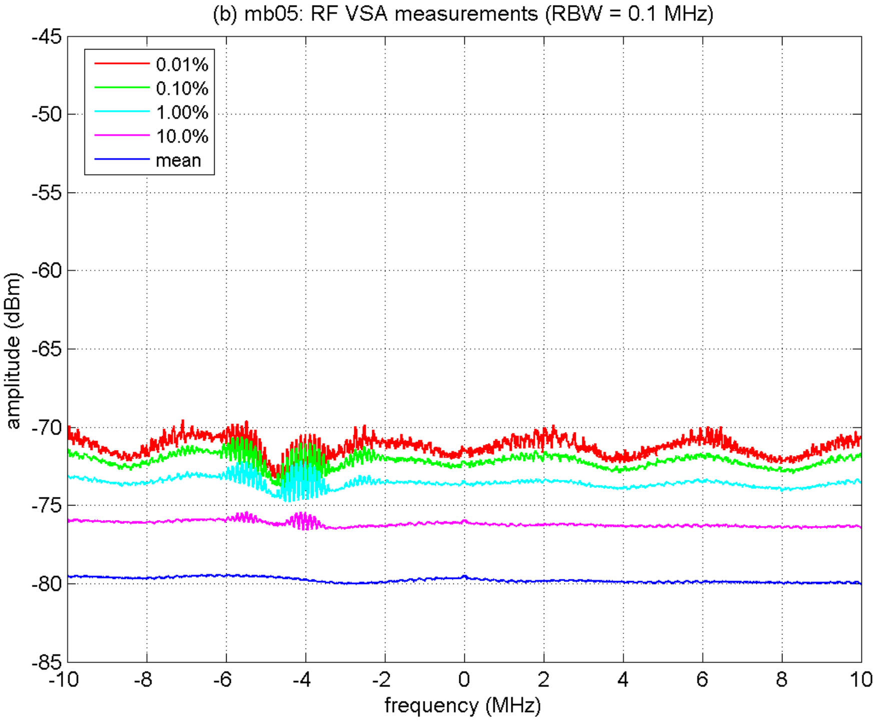

Figure B-77. RF spectral analyses of MB-05 ($b = 7$, $d = 2$).

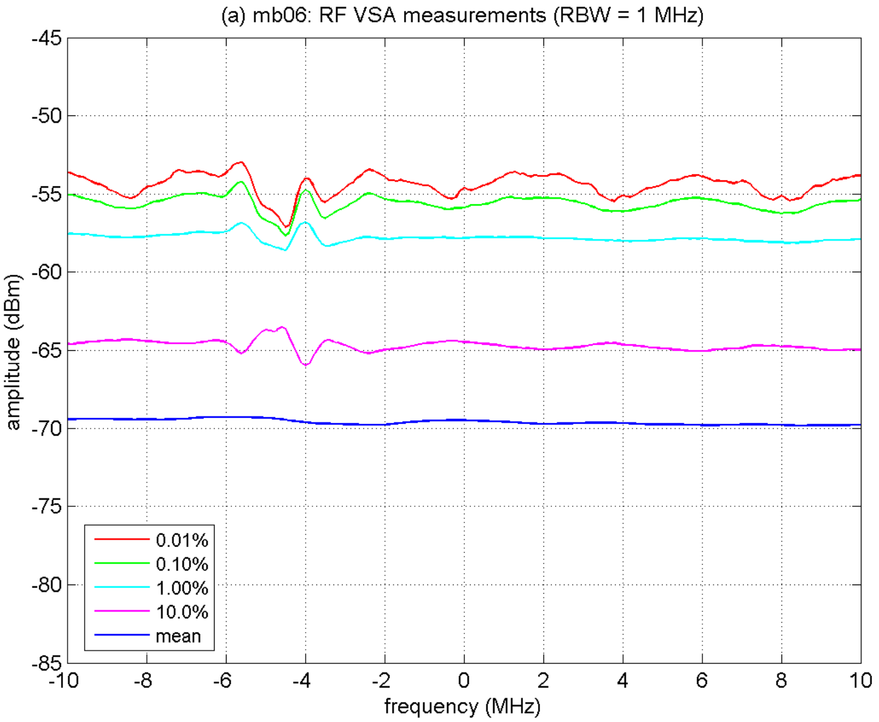

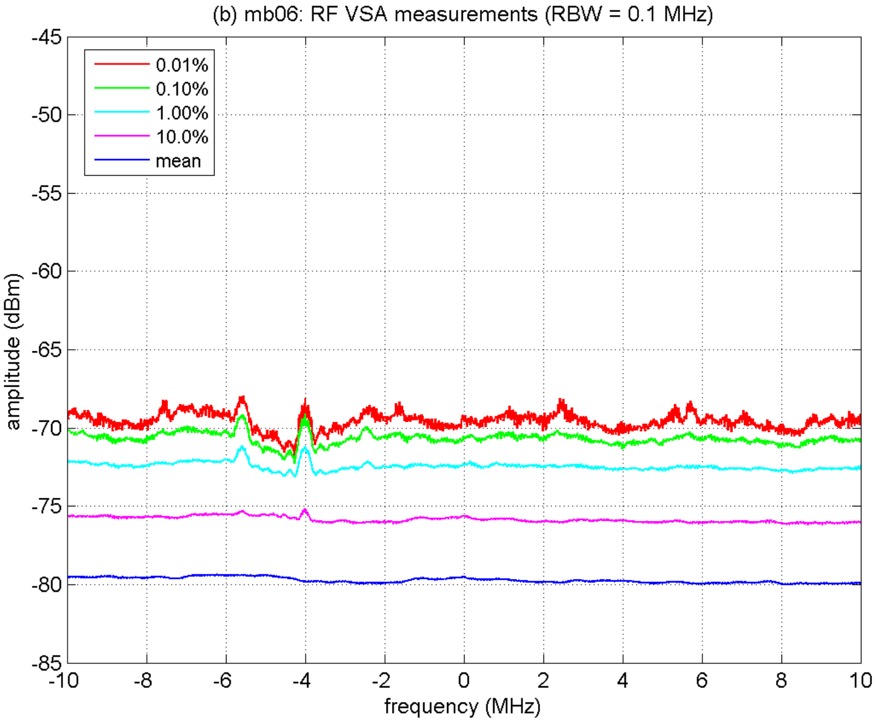

Figure B-78. RF spectral analyses of MB-06 ($b = 7$, $d = 6$).

(a) mb07: RF VSA measurements (RBW = 1 MHz)

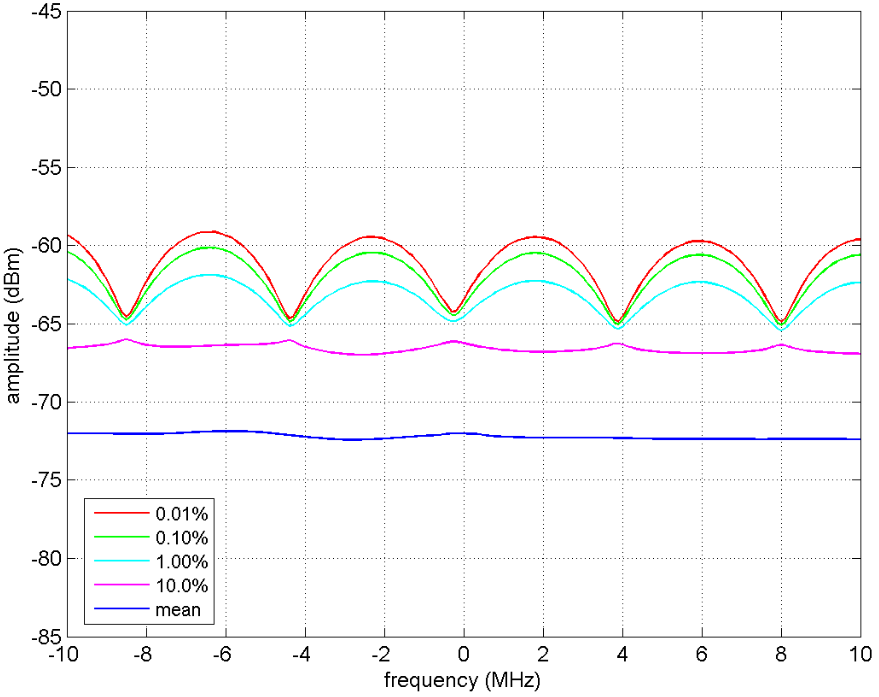

(b) mb07: RF VSA measurements (RBW = 0.1 MHz)

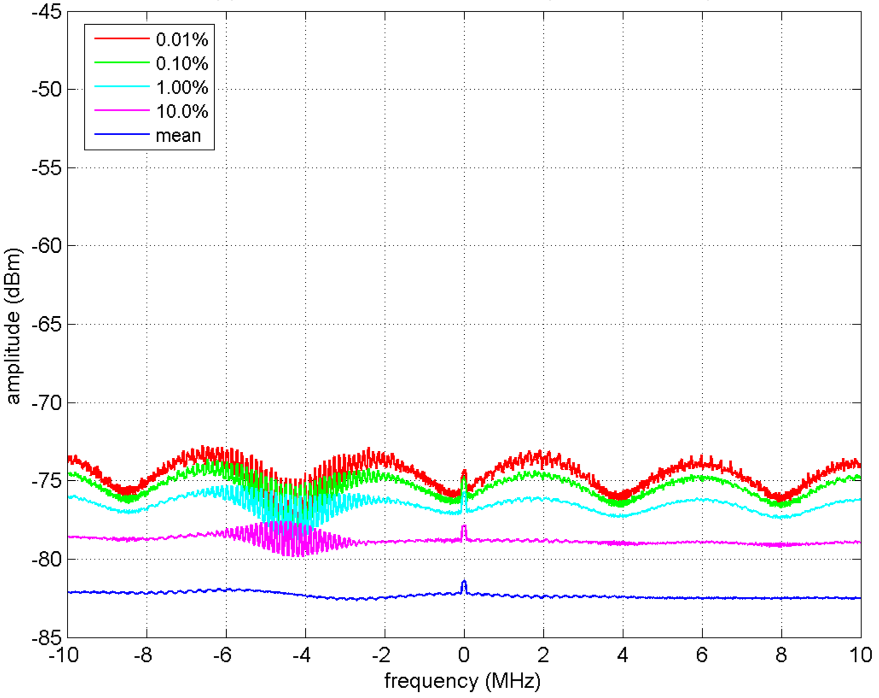

Figure B-79. RF spectral analyses of MB-07 (*b* = 13, *d* = 1).

(a) mb08: RF VSA measurements (RBW = 1 MHz)

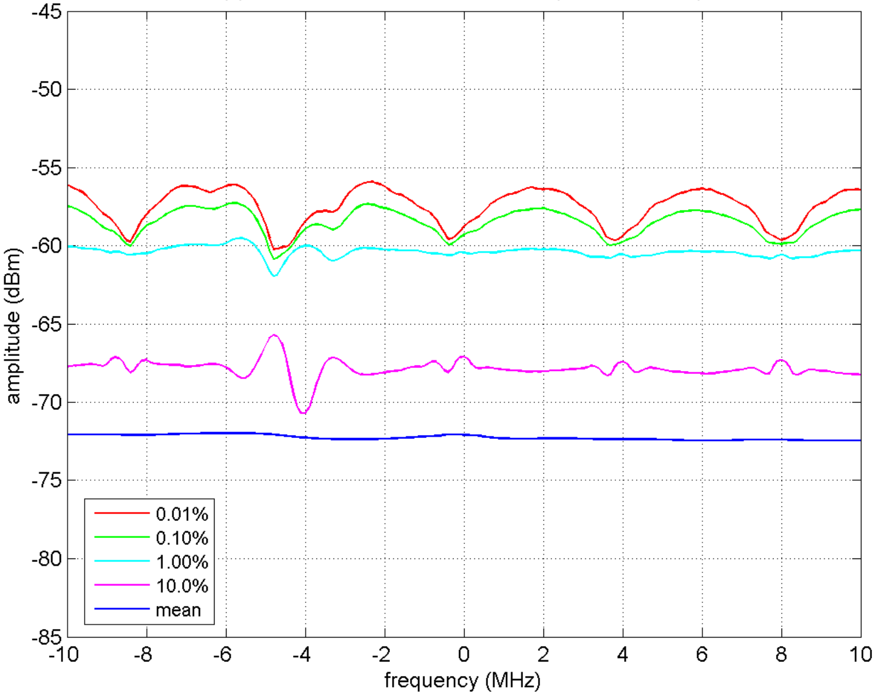

(b) mb08: RF VSA measurements (RBW = 0.1 MHz)

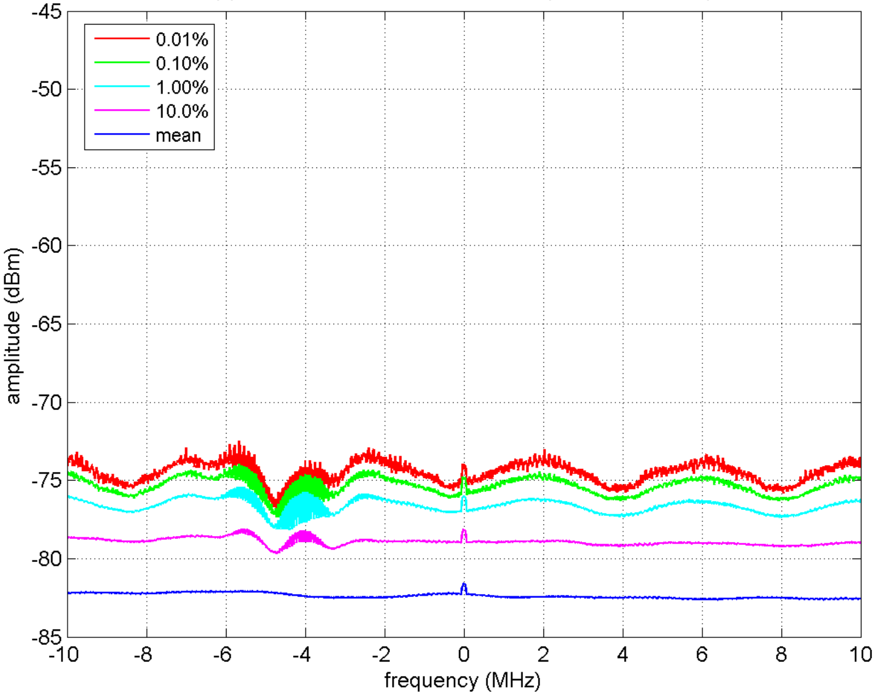

Figure B-80. RF spectral analyses of MB-08 (b = 13, d = 2).

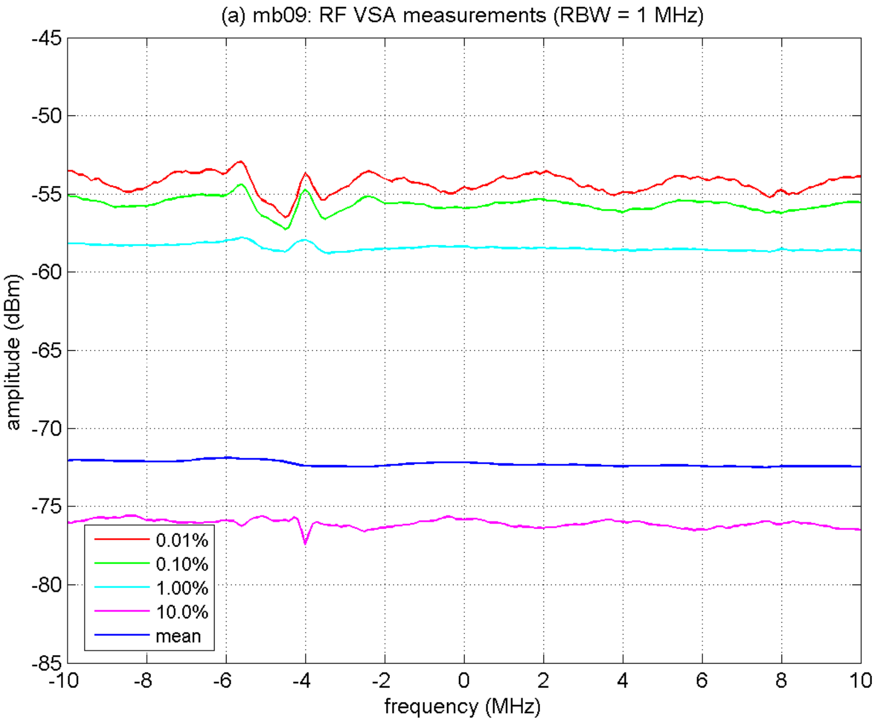

(a) mb09: RF VSA measurements (RBW = 1 MHz)

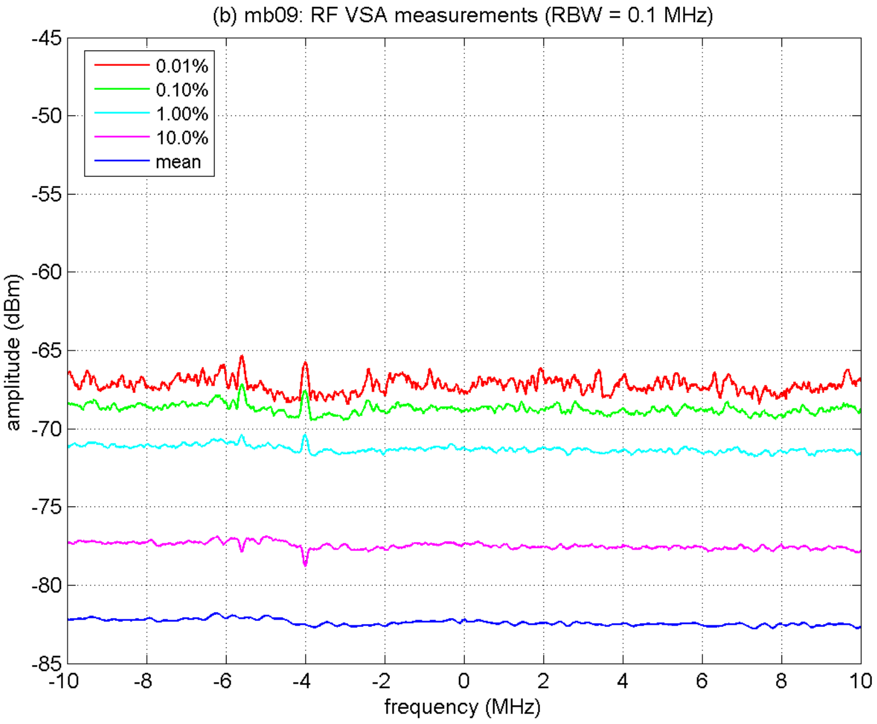

(b) mb09: RF VSA measurements (RBW = 0.1 MHz)

Figure B-81. RF spectral analyses of MB-09 (*b* = 13, *d* = 12).

FORM **NTIA-29**
(4-80)

U.S. DEPARTMENT OF COMMERCE
NAT'L. TELECOMMUNICATIONS AND INFORMATION ADMINISTRATION

BIBLIOGRAPHIC DATA SHEET

1. PUBLICATION NO. TR-06-437	2. Government Accession No.	3. Recipient's Accession No.

4. TITLE AND SUBTITLE Interference Potential of Ultrawideband Signals --- Part 3: Measurements of Ultrawideband Interference to C-Band Satellite Digital Television Receivers	5. Publication Date February 2006
	6. Performing Organization Code 511-6592000-300
7. AUTHOR(S) Michael Cotton, Robert Achatz, Jeffery Wepman, and Roger Dalke	9. Project/Task/Work Unit No.
8. PERFORMING ORGANIZATION NAME AND ADDRESS NTIA/ITS U.S. Department of Commerce 325 Broadway Boulder, CO 80305	10. Contract/Grant No.
11. Sponsoring Organization Name and Address	12. Type of Report and Period Covered

14. SUPPLEMENTARY NOTES

15. ABSTRACT (A 200-word or less factual summary of most significant information. If document includes a significant bibliography or literature survey, mention it here.)

This report provides results from tests that measured digital television (DTV) susceptibility to ultrawideband (UWB) interference. A test system was developed to inject interference with known characteristics into a victim receiver and quantitatively measure susceptibility. In this experiment, a C-band satellite DTV victim receiver was injected with Dithered-Pulse (DP), Direct-Sequence (DS), and Multi-Band OFDM (MB) UWB interference. Results showed that the UWB signals could be categorized into three signal sets of common DTV susceptibility behavior. Interestingly, the categorized signals, band-limited by the DTV receiver filter, also had common characteristics. Set 1 consists of signals whose DTV susceptibility and band-limited signal characteristics resemble Gaussian noise. Set 2 consists of signals more deleterious than Gaussian noise interference. Notably, these signals had a wide range of band-limited signal characteristics and susceptibilities. Set 3 consists of a signal that is relatively benign. Results also showed that measurable band-limited characteristics, e.g., burst duration (*BD*), burst interval (*BI*), fractional on-time (ζ_{DTV}), and peak-to-average ratio (*P/A*), of the interfering signal are useful for predicting susceptibility. Finally, it was determined that continuous and gated noise signals can be used to emulate the interference effects of DS and MB signals for the DTV victim receiver and operational scenarios tested in this study. This might not be true, however, for testing the susceptibility of other victim receivers operating in narrower bandwidths as indicated by amplitude probability distributions as a function of frequency for MB signals band-limited to relatively narrow bandwidths.

16. Key Words (Alphabetical order, separated by semicolons)
Digital television; interference; satellite communications; ultrawideband

17. AVAILABILITY STATEMENT UNLIMITED.	18. Security Class. (This report)	20. Number of pages
	19. Security Class. (This page)	21. Price:

NTIA FORMAL PUBLICATION SERIES

NTIA MONOGRAPH (MG)

A scholarly, professionally oriented publication dealing with state-of-the-art research or an authoritative treatment of a broad area. Expected to have long-lasting value.

NTIA SPECIAL PUBLICATION (SP)

Conference proceedings, bibliographies, selected speeches, course and instructional materials, directories, and major studies mandated by Congress.

NTIA REPORT (TR)

Important contributions to existing knowledge of less breadth than a monograph, such as results of completed projects and major activities. Subsets of this series include:

NTIA RESTRICTED REPORT (RR)

Contributions that are limited in distribution because of national security classification or Departmental constraints.

NTIA CONTRACTOR REPORT (CR)

Information generated under an NTIA contract or grant, written by the contractor, and considered an important contribution to existing knowledge.

JOINT NTIA/OTHER-AGENCY REPORT (JR)

This report receives both local NTIA and other agency review. Both agencies' logos and report series numbering appear on the cover.

NTIA SOFTWARE & DATA PRODUCTS (SD)

Software such as programs, test data, and sound/video files. This series can be used to transfer technology to U.S. industry.

NTIA HANDBOOK (HB)

Information pertaining to technical procedures, reference and data guides, and formal user's manuals that are expected to be pertinent for a long time.

NTIA TECHNICAL MEMORANDUM (TM)

Technical information typically of less breadth than an NTIA Report. The series includes data, preliminary project results, and information for a specific, limited audience.

For information about NTIA publications, contact the NTIA/ITS Technical Publications Office at 325 Broadway, Boulder, CO, 80305 Tel. (303) 497-3572 or e-mail info@its.bldrdoc.gov.

This report is for sale by the National Technical Information Service, 5285 Port Royal Road, Springfield, VA 22161,Tel. (800) 553-6847.